

Idiopathic pulmonary fibrosis: a study using volumetric imaging and functional data in a computational lung model

Yuwen Zhang

A thesis submitted in fulfilment of the requirements for the degree of Doctor of
Philosophy in Bioengineering.

This thesis is for examination purposes only and is confidential to the examination
process.

Auckland Bioengineering Institute

The University of Auckland

2018

Abstract

Idiopathic pulmonary fibrosis (IPF), the most aggressive and frequent form of idiopathic interstitial pneumonias (IIPs), is a chronic and life-threatening disease of unknown cause. It is characterized by progressive worsening of dyspnea and lung function and is associated with a poor prognosis. IPF occurs primarily in middle-aged and elderly adults, and is more frequent in males than females. Even worse, the aetiology of IPF remains elusive, and its progression is variable and unpredictable, hence there are no biomarkers that can indicate the likely progression of the disease. A consistent quantification scheme that allows recognition of disease identically across radiology, pulmonary and pathology disciplines remains difficult.

High resolution computed tomography (HRCT) has played an essential role in evaluating lung disease through recognizing visual patterns and features of disease regions. In this study, a computational modeling of lung function in IPF was developed, combined with quantitative information extracted from HRCT imaging and clinical knowledge to help with a better understanding of the progression of IPF and investigate strategies for patient-specific diagnosis and treatment planning for IPF patients.

First, an automatic lung lobe segmentation method from HRCT images was developed. A principle component analysis based statistical finite element shape model of lobes was applied to guide lobar segmentation that can predict the likely region of fissure

locations initially. An eigenvalue of Hessian matrix analysis and a connected component eigenvector based analysis were subsequently used to determine a set of fissure-like candidate points. A smooth multi-level B-spline curve is fitted to the most fissure-like points to generate the final lobar boundaries. The result shows that the method was able to estimate the fissure location in 100% of cases including both normal healthy and IPF subjects, whereas two comparison segmentation softwares that use anatomy-based methods will fail for some of them.

Second, tissue abnormalities in IPF lungs were classified and quantified from HRCT images. Lung tissues were classified as normal, reticular, ground glass, or emphysema using CALIPER (Computer-Aided Lung Informatics for Pathology Evaluation and Ratings) software. The classified data was mapped to a statistical shape model, and quantitative approaches was used to analyze tissue density, tissue volume, the spatial distribution of abnormalities, and regional changes in tissue over time. Principle component analysis (PCA) based statistical shape model was applied to understand lung shape differences between IPF and normal older lungs through quantifying principal modes of shape variation of both IPF and old normal subjects. The result shows that fibrosis has higher tissue density compared with normal tissue, and presented predominantly basally and peripherally. In contrast, emphysema has lower tissue density and mostly located in upper lobes. The first principal SSM mode ($> 20\%$ of the shape variation in normal lungs) is significantly different between IPF and normal and strongly correlated with fibrosis extent in IPF lungs.

Third, a computational model of lung function was developed which integrated quantification analysis from volumetric CT data and pulmonary functional test to understand differences between IPF and normal older lungs. For each patient, a subject-specific lung mesh that represents the statistical lung shape of old normal people with

the same individual information was predicted using statistical shape model. Anatomically based airway and blood vessel trees were generated derived from HRCT images, respectively matched to IPF lung mesh and the corresponding old normal lung mesh. The ventilation, perfusion and gas exchange models were then constricted to simulate \dot{V} , \dot{Q} distribution and gas transport in normal and disease constricted condition, respectively. The result shows that the computational model can reasonably predict the patient-specific ventilation, perfusion and gas exchange in IPF lung, and quantify the difference of lung function between IPF patient and older normal people. The abnormalities on volumetric CT imaging may be not able to provide enough information to explain the decline of lung function in IPF patient, and the impaired gas exchange will happen in not only abnormal region but also in CT-visualized 'normal' tissues.

IPF is a complex and progressive disease that has multifarious physiological processes and significant individual differences. The methods and models presented in this thesis provide a basis for application to research in IPF lung function, and further investigations of the underlying relationship between physiology mechanisms and disease progressions of IPF.

Acknowledgement

I would like to thank...

Table of Contents

Abstract	v
Acknowledgement	vii
Table of Contents	xiv
List of Figures	xxxv
List of Tables	xxxix
List of Abbreviations	xliii
1 Introduction	1
1.1 Motivation	1
1.2 Thesis Objectives	2
1.3 Thesis Overview	3
2 Background	7
2.1 Introduction to idiopathic pulmonary fibrosis	7
2.1.1 Definition	7
2.1.2 Disease classification	8

2.2 Epidemiology, etiology and pathogenesis	10
2.2.1 Epidemiology	10
2.2.2 Pathogenesis and potential contributors to etiology	10
2.3 Diagnosis	12
2.3.1 Clinical presentations	13
2.3.2 Radiographic features	14
2.3.3 Histopathology	15
2.3.4 Diagnostic criteria	17
2.4 Clinical course	19
2.4.1 Slow and rapid progressive course	20
2.4.2 Acute exacerbations of IPF	20
2.5 Complications and comorbidities	21
2.5.1 IPF and emphysema	22
2.5.2 IPF and pulmonary hypertension	23
2.6 Physiological alterations	24
2.6.1 Alterations in the mechanical properties of the lung	24
2.6.2 Alterations in pulmonary gas exchange	29
2.7 Summary	32
3 Pulmonary lobar segmentation from CT scans	35
3.1 Background	36
3.1.1 Pulmonary lobe anatomy	36
3.1.2 High resolution computed tomography	37
3.1.3 The importance of pulmonary lobar segmentation	38

3.1.4	Challenges of automatic pulmonary lobar segmentation from CT scans	39
3.2	Review of current published methods for pulmonary lobar segmentation	40
3.2.1	Lung segmentation	41
3.2.2	Fissure detection	47
3.3	Methods: automatic statistical shape model based lobar segmentation method	52
3.3.1	Lung segmentation	55
3.3.2	Statistical finite element models of lung and fissure shape	55
3.3.3	Initial prediction of lobar location in an individual	62
3.3.4	Multiscale Hessian-based fissure detection	65
3.3.5	Interactive user control interface	72
3.4	Experiments	77
3.4.1	Testing CT dataset	77
3.4.2	Test and results	78
3.5	Discussion	88
3.6	Summary	92
4	Quantitative computerized analysis of idiopathic pulmonary fibrosis	93
4.1	Background	94
4.1.1	Challenges of IPF diagnosis	94
4.1.2	Advantages of quantitative analysis using HRCT	95
4.1.3	Review of current published methods of quantitative analysis of lung disease	97

4.1.4 Computer-Aided Lung Informatics for Pathology Evaluation and Ratings	100
4.2 Methods: quantitative analysis of IPF lungs	104
4.2.1 Tissue classification of IPF lungs	104
4.2.2 Tissue quantification of IPF lungs	108
4.2.3 Volume analysis of IPF lungs	110
4.2.4 SSM based shape analysis of IPF lungs	111
4.3 Results	113
4.3.1 Normalization of classified data	113
4.3.2 Tissue quantification of IPF lungs	115
4.3.3 Volume analysis of IPF lungs	133
4.3.4 SSM based shape analysis of IPF lungs	135
4.4 Discussion	141
4.5 Summary	143
5 Functional modeling of idiopathic pulmonary fibrosis	145
5.1 Respiratory function in older people	146
5.1.1 Aging-associated alterations in chest wall and respiratory muscle function	147
5.1.2 Aging-associated alterations in pulmonary mechanics and lung volumes	149
5.1.3 Aging-associated alterations in gas exchange	150
5.2 Methods: Patient-specific modeling of IPF lung function	151
5.2.1 Clinical data	153
5.2.2 Construction of lung lobe geometry	153

5.2.3	Construction of airway/vasculature geometry	156
5.2.4	Construction of computational models	161
5.2.5	Model solutions	172
5.3	Results	176
5.3.1	Construction of lung lobe geometry	176
5.3.2	Construction of airway/vasculature geometry	177
5.3.3	Deep inspiration modeling	181
5.3.4	Gas exchange model	182
5.4	Discussion	187
5.5	Summary	189
6	Conclusion	191
6.1	Thesis Summary	191
6.2	Future directions	195
6.2.1	Improvement of statistical shape model	195
6.2.2	Involvement of diffusing capacity for carbon monoxide in the lung functional model	195
6.2.3	Relationship between lung vasculature and tissue abnormality or lung function in patients with IPF	196
Appendices		199
A	Spatial distribution of abnormalities for each patient	201
A.1	Basal-to-apical distribution over time for each patient	201
A.2	Dorso-to-ventral distribution over time for each patient	213
A.3	Lobar distribution over time for each patient	223

B Figures of V/Q ratio and arterial oxygen distribution	233
--	------------

List of References	245
---------------------------	------------

List of Figures

2.1 Classification of the interstitial lung diseases. IPF belongs to the family of interstitial lung disease (ILD), and belongs to a subgroup known as idiopathic interstitial pneumonia (IIP). Reproduced from (Troy and Corte, 2012).	9
2.2 HRCT images of UIP pattern from two patients. The first is from a woman with progressive cough and dyspnoea, showing her upper (a), lower (b) lung zones and a sagittal plane of the lungs (c). These images show lower lobe-predominant peripheral honeycomb change (b and c, arrows), which is typical of UIP pattern. This patient had no systemic disease or exposures that would exclude idiopathic disease, the diagnosis of IPF is certain. In contrast, the second is a woman with progressive breathlessness, who could be diagnosed with possible IPF. The upper (d), lower (e) lung zones and sagittal image of the lungs (f) demonstrate peripheral, basilar-predominant, reticular densities with traction bronchiectasis (e and f, arrows) consistent with fibrosis. Surgical lung biopsy is suggested. Reproduced from (Martinez et al., 2017).	15

3.3 Illustration of the performance of conventional 3D thresholding lung segmentation methods on pathological abnormal lungs. Lung borders are not recognized accurately because of the higher densities of the abnormalities compared to the normal tissues. Reproduced from (Van Rikxoort and Van Ginneken, 2013).	44
3.4 (a) Segmented volumes of the vascular tree. There are no large vessels in the vicinity of lobar fissures. (b) Anatomically labeled airway tree showing lobar subtrees. The airway tree can be classified corresponding to five lobes. Reproduced from (Ukil and Reinhardt, 2009).	47
3.5 Flow diagram of the lobar segmentation process.	54
3.6 Lung segmentation result. (a) Raw CT image. (b) Segmented lungs. . .	55
3.7 Finite element modeling of lung lobe shape. (a) Lung surface data extracted from segmented lung masks (purple points for left lung, blue points for right lung). (b) Manual digitized fissure points in 2D sagittal image of right lung (purple points for right oblique fissure, blue points for right horizontal fissure). (c) Manual digitized fissure points shown in 3D (pink points for left oblique fissure, purple points for right oblique fissure, blue points for right horizontal fissure). (d) Lobe shape fitting with lung surface data and digitized fissure data of right lung.	60
3.8 Statistical shape model construction based on principle component analysis. (a) Procrustes aligned meshes of 50 subjects. (b) Average shape model of 50 training subjects. All the weight values are zero for this shape model.	63

3.9 Fissure prediction results compared to ground truth fissure points. The fissure surface meshes are estimated fissure locations and the red points are manual tracing fissure points by an expert. (a) Left lung. (b) Right lung.	64
3.10 The three eigenvectors of the Hessian matrix representing plane-like structure (fissure). λ_1 and λ_2 are parallel to fissure plane, λ_3 is perpendicular to fissure plane.	69
3.11 The three eigenvectors of the Hessian matrix representing tube-like structure (vessel). λ_1 is parallel to vessel tube, λ_2 and λ_3 are perpendicular to vessel tube.	71
3.12 Hessian-based multiscale fissure detection results. (a) Hessian-based plane-like structure enhancement filter. (b) Remove vessel voxels (tube-like structures). (c) Selected search regions for fissure detection based on SSM initial fissure prediction. (d) 2D and 3D eigenvector based connected component filter. (e) Fissure candidate points. (f) β -spline curve fissure surface fitting.	73
3.13 PTK User interactive interface. It consists of data input section, image visualization section, user plugin section and toolbar section.	75
3.14 Fissure detection results before and after control the search regions. (a) Fissure detection result with a search distance of default 20 voxels. (b) Fissure detection result after setting a specific search distance depend on the accuracy of initial fissure guessing.	76

3.15 Manual correction on automatic fissure detection results (a) Manually select a set of landmarks on real fissure lines shown in raw images to correct automatic fissure detection results (red landmarks are for left oblique fissure, green landmarks are for right oblique fissure, blue landmarks are for right horizontal fissure). (b) Corrected fissure detection results shown with raw images. The corrected fissure lines can match the real fissure locations.	77
3.16 Sagittal, axial, and coronal views illustrating raw image, SSM based initial fissure guessing and automatic fissure detection results of a normal healthy subject. (a), (d), (g) are sagittal, axial and coronal raw images. (b), (e), (h) are sagittal, axial and coronal SSM based initial fissure guessing results. (c), (f), (i) are sagittal, axial and coronal automatic fissure detection results.	79
3.17 Sagittal, axial, and coronal views illustrating raw image, SSM based initial fissure guessing and automatic fissure detection results of an IPF subject. (a), (d), (g) are sagittal, axial and coronal raw images. (b), (e), (h) are sagittal, axial and coronal SSM based initial fissure guessing results. (c), (f), (i) are sagittal, axial and coronal automatic fissure detection results.	80
3.18 The spatial distribution of error between the gold-standard and semi-automatic methods for three representative subjects, highlighting localized regions of low accuracy.	82

3.19 An inaccurate initial fissure estimate for an IPF subject caused by mislabeling of lobar airway branches using marker-based interactive watershed transformation algorithm (sagittal view, left lung). (a) The mislabeling of lobar airway branches. Purple is for left upper branches and yellow is for left lower branches. The lower branches in the red box are mis-detected as upper branches. (b) The initial fissure guessing based on the erroneous airway branch labeling result. The approximate fissure has a significant erroneous shift in the red box where mislabeling of lobar airway branches occurs.	84
4.1 Computed tomography images demonstrating appearance and various visual manifestations of idiopathic pulmonary fibrosis: a) normal, b) ground glass, c) reticular changes (arrows), d) honeycombing (arrows) and e) emphysema (arrow). In training datasets, the consensus of four thoracic radiologists was used to identify multiple VOIs corresponding to normal, ground-glass density, reticular abnormalities, honeycombing and emphysema. Reproduced from (Maldonado et al., 2013).	101
4.2 Color labelled classification result of one subject diagnosed with IPF by CALIPER. (a) Transverse plane. (b) Coronal plane. (c) Sagittal plane. (d) 3D color labelled lung.	103
4.3 Diagram of gap filling steps within the mapped data. (a) Get axial slices of mapped data (with gaps). (b) Define lung boundary (SSM defined). (c) Get lung mask. (d) Fill the gaps within lung mask.	107
4.4 Diagram of subpleural-to-internal percentage measurement.	109

4.5 Classified data (top row) and mapped data (bottom row) of three time points from one subject diagnosed with IPF. (a) The first time point, scan time: 0 month. (b) The second time point, scan time: 15 months. (c) The third time point, scan time: 20 months	114
4.6 Axial slices with gaps (top row) and axial slices after gap filling (bottom row) of three time points from one subject diagnosed with IPF. (a) The first time point, scan time: 0 month. (b) The second time point, scan time: 5 months. (c) The third time point, scan time: 20 months.	115
4.7 Average tissue density (g/cm^3) of each CT pattern in IPF lungs. Each data point represents the tissue density of one time point from one patient. X axis represents the month interval of scan time for each patient, and "0" represents the first scan for this patient. (a) Tissue density of left lung. (b) Tissue density of right lung.	116
4.8 Volume percentage of each tissue classification plotted against lung height (cranio-caudal axis) in IPF left and right lungs. The average percentage was calculated within 5% sections of the lung height from the base to apex. Red shows the average value at each position across all patients, and blue shows the standard deviation. (a) (b) is ground-glass distribution. (c) (d) is reticular distribution. (e) (f) is honeycomb distribution. (g) (h) is emphysema distribution.	118

4.12 Volume percentage of each tissue classification plotted in the direction of dorso-ventral axis in IPF left and right lungs at month 0. The average percentage was calculated within 5% sections along dorso-ventral axis from the back to front. Red shows the average value at each position across all patients, and blue shows the standard deviation. (a) (b) is ground-glass distribution. (c) (d) is reticular distribution. (e) (f) is honeycomb distribution. (g) (h) is emphysema distribution.	124
4.13 Volume percentage of each tissue classification plotted in the direction of dorso-ventral axis from one patient diagnosed with IPF in left and right lungs over time. The average percentage was calculated within 5% sections along dorso-ventral axis from the back to front. (a) (b) is ground-glass distribution. (c) (d) is reticular distribution. (e) (f) is honeycomb distribution. (g) (h) is emphysema distribution.	126
4.14 Subpleural-to-internal percentage of connected cluster of disease in IPF left and right lung. (a) Left lung. (b) Right lung.	127
4.15 Average lobar distribution of disease CT patterns. The tissue percentage in different lobe is shown in different color, and each bar represents the volume percentage of the CT pattern for one lobe across all the subjects. The black line represents the standard deviation. (a) Ground-glass lobar distribution. (b) Reticular lobar distribution. (c) Honeycomb lobar distribution. (d) Emphysema lobar distribution.	129

4.16 Lobar distribution of disease CT patterns of one patient diagnosed with IPF over time. The tissue percentage in different lobe is shown in different color, and each bar represents the volume percentage of the CT pattern for one lobe. (a) Ground-glass lobar distribution. (b) Reticular lobar distribution. (c) Honeycomb lobar distribution. (d) Emphysema lobar distribution.	130
4.17 CALIPER tissue classification overlapping on raw image. Green is the normal region, red is the reticular region, yellow is the ground-glass region, and blue is the mildLAA region. (a) Axial view. (b) Sagittal view.	133
4.18 Shape differences between IPF subjects and old normal subjects of the first three modes (shown with different time point). (a) Mode 1 weight. (b) Mode 2 weight. (c) Mode 3 weight.	136
4.19 PCA-derived shape variation of the first shape mode, with different values of standard deviation (- 3σ , - 1σ , μ , 1σ , 3σ) added to the mean shape model. (a) Anterior view. (b) Basal view. (c) Posterior view.	138
4.20 The Linear regression of the PCA-derived first three modes with respect to overall fibrosis percentage. (a) Mode 1 weight. (b) Mode 2 weight. (c) Mode 3 weight.	140
5.1 Computational modeling framework for IPF and older normal lung function.	152

5.2 Generation of airway tree. (a) Manual digitized upper airway tree from HRCT images in 3D. Blue lines are the centerlines of upper airway tree, and red points represent airway nodes. (b) Geometry of full conducting airway tree generated using volume-filling algorithm. The model is shown from the anterior view, with the left lung on right, and right lung on left.	158
5.3 Disease labeled airway nodes. Green is the normal region, blue is the fibrosis region, and red is the emphysema region.	173
5.4 Lung mesh of IPF and the corresponding predicted lung mesh of old normal. (a) IPF lung mesh generated from CT imaging of a patient with IPF. (b) Old normal lung mesh predicted with the individual information of the same patient.	176
5.5 Generated normal airway tree (top row) and IPF airway tree (bottom row) for one patient diagnosed with IPF. (a) Anterior view. (b) Left lung side. (c) Right lung side.	178
5.6 Generated geometry of vessel tree. (a) IPF vessel tree. (b) Old normal vessel tree. The radius of branches were visualized with different colors. The colorbar shows the range of radius.	179
5.7 Deep inspiration and muscle pressure curve. The red line is the muscle pressure curve. The blue lines is the CT-based simulated inspiration curve with CAPLIPER fibrosis labeled, and red line is the PFT-based simulated inspiration curve with additional fibrosis labeled.	182

5.8 V/Q ratio distribution and arterial oxygen distribution of normal, CT-based and PFT-based simulation result of one time point from one patient diagnosed with IPF using MIGET). (a) V and Q flow with respect to V/Q ratio. (b) V and Q percentage with respect to arterial oxygen level.	184
5.9 Ventilation, perfusion and V/Q ratio distribution against lung height (cranio-caudal axis). (a) Ventilation distribution against lung height. (b) Perfusion distribution against lung height. (c) V/Q ratio distribution against lung height.	186
A.1 Volume percentage of each tissue classification plotted against lung height (cranio-caudal axis) of case IPF2 in left and right lungs over time. The average percentage was calculated within 5% sections of the lung height from the base to apex. (a) (b) is ground-glass distribution. (c) (d) is reticular distribution. (e) (f) is honeycomb distribution. (g) (h) is emphysema distribution.	202
A.2 Volume percentage of each tissue classification plotted against lung height (cranio-caudal axis) of case IPF3 in left and right lungs over time. The average percentage was calculated within 5% sections of the lung height from the base to apex. (a) (b) is ground-glass distribution. (c) (d) is reticular distribution. (e) (f) is honeycomb distribution. (g) (h) is emphysema distribution.	203

A.3 Volume percentage of each tissue classification plotted against lung height (cranio-caudal axis) of case IPF5 in left and right lungs over time. The average percentage was calculated within 5% sections of the lung height from the base to apex. (a) (b) is ground-glass distribution. (c) (d) is reticular distribution. (e) (f) is honeycomb distribution. (g) (h) is emphysema distribution.	204
A.4 Volume percentage of each tissue classification plotted against lung height (cranio-caudal axis) of case IPF6 in left and right lungs over time. The average percentage was calculated within 5% sections of the lung height from the base to apex. (a) (b) is ground-glass distribution. (c) (d) is reticular distribution. (e) (f) is honeycomb distribution. (g) (h) is emphysema distribution.	205
A.5 Volume percentage of each tissue classification plotted against lung height (cranio-caudal axis) of case IPF9 in left and right lungs over time. The average percentage was calculated within 5% sections of the lung height from the base to apex. (a) (b) is ground-glass distribution. (c) (d) is reticular distribution. (e) (f) is honeycomb distribution. (g) (h) is emphysema distribution.	206
A.6 Volume percentage of each tissue classification plotted against lung height (cranio-caudal axis) of case IPF10 in left and right lungs over time. The average percentage was calculated within 5% sections of the lung height from the base to apex. (a) (b) is ground-glass distribution. (c) (d) is reticular distribution. (e) (f) is honeycomb distribution. (g) (h) is emphysema distribution.	207

A.7 Volume percentage of each tissue classification plotted against lung height (cranio-caudal axis) of case IPF13 in left and right lungs over time. The average percentage was calculated within 5% sections of the lung height from the base to apex. (a) (b) is ground-glass distribution. (c) (d) is reticular distribution. (e) (f) is honeycomb distribution. (g) (h) is emphysema distribution.	208
A.8 Volume percentage of each tissue classification plotted against lung height (cranio-caudal axis) of case IPF14 in left and right lungs over time. The average percentage was calculated within 5% sections of the lung height from the base to apex. (a) (b) is ground-glass distribution. (c) (d) is reticular distribution. (e) (f) is honeycomb distribution. (g) (h) is emphysema distribution.	209
A.9 Volume percentage of each tissue classification plotted against lung height (cranio-caudal axis) of case IPF15 in left and right lungs over time. The average percentage was calculated within 5% sections of the lung height from the base to apex. (a) (b) is ground-glass distribution. (c) (d) is reticular distribution. (e) (f) is honeycomb distribution. (g) (h) is emphysema distribution.	210
A.10 Volume percentage of each tissue classification plotted against lung height (cranio-caudal axis) of case IPF21 in left and right lungs over time. The average percentage was calculated within 5% sections of the lung height from the base to apex. (a) (b) is ground-glass distribution. (c) (d) is reticular distribution. (e) (f) is honeycomb distribution. (g) (h) is emphysema distribution.	211

A.11 Volume percentage of each tissue classification plotted in the direction of dorso-ventral axis of case IPF2 in left and right lungs over time. The average percentage was calculated within 5% sections along dorso-ventral axis from the back to front. (a) (b) is ground-glass distribution. (c) (d) is reticular distribution. (e) (f) is honeycomb distribution. (g) (h) is emphysema distribution.	213
A.12 Volume percentage of each tissue classification plotted in the direction of dorso-ventral axis of case IPF3 in left and right lungs over time. The average percentage was calculated within 5% sections along dorso-ventral axis from the back to front. (a) (b) is ground-glass distribution. (c) (d) is reticular distribution. (e) (f) is honeycomb distribution. (g) (h) is emphysema distribution.	214
A.13 Volume percentage of each tissue classification plotted in the direction of dorso-ventral axis of case IPF5 in left and right lungs over time. The average percentage was calculated within 5% sections along dorso-ventral axis from the back to front. (a) (b) is ground-glass distribution. (c) (d) is reticular distribution. (e) (f) is honeycomb distribution. (g) (h) is emphysema distribution.	215
A.14 Volume percentage of each tissue classification plotted in the direction of dorso-ventral axis of case IPF6 in left and right lungs over time. The average percentage was calculated within 5% sections along dorso-ventral axis from the back to front. (a) (b) is ground-glass distribution. (c) (d) is reticular distribution. (e) (f) is honeycomb distribution. (g) (h) is emphysema distribution.	216

A.15 Volume percentage of each tissue classification plotted in the direction of dorso-ventral axis of case IPF9 in left and right lungs over time. The average percentage was calculated within 5% sections along dorso-ventral axis from the back to front. (a) (b) is ground-glass distribution. (c) (d) is reticular distribution. (e) (f) is honeycomb distribution. (g) (h) is emphysema distribution.	217
A.16 Volume percentage of each tissue classification plotted in the direction of dorso-ventral axis of case IPF10 in left and right lungs over time. The average percentage was calculated within 5% sections along dorso-ventral axis from the back to front. (a) (b) is ground-glass distribution. (c) (d) is reticular distribution. (e) (f) is honeycomb distribution. (g) (h) is emphysema distribution.	218
A.17 Volume percentage of each tissue classification plotted in the direction of dorso-ventral axis of case IPF13 in left and right lungs over time. The average percentage was calculated within 5% sections along dorso-ventral axis from the back to front. (a) (b) is ground-glass distribution. (c) (d) is reticular distribution. (e) (f) is honeycomb distribution. (g) (h) is emphysema distribution.	219
A.18 Volume percentage of each tissue classification plotted in the direction of dorso-ventral axis of case IPF14 in left and right lungs over time. The average percentage was calculated within 5% sections along dorso-ventral axis from the back to front. (a) (b) is ground-glass distribution. (c) (d) is reticular distribution. (e) (f) is honeycomb distribution. (g) (h) is emphysema distribution.	220

A.19 Volume percentage of each tissue classification plotted in the direction of dorso-ventral axis of case IPF15 in left and right lungs over time. The average percentage was calculated within 5% sections along dorso-ventral axis from the back to front. (a) (b) is ground-glass distribution. (c) (d) is reticular distribution. (e) (f) is honeycomb distribution. (g) (h) is emphysema distribution.	221
A.20 Volume percentage of each tissue classification plotted in the direction of dorso-ventral axis of case IPF21 in left and right lungs over time. The average percentage was calculated within 5% sections along dorso-ventral axis from the back to front. (a) (b) is ground-glass distribution. (c) (d) is reticular distribution. (e) (f) is honeycomb distribution. (g) (h) is emphysema distribution.	222
A.21 Lobar distribution of disease CT patterns of case IPF2 diagnosed with IPF over time. The tissue percentage in different lobe is shown in different color, and each bar represents the volume percentage of the CT pattern for one lobe. (a) Ground-glass lobar distribution. (b) Reticular lobar distribution. (c) Honeycomb lobar distribution. (d) Emphysema lobar distribution.	223
A.22 Lobar distribution of disease CT patterns of case IPF3 diagnosed with IPF over time. The tissue percentage in different lobe is shown in different color, and each bar represents the volume percentage of the CT pattern for one lobe. (a) Ground-glass lobar distribution. (b) Reticular lobar distribution. (c) Honeycomb lobar distribution. (d) Emphysema lobar distribution.	224

A.23 Lobar distribution of disease CT patterns of case IPF5 diagnosed with IPF over time. The tissue percentage in different lobe is shown in different color, and each bar represents the volume percentage of the CT pattern for one lobe. (a) Ground-glass lobar distribution. (b) Reticular lobar distribution. (c) Honeycomb lobar distribution. (d) Emphysema lobar distribution.	225
A.24 Lobar distribution of disease CT patterns of case IPF6 diagnosed with IPF over time. The tissue percentage in different lobe is shown in different color, and each bar represents the volume percentage of the CT pattern for one lobe. (a) Ground-glass lobar distribution. (b) Reticular lobar distribution. (c) Honeycomb lobar distribution. (d) Emphysema lobar distribution.	226
A.25 Lobar distribution of disease CT patterns of case IPF9 diagnosed with IPF over time. The tissue percentage in different lobe is shown in different color, and each bar represents the volume percentage of the CT pattern for one lobe. (a) Ground-glass lobar distribution. (b) Reticular lobar distribution. (c) Honeycomb lobar distribution. (d) Emphysema lobar distribution.	227
A.26 Lobar distribution of disease CT patterns of case IPF10 diagnosed with IPF over time. The tissue percentage in different lobe is shown in different color, and each bar represents the volume percentage of the CT pattern for one lobe. (a) Ground-glass lobar distribution. (b) Reticular lobar distribution. (c) Honeycomb lobar distribution. (d) Emphysema lobar distribution.	228

A.27 Lobar distribution of disease CT patterns of case IPF13 diagnosed with IPF over time. The tissue percentage in different lobe is shown in different color, and each bar represents the volume percentage of the CT pattern for one lobe. (a) Ground-glass lobar distribution. (b) Reticular lobar distribution. (c) Honeycomb lobar distribution. (d) Emphysema lobar distribution.	229
A.28 Lobar distribution of disease CT patterns of case IPF14 diagnosed with IPF over time. The tissue percentage in different lobe is shown in different color, and each bar represents the volume percentage of the CT pattern for one lobe. (a) Ground-glass lobar distribution. (b) Reticular lobar distribution. (c) Honeycomb lobar distribution. (d) Emphysema lobar distribution.	230
A.29 Lobar distribution of disease CT patterns of case IPF15 diagnosed with IPF over time. The tissue percentage in different lobe is shown in different color, and each bar represents the volume percentage of the CT pattern for one lobe. (a) Ground-glass lobar distribution. (b) Reticular lobar distribution. (c) Honeycomb lobar distribution. (d) Emphysema lobar distribution.	231
A.30 Lobar distribution of disease CT patterns of case IPF21 diagnosed with IPF over time. The tissue percentage in different lobe is shown in different color, and each bar represents the volume percentage of the CT pattern for one lobe. (a) Ground-glass lobar distribution. (b) Reticular lobar distribution. (c) Honeycomb lobar distribution. (d) Emphysema lobar distribution.	232

B.1 V/Q ratio distribution and arterial oxygen distribution of normal, CT-based and PFT-based simulation result of the first time point of case IPF5 using MIGET). (a) V and Q flow with respect to V/Q ratio. (b) V and Q percentage with respect to arterial oxygen level.	234
B.2 Ventilation, perfusion and V/Q ratio distribution against lung height (cranio-caudal axis) of the first time point of case IPF5. (a) Ventilation distribution against lung height. (b) Perfusion distribution against lung height. (c) V/Q ratio distribution against lung height.	235
B.3 V/Q ratio distribution and arterial oxygen distribution of normal, CT-based and PFT-based simulation result of the second time point of case IPF5 using MIGET). (a) V and Q flow with respect to V/Q ratio. (b) V and Q percentage with respect to arterial oxygen level.	236
B.4 Ventilation, perfusion and V/Q ratio distribution against lung height (cranio-caudal axis) of the second time point of case IPF5. (a) Ventilation distribution against lung height. (b) Perfusion distribution against lung height. (c) V/Q ratio distribution against lung height.	237
B.5 V/Q ratio distribution and arterial oxygen distribution of normal, CT-based and PFT-based simulation result of the third time point of case IPF5 using MIGET). (a) V and Q flow with respect to V/Q ratio. (b) V and Q percentage with respect to arterial oxygen level.	238
B.6 Ventilation, perfusion and V/Q ratio distribution against lung height (cranio-caudal axis) of the third time point of case IPF5. (a) Ventilation distribution against lung height. (b) Perfusion distribution against lung height. (c) V/Q ratio distribution against lung height.	239

B.7 V/Q ratio distribution and arterial oxygen distribution of normal, CT-based and PFT-based simulation result of the first time point of case IPF14 using MIGET). (a) V and Q flow with respect to V/Q ratio. (b) V and Q percentage with respect to arterial oxygen level.	240
B.8 Ventilation, perfusion and V/Q ratio distribution against lung height (cranio-caudal axis) of the first time point of case IPF14. (a) Ventilation distribution against lung height. (b) Perfusion distribution against lung height. (c) V/Q ratio distribution against lung height.	241
B.9 V/Q ratio distribution and arterial oxygen distribution of normal, CT-based and PFT-based simulation result of the second time point of case IPF14 using MIGET). (a) V and Q flow with respect to V/Q ratio. (b) V and Q percentage with respect to arterial oxygen level.	242
B.10 Ventilation, perfusion and V/Q ratio distribution against lung height (cranio-caudal axis) of the second time point of case IPF14. (a) Ventilation distribution against lung height. (b) Perfusion distribution against lung height. (c) V/Q ratio distribution against lung height.	243

List of Tables

2.1	Alterations of lung function tests in idiopathic pulmonary fibrosis (IPF) Reproduced from (Plantier et al., 2018)	25
3.1	Summary of lung segmentation methods	42
3.2	Summary of fissure detection methods	48
3.3	Summarized demographics for the AGING and HLA datasets.	57
3.4	Possible structures on images in 2D and 3D, and its corresponding eigenvalues λ_k . H and L describe the absolute value of λ_k , H is high, L is low, +/- indicate the sign of the eigenvalue. The eigenvalues relationship here is: $ \lambda_1 \leq \lambda_2 \leq \lambda_3 $	67
3.5	Summary of interactive user control parameters	74
3.6	Mean error and percentile accuracy of normal healthy and IPF subjects (mean value \pm standard deviation).	82
3.7	Mean error and percentile accuracy of left oblique fissure for each subject	85
3.8	Mean error and percentile accuracy of right horizontal fissure for each subject	86
3.9	Mean error and percentile accuracy of right oblique fissure for each subject	87

3.10 Mean square error (MSE) (mm) and percentile accuracy(%) of segmented left oblique (LO), right horizontal (RH), and right oblique (RO) fissures before and after manual correction	88
4.1 Demographic data.	105
4.2 Mean tissue density of each CT pattern for left and right lung (mean value \pm standard deviation)	116
4.3 Change in classification of tissue CT pattern over time of left lung from one subject diagnosed with IPF (subject 6 with three time points) (%). . .	132
4.4 Change in classification of tissue CT pattern over time of right lung from one subject (subject 6 with three time points) diagnosed with IPF (%).	132
4.5 Whole volume of left and right lung for each time point($1.0e5 * mm^3$). .	134
4.6 Lobe volume comparison between IPF subjects and older normal subjects.	135
4.7 Results for linear regression of shape mode weighting against extent of fibrosis.	139
5.1 Age-associated changes in respiratory function and their relationships to clinical presentations (Reproduced from (Sprung et al., 2006; Lalley, 2013))	148
5.2 Parameter values and their source used in computational models	171
5.3 Individual information used for normal lung prediction from one patient with IPF	176
5.4 Average lobe volume proportion of IPF lung mesh and predicted old normal lung mesh.	177
5.5 Parameters of old normal and IPF airway tree	180

5.6	Parameters of old normal and IPF vessel tree	180
5.7	Reference normal, simulated and PFT measured inspiration volume. . .	181
5.8	Percentage of CT-based fibrosis and PFT-based fibrosis.	182
5.9	Values of PaO ₂ and PaCO ₂ of older normal, CT-based and PFT-based modeling results.	185

List of Abbreviations

ADHB Auckland District Health Board.

AGING human aging cohort.

AIC Akaike information criterion.

ANNs artificial neural networks.

ATS American Thoracic Society.

BIC Bayesian information criterion.

COPD chronic obstructive pulmonary disease.

CPFE combined pulmonary fibrosis and emphysema.

CT computed tomography.

CVM Cramer Von Mises Distance.

DLCO diffusion capacity for carbon monoxide.

DoF degrees of freedom.

DPLD diffuse parenchymal lung diseases.

ERS European Respiratory Society.

FRC functional residual capacity.

FVC forced vital capacity.

GER gastroesophageal reflux.

GPA General Procrustes Alignment.

HDEC Health and Disability Ethics Committees.

HLA Human Lung Atlas.

HRCT high resolution computed tomography.

I-Clic Iowa Comprehensive Lung Imaging Center.

IP idiopathic interstitial pneumonia.

ILD interstitial lung disease.

IPF idiopathic pulmonary fibrosis.

KCO carbon monoxide transfer coefficient.

LAA low attenuation areas.

MDS multi-dimensional scaling.

MLD mean lung density.

NSIP non-specific interstitial pneumonia.

PCA principle component analysis.

PFT pulmonary functional test.

PVV pulmonary vessel volume.

QLF quantitative lung fibrosis.

QOL quality of life.

RBC red blood cell.

RMS root mean square.

RV pulmonary functional test.

SFeaL Statistical Finite element analysis of Lobe.

SSM statistical shape model.

TLC total lung capacity.

UIP usual interstitial pneumonia.

VC vital capacity.

VOIs volumes of interest.

Chapter 1

Introduction

1.1 Motivation

Idiopathic pulmonary fibrosis (IPF) is a lethal fibrosing lung disorder that typically affects adults in the sixth to seventh decade of life (Meltzer and Noble, 2008; King Jr et al., 2011). IPF is more frequent in males than females, and is associated with environmental factors such as smoking or dust exposure, but as its name suggests does not have a clear aetiology. There is no known cure, although some very new therapies have been suggested to slow the rate of physiologic decline (Raghu et al., 2011). IPF belongs to the family of interstitial lung disease (ILD), and is the most frequent diffuse interstitial lung disease (Meltzer and Noble, 2008). In IPF lungs, healthy tissues are gradually replaced by an abnormal and excessive deposition of collagen (fibrosis), which may lead to a reduction in lung volumes, decreased lung compliance, mismatching at ventilation and perfusion, impaired gas exchange, and ultimately respiratory failure and death (Richeldi et al., 2017).

Diagnosis of IPF relates to a histopathological or radiological pattern typical of usual

interstitial pneumonia (UIP) (Raghu et al., 2011; Xaubet et al., 2017). UIP pattern is usually associated with honeycombing (subpleural cystic airspaces with well-defined walls), reticular opacities and ground-glass abnormalities (Raghu et al., 2011; Richeldi et al., 2017). These abnormalities in IPF typically develop preferentially in posterior-basal lung regions, and often co-exists with emphysema, which causes a progressive and irreversible decline in lung function. Currently it is not clear how - or whether - the spatial distribution of tissue abnormalities in IPF (including classifications of tissue type) correlate with pulmonary functional test (PFT). In addition, the progression of IPF is variable between individuals, no established quantitative tools exist to assess its development and how the tissue abnormalities change over time. Therefore, developing a computational modeling of lung function in IPF over time, together with clinical knowledge, will be helpful for clinician to have a better understanding of patient prognosis, and presents potential novel ways of investigating strategies for patient-specific diagnosis and treatment planning for IPF patients.

1.2 Thesis Objectives

The primary aim of this thesis is to develop a new quantitative tool that integrates data from volumetric imaging, PFTs, and computational models for lung function, to take steps toward predicting the development of IPF over time, and to understand differences, including lung shape and lung function, between IPF and normal older lungs.

The specific objectives of this thesis are:

Objective 1: Develop an automatic lung lobe segmentation method based on HRCT images that can consistently estimate lobar boundaries even if the boundary is not clear

along its entire length. The method needs to be tested on both healthy subjects and IPF subjects. Ideally the algorithm will be automatic , or semi-automatic.

Objective 2: Classify and quantify tissue abnormalities from HRCT scans of IPF lungs. Analyze the density, volume, spatial distribution, and their change over time.

Objective 3: Investigate the difference of lung shape between IPF and older normal lungs, and explore the correlation of lung shape change in IPF with the extent fibrosis.

Objective 4: Integrate the image-based tissue quantification, pulmonary functional test and computational modeling to simulate the lung function in IPF, compared with the older normal people, and to use these tools to estimate the impact of CT features of IPF on lung function.

1.3 Thesis Overview

Chapter 2 In order to quantitatively explore the link between structure and lung function of patients with IPF, some background knowledge of this disease is summarized in this chapter. The first part provides an basic introduction of IPF, including its epidemiology, etiology, pathogenesis, diagnosis, clinical courses and comorbidities. The second part describes some physiological alterations in IPF lungs. The changes in the mechanical properties of the lungs in IPF and the changes in pulmonary gas exchange are discussed in details, respectively.

Chapter 3 Automatic identification of pulmonary lobes from imaging is important for the further image-based analysis of lung function and disease progression. In or-

der to overcome difficulties in identifying pulmonary fissures, especially in disease, a statistical finite element shape model of lobes is applied to guide lobar segmentation in this chapter. By deforming a principle component analysis based statistical shape model onto an individuals lung shape, the likely region of fissure locations is predicted to initialize the search region for fissures. Then, an eigenvalue of Hessian matrix analysis and a connected component eigenvector based analysis are used to determine a set of fissure-like candidate points. A smooth multi-level B-spline curve is fitted to the most fissure-like points (those with high fissure probability) and the fitted fissure plane is extrapolated to the lung boundaries. The method is tested on 20 inspiratory and expiratory CT scans, and the results show that the algorithm performs well both in healthy young subjects and older subjects with IPF.

Chapter 4 This chapter outlines the study of quantitative analysis of IPF disease based on HRCT scans, including both the tissue abnormality quantification and lung lobe shape analysis, to provide consistent potential tissue-level and shape-level biomarkers that can indicate the likely progression of the disease over time. Lung tissues are classified as normal, reticular, ground glass, or emphysema using CALIPER (Computer-Aided Lung Informatics for Pathology Evaluation and Ratings) software. The classified data is then mapped to a statistical shape model (SSM), which allows a reliable comparison between different patients or within one patient of different time points. Quantitative approaches are used to analyze tissue density, tissue volume, the spatial distribution of abnormalities, and regional changes in tissue over time. Principle component analysis (PCA) based SSM is applied to understand lung shape differences between IPF and normal older lungs through quantifying principal modes of shape variation of both IPF and old normal subjects.

Chapter 5 In this chapter, data from volumetric imaging, quantitative tissue-level and shape-level features, and PFT are integrated to guide a patient-specific computational models of lung function of IPF. In order to make a comparison of lung function between IPF patient and older normal people, for each patient, a subject-specific lung mesh that represents the statistical lung shape of old normal individual with the same age, BMI and pulmonary functional data is predicted using SSM. Anatomically based airway and blood vessel trees are generated derived from HRCT images, respectively matched to IPF lung mesh and the corresponding old normal lung mesh. The ventilation, perfusion and gas exchange models are then constricted to simulate \dot{V} , \dot{Q} distribution and gas transport in normal and disease constricted condition, respectively.

Chapter 6 Key findings of this thesis are summarized in this chapter by discussing the main methods, models and outcomes. Potential future directions that need to be addressed to develop the modeling framework are also discussed.

Chapter 2

Background

In order to quantitatively explore the link between structure and function of patients with idiopathic pulmonary fibrosis (IPF), some background knowledge of the disease is required. This chapter provides an introduction to IPF of its epidemiology, etiology, pathogenesis, diagnosis, clinical courses, comorbidities, and physiological alterations.

2.1 Introduction to idiopathic pulmonary fibrosis

2.1.1 Definition

Idiopathic pulmonary fibrosis is a chronic, progressive, irreversible, and lethal lung disease of unknown cause. It usually manifests over several years during which progressive scarring occurs in the supporting structural framework (interstitium) of the lung tissue (Meltzer and Noble, 2008; Raghu et al., 2011). It is the scarring of the tissue that is termed fibrosis. This fibrotic condition is generally thought to result from abnormal wound healing after repeated pulmonary tissue damage (King Jr et al., 2011). Several causes of alveolar injury have been implicated in IPF, including cigarette smoke, envi-

ronmental exposure to toxins (e.g. asbestos, avian toxins), gastro-oesophageal reflux, viral infection, and internal mechanisms such as autoimmunity, genomic instability or telomerase length (Raghu et al., 2011; Ahluwalia et al., 2014).

In IPF patients' lungs, some healthy tissues are replaced by altered extracellular matrix and a destroyed alveolar architecture, which leads to decreased lung compliance, disrupted gas exchange, and ultimately respiratory failure and death (Richeldi et al., 2017). The fibrosing areas are generally observed to arise first at the basal and peripheral region of the lungs, and then gradually progress to involve all lung tissues (Martinez et al., 2017). The prominent symptoms of IPF are exercise-induced breathlessness and chronic dry cough (Meltzer and Noble, 2008), which will eventually have a devastating effect on a patients quality of life (QOL) (Kim et al., 2015b). IPF usually affects middle-aged and elderly adults (median age at diagnosis 66 years, range 55-75 years). The disease is isolated to the lungs, and is associated with the radiological and/or histological pattern of UIP (King Jr et al., 2011; Raghu et al., 2011; Xaubet et al., 2017). A typical UIP pattern is usually characterized by honeycombing, traction bronchiectasis, and peripheral alveolar septal thickening (Martinez et al., 2017), which will be introduced briefly in Section 2.3.2.

2.1.2 Disease classification

IPF belongs to the family of interstitial lung disease (ILD) or, more accurately, the diffuse parenchymal lung diseases (DPLD). All ILDs result in damage to the lung interstitium, with varying patterns of inflammation and fibrosis. Within the broad category of ILDs, IPF belongs to a subgroup known as idiopathic interstitial pneumonia (IIP) (Meltzer and Noble, 2008). By definition, the etiology of IIPs is unknown. The

distinction between IPF and other kinds of IIP is particularly important (Corte et al., 2015; Troy and Corte, 2012), as the prognosis for other IIPs is generally much more favorable than that for IPF (Meltzer and Noble, 2008). Over the past decade, IIPs have been classified into seven distinct diseases, differentiated by specific clinical features and pathological patterns, which includes: idiopathic pulmonary fibrosis, non-specific interstitial pneumonia, cryptogenic organising pneumonia, acute interstitial pneumonia, respiratory bronchiolitis-interstitial lung disease, desquamative interstitial pneumonia, and lymphocytic interstitial pneumonia (Katzenstein and Myers, 1998; Troy and Corte, 2012) (Figure 2.1).

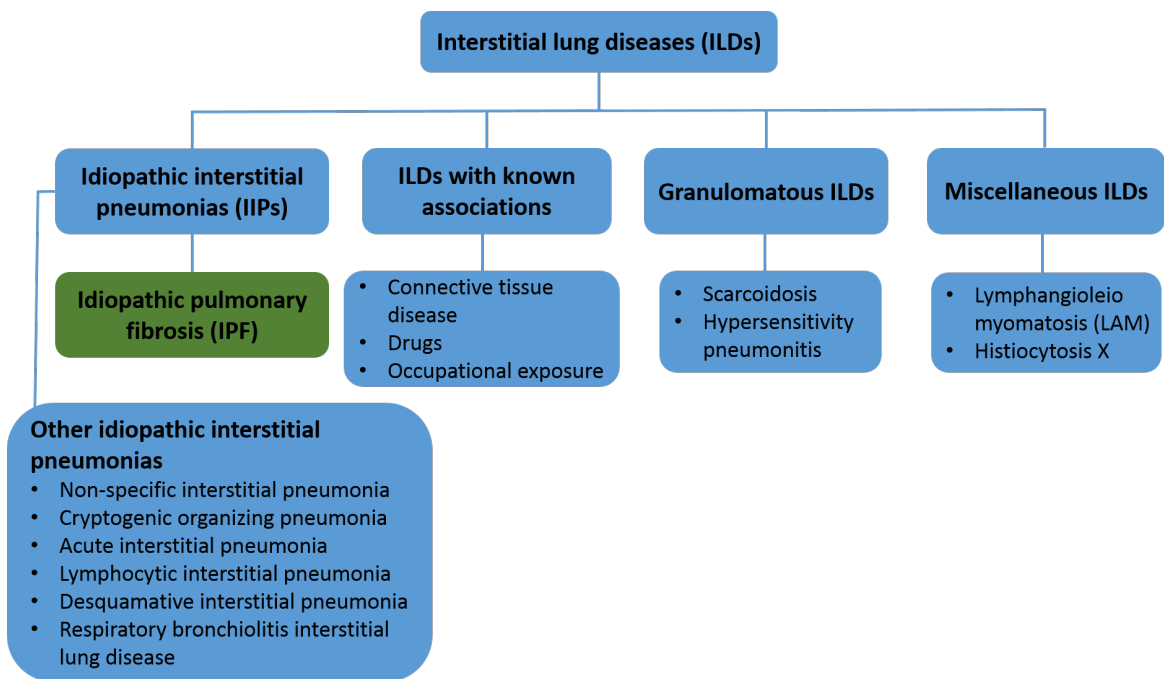


Figure 2.1: Classification of the interstitial lung diseases. IPF belongs to the family of interstitial lung disease (ILD), and belongs to a subgroup known as idiopathic interstitial pneumonia (IIP). Reproduced from (Troy and Corte, 2012).

2.2 Epidemiology, etiology and pathogenesis

2.2.1 Epidemiology

Although IPF is considered a rare disease, this disease is the most common form of IIP (Travis et al., 2013). The incidence of IPF is similar to that of stomach, brain, and testicular cancers and has recently been demonstrated to be rising over time (Richeldi et al., 2017). A cohort study including patients diagnosed with ILDs at Aarhus University Hospital showed that IPF was the most common diagnosis (28%) followed by connective tissue disease-related ILD (14%), hypersensitivity pneumonitis (7%) and non-specific interstitial pneumonia (NSIP) (7%) (Hyldgaard et al., 2014). Although there is little data available estimating worldwide incidence, a recent study showed that in Europe and North America, the prevalence of IPF is estimated to range between 2.8 and 18 cases per 100,000 people per year, and this value might be lower in Asia and South America, where it is estimated to range from 0.5 to 4.2 cases per 100,000 individuals per year (Richeldi et al., 2017). IPF is more likely to affect men than women, and is rare in people younger than 50 years (Raghu et al., 2011, 2006). The incidence is estimated to be 13 cases/100,000 in women and 20 cases/1000,000 in men (Xaubet et al., 2017). In addition, the incidence of IPF increases with age (Meltzer and Noble, 2008). The reason that incidence is becoming higher in recent years is most likely because of improved diagnostic methods and increased life expectancy (Xaubet et al., 2017).

2.2.2 Pathogenesis and potential contributors to etiology

Historically, IPF was considered a chronic inflammatory disorder, which gradually progressed to established fibrosis (Richeldi et al., 2017). Now IPF is generally regarded as

a consequence of multiple interacting factors, in which repetitive local micro-injuries to an ageing alveolar epithelium plays an important role (Richeldi et al., 2017). These micro-injuries initiate aberrant epithelial-fibroblast communication, the induction of matrix-producing myofibroblasts, and considerable extracellular matrix accumulation and remodelling of lung interstitium (Richeldi et al., 2017). Although the etiology of IPF is unknown, currently, environmental exposures and genetic factors have been supported by some researchers as providing important inducement (Taskar and Coultas, 2006; Meltzer and Noble, 2008; Xaubet et al., 2017; Richeldi et al., 2017). In addition, gastroesophageal reflux (GER), exposure to silica, brass, steel and wood dust, livestock and agriculture work, and the construction of wooden houses are also potential risk factors for the pathogenesis of IPF (Taskar and Coultas, 2006; Xaubet et al., 2017).

Environmental exposures

The relationship between environmental exposures and IPF has been consistently demonstrated by case studies. Asbestosis, for example, is a case in which environmental material is associated with pulmonary fibrosis (Meltzer and Noble, 2008). There are studies indicating that the pathogenesis and progression of IPF are influenced by particulate inhalation, which is supported by the fact that the development of IPF consistently relates to cigarette smoking history in most patients (Baumgartner et al., 1997; Richeldi et al., 2017). Additionally, other environmental factors including metal and wood dusts, agriculture and farming, viruses, and stone and silica have also been proposed (Raghu et al., 2011; Taskar and Coultas, 2006).

Genetic factors

Increasing evidence indicates that genetic predisposition plays an essential part in the development of IPF (Xaubet et al., 2017; Richeldi et al., 2017). This evidence is based on the existence of familial forms of the disease, and it has been shown that around 2.2% to 3% of IPF cases are familial (Xaubet et al., 2017). The most likely mode of genetic transmission of pulmonary fibrosis in familial cases is autosomal-dominant with variable penetrance (Steele et al., 2005; Allam and Limper, 2006; Lee et al., 2005; Musk et al., 1986). Rare genetic variants have been identified in cases where ILDs affect two or more members of the same biological family, including genes associated with alterations in host defence (MUC5B, ATP11A, TOLLIP), telomere maintenance (TERT, TERC, PARN, RTEL, OBFC1), surfactant dysfunction (SFTPC, SFTPA2) and epithelial barrier function (DSP, DPP9) (Alder et al., 2008; Raghu et al., 2011; Seibold et al., 2011; Xaubet et al., 2017). Among them, MUC5B, a promoter site of an airway mucin gene, is the most strongly associated with development of both familial and sporadic IPF (Richeldi et al., 2017). MUC5B encodes a mucin-5B precursor protein that contributes to airway mucous production and might have an important role in lung host defense. It has also been noted that members of the same biological family may be affected by different types of ILDs, such as non-specific interstitial pneumonia and cryptogenic organizing pneumonia (Xaubet et al., 2017).

2.3 Diagnosis

The diagnosis of IPF often requires a multidisciplinary discussion, involving pulmonologists, chest radiologists, and chest pathologists experienced in the field of ILDs (Flaherty et al., 2004; King Jr et al., 2011; Raghu et al., 2011). This multidisciplinary

approach has been accepted in consensus guidelines all over the world and has helped to standardize IPF diagnosis (Raghu et al., 2011; Richeldi et al., 2017). Usually, IPF is diagnosed by identification of a pattern of UIP on the basis of radiological or histological criteria in patients without evidence of an alternative cause. The biggest challenge of diagnosis for clinicians is how to exclude other idiopathic interstitial pneumonias, fibrotic nonspecific interstitial pneumonia, and interstitial lung disease associated with occupational or environmental exposure, connective tissue disease, and drugs (King Jr et al., 2011; Richeldi et al., 2017). This differential diagnosis is really important, since typical UIP is not exclusive to IPF, but may associate with some other conditions, such as chronic hypersensitivity pneumonitis and asbestosis. Many patients have a history of environmental exposures or medical treatments which clinicians need to take into consideration for diagnosis (Richeldi et al., 2017).

2.3.1 Clinical presentations

Patients with IPF usually suffer from unexplained progressive dyspnea on exertion and chronic dry cough, bibasilar inspiratory crackles, and finger clubbing. Bibasilar inspiratory crackles are heard on chest auscultation and finger clubbing is found in about 30% of patients (Raghu et al., 2011; King Jr et al., 2011; Richeldi et al., 2017). Chest pain, fatigue, malaise, and weight loss are also typical symptoms for IPF patients (Douglas et al., 2000; King Jr et al., 2001). These clinical presentations might initially be attributed to aging or some comorbidities such as cardiovascular disease, or obesity (Richeldi et al., 2017). Therefore, in order to avoid diagnostic delays, it is necessary for primary care physicians to have clinical suspicion of IPF. Some patients, usually accompanied by fever and influenza-like symptoms, may present with acute respiratory

exacerbations within a few days or weeks. In these cases, clinicians require careful diagnostic distinction from other forms of acute ILDs (Richeldi et al., 2017). Pulmonary function tests (PFTs) from IPF patients usually show a restricted pattern with low percent predicted total lung capacity (TLC) and diffusion capacity for carbon monoxide (DLCO). But for some patients with early disease, PFT results might be normal or mildly abnormal (Douglas et al., 2000; Raghu et al., 2006).

2.3.2 Radiographic features

HRCT of the chest has become an essential tool for the diagnosis of IPF, which is usually associated with identification of a UIP pattern. The presence of UIP pattern on HRCT is characterised by appearance of honeycombing cysts, reticular opacities and ground-glass abnormalities (Figure 2.2) (King Jr et al., 2011; Raghu et al., 2011; Richeldi et al., 2017). Honeycombing is common, and essential for a definite diagnosis (Raghu et al., 2011). On HRCT, honeycombing is presented as clustered cystic airspaces with a typical diameter of 3-10 mm but occasionally as large as 2.5 cm, and in a predominantly subpleural and posterior basal distribution (Hansell et al., 2008; Richeldi et al., 2017). Reticular opacities are often associated with traction bronchiectasis (Nishimura et al., 1992; Johkoh et al., 1999). Groundglass is a common characteristic of UIP pattern, although it is sometimes less extensive than reticular. The distribution of abnormalities are often basal, peripheral and patchy (Raghu et al., 2011). If patients show micronodules, air trapping, nonhoneycomb cysts, extensive ground glass opacities, consolidation, or a peribronchovascular-predominant distribution, alternative diagnosis should be taken into account (Hwang et al., 2009; Souza et al., 2006). If patients show reticular abnormalities located in subpleural and basal regions, but no honeycombing appearance,

possible UIP patterns should be taken into consideration, then a surgical lung biopsy is suggested to make a definite diagnosis (Raghu et al., 2011; Richeldi et al., 2017).

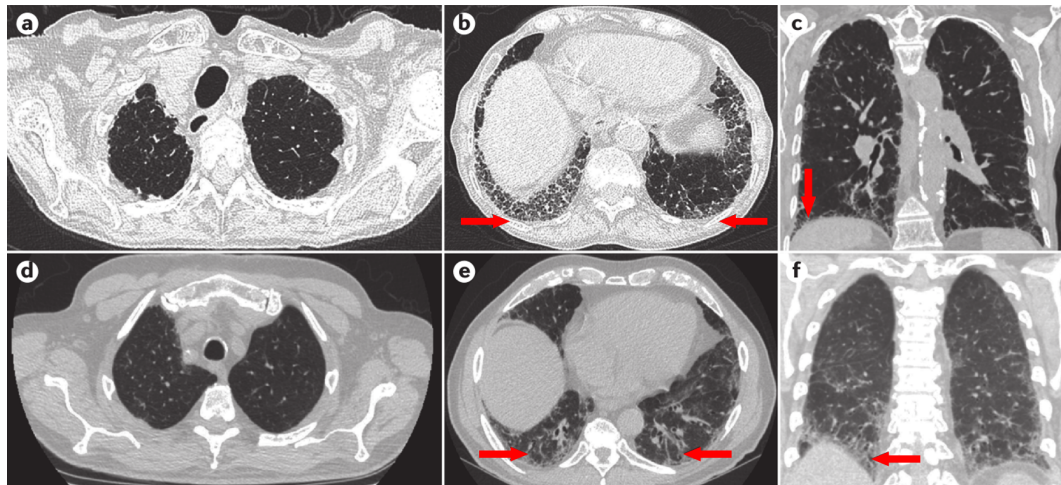


Figure 2.2: HRCT images of UIP pattern from two patients. The first is from a woman with progressive cough and dyspnoea, showing her upper (a), lower (b) lung zones and a sagittal plane of the lungs (c). These images show lower lobe-predominant peripheral honeycomb change (b and c, arrows), which is typical of UIP pattern. This patient had no systemic disease or exposures that would exclude idiopathic disease, the diagnosis of IPF is certain. In contrast, the second is a woman with progressive breathlessness, who could be diagnosed with possible IPF. The upper (d), lower (e) lung zones and sagittal image of the lungs (f) demonstrate peripheral, basilar-predominant, reticular densities with traction bronchiectasis (e and f, arrows) consistent with fibrosis. Surgical lung biopsy is suggested. Reproduced from (Martinez et al., 2017).

2.3.3 Histopathology

When HRCT features are not enough for a certain diagnosis of IPF, surgical lung biopsy is suggested (Richeldi et al., 2017). The main histopathologic hallmarks of UIP pattern is characterized by a heterogeneous appearance, best seen at low magnification, in the areas of subpleural fibrosis with carring and honeycomb (i.e. cystic fibrotic airspaces lined by bronchiolar epithelium and often filled by mucin and variable numbers of inflammatory cells), alternating with areas of less affected or normal parenchyma (Society

et al., 2000; Travis et al., 2002) (Figure 2.3). Small areas of active fibrosis (fibroblast foci) are present in the background of collagen deposition, and they reflect the temporal heterogeneity of the process and indicate current ongoing disease (King Jr et al., 2011). Another feature of UIP pattern is that the inflammation is often absent or mild and consists of a patchy interstitial infiltrate of lymphocytes and plasma cells (Raghu et al., 2011; King Jr et al., 2011). Although surgical lung biopsy is essential for a correct diagnosis, careful consideration is required for every patient to estimate whether the risks of surgical lung biopsy outweigh the potential benefits of the histopathologic information. For older patients with comorbidities or clinically significant physiological impairment, it is suggested to avoid surgical lung biopsy (Richeldi et al., 2017).

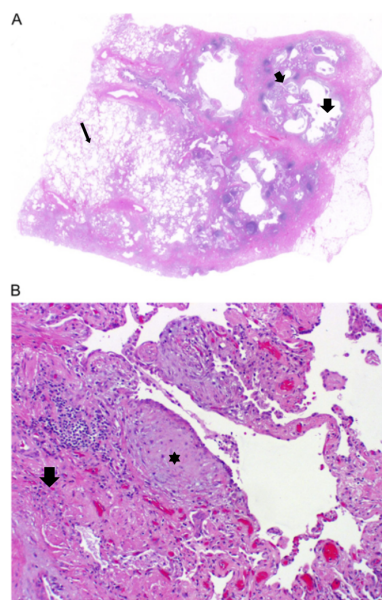


Figure 2.3: Surgical lung biopsy specimens of UIP pattern. (A) Scanning power microscopy showing a patchy process with honeycomb spaces (thick arrow), some preserved lung tissue regions (thin arrow), and fibrosis extending into the lung from the subpleural regions. (B) Adjacent to the regions of more chronic fibrosis (arrow) is a fibroblast focus (asterisk), recognized by its convex shape and composition of edematous fibroblastic tissue, suggestive of recent lung injury. Reproduced from (Raghu et al., 2011).

2.3.4 Diagnostic criteria

"Gold standard" diagnostic criteria for IPF have been developed by the American Thoracic Society (ATS) and the European Respiratory Society (ERS) in a statement of published guidelines (Raghu et al., 2011):

1. Exclusion of other known causes of ILD (e.g. domestic and occupational environmental exposures, connective tissue disease, and drug toxicity).
2. The presence of a UIP pattern on HRCT in patients not subjected to surgical lung biopsy.
3. Specific combinations of HRCT and surgical lung biopsy pattern in patients subjected to surgical lung biopsy.

Beyond that, minor criteria have also been set for the diagnosis of IPF in the absence of a surgical lung biopsy (Raghu et al., 2011):

1. Age > 50 years.
2. Insidious onset of otherwise unexplained dyspnea on exertion.
3. Duration of illness being over 3 months.
4. Bibasilar inspiratory crackles (dry or "Velcro" type).

Figure 2.4 shows the diagnostic workflow for adult patients with ILD and suspected IPF. If the high-quality HRCT evidence is sufficient enough for the recognition of histopathologic UIP pattern, surgical lung biopsy is not essential (Hunninghake et al., 2001; Raghu et al., 1999; Flaherty et al., 2003; Quadrelli et al., 2010). However,

the multidisciplinary discussion among experienced clinical, radiologic and histopathologic experts is particularly important when the radiologic and histopathologic patterns are discordant (e.g., HRCT is inconsistent with UIP and histopathology suggests UIP) (Raghu et al., 2011). Radiologic or pathologic UIP pattern is not 100% specific to IPF (Lynch et al., 2006; Trahan et al., 2008; Silva et al., 2008a).

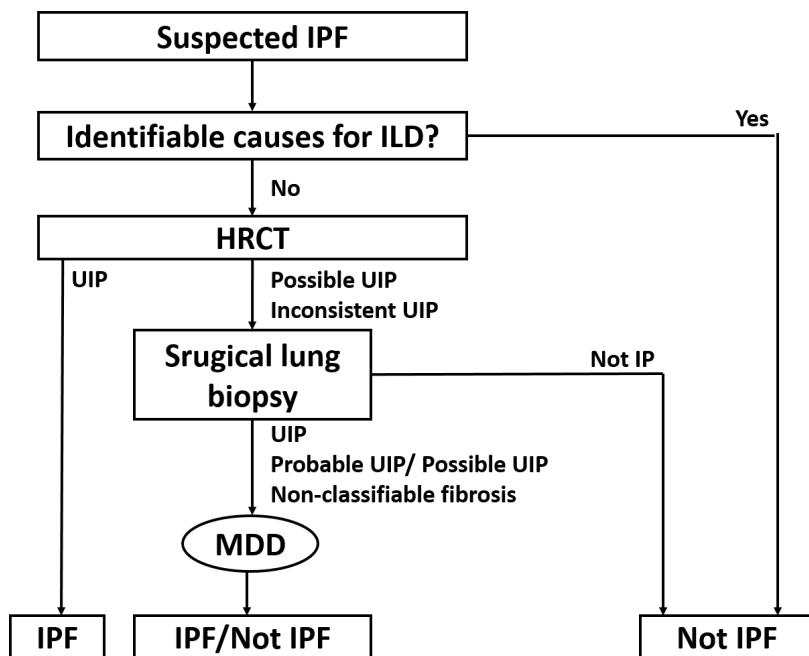


Figure 2.4: Diagnostic algorithm for IPF. Patients with suspected IPF (i.e., patients with unexplained dyspnea on exertion and/or cough with evidence of ILD) should be carefully evaluated for identifiable causes of ILD. In the absence of an identifiable cause for ILD, an HRCT demonstrating UIP pattern is diagnostic of IPF. In the absence of UIP pattern on HRCT, IPF can be diagnosed by the combination of specific HRCT and histopathological patterns. The accuracy of the diagnosis of IPF increases with multidisciplinary discussion (MDD) among ILD experts. Reproduced from (Raghu et al., 2011).

2.4 Clinical course

Some studies indicate that IPF patients have median survival time between two and three years from the time of diagnosis (Bjoraker et al., 1998; Flaherty et al., 2002; Nicholson et al., 2000; Rudd et al., 2007; KING JR et al., 2001; King Jr et al., 2011). For most IPF patients, the clinical course has been described as a general decline in pulmonary function until eventual death from respiratory failure or complicating comorbidity (Carrington et al., 1978; Tukiainen et al., 1983; Gross and Hunninghake, 2001), however, the individual disease progression can be highly variable (Kim et al., 2006b; Meltzer and Noble, 2008). It appears that there are several possible clinical courses for patients with IPF (shown in Figure 2.5) (Raghu, 1987): slow and gradual progression over many years (the most common) (Ryu et al., 2014; Meltzer and Noble, 2008; Raghu et al., 2011); rapid and accelerated decline (Kim et al., 2006b; Selman et al., 2007); and acute exacerbations (King Jr et al., 2011; Xaubet et al., 2017). Currently, it is difficult to predict the natural history of disease progression for a given patient at the time of the diagnosis (Raghu et al., 2011). Whether the different clinical courses are influenced by geographic, ethnic, cultural, racial, or other factors remains unknown. But some evidence has been suggested that worsening prognosis may be associated with older people (> 70 years old), smoking history, low body mass index (BMI), severe physiological impairment, and large radiological extent of disease (Ley et al., 2011). Other comorbidities such as emphysema and pulmonary hypertension may also have an impact on the disease course (Mejía et al., 2009; Wells et al., 2003; Lettieri et al., 2006).

2.4.1 Slow and rapid progressive course

Most IPF patients deteriorate relatively slowly, and their pulmonary function usually decreases gradually over months to years after the first clinical symptoms (cough and progressive dyspnoea) (Ryu et al., 2014; Meltzer and Noble, 2008; Raghu et al., 2011). Patients usually experience reduction of lung volumes and hypoxemia at rest that worsens with exercise. This is accompanied by a decline of forced vital capacity (FVC) by a mean of 0.13 L to 0.21 L per year (Ley et al., 2011). In contrast, a subgroup of patients with IPF, mainly male cigarette smokers, experience a rapid worsening of symptoms, and insufficiency of pulmonary function (Kim et al., 2006b; King Jr et al., 2011), known as accelerated IPF. The patients with rapid progression have reduced survival time relative to those with a slowly progressive clinical course.

2.4.2 Acute exacerbations of IPF

Acute exacerbation was first proposed by Japanese physicians to describe acute, unexpected worsening of respiratory functions and severe hypoxemia in patients with IPF, without a clear trigger (Kondoh et al., 1993; Gross, 1962). The rapid deterioration occurs in a small minority of patients with IPF (about 5-10%), with absence of infection, heart failure, pneumothorax, or pulmonary embolism (Azuma et al., 2005; King Jr et al., 2011; Raghu et al., 2011). The prognosis for patients with acute exacerbations is poor, and it may happen at any stage in the course of IPF (Kim et al., 2006a; Parambil et al., 2005; Sakamoto et al., 2009; Kondoh et al., 2010). Patients with this acute exacerbation usually experience poor respiratory decline, worsened cough, fever and increased sputum production (Ambrosini et al., 2003; Kim et al., 2006a). The mortality rate for patients with acute exacerbations is over 60% (Wootton et al., 2011; Lettieri et al., 2006);

for cases requiring mechanical ventilation, the mortality is close to 100% (King Jr et al., 2011; Xaubet et al., 2017).

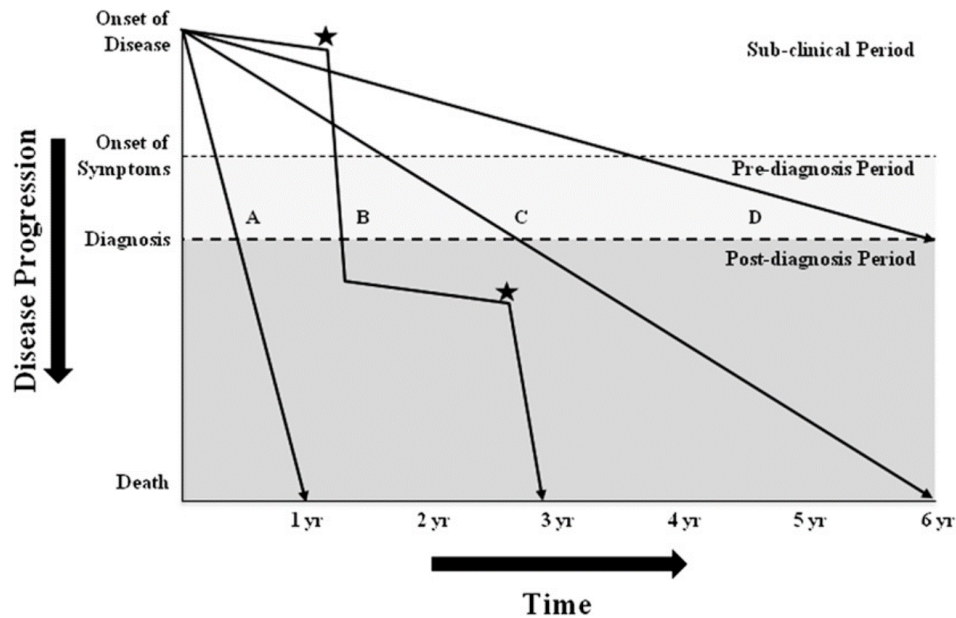


Figure 2.5: Schematic representation of potential clinical courses of IPF. A subclinical period of disease progression exists during which only radiographic evidence of disease may be noted. This is followed by a symptomatic phase comprising clinical stages (both pre-diagnosis and post-diagnosis). The rate of deterioration and progression to death may be fast (line A), mixed (line B), or slow (lines C and D), with phases of relative disease stability interspersed with acute decline (asterisks). Reproduced from (Ley et al., 2011).

2.5 Complications and comorbidities

Complications and comorbidities can occur in patients with IPF that may influence the clinical course and prognosis (Xaubet et al., 2017; King and Nathan, 2017; Martinez et al., 2017). It is reported that only 12% of patients with IPF have no comorbid illness, and most patients have comorbidities (Raghu et al., 2011; Kim et al., 2015b; Harari et al., 2016; Kreuter et al., 2016). Emphysema and pulmonary hypertension are both im-

portant comorbid conditions in IPF patients (Raghu et al., 2015; Martinez et al., 2017), and are briefly outlined here.

2.5.1 IPF and emphysema

Several research groups have described a syndrome in which IPF coexists with pulmonary emphysema (Wells et al., 1997, 2003; Cottin et al., 2005; Meltzer and Noble, 2008). In 2005, Cottin et al. (2005) presented a syndrome named combined pulmonary fibrosis and emphysema (CPFE). Both IPF and emphysema are associated with a significant smoking history, and CPFE is strongly associated with exercise hypoxemia, severe dyspnea on exertion, upper lobe emphysema and lower lobe fibrosis, unexpected subnormal lung volumes, and severe reduction of carbon monoxide transfer (Silva et al., 2008b; Mejía et al., 2009; Cottin et al., 2010; King Jr et al., 2011; Lin and Jiang, 2015). Currently, whether CPFE is a distinct clinical entity or not remains unknown, i.e. whether this is just the presence of two different diseases running in parallel is unclear (King Jr et al., 2011; Lin and Jiang, 2015). Some researchers suggest that CPFE should be regarded as a distinct clinical entity, since it has a characteristic pulmonary function feature and unique natural history that is different from pure emphysema or IPF alone (Cottin et al., 2005; Lin and Jiang, 2015; Xaubet et al., 2017). CPFE occurs more frequently in males than in females and its prevalence is about 30% to 47% in patients with IPF (Xaubet et al., 2017). It is often associated with a significant drop of DLCO and severe hypoxemia during exercise due to the additive effect of emphysema and fibrosis (Xaubet et al., 2017).

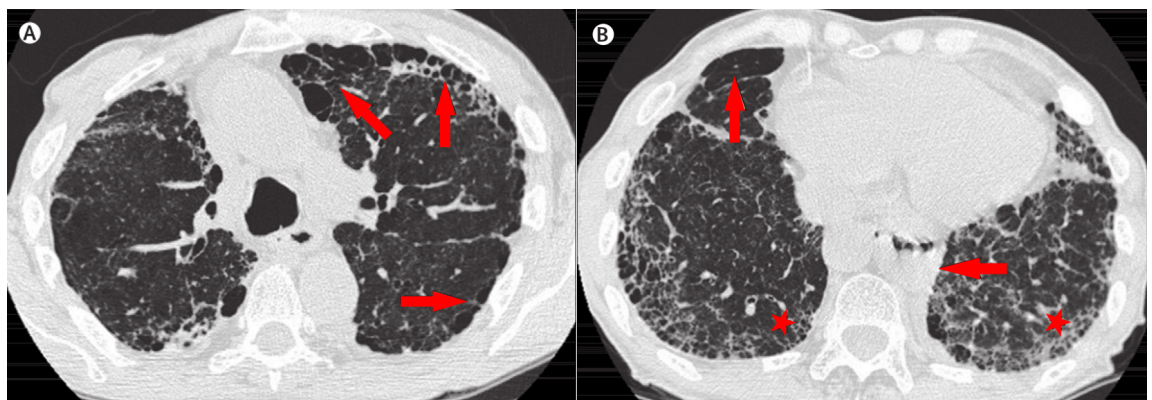


Figure 2.6: Combined pulmonary fibrosis and emphysema. High-resolution CT shows emphysematous lesions (arrows) in the upper lobes (in Figure A) Emphysema (arrow) and usual interstitial pneumonia-like lesions (stars) in the lower lobes (in Figure B). Reproduced from (King Jr et al., 2011).

2.5.2 IPF and pulmonary hypertension

Pulmonary hypertension (PH), defined as a mean pulmonary artery pressure of > 25 mm Hg at rest, is a frequent form of comorbid condition in patients with IPF and is the main determinant of poor prognosis (Raghu et al., 2011; Xaubet et al., 2017). It is estimated that the incidence of pulmonary hypertension is around 30% to 50% in IPF patients (King and Nathan, 2017). In general, pulmonary hypertension occurs due to several factors, with chronic hypoxia-induced vasoconstriction and destruction of the pulmonary capillary bed induced by fibrosis being the two main causes (Hayes Jr et al., 2016). The presence and development of pulmonary hypertension is associated with significant dyspnea, functional impairment (particularly in DLCO) and decreased exercise capacity, and may increase risk of mortality for patients with IPF (Mejía et al., 2009; Lettieri et al., 2006; Nadrous et al., 2005). Some studies show that combined pulmonary fibrosis and pulmonary hypertension has a significantly negative effect on the survival in patients with IPF, probably caused by the increased pulmonary vascular

resistance (Raghu et al., 2011; King Jr et al., 2011). Currently, whether IPF with pulmonary hypertension represents a distinct clinical entity (IPFPH) is still unclear (Raghu et al., 2011).

2.6 Physiological alterations

The clinical presentation of IPF is often strongly related to multiple physiological alterations of the lung. These alterations have a complex and negative impact on all compartments of the respiratory system, from lung volume and compliance to gas exchange, from conducting airways to lung vasculature (Plantier et al., 2018). In general, patients with IPF usually have reduced lung volumes, reduced lung compliance, reduced diffusing capacity, increased forced expiratory volume in 1 second (FEV_1)/forced vital capacity (FVC), and arterial hypoxemia that worsens with exercise (Crystal et al., 1976; Society et al., 2000; Cortes-Telles et al., 2014; Plantier et al., 2018). These multiple alterations in lung physiology are summarized in Table 2.1.

2.6.1 Alterations in the mechanical properties of the lung

Reduction in lung compliance

IPF disease often results in reduction in lung compliance (i.e. increase in the lung tissue stiffness). Studies have shown that the reduced lung compliance is caused by reduction in the compliance of the lung extracellular matrix and by alterations in the pulmonary surfactant (Plantier et al., 2018). In patients with IPF, lung surfactant shows alterations in its lipid profile (Gunther et al., 1999; Schmidt et al., 2002), which leads to severely impaired surface activity (Gunther et al., 1999). In the meantime, the reduction in lung

Table 2.1: Alterations of lung function tests in IPF Reproduced from (Plantier et al., 2018)

	Mild IPF	Moderate to severe IPF
Static lung volumes		
- TLC	Normal	Decreased
- FRC	Normal	Decreased
Spirometry		
- FVC	Normal	Decreased
- FEV ₁ /FVC	Normal or increased	Normal or increased
Airways		
- Cough reflex	Increased	Increased
- Airway resistance	Decreased	Decreased
Blood gases at rest		
- P_aO_2	Normal	Decreased
- P_aCO_2	Normal	Decreased
Carbon monoxide transfer		
- DLCO	Decreased	Decreased
- V_A	May be normal	Decreased
- K_{CO}	May be normal	Decreased
Exercise physiology		
- Peak V_{O_2}	May be normal	Decreased
- V_D/V_T	Increased	Increased
- V_E/V_{CO_2}	Increased	Increased
- PAP at exercise	Increased	Increased
- $P_{A-a}O_2$ at exercise	Increased	Increased
Pulmonary haemodynamics at rest		
- PAP	May be increased	Frequently increased
- PCWP	Normal	May be increased

FVC: forced vital capacity; FEV₁ : forced expiratory volume in 1 s; TLC: total lung capacity; FRC: functional residual capacity; P_aO_2 : arterial oxygen tension; P_aCO_2 : arterial carbon dioxide tension; DLCO : diffusing capacity of the lung for carbon monoxide; V_A : alveolar volume; K_{CO} : transfer constant of carbon monoxide; PAP: pulmonary artery pressure; PCWP: pulmonary capillary wedge pressure; V_{O_2} : oxygen uptake; V_D/V_T : ratio of dead space volume to tidal volume; V_E/V_{CO_2} : ratio of minute ventilation to carbon dioxide elimination; $P_{A-a}O_2$: alveolararterial oxygen tension difference.

compliance may happen from an early stage of IPF (Plantier et al., 2018). A study with 31 IPF patients from Zielonka et al. (2010) showed that the static lung compliance was consistently and significantly reduced (by $44 \pm 6\%$). A similar result was found by Orens et al's group (Orens et al., 1995) that all of their measured IPF patients had abnormal static lung compliance, which suggests that the measurement of lung compliance could help with the early diagnosis of IPF.

The alterations of lung compliance in IPF patients appear to be strongly correlated with the degree of lung fibrosis as assessed by scoring of lung biopsies (Fulmer et al., 1979; Plantier et al., 2018). Nava and Rubini (1999) measured the dynamic lung compliance in seven patients with end-stage IPF, which showed that the reduction in lung compliance may be correlated with progress of disease. Currently, whether the reductions in lung compliance relate to clinical presentations (e.g. dyspnoea) remains unclear, but it is highly likely that the lung compliance has a strong relationship with the respiratory muscles and thus has an impact on the work of breathing (Plantier et al., 2018). In addition, as the distribution of disease is heterogeneous in IPF lungs, the lung compliance is expected to be uneven between different lung regions (Organ et al., 2015), but more evidence is needed to understand the implications of this.

Reduction of lung volumes

The restriction of lung volumes (total lung capacity (TLC), functional residual capacity (FRC), forced vital capacity (FVC), and pulmonary functional test (RV)) is typical in patients with IPF, and often occurs at some time point in the clinical course of IPF (Society et al., 2000; Plantier et al., 2018). However, sometimes lung volumes may be normal in the early stage of IPF, especially for patients with superimposed chronic obstructive pulmonary disease (Martinez and Flaherty, 2006). Cherniack et al. (1995)

studied 96 patients with biopsy-confirmed IPF. The range of TLC was from 42% to 125% predicted and the range of FVC was from 26% to 112% predicted. A reduction in lung volumes consistently relates to an increased risk of death (Martinez and Flaherty, 2006), and is weakly associated with dyspnoea or quality of life (Du Bois et al., 2011). However, whether the reduced lung volumes reflects the disease progression of IPF is still unknown (Plantier et al., 2018). Interestingly, patients with CPFE have higher RV and TLC compared to the patients with IPF alone (Mura et al., 2006), which may be caused by the effects of comorbid pulmonary emphysema on lung compliance (Doherty et al., 1997).

Alterations in the conducting airways

Some evidence suggests that alterations also occur in conducting airways in patients with IPF, including airway epithelial cell proliferation (Vuorinen et al., 2008) and differentiation (Plantier et al., 2016), and increased numbers of visible bronchioles in the distal regions (Chilosi et al., 2002). A reduction in conducting airway resistance was found in IPF lungs compared with normal, which may contribute to an increased ratio of FEV₁ to FVC (Pastre et al., 2015). Plantier et al. (2016) used volumetric capnography to estimate the volume of conducting airways in patients with IPF, patients with other ILDs, and healthy people. The results showed that conducting airway volume was significantly higher in IPF lungs in comparison with non-IPF ILD lungs and healthy lungs. However, this change in airway volume was not associated with the severity of alveolar lesions, dyspnea, cough or quality of life (Plantier et al., 2016). The increase in airway volume in IPF may reflect dilation of airways consistent with the characteristic extent of bronchiectasis in this disease, and a commonly accepted view is that bronchiectasis in IPF may be caused by fibrotic retraction of peribronchiolar alveolar attachments and

subsequent airway dilation (Sumikawa et al., 2008). However, a recent study found that bronchiectasis had a weak relationship with total fibrosis extent observed from CT imaging (Walsh et al., 2015), which means the remodeling of conducting airways in IPF may be dissociated from alveolar fibrosis (Plantier et al., 2016). Patients with IPF usually have more rapid breaths with the progression of disease (Kornbluth and Turino, 1980; Renzi et al., 1982), and have a relatively increased flow rate in the conducting airways due to the increased static elastic recoil (Society et al., 2000). Additionally, it has been suggested that at least part of the ventilation abnormalities seen in IPF is associated with small airways disease with peribronchiolar fibrosis and inflammation, and 70% of IPF patients have narrowed small airways (Crystal et al., 1976).

Alterations in the lung vasculature

Vascular lesions are observed in the pulmonary vasculature in patients with IPF, and often lead to disproportionate increases in the pulmonary vascular resistance and pulmonary hypertension (Plantier et al., 2018). The tissues adjacent to the areas of fibrosis have been shown to have an increase in vessel profusion, whereas the fibrotic tissue itself demonstrates a reduced number of vessels (Cosgrove et al., 2004; Ebina et al., 2004). Jacob et al. (2016a) explored the relationship between pulmonary vessel volume (PVV) and ILD extent (includes ground glass, reticular and honeycomb patterns). It was found that PVV had strong links with ILD extent ($R^2 = 0.73$, $P < 0.0001$) when using linear regression analysis. Furthermore, PVV was demonstrated to be an independent predictor of mortality and a stronger predictor of mortality than all the other traditional CT features and pulmonary functional variables (Jacob et al., 2016a). The increase in PVV seen in more advanced fibrosis may be caused by the vascular capacitance of spared lung (the upper and middle lobes in patients with IPF, which is a predominantly

basal disease), and may also relate to the increased negative intrathoracic pressure which noncompliant fibrotic lungs need to generate during inspiration (Jacob et al., 2016b).

2.6.2 Alterations in pulmonary gas exchange

IPF is associated with multiple pathophysiological changes in pulmonary gas exchange. The lesions of the alveolar-capillary membrane in IPF lungs will impair both the diffusion capacity and ventilation/perfusion (V/Q) relationship, increase dead space ventilation and alveolar-arterial oxygen tension difference ($P_{A-a}O_2$), and finally cause chronic arterial hypoxaemia (Crystal et al., 1976; Plantier et al., 2018; Society et al., 2000).

Reduced diffusing capacity of the lung

The diffusing capacity of oxygen is reduced in almost all patients with IPF. However, in clinical examination, this diffusing capacity is technically very difficult to measure. Therefore, clinical tests actually measure the diffusing capacity of carbon monoxide (DLCO) which provides an estimate of the gas-exchange function of the whole lungs (Plantier et al., 2018). DLCO is a measure of the conductance of gas transfer from inspired gas to the red blood cells, and is usually tested in a single breath where the partial pressure difference between inspired and expired carbon monoxide is recorded (Rosenberg, 1996; Plantier et al., 2018). The carbon monoxide transfer coefficient (KCO) is an index of the efficiency of alveolar transfer of carbon monoxide. It can be referred to as DLCO/VA, where VA is the alveolar volume where gas exchange takes place (Graham et al., 2017).

It has been shown that DLCO is reduced in 98% of IPF patients at the initial diagnosis, although 27% of patients have normal TLC volumes, and 56% have normal

FVC (Cortes-Telles et al., 2014). Interestingly, KCO is within the normal range in up to 30% of IPF patients (Wallaert et al., 2012), particularly in patients with moderately reduced DLCO (Pastre et al., 2015). But a normal KCO value in IPF patients does not mean that pulmonary gas exchange is normal (Plantier et al., 2018). It has been noted that both DLCO and KCO are significantly associated with the degree of IPF measured from CT scans (Wells et al., 1997), but DLCO correlates more strongly with exertional increases of $P_{A-a}O_2$ (Agustí et al., 1994) and highly relates to both dyspnoea (Swigris et al., 2012) and survival time (Hamada et al., 2007).

Dead space ventilation

Increased physiologic dead space ventilation (increased ratio of dead space volume to tidal volume V_D/V_T) is an important characteristic of lungs with fibrosis and happens in most IPF patients both at rest and at exercise (Fulmer et al., 1976; Crystal et al., 1976; Agustí et al., 1991; Miki et al., 2009). The increased dead space is mainly caused by two physiologic features: the first is the increased anatomical dead space, which is a result of the dilation of conducting airways in IPF as discussed in Section 2.6.1 (Plantier et al., 2016); the second is the regional ventilation-perfusion mismatch (increased variation in regional ventilation-perfusion ratio, V/Q), which increases the physiologic dead space. In IPF lungs, the fibrotic (i.e. honeycomb or reticular) areas that are not perfused or poorly perfused but still receive ventilation will have an increased regional V/Q ratio (Strickland et al., 1993; Plantier et al., 2018). An early paper indicated that patients with IPF will often have a VD/VT ratio of greater than 0.4 compared with a normal person (approximate 0.3 for normal) (Crystal et al., 1976). In normal individuals the efficiency of ventilation improves with exercise (that is the VD/VT falls) (Jones et al., 1966; Wasserman and Whipp, 1975), but in more than 90% of IPF patients VD/VT ratio

stays constant or may increase (Crystal et al., 1976).

Ventilation-perfusion mismatching

It is generally thought that the hypoxemia of IPF is related to V/Q mismatching (Wagner et al., 1976; Crystal et al., 1976; Society et al., 2000). The V/Q mismatching may be associated with abnormalities both in ventilation and perfusion (Crystal et al., 1976; Strickland et al., 1993). Crystal et al. (1976) showed an equilibrium picture of ^{127}Xe distribution, which was used to reflect ventilated proportion of the lung, which showed that patients with IPF have patchy, nonsegmental areas of decreased ventilation where airway obstruction or alveolar destruction occurred. As for perfusion, a shift of perfusion was observed to the upper lobes (reflecting pulmonary hypertension) due to the basal distribution of fibrotic lesions, so that areas of relatively low V/Q ratios mostly presented in the upper zones (Crystal et al., 1976). However, Strickland et al. (1993) indicated that the CT based cystic air spaces (i.e. honeycomb) were observed as poorly perfused (probably due to vascular obliteration) but were usually normally ventilated, which explains the increase in physiologic dead space seen at rest and with exercise. Thus, a higher V/Q ratio can be seen in areas where fibrosis and cystic air spaces are dominant, which could be used to distinguish IPF from emphysema (Strickland et al., 1993). In addition, an increased minute ventilation was found in most patients with IPF during exercise. This is mainly due to the increased respiratory frequency, and in part relates to the increase in dead space ventilation as well (Society et al., 2000).

Arterial hypoxaemia

Alterations in the mechanical properties of the lungs, impairment of diffusion capacity and ventilation-perfusion mismatch will finally lead to early-onset exertional chronic ar-

terial hypoxaemia and later-onset resting chronic arterial hypoxaemia in IPF (Hempleman and Hughes, 1991; Hughes et al., 1991; Plantier et al., 2018). Some studies support that the major cause of arterial hypoxaemia in a large proportion of IPF patients is not the diffusion barrier to oxygen or the anatomic shunts, as was originally suspected, but is due to ventilation-perfusion mismatching (Finley et al., 1962; Wagner et al., 1976; Society et al., 2000). The alveolar-arterial oxygen gradient ($P_{A-a}O_2$), which is calculated from arterial oxygen tension (P_aO_2) and arterial carbon dioxide tension (P_aCO_2) may increase, resulting from the reduced ventilation-perfusion ratio, right-to-left shunting, or impairment of oxygen diffusion (Plantier et al., 2018). The increase in $P_{A-a}O_2$ is theorised to be the main mechanism driving hypoxaemia in IPF (Agustí et al., 1991). In a study of 29 IPF patients, the measured average resting P_aO_2 was 69.3 mmHg, and four had normal resting P_aO_2 . However, although the resting P_aO_2 can be normal in some IPF patients, the resting $P_{A-a}O_2$ is invariably abnormal in about 97% of the patients with IPF (Crystal et al., 1976).

2.7 Summary

IPF is a devastating lung disease characterized by an irreversible decline of lung function, and its incidence increases with years of age. The current efforts of studies in IPF mostly focus on the accurate identification and diagnosis of early IPF, underlying mechanisms of pathogenesis and potential biomarkers that can indicate the patient-specific clinical course. The presence of IPF is variable in most patients, but some common characteristics and progressions can be summarized, although this is challenging. The clinical and physiological features of IPF reviewed in this chapter provides background information for further quantitative analysis (Chapter 4) and computational modeling of

patients with IPF (Chapter 5).

Chapter 3

Pulmonary lobar segmentation from CT scans

Identification of pulmonary lobes is of great importance for image-based analysis of lung function and disease progression: segmentation of lobes can facilitate intra-patient image registration for localizing and tracking fibrosis disease progression over time, since lobes are important structural landmarks (Lassen et al., 2011). Also, knowing the lobar distribution of pulmonary fibrosis disease is helpful to guide a patient-specific functional simulation. However, the pulmonary lobar fissure is usually difficult to segment fully automatically, especially for diseased lungs, as fissures are thin, usually of fuzzy appearance and incomplete, and can be obscured by or confused with features of disease (Ukil and Reinhardt, 2009). The following chapter outlines the development of an automatic pulmonary lobar segmentation method using a statistical finite element shape model of the lungs and lobar fissures to guide segmentation. Unlike 'deep learning' methods, this approach requires relatively few subject images as a training set. Development of this method was motivated by the poor reliability of existing methods

for a guaranteed estimate of fissure location, particularly in volumetric images of IPF, or when only thin-slice CT (non-volumetric images) are available.

3.1 Background

3.1.1 Pulmonary lobe anatomy

Within the thorax, the lungs are enclosed by the ribs, and the base of the lungs rests on the diaphragm. The space in between the two lungs is called the mediastinum, and contains the heart, major blood vessels, the esophagus, the trachea, main bronchi, and several other thoracic structures. The airways, blood vessels and nerves enter the lungs from the mediastinum at the hilum. The lungs themselves comprise airways, vessels and a connective tissue framework referred to as the interstitium.

Human lungs are divided into five distinct anatomical regions, which are called pulmonary lobes. These lobes are each supplied by separate airway and vascular branches, and are largely anatomically independent regions. The separating junctions between these lobes are called the lobar fissures. The left lung consists of the left upper lobe and left lower lobe, which are separated by the left oblique fissure (major fissure). The right lung consists of the right upper lobe, right middle lobe and right lower lobe, which are separated by the right oblique fissure (major fissure) and right horizontal fissure (minor fissure). These fissures contain pleural fluid and provide separation between the lobes while permitting some relative movement. In general, the functions of these lobes are relatively independent from each other since there are no major airways and vessels crossing the lobar fissures (Lassen et al., 2010; Doel et al., 2015; Ukil and Reinhardt, 2009). Figure 3.1 shows a schematic diagram of the lungs. The lungs are bounded by

two layers of membrane (pleura) separated by a thin layer of lubricating pleural fluid.

Diagram of the Human Lungs

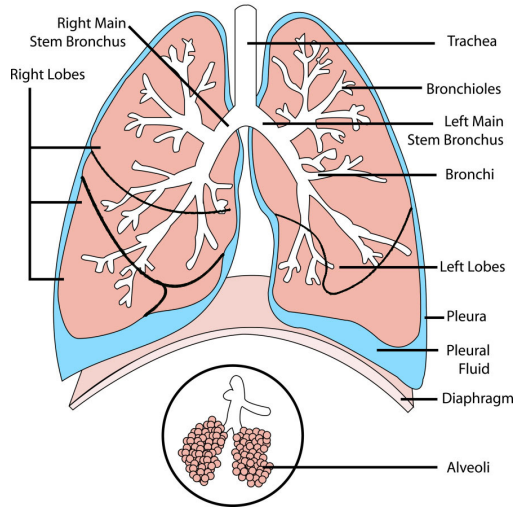


Figure 3.1: Schematic diagram of anatomical lung structure, showing the major airways, lobes and major fissures. The lungs are subdivided into the right upper (RU), right middle (RM), right lower (RL), left upper (LU), and left lower (LL) lobe. The pleural cavity which surrounds the lung consists of a double membrane layer (visceral pleura and parietal pleura) separated by a thin layer of pleural fluid. The inner membrane (visceral pleural) folds inwards between the lobes, creating fissures. Reproduced from (Doel et al., 2015).

3.1.2 High resolution computed tomography

CT imaging is a typical image modality used in diagnosis and management of IPF. It acquires multiple X-ray images at different orientations and reconstructs these images to obtain tomographic views in the region of interest (Zhang et al., 2011). This kind of imaging modality is typically used in clinical applications and research regarding pulmonary structure-function relationship (Hoffman and McLennan, 1997), including detection of both acute and chronic changes in the lung parenchyma. It is particularly relevant here because normal two-dimensional X-rays can not show subtle defects. For

evaluation of chronic interstitial processes (emphysema, fibrosis, and so forth), thin sections with high spatial frequency reconstructions are used (Coxson, 2007). Scans are often performed both in inspiration and expiration. This special technique is called high resolution computed tomography (HRCT). With the help of HRCT scans, a series of high-resolution chest sections can be acquired with slice thickness as low as 0.5mm (Naidich, 2005), which can provide high visibility of the lung boundaries and pulmonary fissures. By making use of some advanced image processing technologies, a wide variety of features can be detected from these images such as density of the lung (Coxson, 2007), volumes of the lung (Hu et al., 2001), the regions of lung disease distributions (El-Baz et al., 2013; Ley-Zaporozhan et al., 2008), airway trees (Graham et al., 2010; Zhu et al., 2010; Diaz et al., 2010) and blood vessels (Shikata et al., 2009). Computed tomography (CT) images acquired at different stages in the breathing cycle can also be used to study lung mechanics and estimate lung ventilation (Hoffman et al., 2006; Yamamoto et al., 2011).

3.1.3 The importance of pulmonary lobar segmentation

The extraction of pulmonary lobes from CT scans is of great importance in applications of lung disease assessment and treatment planning. For clinical applications, the distribution and location of pulmonary disease are beneficial information for doctors to recognize pathogenesis, guide therapy and have further value in surgical planning. That is, because many pulmonary diseases are more prevalent in specific anatomic regions of the lung, often acting at a lobar level. For example, emphysema (Jeffery, 1998), postprimary tuberculosis (Leung, 1999) and silicosis (Rees and Murray, 2007) usually affect the upper lobes, while idiopathic pulmonary fibrosis is commonly present in the lower

lobes (Lin and Jiang, 2015). However, there is currently a lack of quantitative and objective methods for the regional assessment of lung disease. Therefore, techniques are really necessary for identifying the location, shape and volume of the lobes so that lung disease can be measured at a lobar level and the severity can be assessed accurately.

3.1.4 Challenges of automatic pulmonary lobar segmentation from CT scans

The most commonly used method to segment lobes from computed tomography (CT) is by manual assessment of an experienced pulmonary radiologist. However, the process of determining the lobar boundaries is an extremely laborious and time-consuming task, typically taking hours for one patient, since a 3D HRCT image may contain a large number of axial slices which makes the manual segmentation very time consuming. Therefore, doctors rarely use manual lobe segmentation in clinical diagnosis and treatment practice and most clinicians think visual observation subjectively is more effective and convenient. For this reason, an automatic (no user interaction) or semi-automatic (minimal user interaction) lobe segmentation techniques are urgently needed in clinical applications and this has attracted great interest from researchers all over the world (Van Rikxoort and Van Ginneken, 2013; Pu et al., 2009a; Ukil and Reinhardt, 2009).

However, to find an effective and time-saving automatic lobe segmentation method is a challenging task because of anatomical variation and incomplete fissures. Lobar structures vary significantly between subjects, and the anatomical variation in lobe structure is usually associated with age, sex and body type. Pathologies of diseased lungs usually deform the lobar shape abnormally and result in fuzzy appearance of fissures on CT images, in particular when abnormalities are present near the fissures, which makes

fissure segmentation challenging. Even in patients with healthy lung parenchyma, fissures are sometimes incomplete (Gülsün et al., 2006; Doel et al., 2015) (see Figure 3.2).

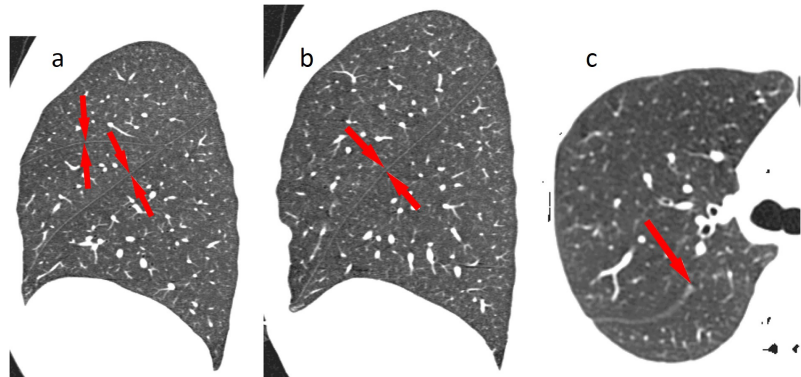


Figure 3.2: Slices of lung CT images illustrating the left and right fissures. Fissures are visible as white lines of high density tissue crossing the low density lung parenchyma. (a) Sagittal slice from the right lung showing the right oblique and horizontal fissures, the horizontal fissure is oriented horizontally. (b) Sagittal slice from the left lung showing the left oblique fissure. (c) Transverse slice from a different data set that show an incomplete right oblique fissure. Reproduced from (Ukil and Reinhardt, 2009).

3.2 Review of current published methods for pulmonary lobar segmentation

In a broad sense, existing lobe segmentation methods usually consist of two steps: the segmentation of lungs and the detection of the three main pulmonary fissures (Van Rikxoort and Van Ginneken, 2013). Currently, quite a number of lung segmentation methods are available and most produce reliable results (Hu et al., 2001; Ukil and Reinhardt, 2005; Sun et al., 2006; Pu et al., 2008; Wang et al., 2009). In contrast, most challenges of automated lobar segmentation lie in the fissure detection, and currently no method has yet been demonstrated to be robust and effective across a wide range of clinical imaging parameters and pathology experienced in clinical practice. Lung lobe segmen-

tation is a complex multi-stage process that cannot be addressed by a simple algorithm (Van Rikxoort and Van Ginneken, 2013; Pu et al., 2009a; Ukil and Reinhardt, 2009). However, to some extent, lung segmentation and fissure detection are two independent parts and can be improved separately. That is, it should be possible for us to change lung segmentation in one way or another without affecting the fissure detection result dramatically. In the following section, existing work is discussed and compared to highlight the key challenges of lobe segmentation algorithms, focusing on these two parts of the process.

3.2.1 Lung segmentation

Segmentation of lung is a prerequisite for the accomplishment of lobe segmentation, as it can provide a boundary condition for the subsequent fissure detection, allow the estimation of lung volumes and detect and quantify abnormalities within the lungs. While not precisely defined, the lung region is usually considered to be the volume enclosed within the pleura, including the lung parenchyma, airways and vessels, but excluding those parts of the major airways and vessels which extend the pleural boundary. In this section, the published methods for lung segmentation are briefly discussed. These methods are summarized in Table 3.1.

Conventional lung segmentation methods

In CT scans from healthy subjects, the air-filled lung parenchyma usually has a different attenuation level compared to surrounding high-density tissue at the pleura. For this reason, quite a lot of conventional lung segmentation algorithms adopt a thresholding approach to search for a large connected region of the air-like values within the

Table 3.1: Summary of lung segmentation methods

Authors	Algorithms	Notes
Kalender et al. (1991); Kemerink et al. (1998); Leader et al. (2003)	2D thresholding method	1. May cause discontinuity between slices; 2. Time consuming
Keller et al. (1981); Heddlund et al. (1982); Hoffman et al. (1983); Hoffman and Ritman (1985)	Early-stage 3D thresholding method combined with manual interaction	Cause too many intra-operator errors
Hu et al. (2001)	1. Automatically choose thresholding value; 2. Separate left and right lung 3. Morphological lung boundary smoothing	First group to apply fully automatic 3D thresholding method
Ukil and Reinhardt (2005)	1. Bounding box defined around mediastinum; 2. Extract left and right main stem bronchi; 3. 3D Morphological boundary closing	Automatic method using air-way tree information
Sun et al. (2006)	1. Anisotropic filtering; 2. Wavelet transform-based interpolation to construct 3D data; 3. Adaptive 3D region growing combined seed-locating to detect lung region; 4. Fuzzy logic algorithm and 3D morphological to fill hole	3D method using signal-to-noise ratio
Kitasaka et al. (2003)	1. Affine transformation to fit a contour shape model to individual images; 2. Active contour model to refine initial segmentations in 3D	Solve the problem of lesions adjacent to the chest wall and mediastinum
Pu et al. (2008)	1. 3D initial thresholding processing; 2. Adaptive border marching	Minimize oversegmentation of adjacent regions such as abdomen and mediastinum
Pu et al. (2011)	1. Principle curvature analysis to eliminate noise; 2. Radius basis function to smooth lung in 3D	Solve the problems of disease, noise or artifacts
Prasad et al. (2008)	1. 3D thresholding algorithm; 2. Adapt lung curvature using rib curvature; 3. Morphologic operation	1. Use rib curvature information to define lung borders; 2. Solve the problem of error detection for lung pathologies
Wang et al. (2009)	1. 3D thresholding processing; 2. Texture analysis to identify abnormal regions; 3. 2D hole filling	Texture feature analysis to segment ILD lungs
Sun et al. (2012)	1. Active shape model to roughly find lung outlines; 2. Optimal surface finding to adapt final segmentations	3D method using rib information

image. Threshold values are acquired from gray level histogram analysis and then the initial lung region is detected and a region growing method for the airways is usually applied subsequently to exclude the trachea and major airway branches. Some thresholding algorithms, especially older studies, are developed in 2D space, which means each axial section of CT imaging needs to be calculated separately (Kalender et al., 1991; Kemerink et al., 1998; Leader et al., 2003; Armato and Sensakovic, 2004). This two-dimensional method is a logical choice in the case of thick-slice CT data, but it may cause discontinuity between slices. Therefore, when higher resolution isotropic data become available, an improved 3D processing method (Hu et al., 2001; Ukil and Reinhardt, 2005; Sun et al., 2006) was developed to avoid slice inconsistencies and reduce time for segmentation.

Most early 3D thresholding-based lung segmentation methods (Keller et al., 1981; Hedlund et al., 1982; Hoffman et al., 1983; Hoffman, 1985; Hoffman and Ritman, 1985) required significant manual interaction, such as manually selecting threshold values or seed points for region growing, and separating left and right lung manually. That means the whole process may be too time consuming and cause too many intra-operator errors. Hu et al. (2001) was the first group to apply a threshold-based algorithm in a fully automatic lung segmentation method. In their study, the lung region was firstly extracted from the CT images by gray-level thresholding processing. Instead of a fixed threshold value, an optimal thresholding method was used to automatically choose a threshold value that reflects the gray-scale characteristics of a specific dataset. The left and right lungs were then separated by identifying the anterior and posterior junctions by dynamic programming. Finally, a sequence of morphological operations was used to smooth the irregular boundary along the mediastinum.

Ukil and Reinhardt (2005) developed an improved automatic lung segmentation

method based on the previous work (Hu et al., 2001) to smooth lung boundaries in 3D using information from the segmented airway trees. A bounding box was firstly defined around the mediastinum for each lung using the information from the segmented human airway trees, and all operations were then performed within the bounding box. After that, all generations of the airway distal branches were defined to the left and right main stem bronchi to be part of the respective lungs, and all the other segmented structures could be excluded. Finally, a fast morphological closing with an ellipsoidal kernel was performed to smooth the surface of the lung. This method solved the problem of irregular and inconsistent lung boundary of the regions near the mediastinum by using a common threshold algorithm.

Sun et al. (2006) presented a 3D-based method for segmenting lungs with higher accuracy. In this paper, an anisotropic filtering method was firstly applied on CT slices to enhance the signal-to-noise ratio. A wavelet transform-based interpolation method was subsequently used to construct the 3D volumetric CT slice data with volume rendering. After that, an adaptive 3D region-growing algorithm was developed to detect lung region, combined with automatic seed-locating methods. Fuzzy logic algorithms and 3D morphological closing approaches were finally used to refine the lung volume and fill the holes in it. The method was effective and robust with an average accuracy rate of 88.5%.

Specially designed lung segmentation methods for abnormal lungs

Although conventional threshold-based methods are fast, robust and accurate for healthy subjects, they may fail to perform well for scans containing physiologic abnormalities, which often results in segmentation errors and requires clinicians to manually edit the results (see in Figure 3.3). Currently, specially designed lung segmentation methods

mostly focus on one kind of disease and therefore can not get a good result across a large population (Kitasaka et al., 2003; Sluimer et al., 2005; Pu et al., 2008, 2011; Prasad et al., 2008; Korfiatis et al., 2008; Wang et al., 2009; van Rikxoort et al., 2009; Sun et al., 2012).

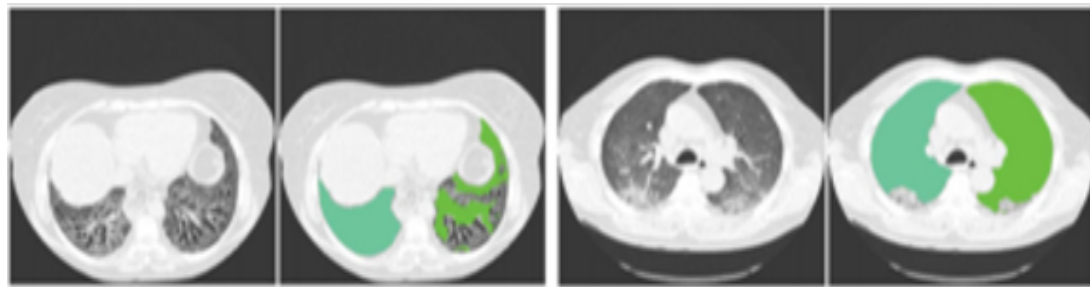


Figure 3.3: Illustration of the performance of conventional 3D thresholding lung segmentation methods on pathological abnormal lungs. Lung borders are not recognized accurately because of the higher densities of the abnormalities compared to the normal tissues. Reproduced from (Van Rikxoort and Van Ginneken, 2013).

To deal with the problem of lesions adjacent to the chest wall and mediastinum, (Kitasaka et al., 2003) developed a lung area extraction method using a shape model. A contour shape model using a Bézier surface was fitted to the contour surface of the individual input images with an affine transformation method. Then, an active contour model was utilized to refine the initial segmentation. The results showed that most lesions could be identified accurately using this method. However, as the lung apex and base were not included in the model, lesions adjacent to the lung apex or diaphragm could result in segmentation errors.

Pu et al. (2008) presented a lung segmentation algorithm based on adaptive border marching (ABM) to include juxtapleural nodules in the lung region since these nodules may be excluded from the results calculated by a conventional threshold-based algorithm. The adaptive border marching algorithm could smooth the lung borders after an

initial thresholding processing and minimize oversegmentation of adjacent regions such as the abdomen and mediastinum. The method was tested on 20 datasets and the results demonstrated that this method could re-include all juxtapleural nodules in the lung regions. An average over-segmentation ratio of this method was 0.43% which was lower than the reference standard average segmentation determined by an expert. In order to deal with the problem of various diseases, image noise or artifacts, and individual anatomical variety, (Pu et al., 2011) developed a shape analysis strategy termed "break-and-repair". A principle curvature analysis was applied to eliminate the problematic regions and then radial basis function (RBF) based implicit surface fitting was used to get a smooth lung surface.

To overcome the problem of error detection for lung pathologies, Prasad et al. (2008) made use of rib curvature information to help with finding the lung borders. The method was based on a threshold-based algorithm followed by a morphologic operation. The core principle of the method was to adapt the threshold value to an individual subject by making the curvature of lung along the ribs be similar to the curvature of the ribs. The curve of the ribs and lung boundary were both represented by polynomial interpolation even though there was minimal deviation from this representation. The results showed that the performance of the rib segmentation method was better than the conventional one.

Wang et al. (2009) proposed a texture analysis-based method to segment ILD lungs. The lung region including normal and mild ILD lung parenchyma was first segmented by a CT value thresholding technique and then texture-feature images derived from the co-occurrence matrix was used to identify abnormal lung regions with severe ILD from the initial results. 2D holes filling was applied to smooth the final lung segmentation. The overlap rate, volume agreement, mean absolute distance (MAD), and maximum ab-

solute distance between the automatically segmented lungs and the reference lungs (delinieated manually by a medical physicist) were employed to evaluate the performance of the segmentation method.

On the basis of the previous studies, (Sun et al., 2012) developed a further approach for segmentation of lungs with high-density pathologies. The method had two main steps. In the first step, a robust active shape model (RASM) matching method was utilized to roughly find the outline of the lungs. To initialize the shape model of RASM, the detected rib information was used subsequently. In the second step, an optimal surface finding approach was applied to further adapt the initial segmentation result to the lung. The method was evaluated on both normal and abnormal subjects and had a good performance.

3.2.2 Fissure detection

The currently published fissure detection methods can be mainly classified into two categories. The first category is anatomical knowledge based methods, which usually depend on either local or global knowledge of the anatomy of lung structure based on two pulmonary anatomical features. The first feature is the fact that there should not be any large vessels in the vicinity of lobar fissures, so fissures should locate in the gaps between airway and vessel trees. Another feature is that the airway bronchi can be classified into five lobar branches using an edge detection method (figure 3.4). The second category of fissure detection is shape based analysis methods. This kind of method commonly makes use of gray-level information and shape information to detect the fissures. The published fissure detection methods are summarized in Table 3.2.

Table 3.2: Summary of fissure detection methods

Authors	Algorithms	Notes
Kuhnigk et al. (2003, 2005)	Watershed transformation method to analyze anatomical structures to help with fissure detection	First group to use lobar airways and vasculature into fissure detection ¹
Ukil and Reinhardt (2009)	1. Watershed transform guided cost image to define initial fissures; 2. Construct ROI; 3. Structure tensor analysis combined with optimal surface detection to find fissure surface; 4. Fast marching method to detect incomplete fissures	1. Developed on Kuhnigk's method; 2. Can detect incomplete fissures ¹
Lassen et al. (2010)	Watershed transformed anatomical structure based method	An extension of Kuhnigk's method ¹
Zhou et al. (2004); Saita et al. (2006)	1. Edge detection to class vessels and bronchi; 2. Hough transform to detect curve surface	Take advantage of linear appearance of fissures ¹
Wang et al. (2004, 2006)	1. Identify initial fissure ROI; 2. "Ridge map" based transformation to enhance initial fissure; 3. Shape-based curve growing to get the final fissures.	2D shape based method ²
Frangi et al. (1998)	Hessian matrix based analysis to extract local image structures	The first paper to apply Hessian matrix analysis on image segmentation in 3D ²
Wiemker et al. (2005)	Combine first derivative and second derivative of image gray values to find fissures	An early paper using Hessian matrix on fissure detection ²
Ochs et al. (2007); van Rikxoort et al. (2008)	Use pattern recognition approach and Hessian matrix and classification operation to detection fissure	An improved Hessian based method ²
Lassen et al. (2011, 2013)	1. Use anatomical structures to acquire initial fissure; 2. Hessian matrix surrounding initial guessing areas; 3. Morphological operations to filter noise	Combine both anatomical information and gray-level information ^{1,2}
Doel et al. (2012)	1. Use both anatomy knowledge and Hessian matrix to find fissure candidate points; 2. Multi-level B-spline curve to get the final fissure surface.	Combine both anatomical information and gray-level information ^{1,2}
Ross et al. (2010, 2013)	1. Particle system combined with Hessian matrix to get candidate fissure points; 2. Maximum a posterior method to remove noise points; 3. Thin plate spline to form final fissure surface.	Effective for lung lobe segmentation in absence of anatomical structures ²

¹ Anatomy knowledge based method.

² Shape based analysis method.

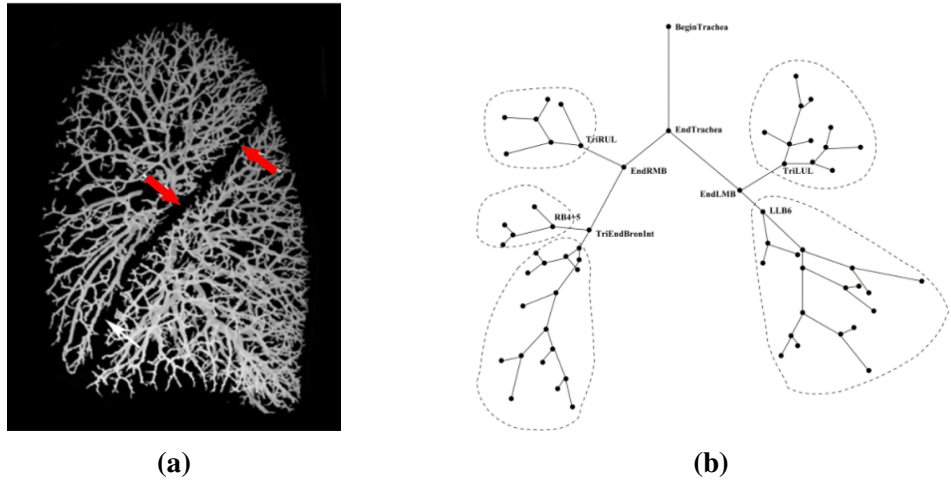


Figure 3.4: (a) Segmented volumes of the vascular tree. There are no large vessels in the vicinity of lobar fissures. (b) Anatomically labeled airway tree showing lobar subtrees. The airway tree can be classified corresponding to five lobes. Reproduced from (Ukil and Reinhardt, 2009).

Anatomy knowledge based method

Methods aiming at detecting the lobar fissures usually start by finding an approximate location of the lobar borders based on prior anatomical knowledge of lung structures in order to narrow the search area for fissure detection (Kuhnigk et al., 2003, 2005; Zhou et al., 2004; Saita et al., 2006; Zhang et al., 2006; Ukil and Reinhardt, 2009; Pu et al., 2009a; Lassen et al., 2010; Doel et al., 2012). This method is developed mainly based on two pulmonary anatomical features. The first feature is the fact that there should not be any large vessels in the vicinity of lobar fissures, so fissures should locate in the gaps between airway and vessel trees. Another feature is that the airway bronchi can be classified into five lobar branching using an edge detection method (figure 3.4). A number of published papers use the segmentation results of airways and vessels to help with localizing the fissures. Usually, the vascular segmentation provides more accurate estimation of lobar fissure locations than the airway trees, since more vessel generations

can be detected from CT scans. These vessels span the entire lung volume which can help us find complete gaps between lobes. However, airways also play an important part in initial estimation of fissures, since airways trees can be more reasonably divided into lobar branching, while the structure of vasculature branching is more complicated and some connections are hard to separate accurately. Therefore, a lot of studies make use of both vessel and airway information to guide fissure detection (Ukil and Reinhardt, 2009; Lassen et al., 2010; Doel et al., 2012).

Kuhnigk et al. (2003, 2005) was an early group to present a framework of taking both lobar airways and vasculature into account for automatic fissure detection. A watershed transformation method has been used to take an analysis of these anatomical structures and this method was widely used and improved by other researchers, but the results calculated by this simple algorithm were not accurate enough even for some clearly visible fissures.

Ukil and Reinhardt (2009) developed Kuhnigk's fissure detection method which used a distance transform to combine segmented vessels, lobar airways, and original chest CT scan as a cost image to guide initial fissure guessing. They found that the improved watershed transform algorithm could provide a close initial approximation to the lobar fissures. Subsequently, a further refinement method was used to construct a region of interest (ROI) which encompasses the fissures. A 3D optimal surface detection algorithm combined with a ridgeness measurement was then applied to enhance the ROI, and find the optimal surface within the ROI. Finally, incomplete fissures were smoothly extrapolated using a fast-marching method based segmentation of a projection of the optimal surface. A significant improvement of this method is that it can segment incomplete fissures.

Lassen et al. (2010) also described the fissure detection method by building a cost image for the watershed transformed segmentation which is an extension of the framework of Kuhnigk. The interactive segmentation method was tested on 25 CT scans comparing to a manual segmentation by a human observer and showed an average error distance of 1.57 ± 0.3 mm. In addition, Zhou et al. (2004) and Saita et al. (2006) took advantage of the linear appearance of fissures to class the vessels and bronchi into five lobe regions using an edge detection method and the Hough transform based curved surface detection method, respectively.

Shape based analysis method

Generally, lobar fissures can be regarded as bright planes crossing the pulmonary volume because of the higher density value of fissures compared to the surrounding tissues. Based on this information, quite a number of published methods use a local filtering algorithm to detect the voxels which lie on these planes, so that these detected voxel points can construct a continuous fissure surface. In 2D space, the fissure appears as a clear curve, therefore some early papers usually detected fissure points based on gray-level information in 2D space. For example, Wang et al. (2004, 2006) presented a 2D fissure detection method based on shape information. In this paper, the fissure was initially denoted as a curve based on the prior knowledge of the fissure shape to identify the surrounding region of fissure, called "fissure region" for subsequent automatic segmentation. Next an image transformation called "ridge map" was proposed for enhancing the appearance of initial fissures. A shape-based curve-growing method modeled by a Bayesian network could then be applied to this "map" to segment the fissure.

In 3D space, the most commonly used method to detect these pulmonary fissure plane structures is taking an eigenvalue analysis of the Hessian matrix (Frangi et al.,

1998; Wiemker et al., 2005; Kitasaka et al., 2006; Ochs et al., 2007; van Rikxoort et al., 2008; Lassen et al., 2011, 2013; Ross et al., 2010; Doel et al., 2012). Frangi et al. (1998) was the first to present an eigenvalue analysis of the Hessian matrix to detect plane structure (fissure) and tube structure (vessel) on CT images. The three eigenvalues of the Hessian matrix gives a fissure probability for each voxel and the relationship between the eigenvalues of the Hessian matrix describes the local image structure. Wiemker et al. (2005) was also an early paper to use the Hessian matrix for fissure detection and two 3D filter approaches were proposed in this paper. The first filter was based on the first derivatives of the image gray values and utilized the eigenvalues of the local structure tensor. The second filter was based on the second derivatives and utilized the eigenvalues of the local Hessian matrix.

Ochs et al. (2007) and van Rikxoort et al. (2008) used a pattern recognition approach to detect pulmonary fissures combined with eigenvalue analysis of the Hessian matrix as feature and classification was also performed on these fissures. Lassen et al. (2011, 2013) combined both anatomical based and shape based methods which successfully eliminated most false points. The first anatomic-based method found a region of interest, and then the Hessian matrix analysis was used only in the surrounding area of the initial guess for fissure locations. Subsequently, morphological operations such as direction-based connected component analysis were used to further reduce some non-fissure points. Doel et al. (2012) also made use of both an anatomy knowledge based method and the Hessian matrix to find fissure candidate points and proposed a multi-level B-spline smooth curve through the fissure points and extrapolated to the lung borders to get the fissure surfaces.

Ross et al. (2010, 2013) proposed a particle system that sampled the image domain combined with the Hessian matrix to get a set of candidate fissure locations. A maxi-

mum a posteriori (MAP) estimation was then used to eliminate false candidate points, and a post-processing operation was applied to remove remaining noise points. A thin plate spline (TPS) interpolating surface fitting method was lastly performed to form the final fissure surfaces. This method is effective for lung lobe segmentation in the absence of anatomical structures.

3.3 Methods: automatic statistical shape model based lobar segmentation method

Here, a SSM guided method is presented to segment pulmonary lobes from CT images. A three-step approach is followed for the lobe segmentation (shown in Figure 3.5): in the first step, a threshold-based lung segmentation method defines the lung boundary; in the second step, a SSM is deformed to provide a "search region" for fissure locations; in the third step, fissures are located using a Hessian matrix protocol combined with connected component filters and a surface fitting algorithm. This method is able to detect fissures in all test subjects, whereas existing segmentation tools failed in several subjects. The new procedure does not depend on prior segmentation of anatomical structures (airway lobar classification) other than lung shape and has promising potential as a clinically useful automatic lobe segmentation procedure. A user-interactive interface was also developed for the user to control and visualize the whole segmentation process and to allow do some manual correction on the segmented results, if required.

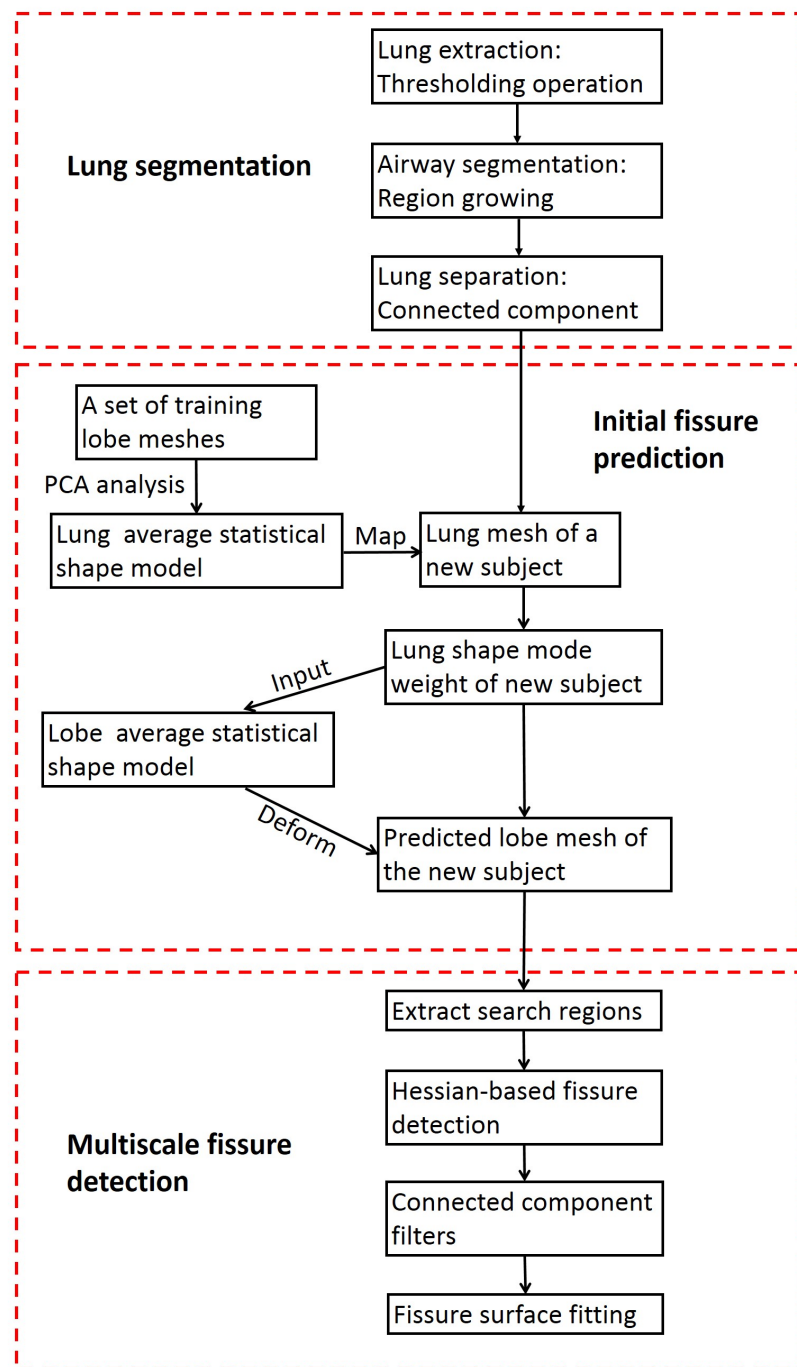


Figure 3.5: Flow diagram of the lobar segmentation process.

3.3.1 Lung segmentation

A good lung segmentation is a prerequisite for the next steps in this study, since all the other segmentations need to be performed inside the two lung regions. In this chapter, a common thresholding method was used to segment the lungs (Ukil and Reinhardt, 2005). The procedure consists of the following steps: The method firstly uses a thresholding operation (-775 Hounsfield Units) and connected component identification to find the initial lung regions and trachea location. By using the most apical point of the trachea as a starting point, a region growing technique was applied to detect the airway trees. Then, left and right lungs were separated as the two largest connected components remaining after removing the trachea and main left and right bronchi. Figure 3.6 shows a typical lung segmentation result.

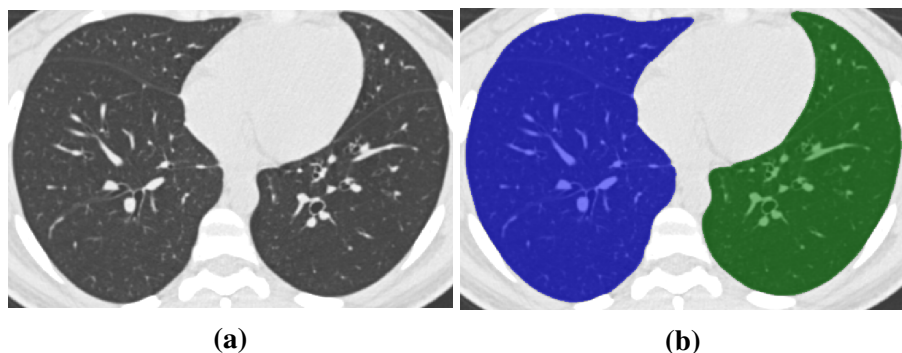


Figure 3.6: Lung segmentation result. (a) Raw CT image. (b) Segmented lungs.

3.3.2 Statistical finite element models of lung and fissure shape

For human organs, there is usually a significant difference in shape and anatomy between different groups of people, such as young and old, male and female, healthy and diseased (Krumpe et al., 1985; Crapo, 1993). This difference is caused by different functional signals and behaviors, and often lead to organ shape variation across populations.

Shape analysis provides a way to understand the underlying mechanisms of those variations in anatomical and physiological processes. The importance of statistical shape analysis in many kinds of biological studies has been well established (Dryden and Mardia, 1998; Stegmann and Gomez, 2002; Styner et al., 2003; Heimann and Meinzer, 2009), because of its potential to capture morphological variation within and between healthy and pathological structures.

Computational model-based approaches of image segmentation have become increasingly popular in the last two decades (Taylor et al., 1995; Kelemen et al., 1999; Tsai et al., 2003; Okada et al., 2008). This technique takes a new image set and matches it to its expected shape information, potentially reducing the impact of image artifacts and other perturbations associated with traditional low-level algorithms (Ecabert et al., 2008; Zhang, 2013). A feasible method to collect individual variations in the lung shape and location of fissures (including how they vary with lung inflation) is to analyze a series of training shapes using statistical techniques, leading to a statistical shape model. This can capture the shape difference and construct a mean shape model for a cohort of different people. A commonly used SSM based segmentation method is to take a new image set and match it to its expected shape information.

Finite element lobar shape modeling

To guide a statistical shape model based segmentation, the first step is to generate the statistical lobar mesh using a set of training data. Statistical shape analysis of a lobe shape model requires a correct lobe shape description using a set of parameters. In this section, a Statistical Finite element analysis of Lobe (SFeaL) based on an active shape model (ASM) (Cootes et al., 1995) of the lung was derived from a training set of segmented lung and fissure surface locations. This approach employs a finite element

shape mesh to specify pulmonary lobar shape which provides an efficient parameterized representation of lobar boundaries and makes shape constraints available during image analysis. The training set consisted of data from 50 subjects. 35 subjects were selected from a study of healthy subjects aged 50 to 100 years, the human aging cohort (AGING) study and a further 15 subjects were selected from a separate study of younger healthy subjects, the Human Lung Atlas (HLA). All the AGING and HLA subjects are healthy non-smoking subjects including both males and females. In the AGING group, HRCT imaging was acquired at Auckland City Hospital using a Phillips Brilliance 16 scanner, with between 400-700 slices per volumetric image. The study was approved by the Northern A Health and Health and Disability Ethics Committees (HDEC), Ministry of Health on 29 April 2013 through the HDEC-Full Review Pathway - ethics reference 13/NT/41. The HRCT images from HLA cohort were obtained at the Iowa Comprehensive Lung Imaging Center (I-Clic) using a Siemens Sensation 64 MDCT scanner, with between 500-700 slices per volumetric image. The study was approved by the University of Iowa Institutional Review Board. A summarized population demographics of the subjects used for statistical shape model construction is listed in Table 3.3

Table 3.3: Summarized demographics for the AGING and HLA datasets.

	AGING (N=35)	HLA (N=15)
Age (years)	72.3 ± 11.41	22 ± 1.9
Sex(M/F)	18/17	5/10
Height(m)	1.66 ± 0.14	1.7 ± 0.1
Weight(kg)	70.6 ± 11.1	67.6 ± 12.2
BMI(kg/m^2)	25.6 ± 3.0	23.3 ± 2.2
Ethnicity		
- Caucasian	25	14
- Māori(AGING only)	1	N/A
- Asian	2	-
- African-American	-	1
- Unknown	7	-

To define the lung shape, volumetric CT images were segmented using the method described in Section 3.3.1. The segmented lung surface was then digitized into a set of data points as a 3D-space representation of lung shape (Figure 3.7a). Fissure surface segmentation was performed manually using the open-source visualization software CMGUI (<https://www.cmiss.org/cogui>) by an expert user, to provide a gold-standard definition of the fissure location for each subject in the training set (Figure 3.7b, 3.7c). A high order (bi-cubic Hermite) finite element template mesh with the same mesh connectivity for each subject was geometry fitted to the lung and fissure surface data for each subject. The current lung lobe mesh consists of two separate meshes which represent the left and right lung enclosing the lung parenchymal tissue volume.

The generation of fitted anatomical lobar mesh consists of two steps: Firstly, an initial linear mesh is created by selecting some data points to be nodes and creating two-dimensional surface elements by joining these node points appropriately using straight lines. The template mesh for the left lung mesh has 35 nodes and 44 elements which described the left lung surface and left oblique fissure, while the right lung mesh has 50 nodes and 62 elements which defined right lung surface, right oblique fissure and right surface fissure. Once the linear surface mesh has been created, an iterative geometric fitting process is subsequently undertaken, where the aim is to adjust the nodal positions and derivatives representing the shape of the lung. The element surfaces were matched to the data as closely as possible, by minimizing an error function. In the second stage, the lung lobe surface was modeled using bi-cubic Hermite basis functions with C1 continuity. This bi-cubic Hermite mesh has the same mesh connectivity as the linear mesh, but has more degrees of freedom (DoFs) as it also contains nodal derivative information. Each node has 12 DoFs which store the global coordinates (x, y and z) and first and second nodal derivatives ($\frac{\partial n}{\partial \xi_1}$, $\frac{\partial n}{\partial \xi_2}$, and $\frac{\partial^2 n}{\partial \xi_1 \partial \xi_2}$), where n is x, y and z, and

ξ is the local element coordinate. In our lung lobe model they are defined such that ξ_1 is in the antero-posterior direction while ξ_2 is in the crano-caudal direction, ξ_1 and ξ_2 have values that range from 0 to 1. Each node of the fitted mesh is either an anatomical landmark (the left/right lung apex, the base vertex, the shape corner and the center point of the middle line of fissure) or a pseudo-landmark (e.g. a specific proportion of the arc-length between two anatomical landmarks). These landmarks allow us to define the coordinate of the control points in consistent positions registered to the geometry of the lung. A least squares fit of the mesh to the lung and fissure surface data was conducted using CMISS (<https://www.cmiss.org>), which is a finite element modeling environment. Specifically, the sum of the distances between each data point and its projection on to the nearest element was minimized during the fitting process. This distance is a function of the element location and shape parameters. In this procedure, the nodal parameters are interpolated to find the projected points. The global coordinates of the projected points are a function of local element coordinates, ξ_1 and ξ_2 , and nodal parameters. Some manual operations were involved to adjust the mesh nodal positions and derivatives to the data cloud, which can help to improve the speed and accuracy of fitting. The average root mean square (RMS) error of this fitting method was 4.79 mm for the 50 training subjects (Figure 3.7d). More details on the fitting procedure can be found in (Bradley et al., 1997; Tawhai and Burrowes, 2003; Fernandez, 2004).

PCA-based statistical shape model construction

A prerequisite of the construction of SSM is object alignment to remove the orientation and scaling differences between shapes. Here a General Procrustes Alignment (GPA) was selected as a registration method (Dryden and Mardia, 1998; Rohlf, 1999). The GPA algorithm finds the optimal rotation matrix and translation vector which minimizes

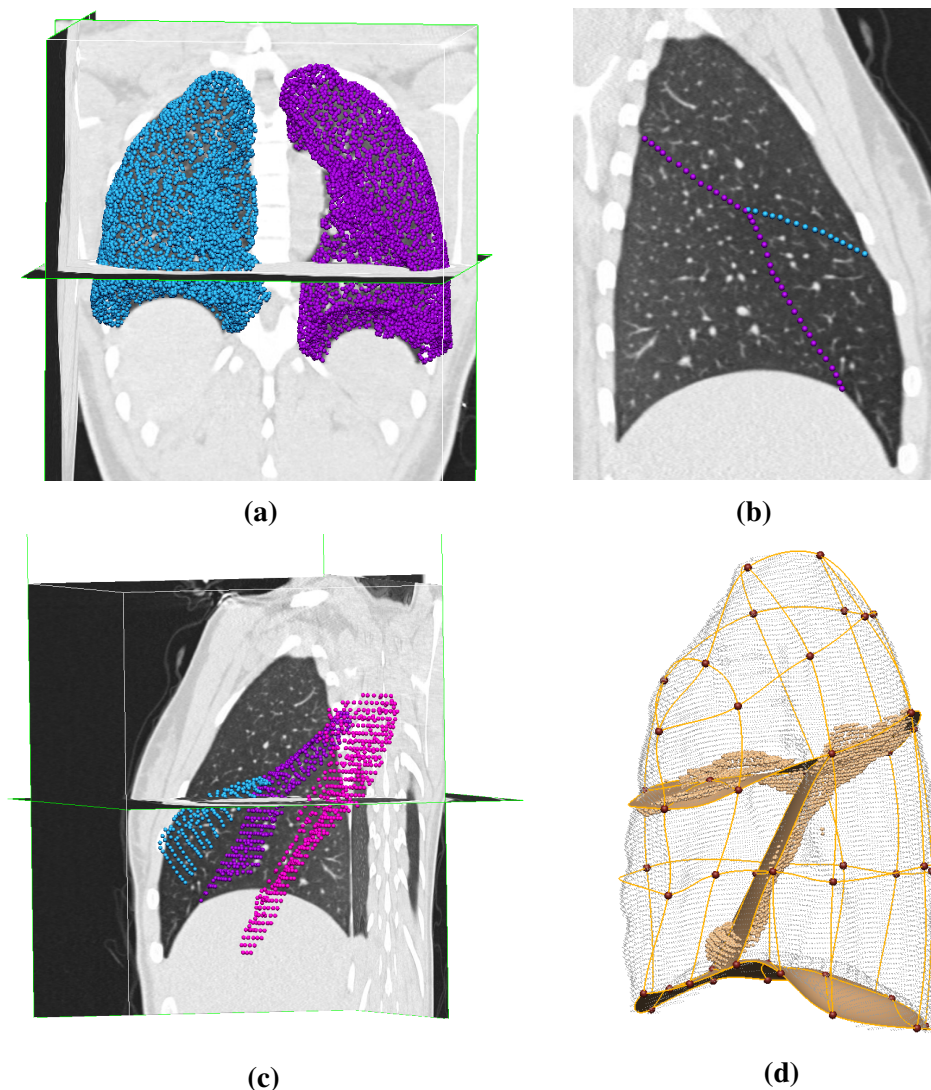


Figure 3.7: Finite element modeling of lung lobe shape. (a) Lung surface data extracted from segmented lung masks (purple points for left lung, blue points for right lung). (b) Manual digitized fissure points in 2D sagittal image of right lung (purple points for right oblique fissure, blue points for right horizontal fissure). (c) Manual digitized fissure points shown in 3D (pink points for left oblique fissure, purple points for right oblique fissure, blue points for right horizontal fissure). (d) Lobe shape fitting with lung surface data and digitized fissure data of right lung.

the overall distance between two sets of points with respect to the Euclidean norm. In our study, a reference lung model sample was randomly chosen from the training set. Then all the other training models were aligned to this reference model. In this process, the volumes of all subjects were normalized to 1 L and any residual rotation and translation were removed as well. The generalized procrustes alignment can be represented as an affine transformation in mathematical terms:

$$\bar{S} = \alpha RS + T, \quad (3.1)$$

where \bar{S} represents the aligned shape vector to the reference shape from the subject shape vector S , R is the rotation matrix and T is the translation vector. Figure 3.8a shows the procrustes aligned meshes of all the 50 subjects. For each subject, the aligned lung shape can also be represented as

$$\bar{S} = [\bar{x}_1 \bar{x}_2 \bar{x}_3 \cdots \bar{x}_{p-1}; \bar{x}_p], \quad (3.2)$$

where \bar{x} are the nodal parameters which contain coordinates and derivatives (12 DoFs), and p represents the number of nodes for both left and right lung ($p = 225$ in this study). The data vector \bar{S} of each lung was then assembled as the concatenation of all lungs, termed \bar{S}_{whole} . \bar{S}_{whole} is an $n \times N$ matrix, where n is the number of nodal parameters for each lung ($n = 12 \times 225 = 2700$ in this study), and N is the number of training subjects ($N = 50$). Thus, \bar{S}_{whole} can be regarded as a cloud of N points in the constructed n -N space. This matrix was decomposed into modes of variation using principle component analysis (PCA). PCA is a commonly used technique in statistical feature space to reduce the dimension of the dataset. It uses an orthogonal transformation to convert a number of (possibly) correlated variables into a set of values of linearly uncorrelated variables

called principal components. The number of distinct principal components is equal to the smaller of the number of original variables or the number of observations minus one. The resulting vectors are an uncorrelated orthogonal basis set.

In order to perform PCA, each shape parameter was centered by subtracting the mean value \bar{x} . Then the covariance matrix was built based on the mean-centered matrix S by $C = SS^T$. After the PCA technique was performed on the covariance matrix C , we obtain a set of eigenvectors $\mathbf{u}_1, \mathbf{u}_2, \dots$, corresponding to a set of non-negative eigenvalues $\lambda_1, \lambda_2, \dots$. Each eigenvalue represents how much variation or variance in the data is captured by the corresponding eigenvector. Each lung shape variation $m_i(w)$ can be approximated by a linear combination of the eigenvector and its corresponding eigenvalue:

$$m_i(w) \approx S_{mean} + \mathbf{u}_i w_i, \quad (3.3)$$

where w_i is a weight factor given to each mode of variation, and $i = 1, \dots, L$ ($L \leq 49$ in this study). S_{mean} is the average shape across all the subjects, which is obtained by:

$$S_{mean} = \frac{1}{N} \sum_{i=1}^N s_i, \quad (3.4)$$

where s_i is the i th lung shape model from the training set, here $i = 1, \dots, N$ ($N=50$ in this study). The average shape model is shown in Figure 3.8b.

3.3.3 Initial prediction of lobar location in an individual

Using the method described in section 3.3.2, the lung shape variation across the training set can be decomposed into a series of modes, and each specific lung shape can

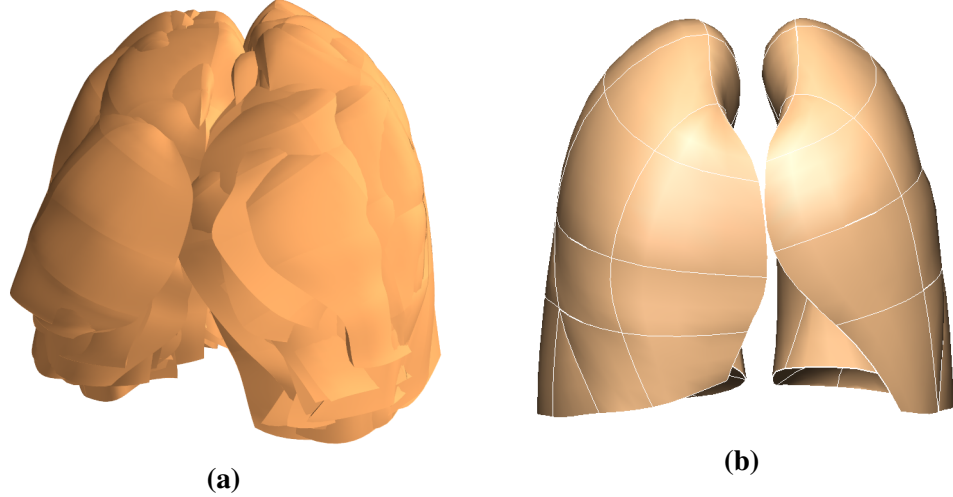


Figure 3.8: Statistical shape model construction based on principle component analysis. (a) Procrustes aligned meshes of 50 subjects. (b) Average shape model of 50 training subjects. All the weight values are zero for this shape model.

be represented with the corresponding mode weight values. In this study each mode represents one type of lung and fissure surface shape variation. In order to predict the fissure location, two PCA-based SSM were constructed using the same training dataset. The first lobe SSM was built using both the lung surface parameters and fissure surface parameters. The second lung SSM was derived for the same training set but did not include the fissure surfaces and so only described the shape of the lung surface.

The two SSMs were used to predict the fissure locations for subjects that were not part of the training set, using only the definition of the lung surface for the subject as input. A finite element mesh of the lung surface (without fissure information) was generated for each new subject. The new fitted lung mesh was procrustes aligned to the same reference model as the training subjects were aligned to. Then this aligned lung surface mesh was projected on to the lung surface SSM (with no fissure surfaces). The principal component weight values were calculated from the projection, which was represented as $w_{new} = [w_{new1}, w_{new2}, \dots, w_{newL}]$ ($L \leq 49$) here. The first seven principal

components accounted for over 90% of the total lung shape variation in the training set. Therefore, the first seven mode weights were used on the lobe SSM (which includes both lung and fissure surfaces) to reconstruct the projected lobe mesh for this new subject:

$$S_{new} = S_{mean} + \sum_{i=1}^7 \mathbf{u}_i w_{newi}, \quad (3.5)$$

where S_{mean} is the average lobe shape model across all the subjects, \mathbf{u}_i is the first seven eigenvectors of the covariance matrix C corresponding to the lobe SSM, and w_{newi} is the projected weight values from the lung SSM. An initial estimation of fissure locations was then made (Figure 3.9). This initial prediction of lobar fissures provides a reduced search area for subsequent image analysis and ensures an estimation of complete lobar structures even if a fissure is incomplete or is difficult to detect.

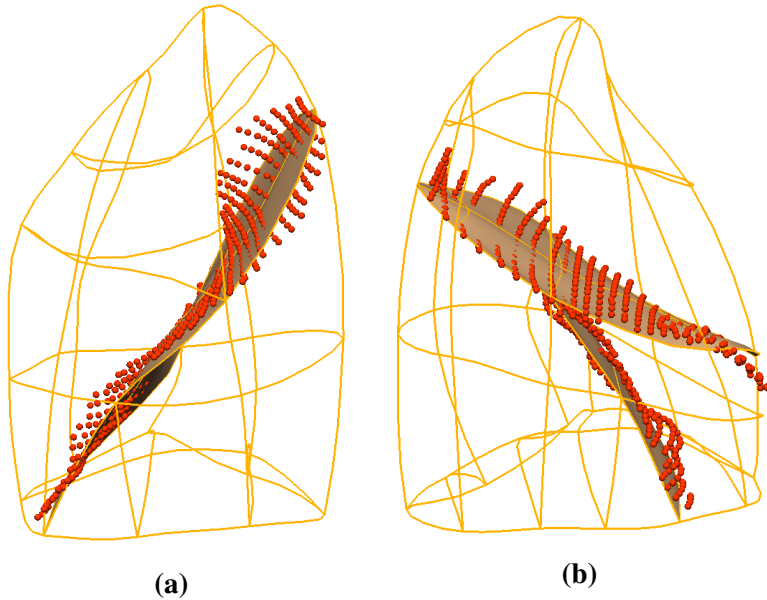


Figure 3.9: Fissure prediction results compared to ground truth fissure points. The fissure surface meshes are estimated fissure locations and the red points are manual tracing fissure points by an expert. (a) Left lung. (b) Right lung.

3.3.4 Multiscale Hessian-based fissure detection

The final fissure detection was accomplished through an enhancement filter. Conventional, enhancement filters are typically based on first (structure tensor) or second (Hessian matrix) order image information. In this study, we used the Hessian matrix based on gray-scale curvature information combined with Gaussian smoothing as a basic operator to enhance the fissure structure. In 3D space, fissures are free-form surfaces in the lungs that locally resemble plate-like structures, since the grey-value increases rapidly from the structure border to the center and decreases again to the opposite border. Hessian-based filters are typically used to enhance and differentiate structures with specific shapes, i.e., blobs, sheets and tubes (Frangi et al., 1998; Lorenz et al., 1997).

A common approach to analyze the local behavior of an image, L , is to consider the local grey-value variations in the neighborhood of a point x_o modeled by a Taylor expansion to the second order,

$$L(x_o + \delta x_o, s) \approx L(x_o, s) + \delta x_o^T \nabla_{o,s} + \delta x_o^T H_{o,s} \delta x_o, \quad (3.6)$$

where $\nabla_{o,s}$ and $H_{o,s}$ are the gradient vector and Hessian matrix, respectively, of the image computed in x_o at scale s .

To calculate these differential operators of L , concepts of linear scale space theory are used (Koenderink, 1984; Florack et al., 1992). In this framework, differentiation is defined as a convolution with derivatives of Gaussians,

$$\frac{\partial L(x, s)}{\partial x} = s^\gamma L(x) * \frac{\partial G(x, s)}{\partial x}, \quad (3.7)$$

where the D-dimensional Gaussian is defined as

$$G(x, s) = \frac{1}{\sqrt{2\pi s^2}^D} e^{-\frac{\|x\|^2}{2s^2}}, \quad (3.8)$$

where s is the kernel size of the Gaussian. The second derivative of a Gaussian is in many cases a good approximation to the optimal filter for a plane-like structure. Through using the second derivative operator combined with Gaussian smoothing as the basic operator (Hessian matrix), we are able to make the non-supervised fissure filter scale-dependent (Lorenz et al., 1997; Li et al., 2003). In order to make sure a variety of sizes of fissures can be captured by the Hessian, we implemented a range of kernel sizes from 0.5mm to 2.5mm in 0.5 mm increments as the kernel size of the Gaussian to obtain a final estimate of 'fissureness':

$$F_{output} = \max_{s_{min} \leq s \leq s_{max}} F_0(s), \quad (3.9)$$

where s_{min} and s_{max} are the minimum scale (0.5mm) and maximum scale (2.5mm). Each scale s gets a response. In the final output of the multiscale enhancement filter, the maximum output over all scales is assigned to each voxel.

At each image voxel, the Hessian matrix was constructed from the six independent second order derivatives as a symmetric matrix

$$\text{Hessian} = \begin{bmatrix} H_{xx} & H_{xy} & H_{xz} \\ H_{yx} & H_{yy} & H_{yz} \\ H_{zx} & H_{zy} & H_{zz} \end{bmatrix}, \quad (3.10)$$

where $H_{ij} = \left| \frac{\partial^2 H}{\partial r_i r_j} \right|$, and r represents the gradient direction.

The idea behind eigenvalue analysis of the Hessian is to extract the principal direc-

tions in which the local second order structure of the image can be decomposed. The eigenvalue decomposition extracts three orthonormal directions which are invariant up to a scaling factor when mapped by the Hessian matrix. In this chapter, λ_k will be the eigenvalue with the k-th smallest magnitude ($|\lambda_1| \leq |\lambda_2| \leq |\lambda_3|$). Under this assumption, Table 3.4 summarizes different structures distinguished by an analysis of the eigenvalues of the Hessian.

Table 3.4: Possible structures on images in 2D and 3D, and its corresponding eigenvalues λ_k . H and L describe the absolute value of λ_k , H is high, L is low, +/- indicate the sign of the eigenvalue. The eigenvalues relationship here is:
 $|\lambda_1| \leq |\lambda_2| \leq |\lambda_3|$

2D		3D			orientation structure
λ_1	λ_2	λ_1	λ_2	λ_3	
L	L	L	L	L	noisy structure
		L	L	H-	bright plane-like structure
		L	L	H+	dark plane-like structure
L	H-	L	H-	H-	bright tubular-like structure
	L	H+	L	H+	dark tubular-like structure
H-	H-	H-	H-	H-	bright blob-like structure
	H+	H+	H+	H+	dark blob-like structure

As shown in Table 3.4, an eigenvector analysis of the Hessian matrix can thus be used to detect fissure structures, and the respective eigenvectors point out singular directions. In 3D space, a light plane on a dark background is characterized by one large positive second derivative (λ_3) perpendicular to the fissure plane, since the grey-value increases rapidly from the plane-structure border to the centerline and decreases again to the opposite border. And two small second derivatives of either sign (λ_1 and λ_2) parallel to the plane should occur (shown in Fig 3.10). Thus, on the bright fissures, the ideal relationship is defined as $|\lambda_1| = |\lambda_2| = 0$ and $\lambda_3 \ll 0$, $|\lambda_1| \leq |\lambda_2| \leq |\lambda_3|$. From these characteristics, we can get a fissure probability of each voxel derived as follows

$$F_0(s) = \Theta S_{plane} S_{noise} \quad (3.11)$$

The parameter Θ suppresses points whose largest eigenvalue λ_3 is positive, since fissures are locally bright, and is defined as

$$\Theta = \begin{cases} 1, & \lambda_3 < 0 \\ 0, & \lambda_3 \geq 0 \end{cases} \quad (3.12)$$

Since the largest eigenvalue $|\lambda_3|$ should be much larger than the other two eigenvectors, the second factor S_{plane} uses the ratio between $|\lambda_2|$ and $|\lambda_3|$ to search sheet-like structures, so that the voxels where $|\lambda_3|$ and $|\lambda_2|$ are significantly different can be detected

$$S_{plane} = \exp\left(-\frac{{R_{plane}}^2}{2\alpha^2}\right), \quad (3.13)$$

$$R_{plane} = \frac{|\lambda_2|}{|\lambda_3|}, \quad (3.14)$$

where α was set to 0.5 in this study. The third factor S_{noise} aims to suppress noise voxels such as blob-like structures. Unlike plane-like structures which have relatively large $|\lambda_2|$ and $|\lambda_3|$ ratio, the noise voxels usually have low $|\lambda_1|$, $|\lambda_2|$ and $|\lambda_3|$ (as shown in Table 3.4). Therefore, here we use

$$S_{noise} = 1 - \exp\left(-\frac{{R_{noise}}^2}{2\beta^2}\right), \quad (3.15)$$

$$R_{noise} = \sqrt{{\lambda_1}^2 + {\lambda_2}^2 + {\lambda_3}^2}, \quad (3.16)$$

with β set to 0.5 for thresholding. $F_0(s)$ then gives a high response to local plane-like structures (fissures) and suppresses other pulmonary structures (noise). An example of this enhancement filter applied in an individual is shown in Figure 3.12a.

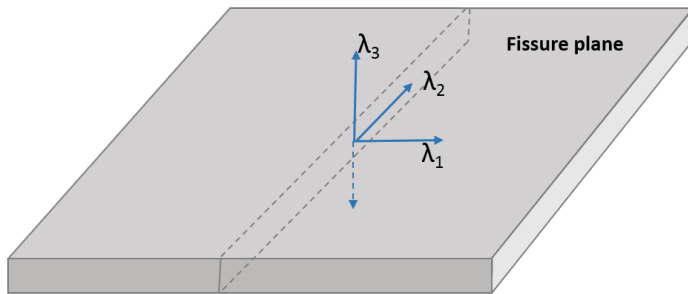


Figure 3.10: The three eigenvectors of the Hessian matrix representing plane-like structure (fissure). λ_1 and λ_2 are parallel to fissure plane, λ_3 is perpendicular to fissure plane.

Blood vessel voxels were subsequently filtered from the fissure enhanced result. The segmentation of vessels was achieved using a classical vessel segmentation method (Frangi et al., 1998). It is also developed on a multiple scale (from 0.5mm to 3.0mm in 0.5 mm increments as the kernel size of Gaussian) Hessian-based enhanced filter, which is similar to the fissure detection filter we described previously. The main difference is here the aim is to search for the tube structure (vessels). In a 3D image, the relationship of Hessian eigenvalues λ_1 , λ_2 and λ_3 of an ideal bright tubular structure in a dark background should be described as $|\lambda_1| \approx 0$, $|\lambda_1| \ll |\lambda_2|$, $\lambda_2 \approx \lambda_3$ (see Figure 3.11). Therefore, we used the following equations as the enhancement filter to detect vesselness structures:

$$V_0(s) = \begin{cases} 0, & \text{if } \lambda_2 > 0, \\ (1 - \exp(-\frac{R_A^2}{a^2})) \exp(-\frac{R_B^2}{2b^2}) (1 - \exp(-\frac{S^2}{2c^2})), & \end{cases} \quad (3.17)$$

where a and b were both set to 0.5, and c was set to 500 in this study. R_A , R_B and S were defined as follows:

$$R_A = \frac{|\lambda_2|}{|\lambda_3|}, \quad (3.18)$$

$$R_B = \frac{|\lambda_1|}{\sqrt{|\lambda_2| |\lambda_3|}}, \quad (3.19)$$

$$S = \|H\|_F = \sqrt{\sum_{j \leq D} \lambda_j^2}, \quad (3.20)$$

where D is the dimension of the image. $V_0(s)$ gives a probability of vesselness for each voxel. Then segmented blood vessels were selected through detecting the voxels whose vesselness value was larger than a specific threshold (threshold = 10 in this study (Frangi et al., 1998)). We used D_{vessel} to represent the distance transform to the segmented vessel line, thus the final fissureness after decreasing the values of vessel voxels was defined as:

$$F_{final}(s) = F_0(s)S_{vessels}, \quad (3.21)$$

$$S_{vessels} = \exp\left(1 - \frac{D_{vessel}^2}{2d^2}\right), \quad (3.22)$$

where d was set to 5mm in this study. High vesselness voxels were therefore suppressed and not detected as fissure points in the final result. Fig 3.12b shows the result after eliminating the vessel voxels.

The initial fissure location predicted by average SSM deformation gives us a region

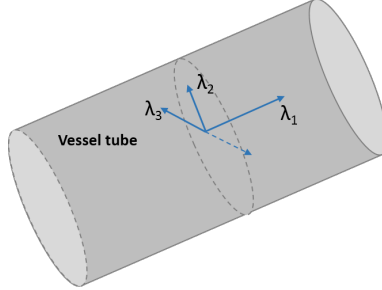


Figure 3.11: The three eigenvectors of the Hessian matrix representing tube-like structure (vessel). λ_1 is parallel to vessel tube, λ_2 and λ_3 are perpendicular to vessel tube.

of interest (ROI) for an accurate fissure detection, see Figure 3.12c. The candidate points are selected within a certain distance of the initial fissure approximation: the search distance was set to 20 voxels (default value) for the initially projected left and right oblique fissures and 15 voxels for the initially projected right horizontal fissure. To remove some spurious responses such as small plane-like structures on the result, a 2D 4-neighborhood connected component filter and a 3D 6-neighborhood vector-based connected component filter were employed successively to eliminate noise arising from small plane-like structures in this search region (Fig 3.12d). A 2D filter was used to eliminate 4-neighbour connected components that were smaller than a minimum small size (set to 10 voxels initially) slice by slice. The 3D vector-based connected component filter used the inner product of the normalized largest eigenvector of the Hessian matrix in adjacent voxels. These largest eigenvectors are perpendicular to the fissure plane, and their inner product provides a criterion for component connection. As the curvature of a fissure is locally low, adjacent fissure voxels should have similar largest eigenvectors and thus the inner product value of their largest eigenvectors should equal to 1 or slightly smaller than 1. Connected boundary condition was set as an inner product ≤ 0.8 to connected component, then 3D 6-neighbour connected component with a volume less

than 100 mm^3 was removed as noise from the result.

The detected points were then divided into a set of small subsections corresponding to different x, y intervals. For each subsection, the point of the highest fissure probability (the highest S value) was selected as the final candidate fissure point (Fig 3.12e). Once the maximum fissureness candidates were found, a morphological dilation with a $3 \times 3 \times 3$ voxel cube as structure element was applied iteratively until the largest connected fissure plane was big enough, so that all the other unconnected outliers could be filtered subsequently. Finally, a continuous smooth fissure surface was generated based on the maximum fissure points using a β -spline method with a thin-plane spline (Lee et al., 1997) and extrapolated to the lung boundaries, see Fig 3.12f.

3.3.5 Interactive user control interface

As discussed above, a series of parameter values need to be chosen correctly to ensure a successful lobar segmentation. However, a fixed parameter value is usually not suitable for all the subjects due to a wide variation of lung tissue and fissure appearances across the population. Therefore, a fast and convenient manual interaction to control the segmentation procedure is reasonable and acceptable. Based on an open source software, Pulmonary Toolkit (PTK, <https://github.com/tomdoel/pulmonarytoolkit>), we developed an improved user-friendly interactive interface to control the segmentation parameters as input (improved version: <https://github.com/qiuyufly/pulmonarytoolkit/tree/yuwen>). PTK is a software developed on Matlab for the analysis of 3D medical lung images for academic research use. It comprises a library of lung analysis algorithms, a GUI application for visualising and analysing clinical lung images and a rapid prototyping framework for users to develop their new algorithms in an easier way. By making use of

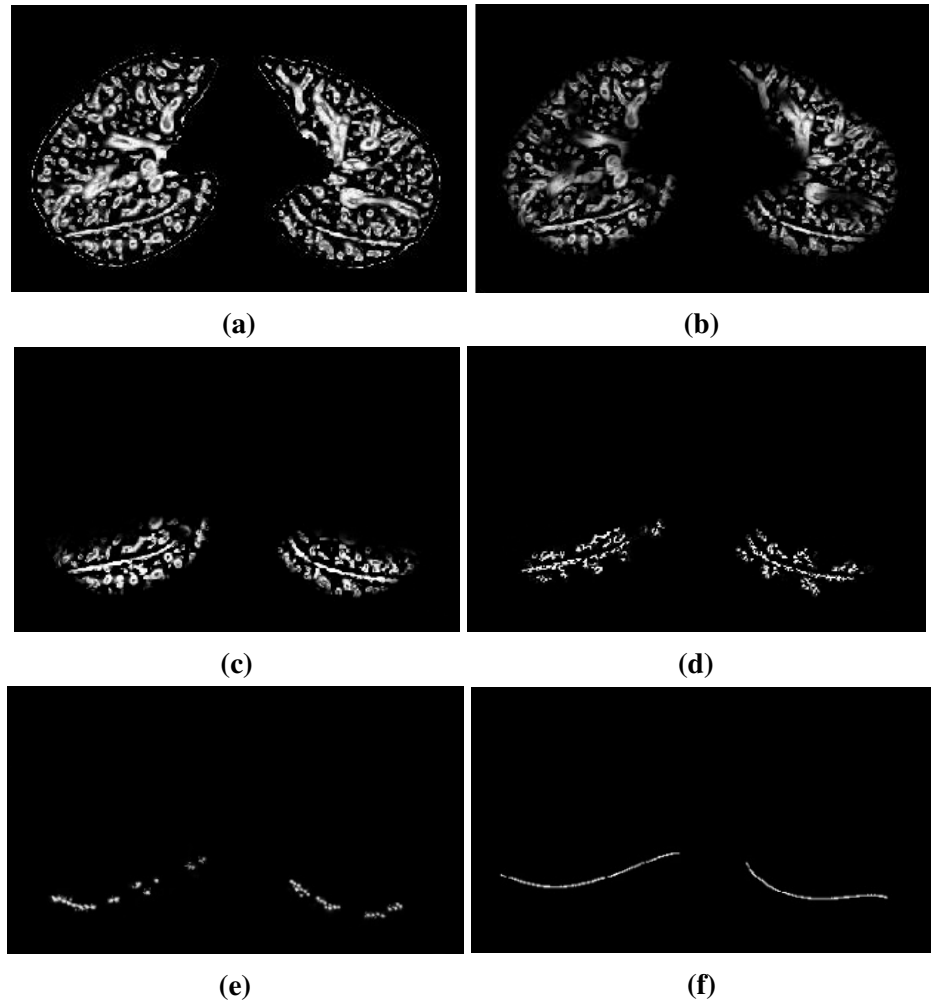


Figure 3.12: Hessian-based multiscale fissure detection results. (a) Hessian-based plane-like structure enhancement filter. (b) Remove vessel voxels (tube-like structures). (c) Selected search regions for fissure detection based on SSM initial fissure prediction. (d) 2D and 3D eigenvector based connected component filter. (e) Fissure candidate points. (f) β -spline curve fissure surface fitting.

some built-in objects and the visualization system of PTK, our lobar segmentation algorithm was added into the algorithm package and parameter control buttons were made available on the interface. Table 3.5 summarises the interactive user control parameters.

Figure 3.13 shows the user interface of PTK.

Table 3.5: Summary of interactive user control parameters

Parameters	Default values	Notes
Search region for left oblique fissure	20 voxels	Increase the value if there are not enough positive candidate points; decrease the value if there is too much noise
Search region for right horizontal fissure	20 voxels	
Search region for right oblique fissure	15 voxels	
Connected component size for left oblique fissure	30 voxels	Decrease the value if there are not enough positive candidate points; increase the value if there is too much noise
Connected component size for right horizontal fissure	30 voxels	
Connected component size for right oblique fissure	30 voxels	
Total connected component size	300 voxels	

Search region control

Fissure candidate points were detected within a certain distance of the initial fissure approximation. The default distance was set to 20 voxels for left and right oblique fissures and 15 voxels for right horizontal fissure. However, with a fixed search distance, fissure detection sometimes could not be implemented efficiently and accurately. The probability of error detection may increase if the search distance is too large, as more noise will be included in the initial search region. In contrast some positive fissure points will be missed if the search distance is too small. Accurate fissure candidate points are an

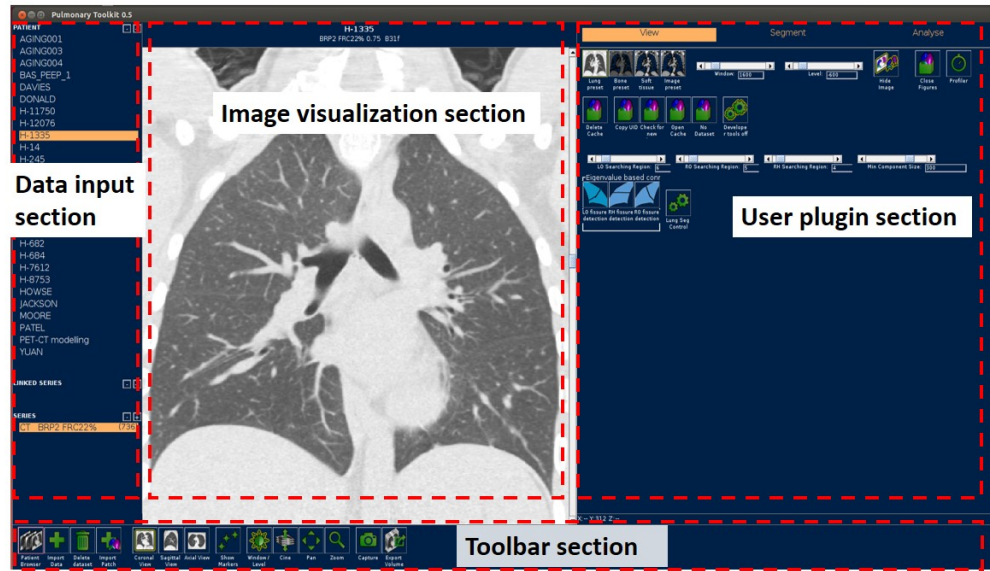


Figure 3.13: PTK User interactive interface. It consists of data input section, image visualization section, user plugin section and toolbar section.

important prerequisite for good fissure surface fitting. Therefore, user interactive slide buttons were developed on the PTK interface to control the search distance. Through inputting SSM based initial fissure prediction mesh, the estimated fissures can be visualized to overlap on the raw images in the PTK visualization section. Then it is possible for users to select a suitable search region for each fissure depending on the accuracy of the initial fissure estimate. The better the initial fissure approximation, the lower the search region should be selected. Figure 3.14 shows the lobe segmentation result before and after change to the search region.

Connected component analysis filter control

Connected component analysis was an important operation to help with noise elimination during fissure detection. A suitable connected component size is able to remove most of the small connected structures as outliers and in the meantime retain true fis-

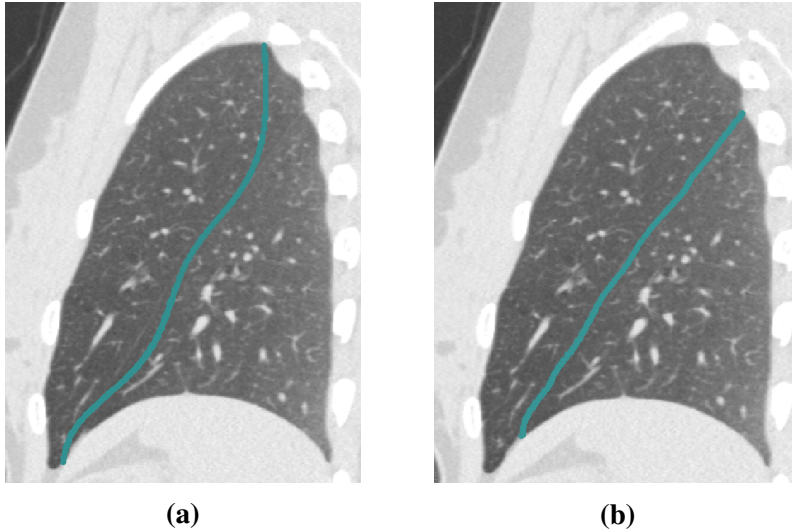


Figure 3.14: Fissure detection results before and after control the search regions. (a) Fissure detection result with a search distance of default 20 voxels. (b) Fissure detection result after setting a specific search distance depend on the accuracy of initial fissure guessing.

sure structures as much as possible. In order to improve the filter performance, we used a slide button to control the connected component size on the PTK user interface. Through changing the component size threshold, it is possible for us to find a balance between spurious response elimination and target points retainment.

Manual correction

Manual correction is an essential part of a lot of lobe segmentation processing. A manual correction tool was available in the PTK software, but in this method only one correct landmark can be selected at a time. We developed a multiple landmark correction method based on PTK built-in packages, and the improved correction tool allows users to modify three fissures points at the same time. By selecting a series of correction landmarks, the corresponding fissure plane is deformed to a new curved surface which passes through all the correct landmarks. The correction region was calculated based

on the distance between the landmark and its corresponding fissure plane, and a 3D Gaussian filter with the landmark as the center was also used to specify the corrected boundary. The correction happens in 3D space so that users don't need to do the correction slice by slice. The whole correction can be finished in a few minutes even when automatic fissure is not complete. Figure 3.15 shows the fissure detection results before and after manual correction.

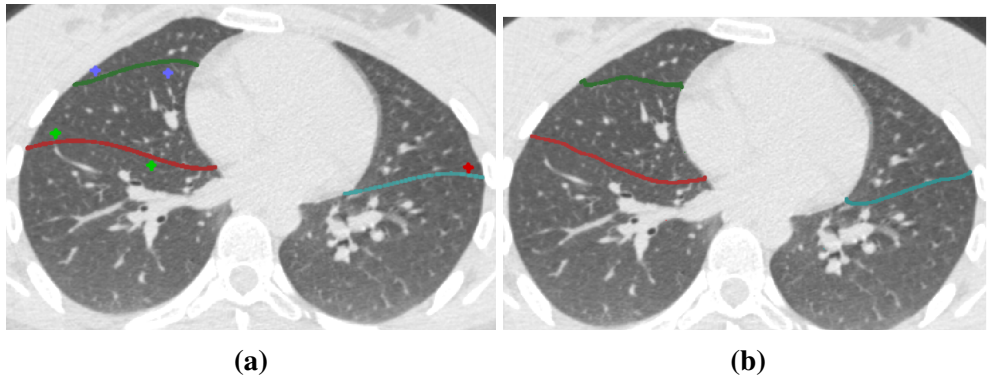


Figure 3.15: Manual correction on automatic fissure detection results (a) Manually select a set of landmarks on real fissure lines shown in raw images to correct automatic fissure detection results (red landmarks are for left oblique fissure, green landmarks are for right oblique fissure, blue landmarks are for right horizontal fissure). (b) Corrected fissure detection results shown with raw images. The corrected fissure lines can match the real fissure locations.

3.4 Experiments

3.4.1 Testing CT dataset

The semi-automatic lobe segmentation method was tested on two datasets: 1) CT images from five young normal subjects taken at different lung volumes (end inspiration and end expiration), in the supine posture, from the HLA dataset (introduced in Section

3.3.2). The selected dataset consists of five end expiration images and five end inspiration images, which were not part of the SSM training set; 2) CT images from older patients (slice thickness 1.25-3.00 mm) acquired during routine diagnostic inspection for idiopathic pulmonary fibrosis (IPF). Data from these subjects were acquired from the Auckland District Health Board (ADHB). Access to clinical data was approved by the Southern Health and Disability Ethics Committee.

3.4.2 Test and results

Figure 3.16 shows raw images, SSM based fissure predicted locations, and the automatic lobar segmentation results (no manual correction) of a normal healthy subject. Figure 3.17 shows the results for an IPF subject.

To evaluate the performance of the automatic lobe segmentation, our SSM based method was compared with two anatomical based lobar segmentation method. A "gold-standard" manual segmentation of the fissures was used for a quantitative evaluation of the performance. The efficiency of manual correction on the segmentation result was also tested.

The gold standard and quantitative evaluations

To allow for a quantitative evaluation of the performance in a healthy normal dataset and an IPF disease dataset, the automatic segmentation results were compared with "gold-standard" manual segmentations of the fissures. The "gold-standard" segmentations were acquired by an experienced researcher manually tracing all the three fissures for each subject by digitizing a series of points. The tracing was done on transverse, sagittal and coronal slices to maximise visualisation of the fissures using a custom-written con-

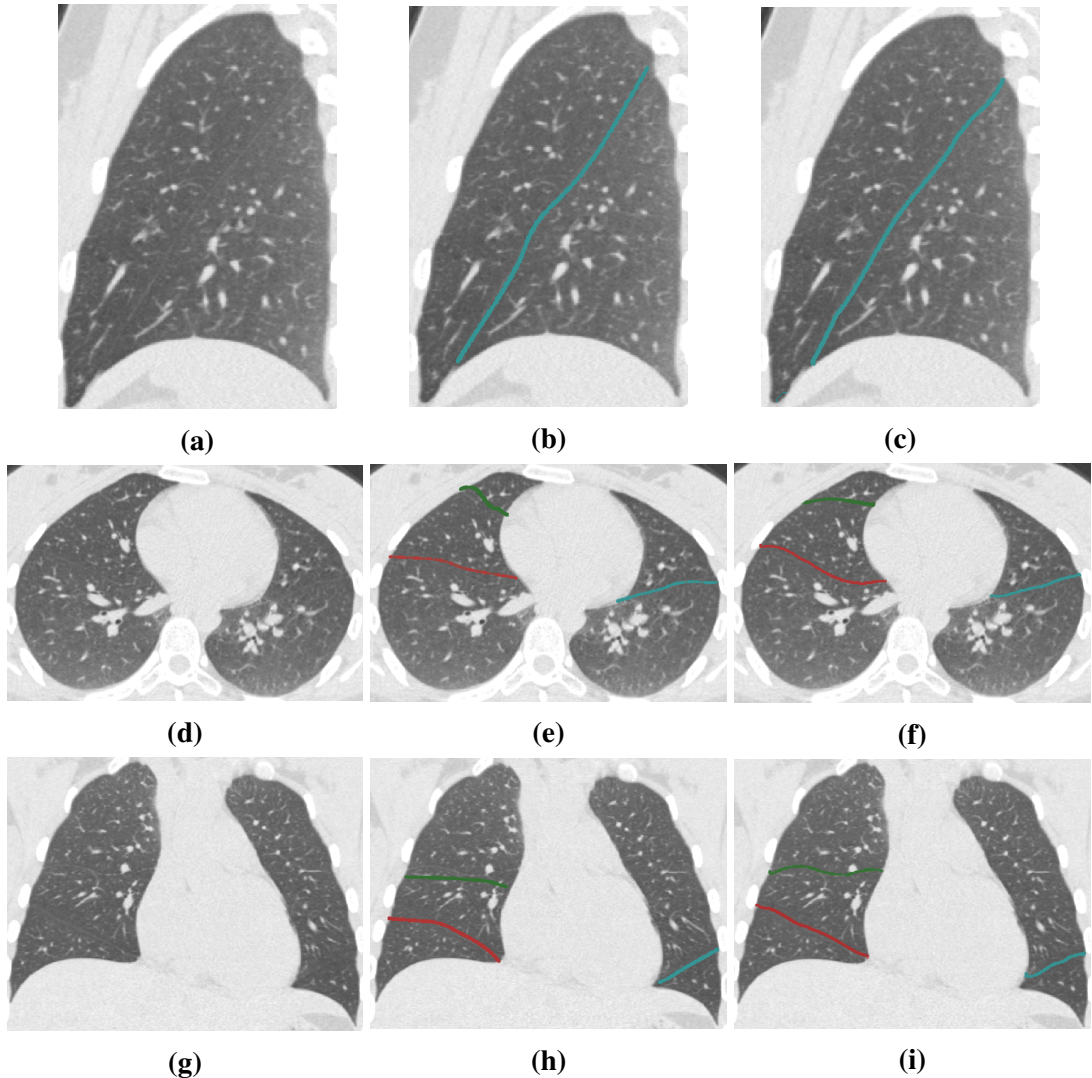


Figure 3.16: Sagittal, axial, and coronal views illustrating raw image, SSM based initial fissure guessing and automatic fissure detection results of a normal healthy subject. (a), (d), (g) are sagittal, axial and coronal raw images. (b), (e), (h) are sagittal, axial and coronal SSM based initial fissure guessing results. (c), (f), (i) are sagittal, axial and coronal automatic fissure detection results.

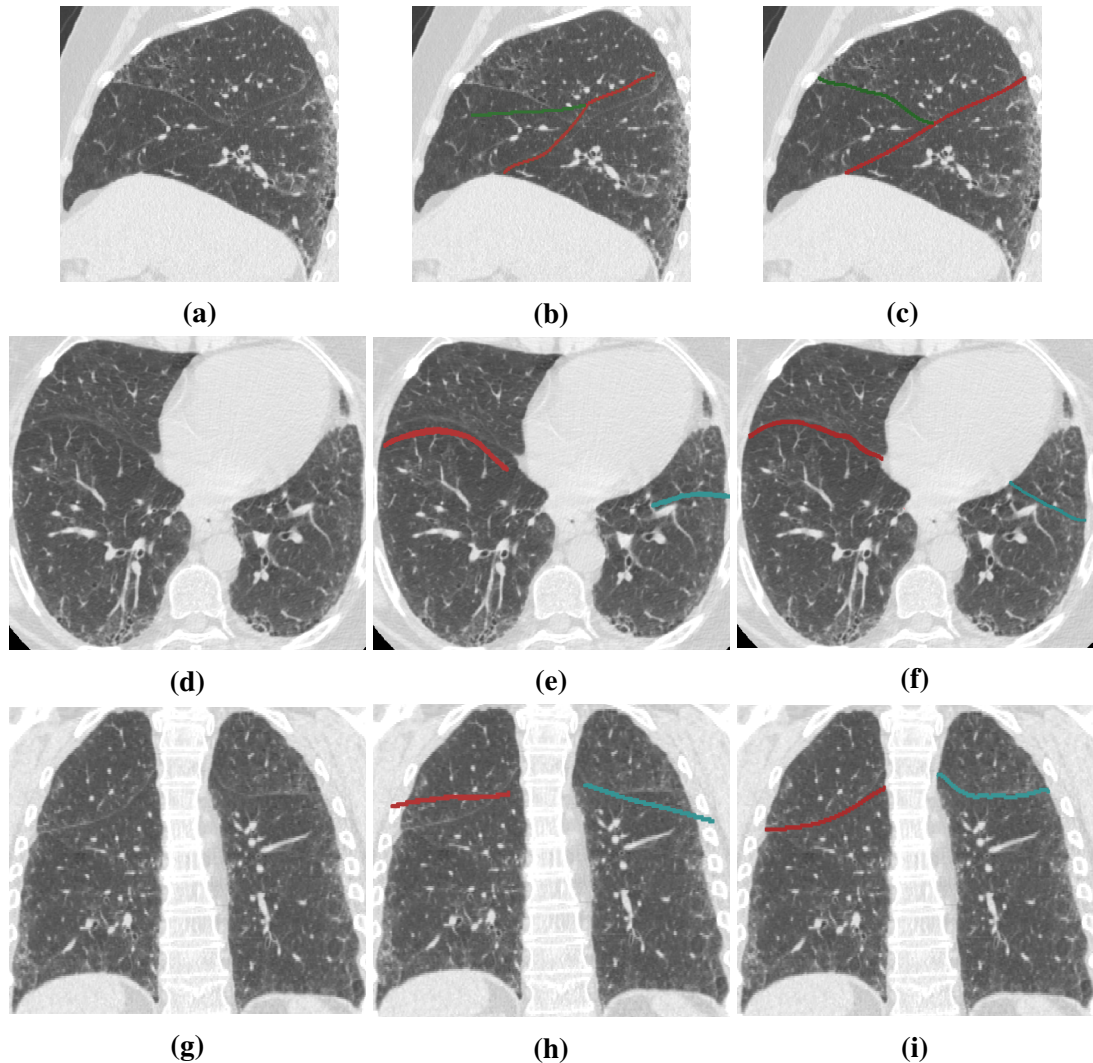


Figure 3.17: Sagittal, axial, and coronal views illustrating raw image, SSM based initial fissure guessing and automatic fissure detection results of an IPF subject. (a), (d), (g) are sagittal, axial and coronal raw images. (b), (e), (h) are sagittal, axial and coronal SSM based initial fissure guessing results. (c), (f), (i) are sagittal, axial and coronal automatic fissure detection results.

figuration of the open source visualization software CMGUI. The observer can select any of the slice section when digitizing the fissure which can give the best contrast, see Figure 3.7 in section 3.3.2. Fissure detection accuracy was assessed by computing the mean distance between manually-defined fissures points and automatic segmented fissures (with a few manual parameter controls, but without manual correction). For each point in the manual "gold-standard" segmentations, the distance was defined between this point and its closest point in the automatic segmentations as follows:

$$d_i = \min_j \left\{ \sqrt{(x_j^A - x_i^M)^2 + (y_j^A - y_i^M)^2} \right\}, \quad (3.23)$$

where (x_i^A, x_i^M) is the manually traced fissure point, and (x_j^A, x_j^M) is the automatic segmented fissure point. Then the mean error was calculated as:

$$d_{mean} = \frac{\sum_{i=1}^N d_i}{N}, \quad (3.24)$$

where N is the number of points in the manually traced fissure. In addition, we evaluated the accuracy of the algorithm using a percentile measurement. The percentile accuracy is defined as the percentage of the distance between manual and automatic point under a 3mm criteria, following the equation:

$$\sqrt{(x_i^A - x_i^M)^2 + (y_i^A - y_i^M)^2} \leq 3\text{mm}, \quad (3.25)$$

since 3mm approximates the thickness of clinical CT images that surgeons and radiologists read in clinical settings (Wei et al., 2009).

For normal subjects, the average mean differences (and accuracies) were 1.76 mm (81%), 3.66 mm (65%), and 2.55 mm (74%), for left oblique, right horizontal and right

oblique fissures, respectively. For IPF subjects, the average mean differences (and accuracies) were 2.82 mm (70%), 5.39 mm (59%), and 4.71 mm (63%), for left oblique, right horizontal and right oblique fissures, respectively (shown in table 3.6).

Table 3.6: Mean error and percentile accuracy of normal healthy and IPF subjects (mean value \pm standard deviation).

	Normal healthy subjects		IPF subjects	
	Mean error (mm)	Accuracy (%)	Mean error (mm)	Accuracy (%)
Left oblique	1.76 \pm 0.68	81.19 \pm 6.61	2.82 \pm 0.71	70.26 \pm 9.10
Right horizontal	3.66 \pm 1.37	64.81 \pm 13.19	5.39 \pm 1.90	58.43 \pm 14.53
Right oblique	2.55 \pm 0.90	73.81 \pm 7.96	4.71 \pm 1.60	62.86 \pm 11.21

Figure 3.18 shows the spatial distribution of error for three representative subjects. Error was highest in regions close to the hilum (where the anatomical structures are complex, and/or the fissure is often incomplete), and where the right fissures meet.

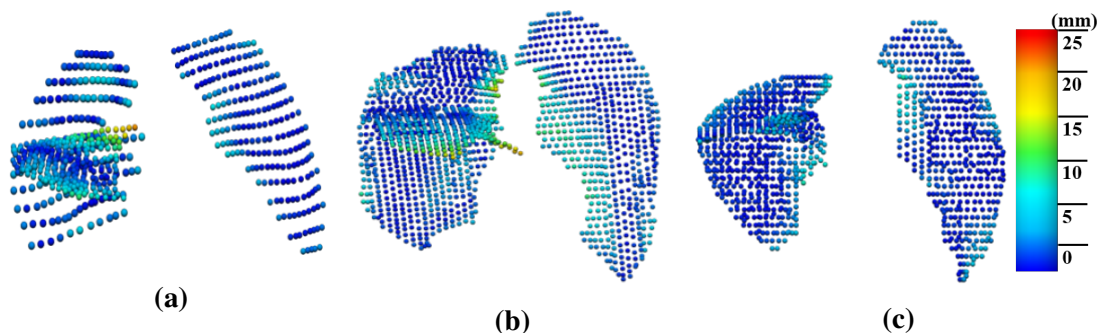


Figure 3.18: The spatial distribution of error between the gold-standard and semi-automatic methods for three representative subjects, highlighting localized regions of low accuracy.

Comparison to anatomical based lobar segmentation method

A marker-based interactive watershed transformation algorithm is a commonly used lobe segmentation method in the current literature (Ukil and Reinhardt, 2009; Pu et al.,

2009b; Lassen et al., 2011, 2013). This method mainly relies on anatomical information of the lung which integrates fissures, bronchi and vessels into a cost image to obtain the lobar boundaries. In our method, we used a lobar statistical shape model constructed based on principle component analysis to provide an initial estimation of fissure locations. This method gets rid of the dependance on prior segmentation of anatomical structures. To investigate the contribution of using the approximated lobe borders from the deformation of SSM, we compared our method to two interactive watershed-based pulmonary lobe segmentation softwares here: 1. Pulmonary Toolkit, PTK, <https://github.com/tomdoel/pulmonarytoolkit> (introduced in Section 3.3.5); 2. Pulmonary Analysis Software Suite, PASS (Guo et al., 2008). PASS is custom-written software developed at the University of Iowa, that integrates quantitative measurements of lung function and structure analysis. Both of these softwares have a built-in lobe segmentation method which is guided by vessel tree and airway tree.

The two segmentation softwares PASS and PTK tested for comparison were unable to segment the lobes for 9/20 and 7/20 subjects respectively (1/10 and 1/10 normal and 8/10 and 6/10 IPF subjects), 3.8, 3.9). In contrast, the model-based method gave an initial estimate for all subjects at all volumes. The main reason for the failure of segmentation is that the airway trees can't be segmented or labelled as lobar branches correctly. Figure 3.19 shows an example of an IPF subject in which airway branches are mislabelled.

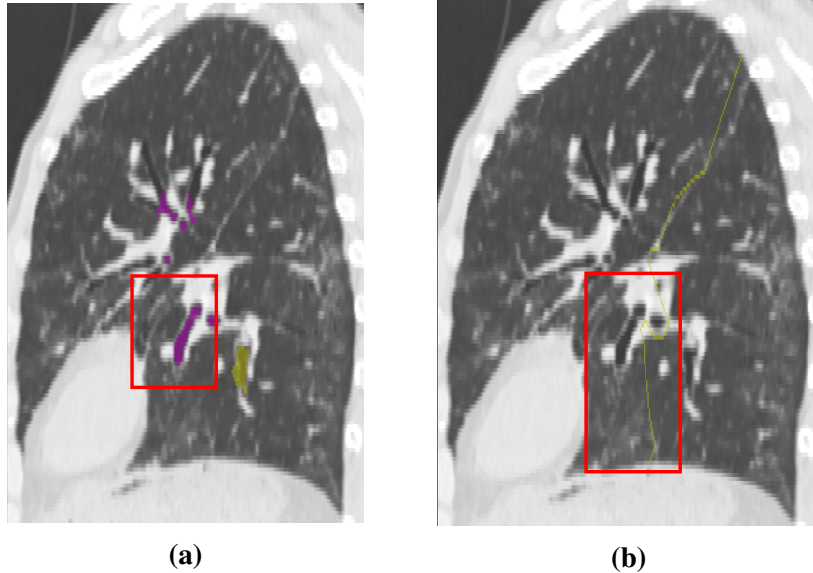


Figure 3.19: An inaccurate initial fissure estimate for an IPF subject caused by mislabeling of lobar airway branches using marker-based interactive watershed transformation algorithm (sagittal view, left lung). (a) The mislabeling of lobar airway branches. Purple is for left upper branches and yellow is for left lower branches. The lower branches in the red box are mis-detected as upper branches. (b) The initial fissure guessing based on the erroneous airway branch labeling result. The approximate fissure has a significant erroneous shift in the red box where mislabeling of lobar airway branches occurs.

The mean square error and percentile accuracy of each fissure for each subject segmented using PTK, PASS and our method (SFeAL) are listed in Table 3.7, 3.8 and 3.9, respectively. Although our model-based method was able to segment all the subjects (whereas PASS and PTK can't), PASS could sometimes perform better on some young healthy subjects. That is probably because in some healthy lungs, it is possible to extract airways and vessels accurately, therefore these structures are able to provide reliable anatomical information to estimate the fissure locations.

Table 3.7: Mean error and percentile accuracy of left oblique fissure for each subject

Subject	SFeaL		PTK		PASS	
	Mean error (mm)	Accuracy (%)	Mean error (mm)	Accuracy (%)	Mean error (mm)	Accuracy (%)
HLA1	0.96	91.29	1.98	77.33	1.14	89.66
HLA2	1.17	85.59	1.58	82.65	0.57	95.88
HLA3	1.74	79.79	3.18	72.86	0.93	92.24
HLA4	2.61	81.20	Fail	Fail	2.65	81.95
HLA5	1.44	81.60	1.25	90.71	Fail	Fail
HLA6	3.31	68.08	3.78	53.57	0.92	95.98
HLA7	1.67	80.18	1.75	76.96	3.54	66.36
HLA8	1.52	83.26	2.99	66.17	2.68	68.02
HLA9	1.20	88.72	5.69	44.26	2.61	70.63
HLA10	2.03	72.22	5.55	49.56	1.89	77.11
IPF1	1.91	81.98	Fail	Fail	Fail	Fail
IPF2	3.15	62.33	17.90	22.89	Fail	Fail
IPF3	2.71	78.97	Fail	Fail	Fail	Fail
IPF4	3.21	61.77	Fail	Fail	4.21	56.23
IPF5	1.93	78.66	Fail	Fail	Fail	Fail
IPF6	3.27	63.24	6.71	39.21	4.54	58.76
IPF7	4.24	57.72	4.97	44.68	Fail	Fail
IPF8	2.65	62.81	Fail	Fail	Fail	Fail
IPF9	3.27	73.01	Fail	Fail	Fail	Fail
IPF10	1.91	82.12	3.13	71.53	2.96	73.26

Table 3.8: Mean error and percentile accuracy of right horizontal fissure for each subject

Subject	SFeaL		PTK		PASS	
	Mean error (mm)	Accuracy (%)	Mean error (mm)	Accuracy (%)	Mean error (mm)	Accuracy (%)
HLA1	2.61	72.81	2.32	73.68	1.77	81.57
HLA2	1.55	84.06	3.21	58.33	1.59	86.74
HLA3	3.34	60.91	2.68	72.59	1.31	88.32
HLA4	1.67	84.85	Fail	Fail	1.61	88.64
HLA5	4.89	57.87	10.01	41.73	Fail	Fail
HLA6	3.57	62.56	2.64	65.44	6.38	56.22
HLA7	6.02	38.99	4.20	54.05	Fail	Fail
HLA8	4.09	69.90	6.61	22.83	4.48	39.23
HLA9	5.02	52.88	21.74	21.88	Fail	Fail
HLA10	3.86	63.28	18.04	11.62	13.11	14.52
IPF1	3.91	75.14	Fail	Fail	Fail	Fail
IPF2	4.99	67.03	10.60	12.24	Fail	Fail
IPF3	2.19	82.05	Fail	Fail	Fail	Fail
IPF4	4.95	58.71	Fail	Fail	10.09	19.19
IPF5	6.99	49.15	Fail	Fail	Fail	Fail
IPF6	6.21	38.51	41.01	0.53	Fail	Fail
IPF7	6.47	53.60	9.2	19.64	Fail	Fail
IPF8	8.04	41.19	Fail	Fail	Fail	Fail
IPF9	7.52	45.43	Fail	Fail	Fail	Fail
IPF10	2.67	73.57	9.31	34.89	7.56	49.39

Table 3.9: Mean error and percentile accuracy of right oblique fissure for each subject

Subject	SFeaL		PTK		PASS	
	Mean error (mm)	Accuracy (%)	Mean error (mm)	Accuracy (%)	Mean error (mm)	Accuracy (%)
HLA1	1.99	79.95	2.54	69.92	1.12	87.72
HLA2	2.03	75.09	2.98	58.12	0.64	96.03
HLA3	1.64	82.42	2.48	72.34	0.66	96.52
HLA4	2.15	82.21	Fail	Fail	1.37	96.44
HLA5	2.07	78.53	3.23	61.40	Fail	Fail
HLA6	4.98	75.69	8.31	45.41	4.93	94.49
HLA7	3.02	55.28	3.17	57.14	3.47	57.76
HLA8	2.33	73.98	3.97	58.93	2.40	71.31
HLA9	3.01	66.58	5.72	50.37	2.89	73.51
HLA10	2.32	68.38	8.61	35.35	2.53	70.70
IPF1	2.52	81.72	Fail	Fail	Fail	Fail
IPF2	2.94	82.45	3.56	55.43	Fail	Fail
IPF3	3.68	59.47	Fail	Fail	Fail	Fail
IPF4	6.23	58.98	Fail	Fail	49.16	6.12
IPF5	4.14	62.00	Fail	Fail	Fail	Fail
IPF6	5.43	48.42	15.88	23.69	6.86	41.56
IPF7	5.07	56.96	11.66	19.33	Fail	Fail
IPF8	7.33	47.79	Fail	Fail	Fail	Fail
IPF9	6.69	63.49	Fail	Fail	Fail	Fail
IPF10	3.06	67.34	4.53	47.81	3.57	67.08

Manual correction

In order to test the efficiency of manual correction for segmented fissures, three students (are able to recognize lobe fissures on raw images accurately) are asked to do the manual corrections on a automatic segmented fissure result within ten minutes. Table 3.10 lists the comparison of the segmentation accuracy before and after ten-minute manual correction.

Table 3.10: Mean square error (MSE) (mm) and percentile accuracy(%) of segmented left oblique (LO), right horizontal (RH), and right oblique (RO) fissures before and after manual correction

	Before correction		After correction					
	MSE	Accuracy	Student 1		Student 2		Student 3	
			MSE	Accuracy	MSE	Accuracy	MSE	Accuracy
LO	3.19	57.55	1.35	89.59	1.21	91.84	1.17	93.47
RH	5.02	39.09	1.85	85.28	1.61	90.36	1.64	87.31
RO	4.83	47.80	1.37	92.67	1.18	89.52	0.98	96.88

3.5 Discussion

In this chapter, we presented a pulmonary lobar segmentation method. Results show that the method can perform well to detect the location of the fissures over most of the fissure surfaces on CT images from normal subjects, and provides a relatively accurate result compared to some existing tools for most of the IPF (abnormal) subjects. Due to lower imaging resolution and tissue abnormalities, the accuracy of the method was lower for the IPF subjects. Automated segmentation of anatomical structures is still challenging in cases with abnormalities, however, the method did not fail, whereas the existing tools will fail sometimes, especially for the abnormal subjects.

For fissure detection, there are usually two types of errors, named false negative

detection and false positive detection. False negative detection indicates the leak detection of some true fissure points where fissures are incomplete or have fuzzy appearance. False positive detection indicates the misdetection of some false fissure points where tissues with small plane like structures are incorrectly identified as fissures. For IPF subjects, both of the two errors may occur during fissure detection. The first type of error exists for most of the subjects, since CT-visualized complete pulmonary fissures are rare, especially for IPF CT imaging, which makes automatic lobe segmentation challenging due to the absence of a physical border. In our method, the β -spline method with thin plane spline based surface fitting is able to provide an automated correction of the first type of error, since the fitting operation may help to estimate "incomplete" fissures in the correct direction through extrapolating "complete" fissures to lung borders. This fissure fitting method is a commonly used fitting algorithm (Lee et al., 1997; Doel et al., 2012), however the accuracy of the fitting performance is heavily reliant on the correct detection of complete fissure and a good initial approximation of fissure. Therefore, for some IPF subjects with lower fissure completeness, more manual operations may be needed.

For the second type of error, incorrect detection is usually caused by accessory fissures and interstitial lung disease tissues such as scarring or fibrosis. Our 2D connected component filter and 3D eigenvector based connected component filter are able to eliminate most of the non-fissure structures within the search region. However, for IPF subjects, it is still difficult to remove all the noise, since fibrosis usually appears surrounding the fissures and may even be connected to the main fissure plane. For some terminal stage IPF patients, severe honeycomb and reticular regions make lung parenchyma really fuzzy and low contrast from the fissures which increases the difficulty of avoiding mis-detection.

Our method performed better on the left oblique fissure than the other two fissures, because the left lung has a simpler anatomic structure with only one fissure. In contrast, error detection happens more often in the area of the right lung where the two fissures come into contact. This is illustrated in Fig 5, which shows the error distribution over the three fissures for three subjects. It can be seen that the method results in higher error in the lung boundary area, since the fissures here are commonly incomplete on CT scans, thus few fissure candidate points can be detected accurately. There is also a high error around the junction area of the right oblique fissure and right horizontal fissure, since the two fissures are too closed in this region and the search regions may overlap with each other.

In our method, we used a statistical shape model to provide an initial fissure estimate. Compared to the current published anatomical structure-based methods, the model-based method can predict the fissure location without requiring an accurate preliminary analysis of other anatomical features. For example, traditional anatomical knowledge-based methods such as the watershed-based lobar segmentation relies on the success of the automatic segmentations of the vessel and airway tree and need to label the airway trees to the five main lobar bronchi to get an initial fissure approximation. When one of those segmentations fails, the method is likely to perform worse (as shown in Figure 3.19). Vessels are distributed all over the lung and due to the high contrast to the lung parenchyma a good segmentation of the vessels is feasible. But in some cases vessels cross the lobar boundaries. Thus, the assumption that there are no vessels at the lobar boundary is not always correct (Pu et al., 2009b). On the other hand, due to the complex radiological appearance of pathological lungs, it is usually difficult to get a reliable airway and vessel tree segmentation (Lassen et al., 2011, 2013). In the current method, no watershed-based lobe segmentation can be performed in case of a

failed bronchi segmentation because the required lobe markers are generated from the labeled bronchi tree. In those cases, the approximated lobar borders might be at the wrong location in the scan. In contrast, our method is largely independent of the knowledge of lung anatomy, so in our comparison of the model-based estimation of fissure location with a watershed-based method, the latter failed for nearly half of the subjects.

The accuracy of the initial fissure prediction is a very important basis for a good segmentation. However, our model-based fissure prediction method still has some limitations. A main disadvantage is that it can only produce lobar shapes close to the shapes represented in the training set, which leads to a larger error in cases where pathological processes had altered the lobe shapes. As shown in Figure 3.16 and 3.17, the SSM based initial fissure estimate usually performs worse in IPF subjects than in normal healthy subjects. In the following chapters, a statistical shape analysis shows that there is a significant shape difference of right middle lobe and right upper lobe between IPF lungs and normal old lungs. That would be a reasonable explanation for the poor estimation of right horizontal fissure and right oblique fissure of the IPF subject shown in Figure 3.17. In the future, a statistical lobar shape model dataset for a variety of pathologies could be developed. A dataset containing a wide range of statistical models for different ages, sexes, lung volume or diseases would be able to help predict a more accurate ROI for fissure detection.

Due to the variation of lung anatomy and pulmonary disease, no automatic segmentation method can ensure a satisfying lobe segmentation result for all cases. Even for a widely used robust lobe segmentation method, it seems impossible to get a highly accurate segmentation result for all subjects, especially for some abnormal subjects. Therefore, manually interactive operation is usually acceptable and involved in a lot of lobe segmentation processing. Combination of an automatic algorithm and manual interac-

tion is an effective way to obtain accurate segmentation. On the one hand, an automatic segmentation algorithm would help researchers save considerable time from laborious and time consuming manual tasks. On the other hand, a fast and intuitive correction is able to improve the automatic segmentation performance within a few minutes.

3.6 Summary

In this chapter, an SSM based lobe segmentation method was developed. Results show that the method can provide a relatively accurate result for most of the IPF subjects, although manual interaction is still needed for some subjects. In the next chapter, the segmented lobe results will be used to construct an FE mesh to describe the lobe shape for each IPF subject. The patient specific lobe mesh will work as a basic geometry structure to guide a further disease distribution analysis and functional simulation.

Chapter 4

Quantitative computerized analysis of idiopathic pulmonary fibrosis

As introduced in Chapter 2, the natural history of IPF is poorly understood, and the clinical course for a given patient is unpredictable. Currently, there is a shortage of accepted biomarkers that can indicate the likely progression of IPF disease (Bartholmai et al., 2013). A successful quantification scheme that allows for recognition of disease across radiology, pulmonary and pathology disciplines still remains difficult. Development of accurate and automatic tools for quantitative assessment of alterations in the lung with IPF will be essential for a rapid patient-specific diagnosis and treatment. This chapter describes a study of quantitative analysis of IPF disease based on HRCT scans, including both assessment of tissue abnormalities and lung lobe shape analysis.

4.1 Background

4.1.1 Challenges of IPF diagnosis

Managing patients with IPF present a substantial health-care burden, due to short survival time and lack of effective treatments (with associated morbidity) (Olson et al., 2007; Raghunath et al., 2014). Accurate assessment and diagnosis of IPF is very challenging, since there is significant individual radiological and physiological variability among patients (Devaraj, 2014). The progression of disease varies considerably, ranging from rapid worsening of symptoms to relatively slow deterioration over several years (King Jr et al., 2011; Richeldi et al., 2017). The American Thoracic Society (ATS) and European Respiratory Society (ERS) develops a diagnostic criteria and schema for adult patients with IPF, and this criteria strongly recommends a multidisciplinary discussion between pulmonologists, radiologists and pathologists for an accurate diagnosis (Raghu et al., 2011; Travis et al., 2013). However, a successful classification and quantification tool that allows recognition of disease identically across radiology, pulmonary and pathology disciplines still remains difficult.

The complex appearances of IPF abnormalities that keep changing in extent over time is difficult to assess by traditional methods. Traditional radiological observation to distinguish disease patterns is tedious and not reproducible, and this manual evaluation is not consistent due to variation of inter- and intra- assessment (Flaherty et al., 2007; Watadani et al., 2013). Specifically, the difference in perception and interpretation of visual features of disease, which is associated with the experience and skills of clinical doctors, may lead to variable description of the same patient or even cause "reader error". However, this "error" can't be fully solved by training or improvement of imaging technologies (Kundel, 2006; Bartholmai et al., 2013). More importantly,

the final decision of clinical diagnosis is often based on independent evaluation from the radiologist, clinician and pathologist, which makes it hard to ensure consistency and dependability of results (Flaherty et al., 2004; Sverzellati et al., 2011). Another challenge of diagnosing IPF is the clinical problem of how to consistently detect and discriminate IPF from other idiopathic interstitial pneumonias (IIPs). These distinctive diseases usually have similar clinical presentations or indeterminate pathologic and radiographic appearances. Some cases may even have mixed restrictive/fibrotic and destructive/obstructive processes (Bartholmai et al., 2013). For example, non-specific interstitial pneumonia (NSIP), a pathological subtype of IIPs, appears to behave similarly to those with IPF/UIP patterns, especially for the cases with coexisting UIP and fibrotic NSIP patterns (Monaghan et al., 2004; Flaherty et al., 2001). All of these various IIPs have distinctly different prognosis, and specific therapy targeted to a particular pathological process is becoming necessary (Lynch et al., 2005). Therefore, non-IPF IIPs must be discriminated from IPF (Bjoraker et al., 1998).

4.1.2 Advantages of quantitative analysis using HRCT

Recent development in radiological imaging techniques offer exciting opportunities to develop radiological patient-specific biomarkers as important indicators of specific phenotypes (Devaraj, 2014; Gotway et al., 2007). HRCT has played an essential role in evaluating lung disease through recognizing visual patterns and features of disease regions such as ground-glass opacities, reticular patterns and honeycombing (Mueller-Mang et al., 2007). HRCT is also a useful diagnostic tool to differentiate between IPF and other pathologies. It is generally believed that the extent of visual lesion presented on HRCT strongly relates to the severity of pathological abnormalities, and therefore

can be used to monitor the progression of disease and then response to therapy (Kazerooni et al., 1997; Kim et al., 1999; Wells et al., 2003; Saketkoo et al., 2011). In addition, it has been noted that the use of HRCT can actually decrease the need for surgical lung biopsy which is risky for older patients with comorbidities (Bartholmai et al., 2013). As a non-invasive tool for visualizing abnormal parenchymal densities, HRCT has its own advantage in IPF diagnosis even for the cases where HRCT fails to show enough specific features to reflect typical UIP pattern, since HRCT can provide guidance for optimizing the site to obtain a surgical lung biopsy (Kazerooni, 2001; Diette et al., 2005; Misumi and Lynch, 2006; Costabel et al., 2007).

Currently, how the changes of disease can be consistently characterized and quantified over time and how these changes can predict disease progression are still challenging tasks. Manual classification and subjective evaluation are usually complicated and not accurate enough. Image-based quantitative analysis is therefore strongly needed for developing a robust and consistent IPF assessment system (Gotway et al., 2007; Lynch et al., 2005). A number of studies has indicated that the quantification of abnormalities on thoracic HRCT has potential to determine the extent of disease and stratify different types of disease with numerous imaging features in variable distribution (Best et al., 2008; Wells et al., 2003; Sumikawa et al., 2008; Bartholmai et al., 2013). The hypothesis is that through quantifying abnormalities from radiological images, robust objective biomarkers can be developed to drive a patient-specific prediction based on specific phenotypes. This will be important for facilitating individualized clinical management and identifying specific phenotypes linked to clinical disease presentations or therapeutic responses (Raghunath et al., 2014).

4.1.3 Review of current published methods of quantitative analysis of lung disease

In the past few years, there has been considerable effort to provide quantitative analysis of lung parenchymal abnormalities on HRCT scans. Fortunately, quantitative methods to analyze disease patterns of chronic obstructive pulmonary disease (COPD) such as emphysema have been well developed over the last 20 years, and have been able to provide reproducible biomarkers used in clinical diagnosis and assessment (da Silva Felix et al., 2008; Gietema et al., 2011; Galbán et al., 2012; Wang et al., 2013; Castaldi et al., 2013). However, quantification of disease patterns of lung fibrosis or other interstitial lung disease is more challenging, since the appearances and changes of these abnormalities are even more complicated than the characteristics seen with emphysema (Lynch, 2007; Delorme et al., 1997; Galbán et al., 2012; Depeursinge et al., 2010). In the early days, first-order textural analysis methods such as mean lung density (MLD) and histogram analysis (HIST) were used to analyze radiological lung imaging (Gilman et al., 1983; Gould et al., 1988; Müller et al., 1988; Kinsella et al., 1990; Knudson et al., 1991; Behr et al., 1992). These approaches to assess CT data are automatic and objective, but they simply examined a single parameter which only extracted lung density information. The measurement of attenuation (which relates to density) is highly dependent upon every slight change in lung volume and can be significantly affected by beam-hardening effects, scatter and drifts in scanner calibration. Therefore, these methods are difficult to apply in the presence of mixed disease.

Uppaluri et al. (1999b,a) was an early group to present a multiple feature based method to automatically quantify and classify pulmonary parenchyma of interstitial lung disease based upon HRCT. An adaptive multiple feature method (AMFM) which

combined statistical texture measures with a fractal measure was developed to initially assess the emphysema regions of the lung, and subsequently extended to study subjects with IPF or sarcoidosis. The AMFM method was further improved to assess as many as 22 independent texture features which enabled classification of pulmonary parenchymas into six tissue patterns, including: honeycombing, ground-glass, bronchovascular, nodular, emphysemalike, and normal. These 22 texture features consist of statistical features (gray level distribution features, run-length features and co-occurrence matrix features) and fractal features (geometric fractal dimension and stochastic fractal dimension). The lung slices were divided regionally into 31×31 pixel regions of interest (ROI). In each ROI, an optimal subset of texture features was evaluated to determine which of the six patterns in the region could be characterized. A nonlinear statistical classifier, the Bayesian classifier, was built to do the classification through calculating the probability that the ROI belongs to each tissue pattern. The whole algorithm contains two stages: the first stage involves training AMFM to recognize different HRCT based tissue patterns using a preselected dataset; the second stage involves a new CT data to be analyzed using the above introduced method. This multiple textural feature based method established the foundation and framework for subsequent studies on quantitative assessment of lung imaging. Xu et al. (2006b,a) enhanced the ability of AMFM based on Uppaluri et al. (1999b,a)'s work. In this study, the 2D textural feature based tissue analysis method was extended to 3D space for quantifying emphysema and early smoking related lung pathologies. The extracted features involved both first-order features (mean, variance, kurtosis and entropy of gray level distribution) and second-order features (run-length and co-occurrence measurements). The results showed that 3D AMFM analysis of lung parenchyma improved discrimination compared to 2D AMFM of the same volume of interests (VOIs).

In the past 15 years, the above introduced AMFM to quantify and classify lung disease from CT imaging has been widely used in a variety of studies (Van Ginneken et al., 2002; Chabat et al., 2003; Best et al., 2003; Uchiyama et al., 2003; Kim et al., 2005; Zavaletta et al., 2006; Arzhaeva et al., 2007; Best et al., 2008; Kim et al., 2010, 2011, 2015a). A general workflow of texture analysis is: 1. preset several types of tissue patterns; 2. divide lung slices into a set of ROIs with a square shape; 3. use texture analysis to extract multiple features for each ROI; 4. select representative expert-labeled ROIs as a training set for a classifier; 5. use the features of ROIs from a new set as input to the classifier to find the corresponding tissue pattern. Currently, most of the published CT based lung tissue analysis methods were developed based on this framework. Different textural features, ROI sizes or classifier types were specifically selected to target different lung disease or clinical requirement. Best et al. (2003, 2008) used mean lung attenuation (MLA), skewness (asymmetry) and kurtosis (peakedness) as features combined with a further univariate and multiple correlation and regression statistical analysis to determine relationships between histogram signals and results of PFTs in patients with IPF. The result showed that CT histograms of the lungs were correlated with results of PFTs, therefore the visual disease extent on CT images can be used as a strong independent predictor of mortality in IPF. Chabat et al. (2003) used similar textural features and classifier to Best et al. (2003, 2008)'s method for differentiating centrilobular emphysema, panlobular emphysema, constrictive obliterative bronchiolitis and normal normal lung tissue. Zavaletta et al. (2007) trained and tested three classifiers which included 10 Nearest Neighbor Classifier, Fisher Linear Discriminant Analysis and Parzen Window to classify normal and abnormal structures in lungs with IPF.

Uchiyama et al. (2003) and Kim et al. (2005) employed multi-layered artificial neural networks (ANNs) with a back-propagation algorithm as classifier to distinguish be-

tween different tissue patterns which includes both normal and diffuse lung disease slices. ANNs, using their simplest definition, are the modeling of the human brain, and their building blocks are neurons. They are excellent tools for finding patterns which are too complex or numerous for a human programmer to extract and teach the classifier to recognize, therefore will increase the accuracy of classification. In addition, Kim et al. (2010, 2011, 2015a) published a series of papers presenting a texture-based computer-aided diagnosis (CAD) scoring system to assess quantitative lung fibrosis (QLF) as a measurement of lung disease severity and as a surrogate imaging marker. The QLF score (in texture feature-based measure) was compared to the CT histogram metric (a global statistical measure), and the baseline severity and early change within 7 months in patients with IPF was assessed. The result concluded that classifier-model-derived scores (QLF scores) were associated with baseline disease extent and were also a sensitive measure of change over time, and a QLF score could be used for measuring the extent of disease severity and longitudinal changes.

Most of the published methods focus on texture-based classification of lung parenchyma or the severity and volumetric quantification of disease as a whole lung (such as QLF score). Currently, very few studies attempt to quantitatively characterize the spatial distribution of each disease pattern or describe how each tissue pattern changes or convert over time. Moreover, many of the existing methods are time consuming and sometimes even require several hours. These real-world limitations present difficulties when translating these techniques into clinical applications (Bartholmai et al., 2013).

In addition, it has been generally believed that there is a decrease in lung volume (both FRC and TLC) in patients with IPF, but up to now, few studies have been presented to explore the lung and lobe shape alteration in IPF lungs compared to normal ones. It is a reasonable assumption that shape changes will be observed in IPF lungs due to

physiologic alterations and disease progression over time.

4.1.4 Computer-Aided Lung Informatics for Pathology Evaluation and Ratings

CALIPER (Computer-Aided Lung Informatics for Pathology Evaluation and Ratings) is a computational image analysis platform developed by the Biomedical Imaging Resource Laboratory at the Mayo Clinic Rochester (Rochester, MN, USA) for the characterization and classification of lung parenchymal findings on HRCT (Maldonado et al., 2013; Bartholmai et al., 2013; Raghunath et al., 2014). The data processing step includes lung region segmentation and classification of the remaining pulmonary parenchyma on the CT dataset. Briefly, CALIPER isolates the lung parenchyma by extracting central airways and vascular structures, and then classifies every parenchymal voxel into the following characteristic CT patterns: normal (N), reticular (R), honeycomb (HC), ground-glass (GG), mild low attenuation areas (LAA), moderate LAA and severe LAA (emphysema). This novel computer-aided method for analyzing pulmonary tissue features provides a consistent and reproducible quantification of lung disease that relates to the semi-quantitative assessment from radiologists(Maldonado et al., 2013). Figure 4.1 shows visual appearance of each characteristic CT pattern.

Pre-processing is conducted before the eventual classification of the pulmonary parenchyma. This required segmentation of anatomic lung regions. The lungs are initially segmented using a adaptive density-based morphology (thresholding) method (Hu et al., 2001). Airways are segmented by thresholding combined with 3D growing processing and vessels are segmented by enhancement filter based on Hessian matrix (Sato et al., 2000), then the final lung segments are extracted.

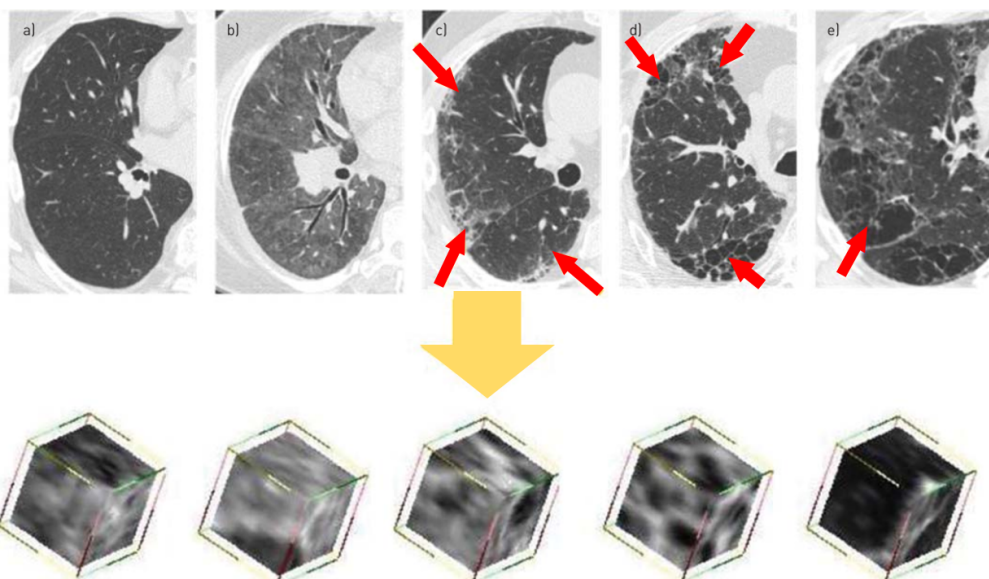


Figure 4.1: Computed tomography images demonstrating appearance and various visual manifestations of idiopathic pulmonary fibrosis: a) normal, b) ground glass, c) reticular changes (arrows), d) honeycombing (arrows) and e) emphysema (arrow). In training datasets, the consensus of four thoracic radiologists was used to identify multiple VOIs corresponding to normal, ground-glass density, reticular abnormalities, honeycombing and emphysema. Reproduced from (Maldonado et al., 2013).

The volumetric detection and classification of pulmonary parenchyma by CALIPER uses a sliding window supervised classification scheme based on histogram signature mapping techniques (Zavaletta et al., 2007). This classification technique is trained by expert radiologist via consensus assessment of pathologically confirmed datasets, which are obtained from the Lung Tissue Research Consortium (LTRC). LTRC is a resource program sponsored by the NIH/NHLBI that provides clinical and physiologic data of human lung tissues to qualified investigators for use in their research and to help investigators develop a better understanding of lung disease. The central part of the classification scheme is the selection of a set of expert-labeled volumes of interest (VOIs) as the training data for a classifier. The training data used in CALIPER is numbers of $15 \times 15 \times 15$ -voxel VOIs acquired from HRCT scans of subjects with proven pathological diagnosis of interstitial lung disease (ILD) or emphysema from the LTRC repository. These VOIs are selected through independent analysis by four experienced thoracic radiologists from CT scans, with instructions and criterion to determine if the visual appearance should represent normal, emphysema or one of the characteristic lung fibrosis CT patterns: honeycomb, reticular or ground-glass (Maldonado et al., 2013; Bartholmai et al., 2013).

The VOIs with agreement on the class of abnormality by all four radiologists are used as exemplars to determine canonical histogram signatures of the CT patterns of visual abnormality by automatic cluster affinity techniques. Quantitative discriminability of a series of pairwise dissimilarity metrics based on the VOI histograms is tested using multi-dimensional scaling (MDS). Cramer Von Mises Distance (CVM), which is found to be most consistent with the expert groupings, is selected as the dissimilarity metric to train CALIPER. For each of the parenchymal voxels needing to be classified, the local histograms of its neighbouring $15 \times 15 \times 15$ voxels are compared against

the histograms of the exemplars identified in the training phase. A CVM dissimilarity measure is used in the comparison and the fundamental type of the exemplar (N,R,H,G or emphysema) with the lowest CVM is assigned as the parenchymal CT pattern to this classified voxel. The parenchymal voxels identified as vessel structures are classified as normal pattern. Figure 4.2 shows a representative dataset with axial, coronal and sagittal sections of a CT lung volume where every voxel of the parenchyma is characterized and color coded into one of the parenchymal patterns (N, R, H, G, and mild, moderate and severe LAA).

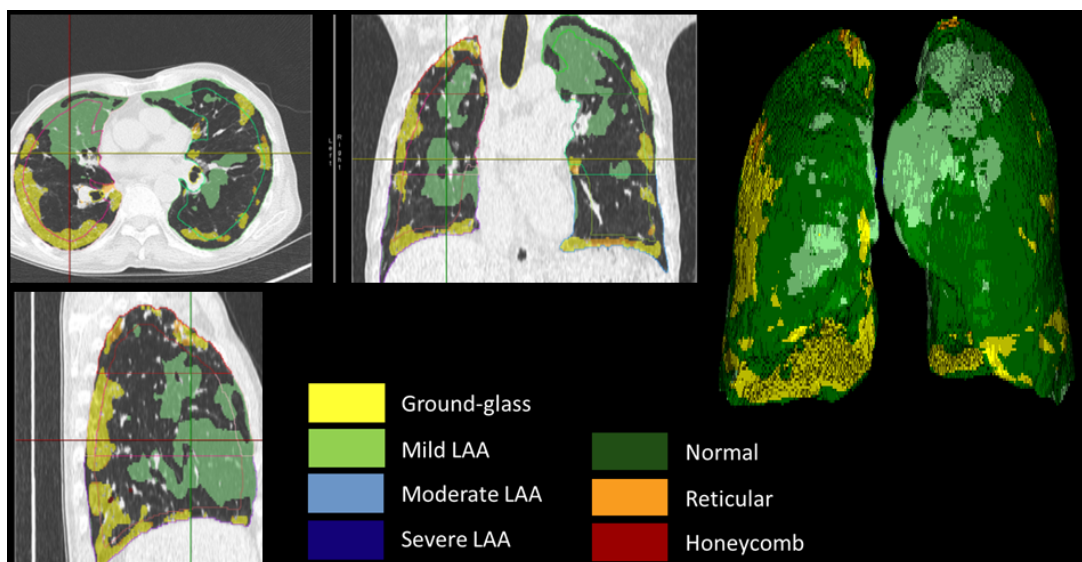


Figure 4.2: Color labelled classification result of one subject diagnosed with IPF by CALIPER. (a) Transverse plane. (b) Coronal plane. (c) Sagittal plane. (d) 3D color labelled lung.

4.2 Methods: quantitative analysis of IPF lungs

This section describes the quantitative methods to analyze and characterize IPF tissue abnormalities and lung lobe shape longitudinally, and in comparison to normal subjects.

In summary, HRCT imaging was classified by pattern using a validated image analysis process (Maldonado et al., 2013; Bartholmai et al., 2013; Raghunath et al., 2014). The tissue classification data was mapped to a mean statistical shape model (SSM) allowing a quantitative approach to analyze tissue pattern density, tissue pattern volume, spatial distribution of abnormalities, and regional changes in tissue abnormalities over time. In the shape analysis, lobar finite element meshes for both IPF and normal subjects were projected to the SSM, and lobe shape differences in IPF were then quantitatively characterized.

4.2.1 Tissue classification of IPF lungs

Imaging and clinical data

Data used in this study was acquired as part of routine clinical diagnosis or follow up. Data use was approved by the Southern Health and Disability Ethics Committee (ETHICS APPROVAL NUMBER). Data include volumetric HRCT and PFTs from 13 patients who were diagnosed with or suspected to have IPF. All patients were under clinical care at Auckland City Hospital, Auckland, New Zealand. Volumetric HRCT images (slice thickness 1.25-5.00 mm) were acquired at the end of inspiration and during routine diagnostic inspection and/or monitoring for IPF disease. 11 of the subjects had more than one serial CT scan within a 5-79 month interval, representing different time points (7 subjects had 3 time points, 4 subjects had 2 time points). The population demographics for these subjects is shown in Table 4.1.

Table 4.1: Demographic data.

Description	
Age years	43-83
Females/Males	3/10
Slice thickness	1.25-5.00 mm
Scan month interval	5-79 month
Slice resolution	512 × 512
Number of slices	68-227

Normalization of classified data

Tissue CT patterns of each patient for each time point were classified using CALIPER software introduced in Section 4.1.4. Then, lung surface data and fissure surface data were acquired using the lobe segmentation method introduced in Chapter 3. A bi-cubic Hermite finite element surface mesh was fitted to the shape of the lung and its fissures via a least squares fit (<https://www.cmiss.org>). The details for the generation of lobe data and the lobe mesh are given in Chapter 3, Section 3.3.2.

There is lung shape variation between different subjects and often between clinical images obtained at different times, as well as variation in the extent to which a patient inhales during imaging, even with careful training. Thus, the classified volumetric lung data was then mapped to a statistical shape model (SSM) of the "normal" older human lung to provide a consistent mapping of tissue abnormalities in individuals to a consistent lung shape. The steps for the construction of the SSM were introduced in Chapter 3, Section 3.3.2, which described an SSM for a cohort aged 21-83. In this chapter we used 35 normal old subjects aged 50 years and older to derive an SSM because this is consistent with the typical age of onset of IPF. The SSM used for mapping data is the average mesh of the lung lobes which was derived from these 35 training subjects, and

it provides a description of a statistical mean lung and fissure surface shape of normal people adults aged ≤ 50 years.

In order to map the individual classified data to the SSM mesh, the bi-cubic Hermite finite element mesh of lung surface was converted to a tri-cubic Hermite volumetric mesh which describes not only the lung surface but also the internal anatomy (Tawhai and Burrowes, 2003). The volumetric mesh has 40 nodes and 30 elements for left lung, and 56 nodes and 38 elements for right lung. For each node, it has 24 DOFs which store the global coordinates (x , y and z) and the first, second and third nodal derivatives ($\frac{\partial n}{\partial \xi_1}$, $\frac{\partial n}{\partial \xi_2}$, $\frac{\partial n}{\partial \xi_3}$, $\frac{\partial^2 n}{\partial \xi_1 \partial \xi_2}$, $\frac{\partial^2 n}{\partial \xi_2 \partial \xi_3}$, $\frac{\partial^2 n}{\partial \xi_1 \partial \xi_3}$ and $\frac{\partial^3 n}{\partial \xi_1 \partial \xi_2 \partial \xi_3}$), where n is x , y and z , and ξ is the local element coordinate.

During the data mapping, all of the classified data should be completely enclosed inside its lobe volume mesh. The position of each point within the finite element mesh was defined locally in each element of the mesh by ξ_i , for $i=1,\dots,3$ with $0 < \xi_i < 1$. ξ_i location denotes the local coordinates of the data point with respect to its element. The local coordinate ξ_i was then used to calculate the global coordinates of the mapped data points using the following equation:

$$u(\xi_i) = \sum_{n=1}^N \psi_n(\xi_i) u_n \quad (4.1)$$

where u_n is a vector of N element nodal parameters of the SSM lobe mesh associated with the interpolation functions ψ_n .

In order to force a uniform data point distribution throughout each lung, the gaps in the mapped data caused by the mapping deformation from individual shape to SSM (shown in Figure 4.3a) were "filled" by matching the classification of their closest neighbor point among the classified data. Uniform data point distribution facilitates

further density and spatial distribution analysis of abnormalities. Briefly, the gaps of the mapped data were filled using the following steps:

1. Mapped data were cut into a series of axial slices (shown in Figure 4.3a).
2. The lung mesh of average SSM was used as a mask to define the lung boundary. (shown in Figure 4.3b).
3. Morphological operations were applied to smooth the lung boundary, then a lung mask was generated (shown in Figure 4.3c).
4. The gaps enclosed inside the lung mask were filled with the CT pattern color of its closest point among the classified data (shown in Figure 4.3d).

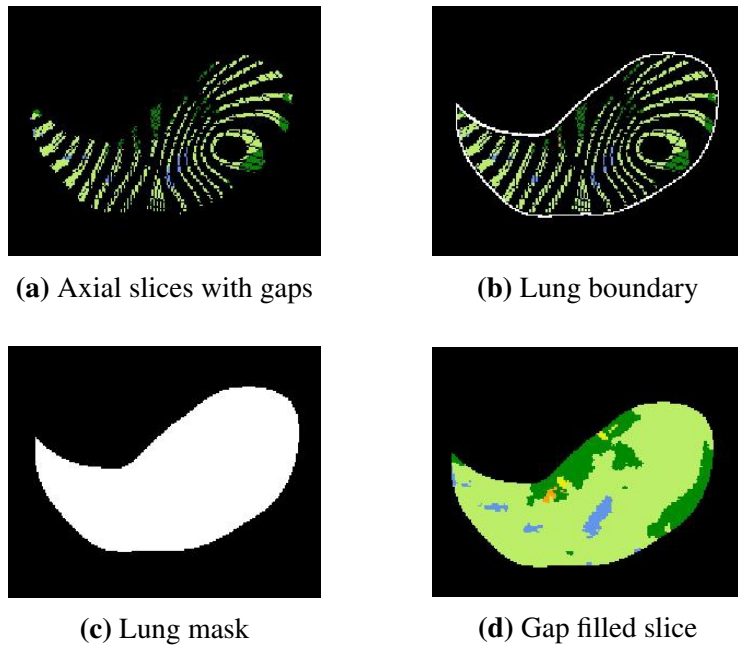


Figure 4.3: Diagram of gap filling steps within the mapped data. (a) Get axial slices of mapped data (with gaps). (b) Define lung boundary (SSM defined). (c) Get lung mask. (d) Fill the gaps within lung mask.

4.2.2 Tissue quantification of IPF lungs

Density analysis

The average density value of each classified CT pattern was calculated. Intensity is measured in Hounsfield units (HU) in a typical CT image, which corresponds linearly to the actual density of the imaged tissue. HU was calculated with the segmentation software PTK calibrated to values of approximately -1024 for air density, zero for water density, and over 40 for blood, bone, and other non-parenchymal tissue. The tissue density (ρ , g/cm^3) was then acquired at each voxel:

$$\rho = \frac{HU}{1024} + 1, \quad (4.2)$$

the average density of each CT pattern was then calculated from individual voxel density.

Spatial distribution analysis

Based on the criteria of IPF defined by the ATS and ERS, the diagnosis of IPF usually associates with the presence of a UIP pattern on HRCT (see details in Chapter 2, Section 2.3.4). The distribution of UIP on HRCT is characteristically basal and peripheral (subpleural), though often patchy. Therefore, in order to quantitatively analyze the spatial distribution of IPF abnormalities, the percentage of honeycomb, reticular, emphysema and ground-glass which represent typical UIP disease patterns on HRCT were calculated in basal-to apical sections, dorso-to-ventral sections, from subpleural to internal and by lobe:

Basal-to-apical: In the direction from base to apex, the volume percentage of each disease region was averaged in 5% lung height (along the cranio-caudal axis).

Dorso-to-ventral: In the direction from back to front, the volume percentage of each disease region was averaged in 5% along the cranio-caudal axis.

Subpleural to internal: The distance from the abnormalities to the boundary of the lung and to the center of the lung were measured to analyze the location of disease with respect to the disease from lung surface. To be specific, the center location of each connected cluster of disease area was firstly extracted, and the subpleural to internal distance percentage $R_{subpleural}$ of each connected cluster, which described how far was the connected cluster from the lung surface, was then calculated as in the diagram shown in Figure 4.4

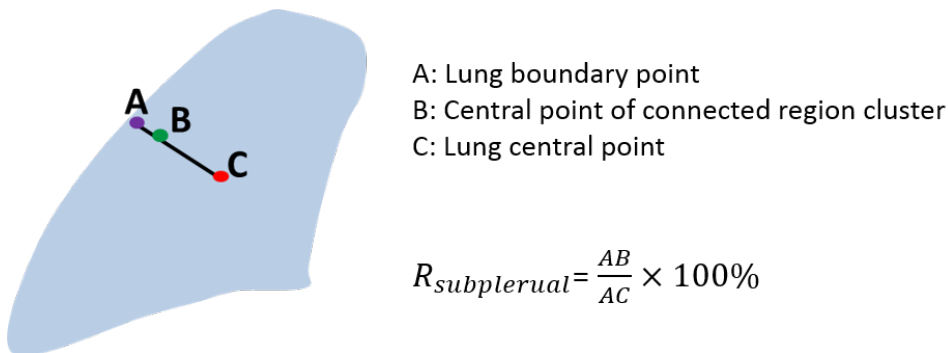


Figure 4.4: Diagram of subpleural-to-internal percentage measurement.

where the coordinate of lung central point $P_{centre}(x, y, z)$ was calculated as:

$$P_{centre}(x, y, z) = \frac{\sum_{i=1}^N P_{surface}(x, y, z)}{N}, \quad (4.3)$$

where $P_{surface}(x, y, z)$ is the coordinate of lung surface data point, and N is the number

of lung surface data point.

Lobar distribution: In order to analyze the lobar distribution of disease, the volume percentage of each disease CT pattern located in each lobe was calculated.

Change in classification of tissue pattern over time

Median survival time of patients with IPF is generally from 3 to 5 years from time of diagnosis. However, individual progression of disease is variable and how the characteristic disease pattern changes over time (e.g. whether a disease region deteriorates and changes to other tissue patterns or stays the same over time) still remains elusive. In our study, the classified data of all subjects and time points have been normalized to a standard lung shape (SSM, as introduced in Section 4.2.1), thus making it possible for us to detect the disease change in specific regions as time goes on by extracting the CT pattern of each voxel at different time points.

4.2.3 Volume analysis of IPF lungs

The change of whole lung volume over time

The volume of each classified tissue pattern in both left and right lung was calculated using the following equation:

$$V_{Region} = N \times R_x \times R_y \times R_z \quad (4.4)$$

where N is the number of voxels of each tissue pattern, R_x , R_y are the x, y resolution of the CT scan, and R_z is the thickness of the CT scan. Then the whole volume of left and right lung was calculated as the sum of the volume of each CT pattern.

Lobe volume difference between old normal lungs and IPF lungs

The lobe volume of the IPF cohort was compared with the older normal cohort described in Section 4.2.1. In order to quantitatively analyze the lobe volume difference between the two groups, the volume proportion of each lobe was calculated:

$$P_i = \frac{V_i}{\sum_{i=1}^5 V_i}, \quad (4.5)$$

where V_i is the volume of each lobe with $i=1$ corresponding to left lower lobe, $i=2$ corresponding to left upper lobe, $i=3$ corresponding to right lower lobe, $i=4$ corresponding to right middle lobe and $i=5$ corresponding to right upper lobe. The differences in lobe volume proportions between IPF subjects and normal subjects were compared statistically using a t-test. In order to further compare lobe volumes between these two groups, the average lobe volume proportion among IPF subjects and among old normal subjects were then calculated respectively.

4.2.4 SSM based shape analysis of IPF lungs

The SSM was used to quantitatively analyze the alterations in lung lobe shapes of patients with IPF. As previously described in Section 4.2.1, 35 normal subjects aged > 50 years from the AGING dataset were used as training data to construct the SSM which contained both lung surface and fissure surface. PCA was used to decomposed the shape variation of the lung lobe into a set of modes, and each mode represented one type of lung and fissure surface shape variation. Thus, each lung lobe shape was described by a linear combination of the mode vector and its corresponding weight:

$$S_{new} = S_{mean} + \sum_{i=1}^L \mathbf{u}_i w_i, \quad (4.6)$$

where S_{mean} is the average lobe shape model across all the training subjects, $\mathbf{u}_i (i = 1, 2, \dots, L, L = 34$ in this study) is the mode vector of shape variation which corresponds to the i^{th} largest principle component from PCA, and w_i is a weight factor given to each mode of variation.

The lung lobe FE mesh of each IPF subject was then procrustes projected on to the average SSM after alignment to the reference model (details can be seen in Chapter 3, Section 3.3.3) The new weight values of all the shape modes $w_{new} = [w_{new1}, w_{new2}, \dots, w_{newL}]$ ($L = 35$) were calculated from the projection. These mode weights can be used as quantitative indexes to analyze and compare the shape variation and difference between IPF and the control group.

Shape difference between IPF lungs and old normal lungs

For the SSM of the control group, the first three shape modes explained over 30% of the total variation in the training set. Therefore, the weight values of the first three modes were used as the measurement to compare the shape difference of lung lobe between controls and IPF. The p values of the first three shape modes between the two groups were calculated using t-test.

Relationship between lung lobe shape and fibrosis and low attenuation area extent

In order to quantitatively investigate the association between fibrosis extent and lung shape variation, the association of the first three mode weightings with the overall volume percentage of fibrosis and low attenuation area (LAA) was estimated using linear

regression. Total fibrosis extent was estimated as the sum of reticulation, honeycombing and ground-glass opacification of both lungs, and total LAA extent was estimated as the sum of mildLAA, moderateLAA, severeLAA and emphysema of both lungs. The behavior of the first three modes with respect to overall fibrosis percentage and LAA percentage was analyzed using linear regression.

4.3 Results

4.3.1 Normalization of classified data

Figure 4.5 shows the mapped classification data for a single subject.

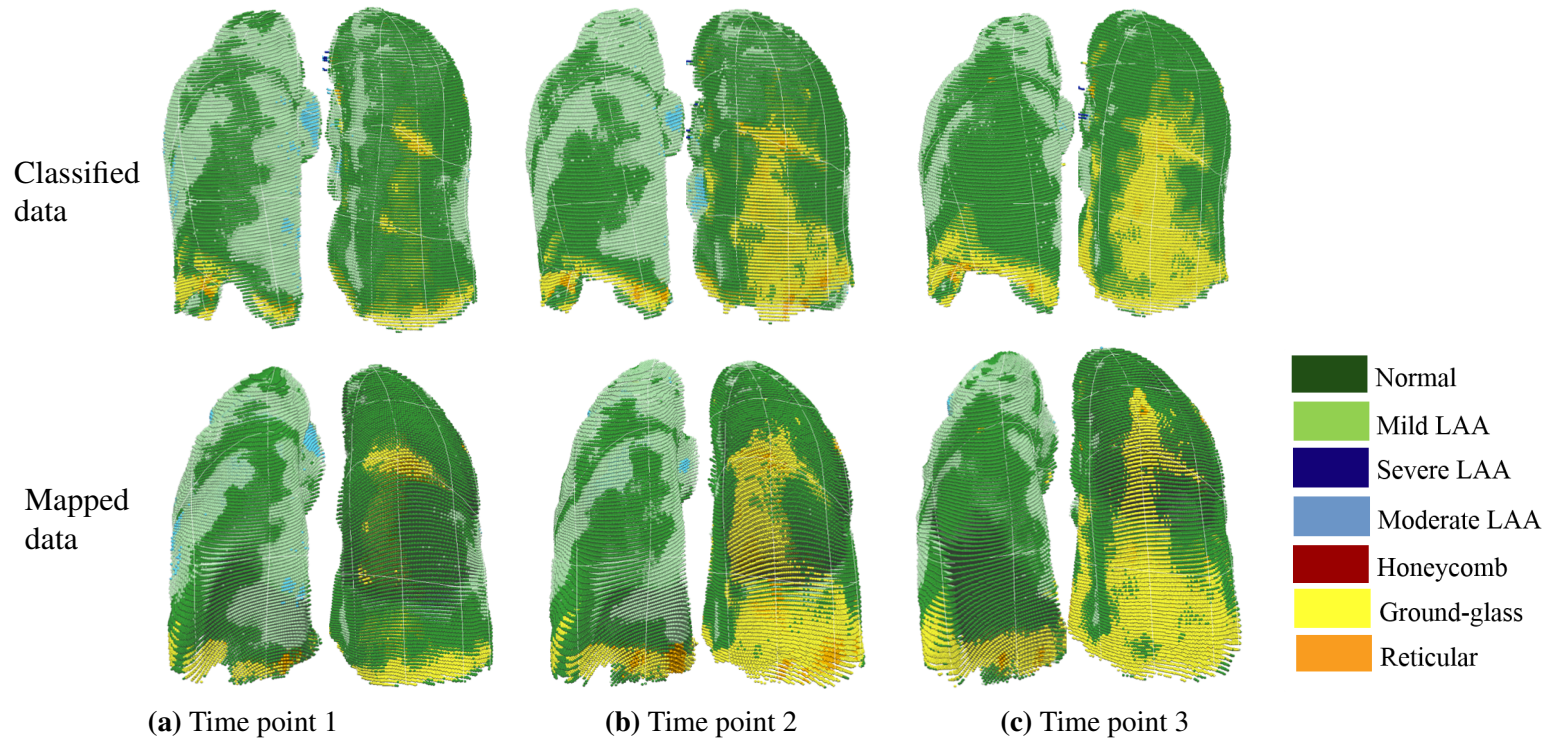


Figure 4.5: Classified data (top row) and mapped data (bottom row) of three time points from one subject diagnosed with IPF. (a) The first time point, scan time: 0 month. (b) The second time point, scan time: 15 months. (c) The third time point, scan time: 20 months

Figure 4.6 shows the slices with gaps and the slices after gap filling for three time points at the same position in the lung.

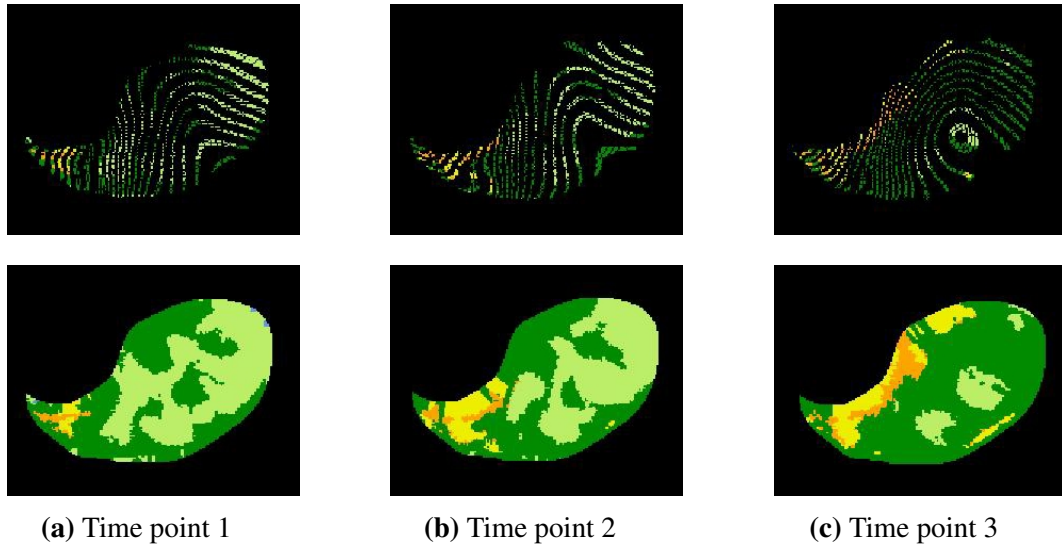


Figure 4.6: Axial slices with gaps (top row) and axial slices after gap filling (bottom row) of three time points from one subject diagnosed with IPF. (a) The first time point, scan time: 0 month. (b) The second time point, scan time: 5 months. (c) The third time point, scan time: 20 months.

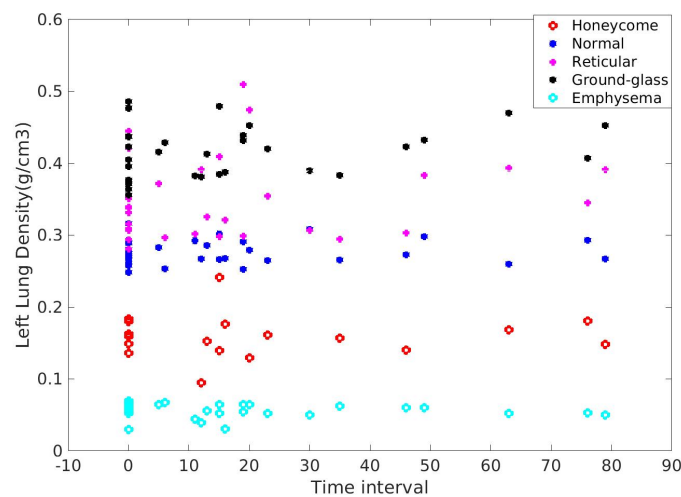
4.3.2 Tissue quantification of IPF lungs

Density analysis

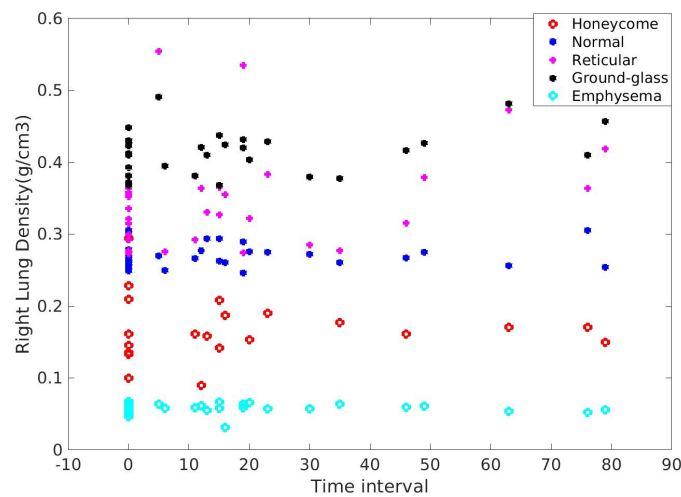
The density analysis result is shown in Figure 4.7 and Table 4.2. It can be seen that the average density of each CT pattern remains consistent and fluctuates only within a specific range over time in both left and right lung. The ground-glass region has the highest average tissue density and emphysema has the lowest average tissue density.

Table 4.2: Mean tissue density of each CT pattern for left and right lung (mean value \pm standard deviation)

	Mean tissue density (left lung)	Mean tissue density (right lung)
Normal	0.280 ± 0.022	0.271 ± 0.015
Honeycomb	0.148 ± 0.039	0.155 ± 0.027
Reticular	0.355 ± 0.054	0.321 ± 0.039
Ground-glass	0.424 ± 0.051	0.404 ± 0.018
Emphysema	0.080 ± 0.014	0.082 ± 0.016



(a) Left lung tissue density



(b) Right lung tissue density

Figure 4.7: Average tissue density (g/cm^3) of each CT pattern in IPF lungs. Each data point represents the tissue density of one time point from one patient. X axis represents the month interval of scan time for each patient, and "0" represents the first scan for this patient. (a) Tissue density of left lung. (b) Tissue density of right lung.

Spatial distribution analysis

Basal-to-apical Figure 4.8 shows the percentage distribution (average value of all time points across the patients) against lung height (cranio-caudal axis) of four characteristic CT patterns: ground-glass, reticular, honeycomb and emphysema for left and right lung. It can be seen from the result that ground-glass mainly locates in the basal part of lung. The percentage of ground-glass decreases gradually with the increasing of the lung height, and the distribution of ground-glass is quite similar in left and right lung. In contrast, the percentage of emphysema trends toward increasing from lung base to apex. The reticular tissue is mainly distributed basal area and apex area, but it seldomly appears in the middle part of lung. The distribution of honeycomb does not have a relationship with lung height.

Figure 4.9 shows the percentage distribution (average value of the first time point across all the patients) against lung height (cranio-caudal axis) of four characteristic CT patterns (ground-glass, reticular, honeycomb and emphysema) in left and right lung at month 0. From the result, the cranio-caudal distribution tendency of the four CT patterns at month 0 are quite similar to the total average distribution shown in Figure 4.8, but the absolute percentages of the abnormalities at month 0 are lower than the total average values. That means the area of disease experiences an increase over time as a whole in IPF lung.

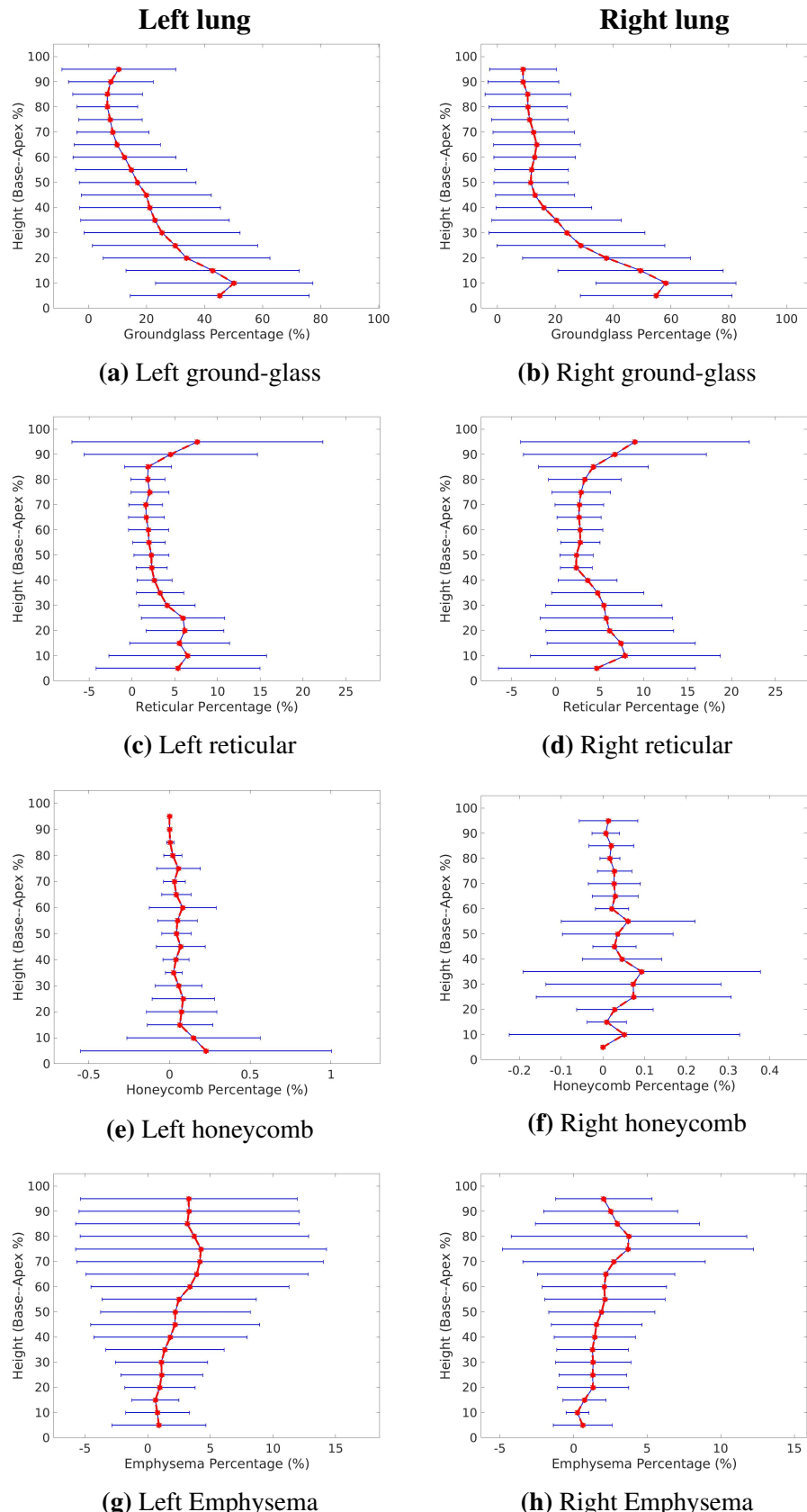


Figure 4.8: Volume percentage of each tissue classification plotted against lung height (cranio-caudal axis) in IPF left and right lungs. The average percentage was calculated within 5% sections of the lung height from the base to apex. Red shows the average value at each position across all patients, and blue shows the standard deviation. (a) (b) is ground-glass distribution. (c) (d) is reticular distribution. (e) (f) is honeycomb distribution. (g) (h) is emphysema distribution.

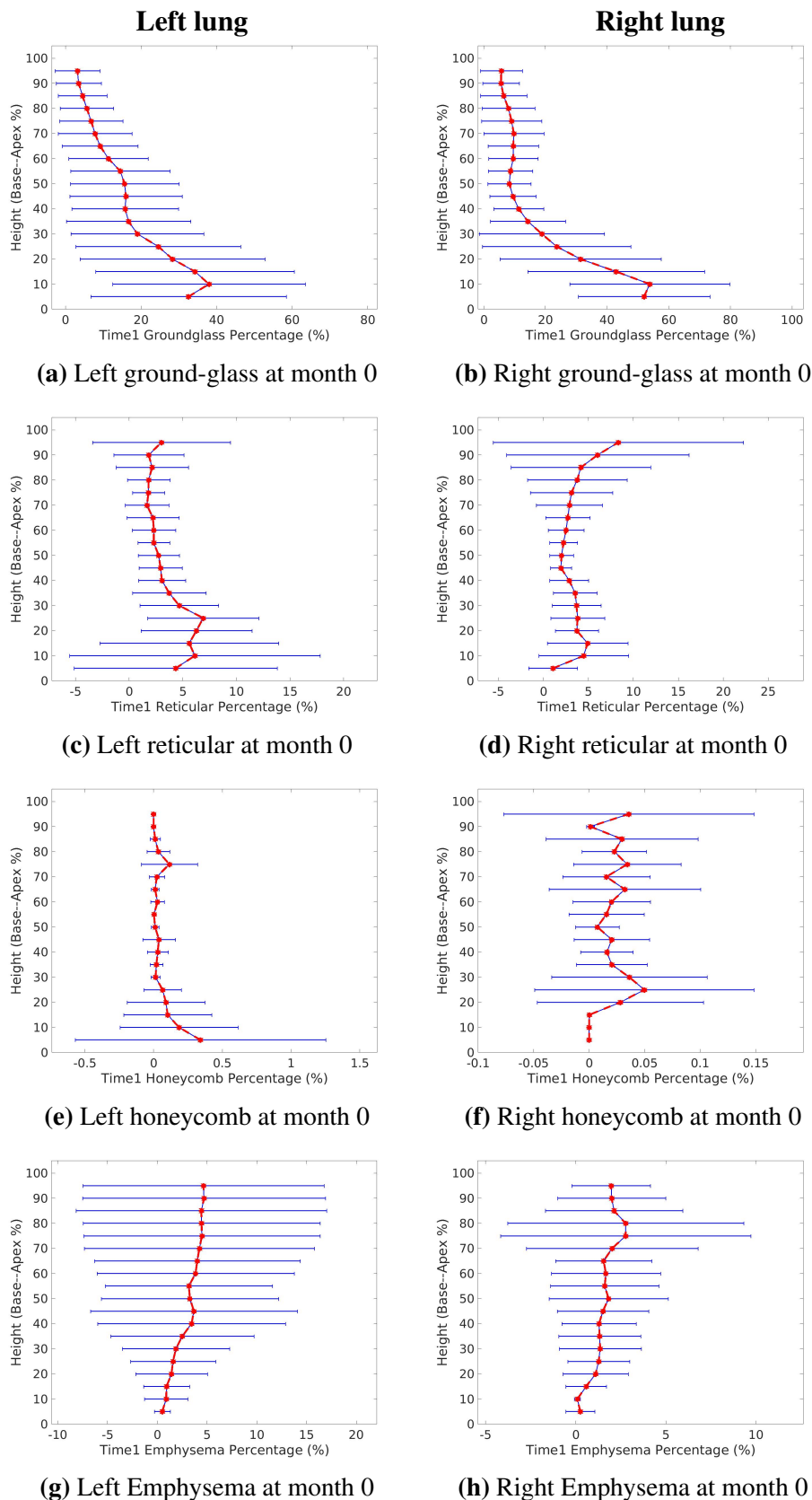


Figure 4.9: Volume percentage of each tissue classification plotted against lung height (cranio-caudal axis) in IPF left and right lungs at month 0. The average percentage was calculated within 5% sections of the lung height from the base to apex. Red shows the average value at each position across all patients, and blue shows the standard deviation. (a) (b) is ground-glass distribution. (c) (d) is reticular distribution. (e) (f) is honeycomb distribution. (g) (h) is emphysema distribution.

Figure A.10 shows the percentage distribution against lung height (cranio-caudal axis) of the four characteristic CT patterns from an individual patient diagnosed with IPF in left and right lung over time. From time point 1 to time point 3, it can be observed an overall increase of the disease regions, even though the percentage of some tissue pattern may fall during this time. The distribution trend in base-to-apex axis doesn't change too much for ground-glass and reticular over time, but the it really has a big fluctuation for honeycomb and emphysema.

The percentage distribution against lung height over time of other patients can be found in Appendix A.

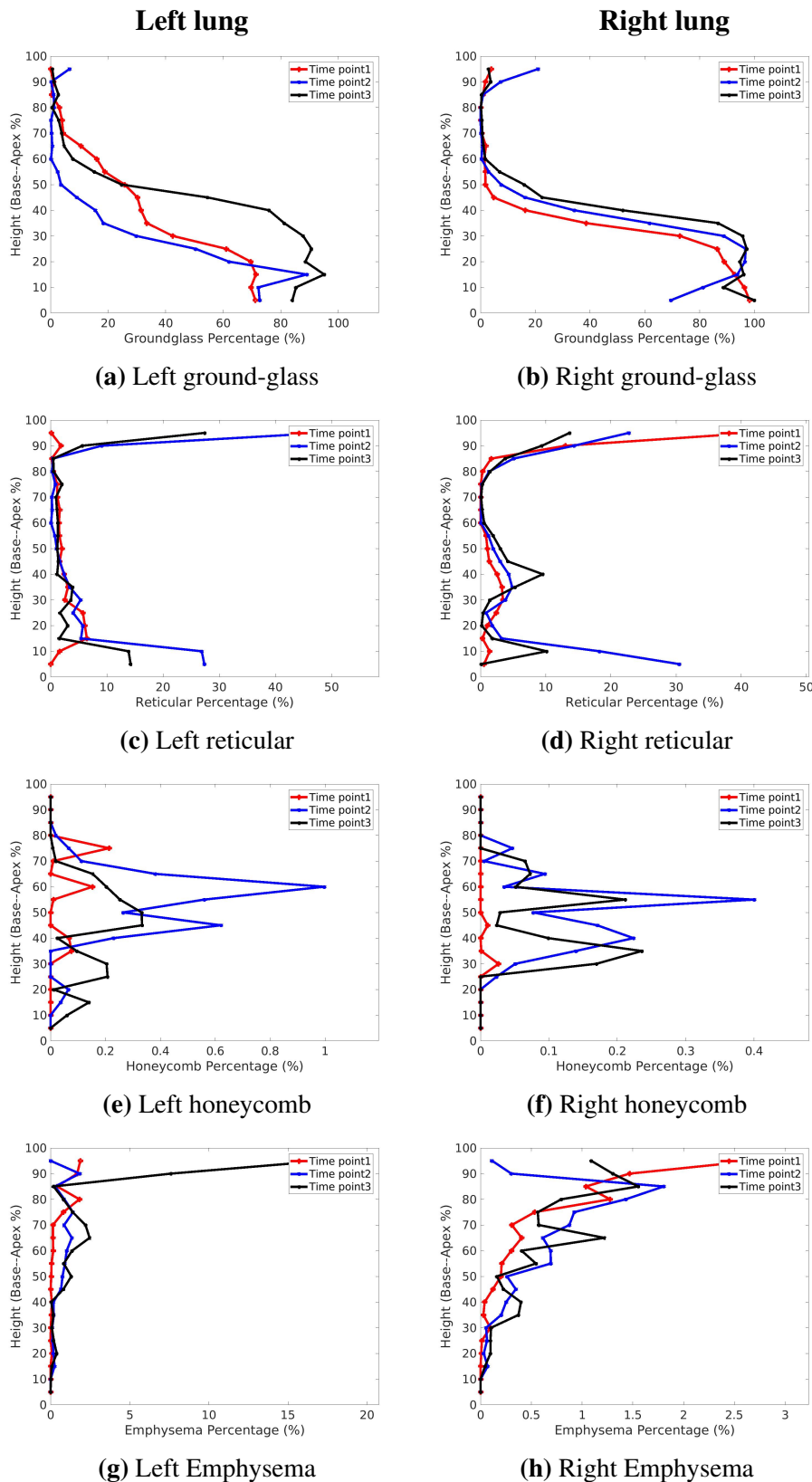


Figure 4.10: Volume percentage of each tissue classification plotted against lung height (cranio-caudal axis) of one patient diagnosed with IPF in left and right lungs over time. The average percentage was calculated within 5% sections of the lung height from the base to apex. (a) (b) is ground-glass distribution. (c) (d) is reticular distribution. (e) (f) is honeycomb distribution. (g) (h) is emphysema distribution.

Dorso-to-ventral Figure 4.11 shows the percentage distribution (average value of all time points from all patients) from back to front of the lung (dorso-ventral axis) of four characteristic CT patterns: ground-glass, reticular, honeycomb and emphysema for left and right lung. The results illustrate that the percentage of ground-glass and reticular keep increasing from back to front, and they mostly locate in the ventral part of the left and right lungs. The distribution of honeycomb and emphysema both show overall steady trend along the dorso-ventral axis, but for honeycomb pattern, there are relatively more abnormalities appearing in the dorso and ventral regions compared to the middle area.

Figure 4.12 show the percentage distribution (average value of the first time point from all the patients) from back to front of the lung (dorso-ventral axis) of four characteristic CT patterns (ground-glass, reticular, honeycomb and emphysema) in left and right lung at month 0. It can be seen from the result, like the cranio-caudal distribution, the distribution shape of the diseases in dorso-ventral axis at the first time point are almost the same to the distribution in Figure 4.12, and the disease percentage at month 0 is slightly lower than the total time averaged value.

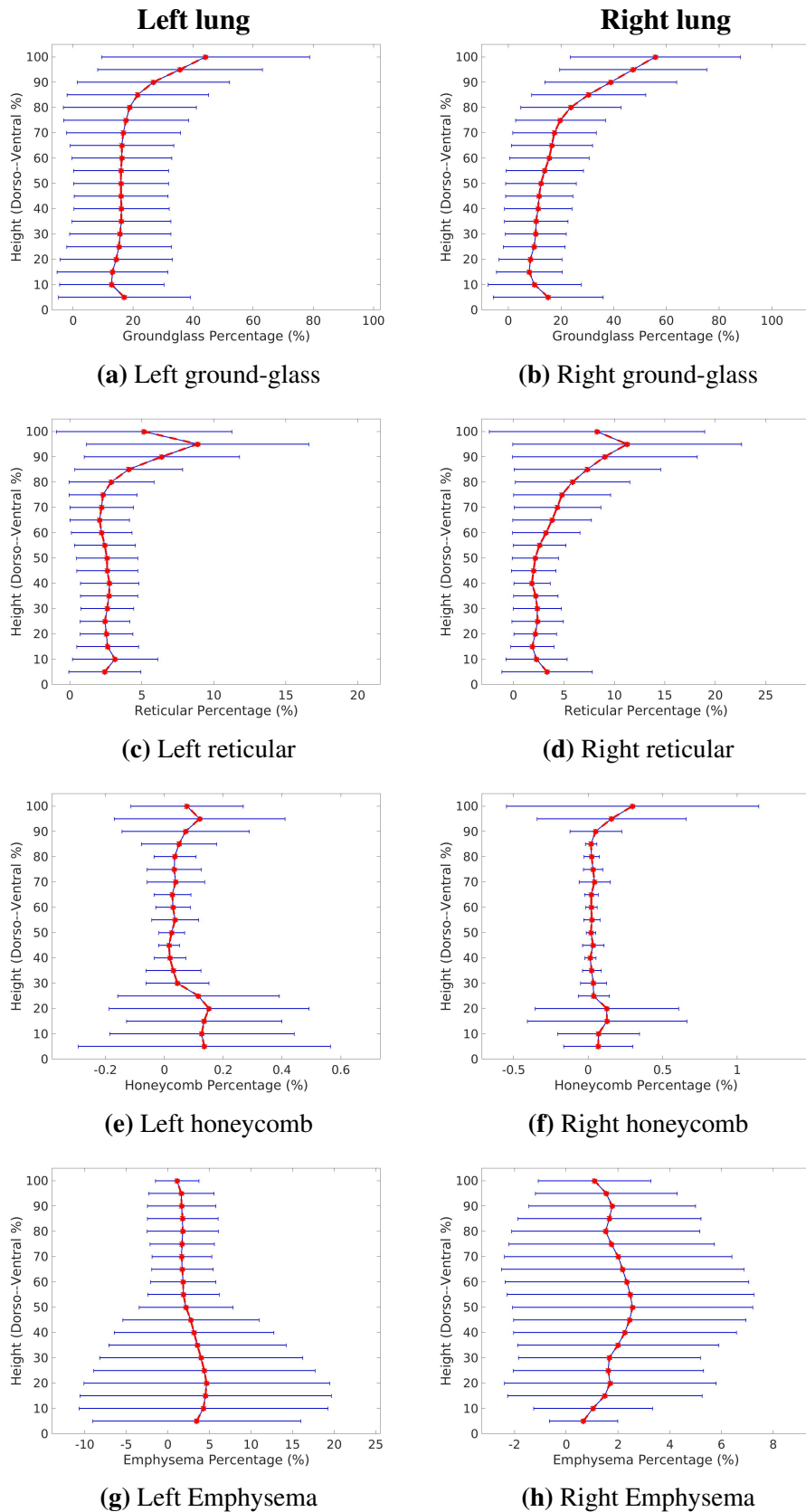


Figure 4.11: Volume percentage of each tissue classification plotted in the direction of dorso-ventral axis in IPF left and right lungs. The average percentage was calculated within 5% sections along dorso-ventral axis from the back to front. Red shows the average value at each position across all patients, and blue shows the standard deviation. (a) (b) is ground-glass distribution. (c) (d) is reticular distribution. (e) (f) is honeycomb distribution. (g) (h) is emphysema distribution.

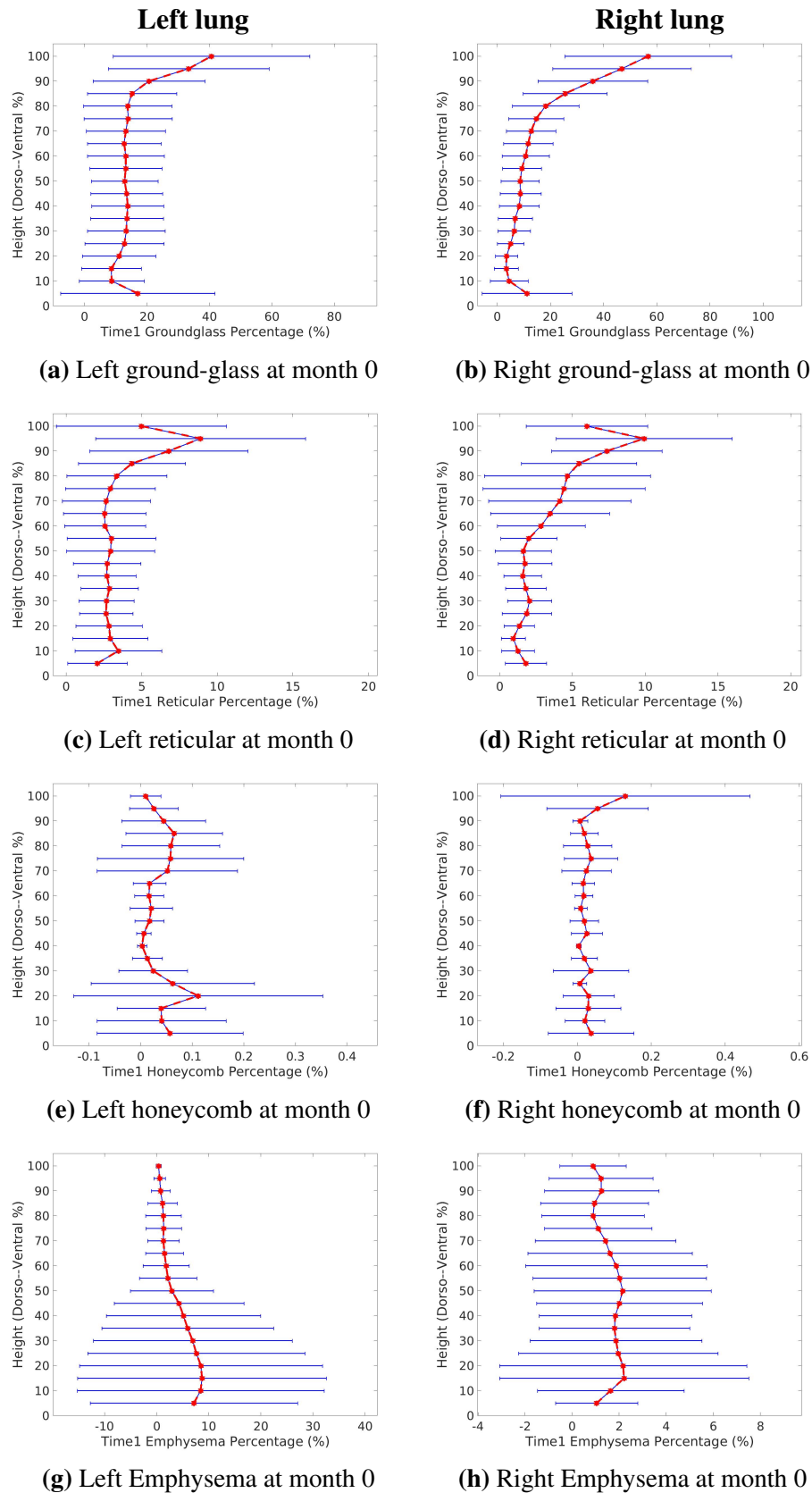


Figure 4.12: Volume percentage of each tissue classification plotted in the direction of dorso-ventral axis in IPF left and right lungs at month 0. The average percentage was calculated within 5% sections along dorso-ventral axis from the back to front. Red shows the average value at each position across all patients, and blue shows the standard deviation. (a) (b) is ground-glass distribution. (c) (d) is reticular distribution. (e) (f) is honeycomb distribution. (g) (h) is emphysema distribution.

Figure A.20 shows the percentage distribution from back to front of the lung (dorso-ventral axis) of the four characteristic CT patterns from an individual patient diagnosed with IPF in left and right lung over time. For ground-glass, emphysema and left honeycomb, it can be seen an increase in the volume percentage over time and the dorso-ventral distribution doesn't change a lot during this period of time. However, the spatial location of reticular and right honeycomb really experience a huge movement in dorso-ventral direction as time goes by, and no regular tendency can be found for these regions.

The percentage distribution in dorso-ventral axis over time of other patients can be found in Appendix A.

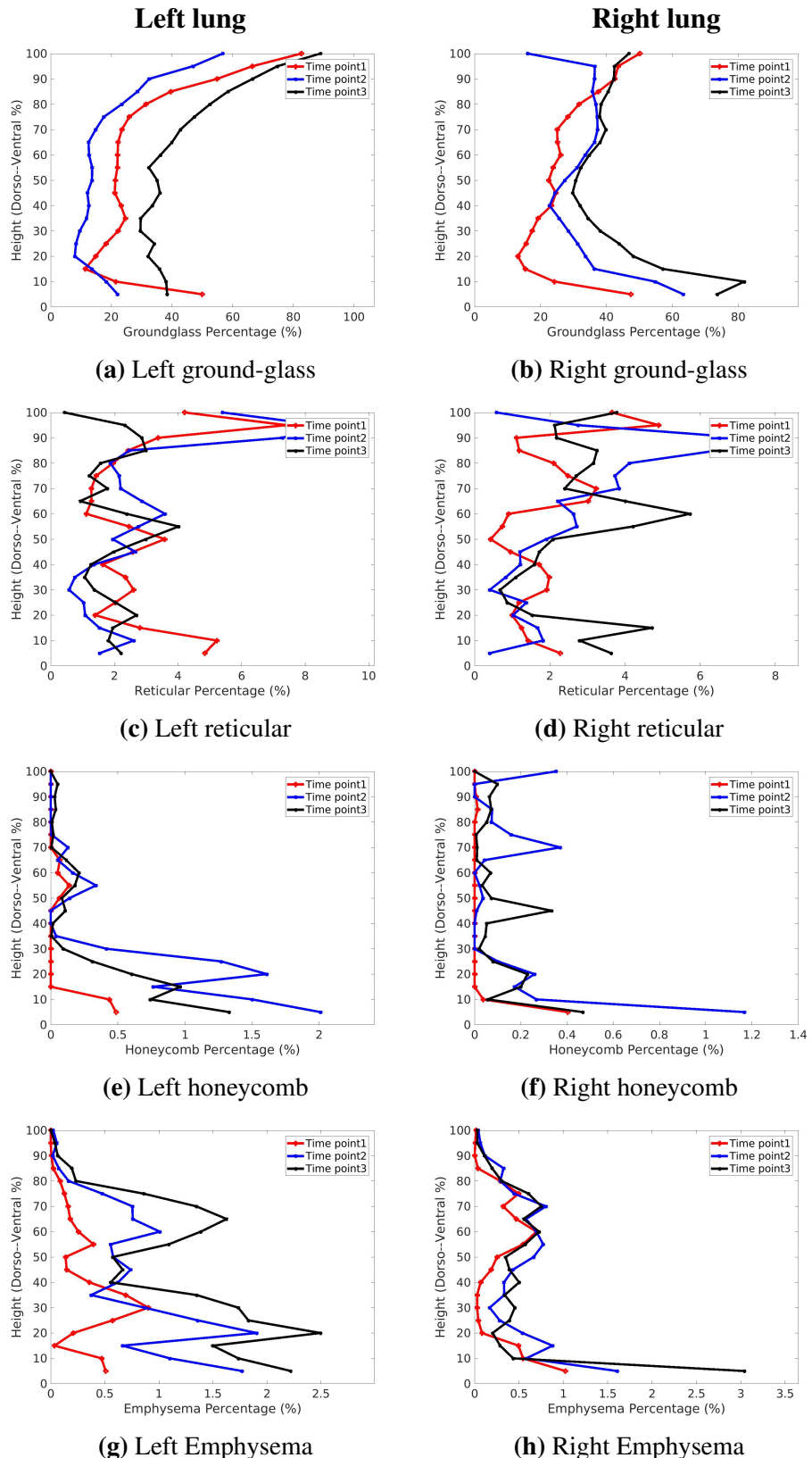
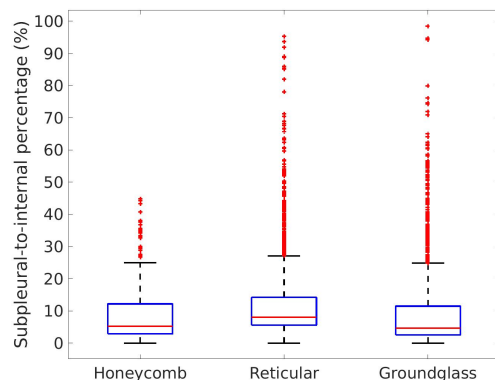
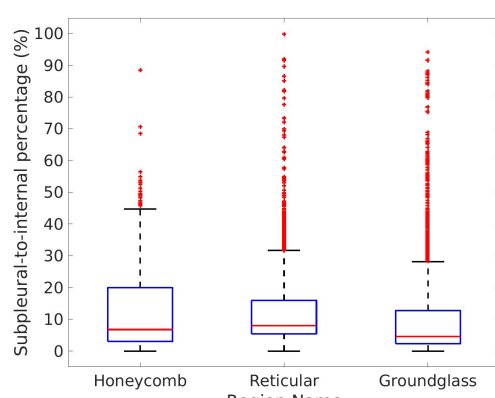


Figure 4.13: Volume percentage of each tissue classification plotted in the direction of dorso-ventral axis from one patient diagnosed with IPF in left and right lungs over time. The average percentage was calculated within 5% sections along dorso-ventral axis from the back to front. (a) (b) is ground-glass distribution. (c) (d) is reticular distribution. (e) (f) is honeycomb distribution. (g) (h) is emphysema distribution.

Subpleural to internal Figure 4.14 plots the subpleural-to-internal distance percentage of each connected cluster of three fibrosis CT patterns: ground-glass, reticular and honeycomb. The result shows that the subpleural-to-internal percentage of most connected disease clusters are $< 20\%$ for both left and right lungs. That is, the fibrosis is located preferentially within 20% of the distance from. Reticular and ground-glass abnormalities are distributed throughout the center to surface, whereas honeycomb is not observed in the central core of the lungs in these subjects.



(a)



(b)

Figure 4.14: Subpleural-to-internal percentage of connected cluster of disease in IPF left and right lung. (a) Left lung. (b) Right lung.

Lobar distribution Figure 4.15 shows the average volume percentage (across all time points from all patients) of ground-glass, reticular, honeycomb and emphysema in the five lobes (left upper, left lower, right upper, right middle, right lower). From the result, more fibrosis locates in the lower lobes (55.39%, 57.65%, 64.52% for honeycomb, reticular, ground-glass) compared to the other two lobes. For reticular pattern, the percentage in the middle lobe is much lower than the percentage of other lobes. Emphysema predominantly presents in the upper lobes (68.14%) and may also appear in the middle lobe of the right lung. Figure A.29 shows the volume percentage of the four tissue patterns in the five lobes at each time point from an individual patient diagnosed with IPF. As shown in the figures, the lobar distribution of the disease keeps almost the same at different time point, with more fibrosis appearing in lower lobes and emphysema presenting mainly in upper lobes. The lobar distribution over time of other patients can be found in Appendix A.

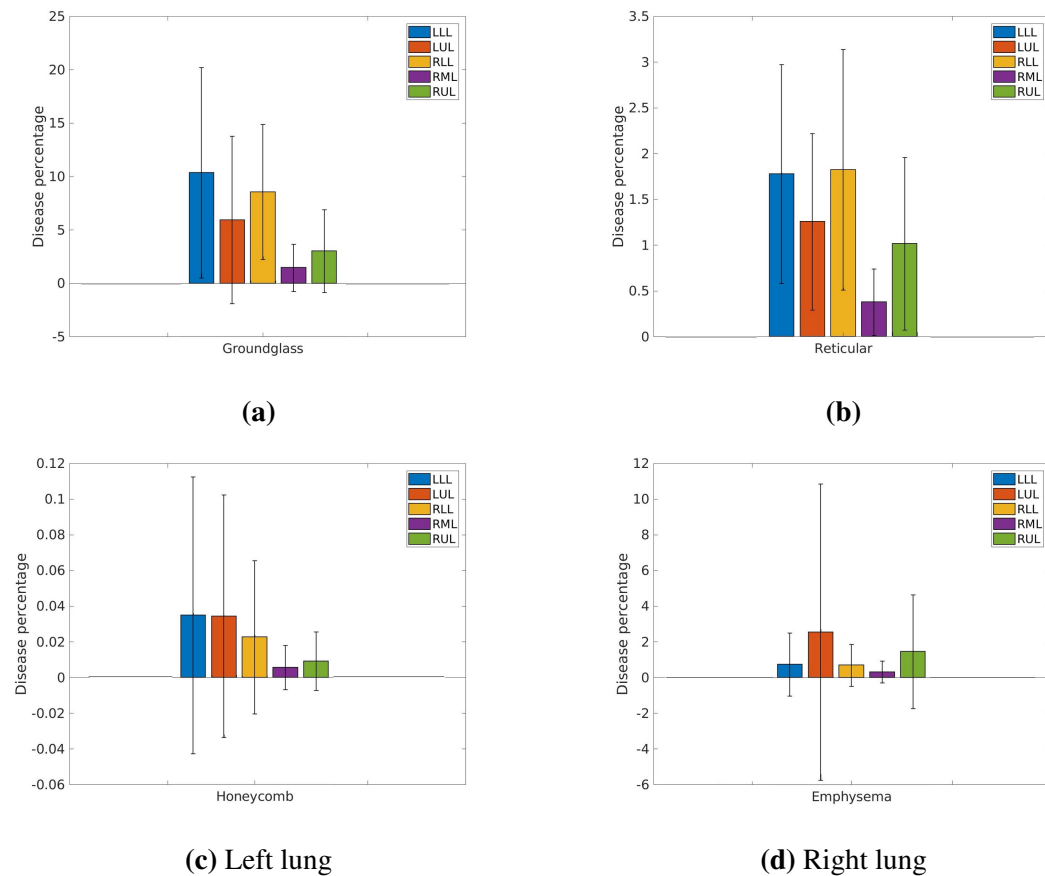


Figure 4.15: Average lobar distribution of disease CT patterns. The tissue percentage in different lobe is shown in different color, and each bar represents the volume percentage of the CT pattern for one lobe across all the subjects. The black line represents the standard deviation. (a) Ground-glass lobar distribution. (b) Reticular lobar distribution. (c) Honeycomb lobar distribution. (d) Emphysema lobar distribution.

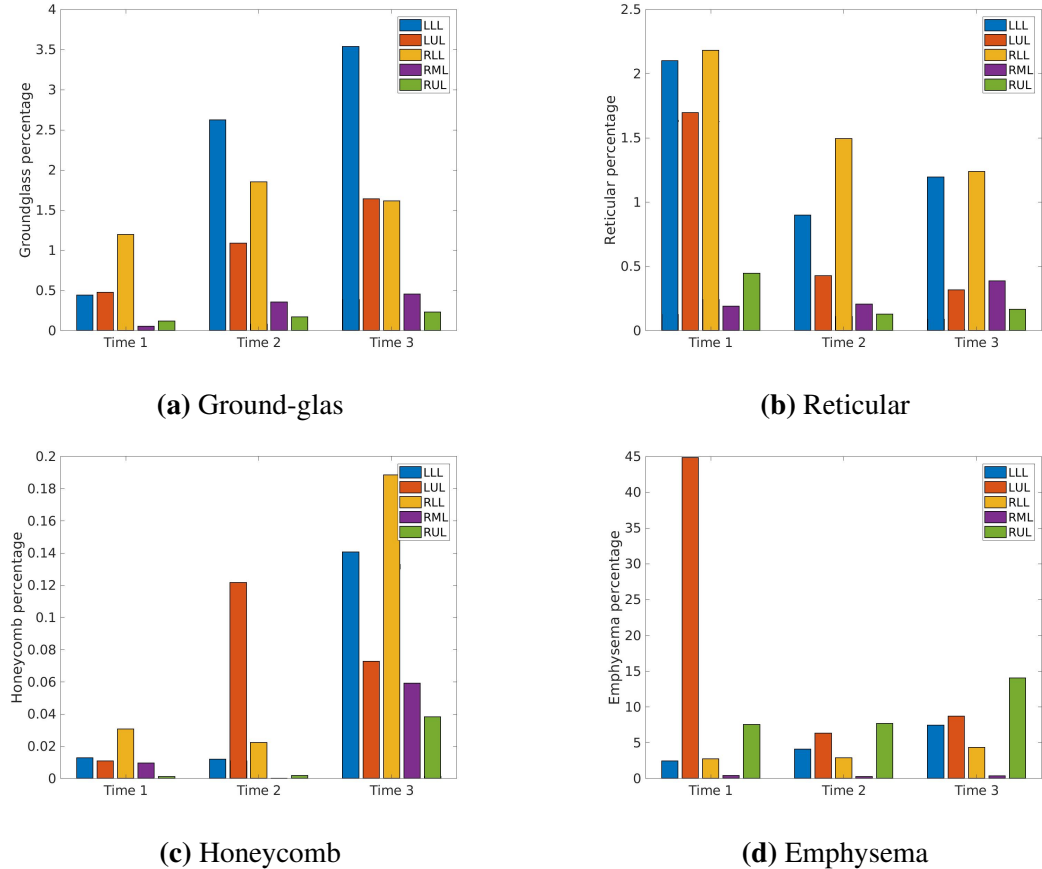


Figure 4.16: Lobar distribution of disease CT patterns of one patient diagnosed with IPF over time. The tissue percentage in different lobe is shown in different color, and each bar represents the volume percentage of the CT pattern for one lobe. (a) Ground-glass lobar distribution. (b) Reticular lobar distribution. (c) Honeycomb lobar distribution. (d) Emphysema lobar distribution.

Change in classification of tissue pattern over time

Table 4.3 and Table 4.4 show the quantitative results for the change in classification of tissue pattern (ground-glass and reticular) of one patient with IPF over time. The change in volume percentage of classified tissue CT patterns between time points is given (from ground-glass or reticular pattern to the other tissue CT patterns). Over 50% of areas initially identified as ground-glass remain the same over time in both left and

right lung, whereas other parts of ground-glass are subsequently classified as reticular or normal tissue as time goes by. As for reticular region, although quite a lot of classified reticular area doesn't change with the development of disease, a large proportion of reticular is recognized as ground-glass in the second and third time point, especially in right lung (more than 50% on average).

Interestingly, from the result, some disease area may even classified back to normal tissue as time goes by, although a decline in lung function can be observed during this period. Around 10%-30% of reticular and ground-glass areas are identified back to normal region during this time. However, that shouldn't happen in the real lung of IPF patient, which may be explained by the two following reasons: 1. The error caused by the lung surface fitting and classified data mapping. As introduced in Chapter 3, Section 3.3.2, the average RMS error of the fitting method for 50 subjects was 4.79 mm, and this error was inevitable. The accuracy of the classified data mapping to the mean SSM was partly relied on accuracy of lung surface fitting, as the local coordinate of within the corresponding element was used during the mapping. 2. The error caused by the CALIPER tissue classification. The distribution of abnormalities in IPF lung is mainly patchy, and the regions of fibrosis and emphysema are usually not large connected areas. Figure 4.17 shows the CALIPER tissue classification overlapping on raw image. As shown in Figure 4.17, different tissue patterns in most of the lung region are mixed and interlaced, which increase the difficulty of identifying tissue pattern in these part accurately.

Table 4.3: Change in classification of tissue CT pattern over time of left lung from one subject diagnosed with IPF (subject 6 with three time points) (%).

		Ground-glass	Mild-LAA	Moderate-LAA	Normal	Reticular	Honeycomb	Severe-LAA
Time1 - Time2	Ground-glass	53.65	0.36	0	37.31	8.65	0	0.03
	Reticular	29.76	3.01	0	28.41	38.82	0	0
Time2 - Time3	Ground-glass	71.61	0.13	0.03	15.41	12.82	0	0
	Reticular	39.94	0.83	0	16.59	42.56	0.07	0
Time1 - Time3	Ground-glass	70.01	0.83	0	20.80	8.35	0.01	0
	Reticular	37.97	4.73	0	15.49	41.81	0	0

The time interval from time point 1 to time point 2 is 15 months, the time interval from time point 1 to time point 2 is 5 months, the time interval from time point 1 to time point 3 is 20 months.

Table 4.4: Change in classification of tissue CT pattern over time of right lung from one subject (subject 6 with three time points) diagnosed with IPF (%).

		Ground-glass	Mild-LAA	Moderate-LAA	Normal	Reticular	Honeycomb	Severe-LAA
Time1 - Time2	Ground-glass	61.76	4.15	0.92	7.14	25.92	0	0.11
	Reticular	47.61	6.88	0.01	11.10	34.37	0	0.03
Time2 - Time3	Ground-glass	78.16	0.08	0.01	18.51	3.23	0	0.05
	Reticular	55.74	0.44	0	31.46	12.35	0.01	0
Time1 - Time3	Ground-glass	79.98	1.82	1.63	12.82	3.45	0	0.30
	Reticular	65.80	3.28	0.02	19.40	11.33	0	0.16

The time interval from time point 1 to time point 2 is 15 months, the time interval from time point 1 to time point 2 is 5 months, the time interval from time point 1 to time point 3 is 20 months.

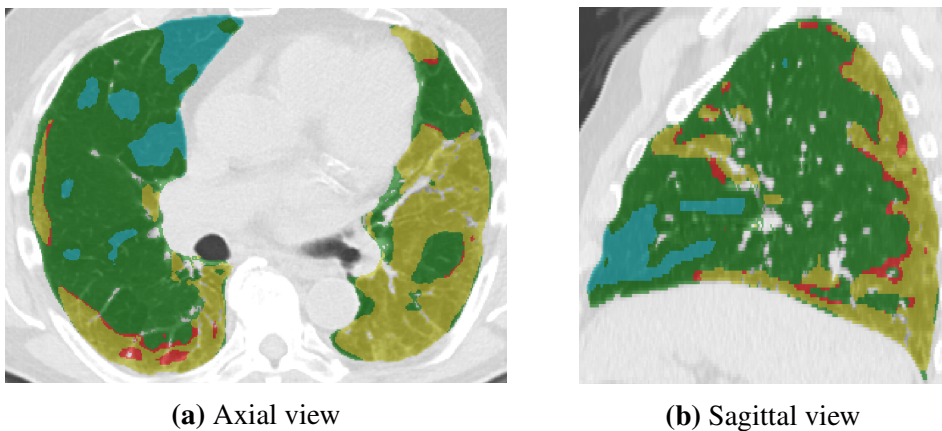


Figure 4.17: CALIPER tissue classification overlapping on raw image. Green is the normal region, red is the reticular region, yellow is the ground-glass region, and blue is the mildLAA region. (a) Axial view. (b) Sagittal view.

4.3.3 Volume analysis of IPF lungs

The change of whole lung volume over time

Table 4.5 shows the whole volume of left and right lung of three subjects for each time point. It can be seen that although the lung volumes of most IPF patients decrease over time, some subjects experience an increase in lung volume as time goes by interestingly.

Lobe volume difference between old normal lungs and IPF lungs

The average lobe volume proportion among IPF subjects and among old normal subjects (the control group) were shown in Table 4.6 (the first two columns). It can be seen that the IPF group has a lower average volume proportion for left lower lobe and right lower lobe compared to the value of the control group. That may probably be caused by the increase in stiffness of lower lobe in IPF lungs, which relates to the basal appearance of fibrosis.

Table 4.5: Whole volume of left and right lung for each time point($1.0e5 * mm^3$).

Sub No.	Time point	Scan time	Left lung	Right lung
IPF2	Time point1	0 month	1.39	2.04
	Time point2	15 month	1.88	2.72
	Time point3	35 month	1.83	2.68
IPF3	Time point1	0 month	1.55	2.34
	Time point2	11 month	1.38	2.11
	Time point3	30 month	1.28	2.05
IPF5	Time point1	0 month	1.73	1.49
	Time point2	12 month	1.58	1.31
	Time point3	23 month	1.67	1.43
IPF6	Time point1	0 month	2.41	3.47
	Time point2	15 month	2.13	3.01
	Time point3	20 month	2.06	3.09
IPF9	Time point1	0 month	1.35	1.49
	Time point2	7 month	1.22	1.43
	Time point3	20 month	1.23	1.53
IPF10	Time point1	0 month	1.34	1.66
	Time point2	14 month	1.01	1.25
IPF13	Time point1	0 month	1.94	1.58
	Time point2	16 month	1.85	2.40
IPF14	Time point1	0 month	2.45	2.74
	Time point2	46 month	2.16	2.33
IPF15	Time point1	0 month	3.72	3.37
	Time point2	13 month	2.86	3.38
	Time point3	76 month	3.04	3.72
IPF21	Time point1	0 month	2.24	2.31
	Time point2	63 month	1.88	1.86
	Time point3	79 month	1.73	1.85

The difference in lobe volume proportions between IPF subjects and the control group were compared statistically using t-test. Table 4.6 (the third column) shows the p values of the five lobes between the two groups. The result show a significant difference in the volume proportion for both right lower lobe and right middle lobe between IPF subjects and the controls ($p < 0.001$).

Table 4.6: Lobe volume comparison between IPF subjects and older normal subjects.

Lobe	IPF	Older normal	P-value
Left lower lobe	0.205	0.211	0.532
Left upper lobe	0.251	0.242	0.352
Right lower lobe	0.210	0.254	$\ll 0.001$
Right middle lobe	0.119	0.087	$\ll 0.001$
Right upper lobe	0.214	0.207	0.559

4.3.4 SSM based shape analysis of IPF lungs

Shape difference between IPF lungs and old normal lungs

Figure 4.18 shows the weight value distribution of the first three modes for IPF and the controls.

The results show that there is a significant difference of the first mode weight between IPF and controls ($p \ll 0.001$). However, for mode 2 and mode 3, no significant shape difference was observed between the two groups ($p = 0.017$ and $p = 0.641$, respectively). Figure 4.19 illustrates overall shape variation of the first mode with added different values of standard deviation to the mean shape model. The first shape mode accounts for over 20% of the entire shape variation in old normal lungs. It is demonstrated from Figure 4.19 that the first mode relates to the largest change in the anteroposterior diameter of the lung with a lateromedial tilt towards both apices, and is also associated

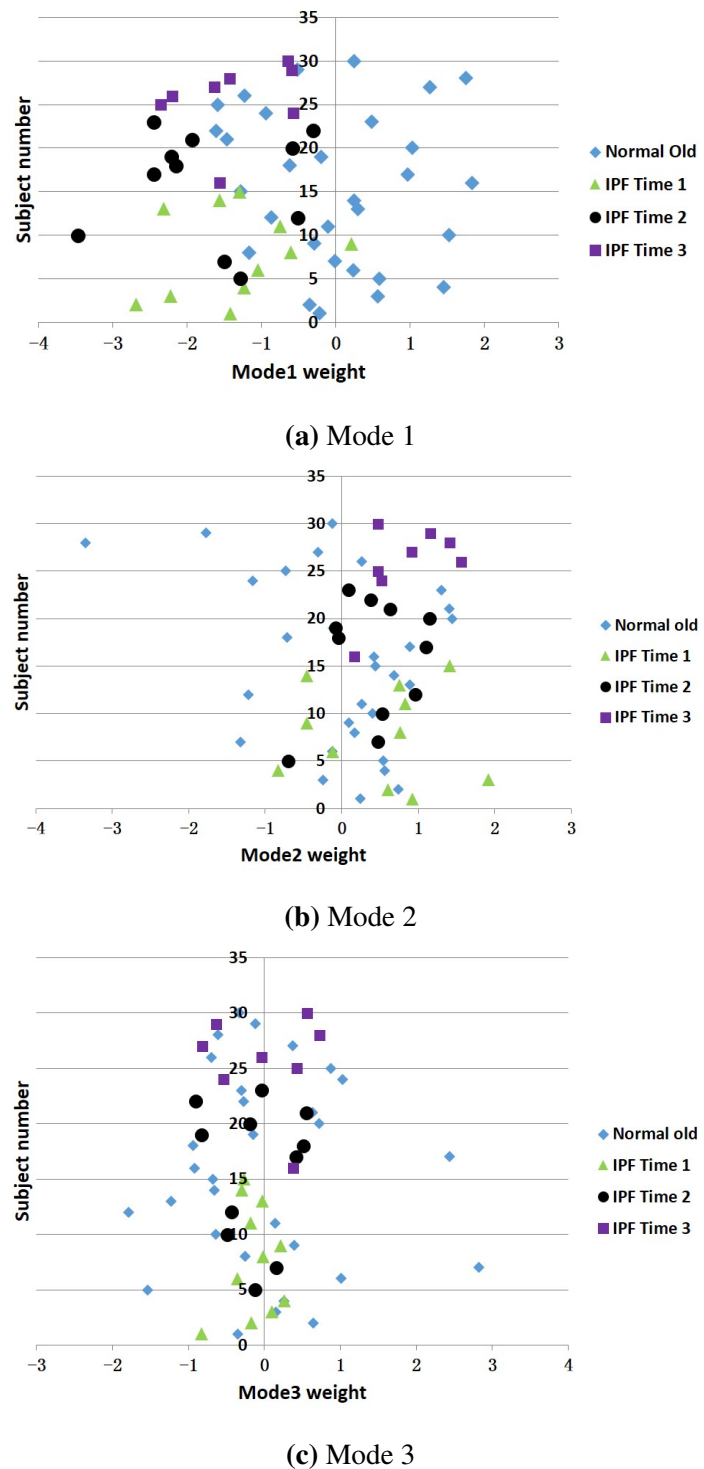


Figure 4.18: Shape differences between IPF subjects and old normal subjects of the first three modes (shown with different time point). (a) Mode 1 weight. (b) Mode 2 weight. (c) Mode 3 weight.

with the ratio of apical to basal diameters. With the positive or negative standard deviation added to the mean shape model, there is a variation in the right anterior edge, the inferior lingular segment of the left superior lobe, the medial basal segment of the right middle lobe, and the left oblique fissure. In addition, there is a shape change in the "roundness" of the lateral surface in both left and right lung, and the variation in the distance of left and right lungs in the apex and base is also observed. As shown in Figure 4.18a and Figure 4.19, the weight values of Mode 1 for IPF subjects are mostly distributed across negative values, where the negative weight corresponds to a larger ratio of anteroposterior diameter to lung height compared to control lungs.

In Figure 4.18, the data of different time point were shown in different colors. As we can see from the figures, the first three modes of lung shape don't illustrate significant difference between different time point (with all the p values > 0.1 between time point 1 and time point 2, time point 1 and time point 3, time point 2 and time point 3). All the three shape modes are not found a regular tendency of change over time.

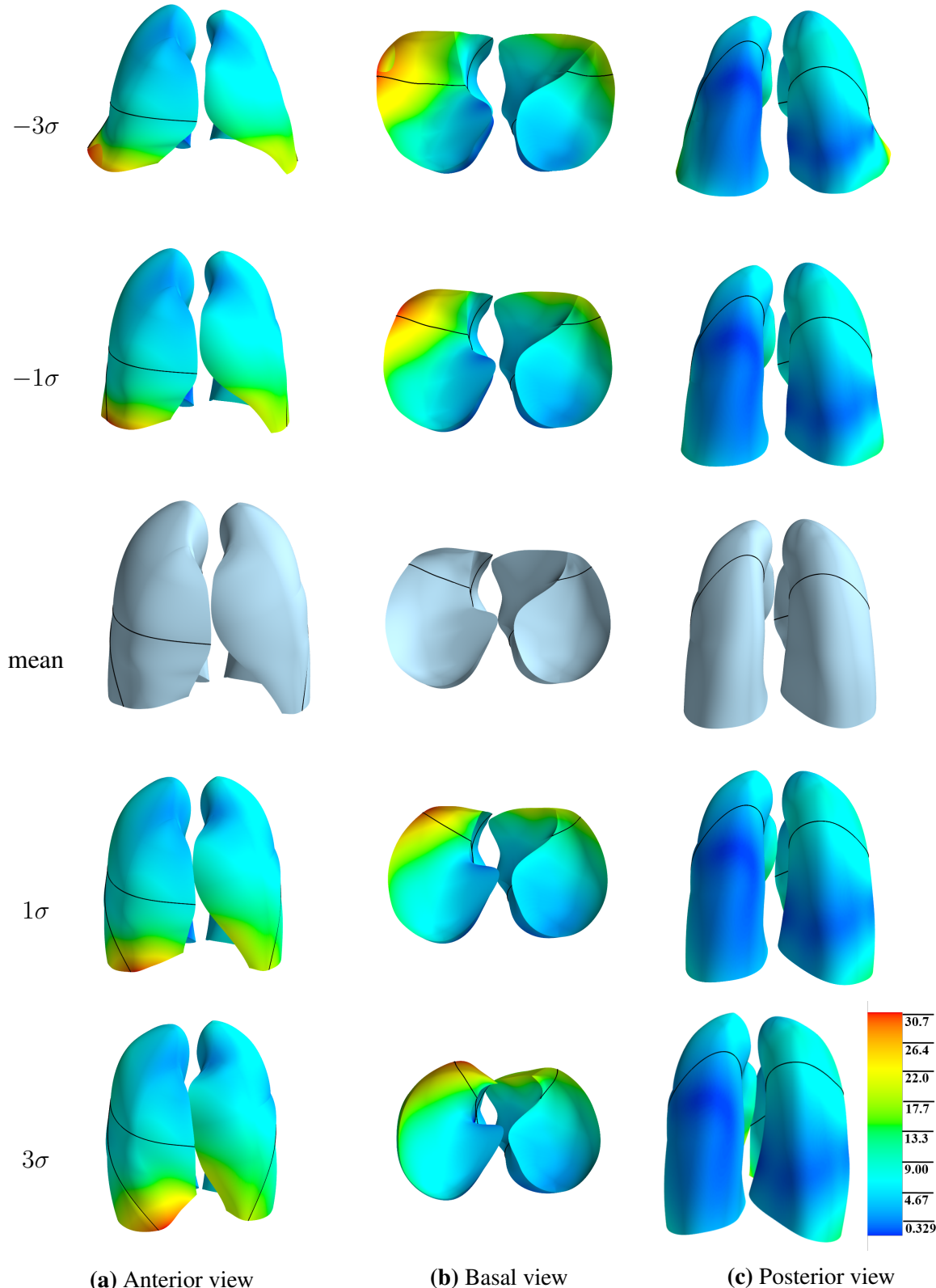


Figure 4.19: PCA-derived shape variation of the first shape mode, with different values of standard deviation (-3σ , -1σ , μ , 1σ , 3σ) added to the mean shape model. (a) Anterior view. (b) Basal view. (c) Posterior view.

Relationship between lung lobe shape and fibrosis and low attenuation area extent

Table 4.7 lists the P values and R from linear regression of the correlation of the first three modes with fibrosis and LAA percentage. Figure 4.20 shows the behavior of the first three modes with respect to overall fibrosis percentage.

From the results, no correlations are found between the three shape modes and LAA extent, and only the first shape mode shows a significant relationship with the percentage of fibrosis ($p < 0.0001$). With the increase of the percentage of fibrosis, the weight value of mode 1 becomes increasingly negative which corresponds to a larger shape difference from the mean control lung shape. Negative weighting of M1 is also associated with increased ratio of anteroposterior diameter to the height of the lung, which makes lung appear 'fatter' and 'shorter'. Therefore in general, the lung shape change in patients with IPF is strongly associated with the fibrosis extent, and the more extensive the fibrosis the lung involves, the more 'abnormal' the lung shape is.

Table 4.7: Results for linear regression of shape mode weighting against extent of fibrosis.

Mode	Fibrosis		LAA	
	P-value	R	P-value	R
Mode 1	$<< 0.001$	0.640	0.168	0.265
Mode 2	0.017	0.710	0.578	0.110
Mode 3	0.170	0.254	0.796	0.047

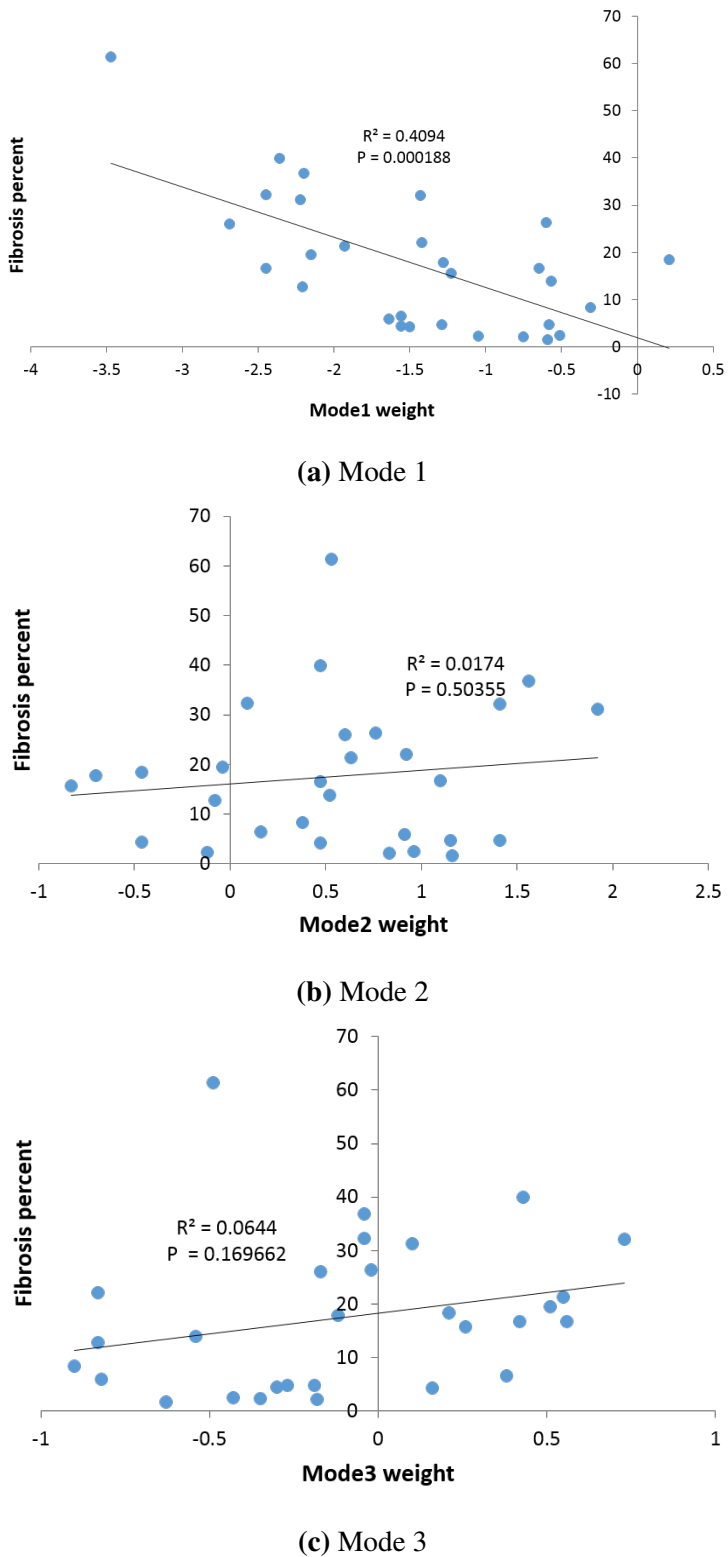


Figure 4.20: The Linear regression of the PCA-derived first three modes with respect to overall fibrosis percentage. (a) Mode 1 weight. (b) Mode 2 weight. (c) Mode 3 weight.

4.4 Discussion

Individualized treatment strategies are urgently needed in clinical applications and are the ultimate goal of modern pulmonary medicine. A quantitative analysis of IPF based on HRCT images has the potential to build a reliable relationship between imaging tissue-level biomarkers and clinical endpoints. As shown here, tissue density, tissue volume, spatial distribution of abnormalities, and lung shape are all important indexes for representing a statistical progression of IPF disease. Through quantifying these features instead of qualitative evaluation, subjective errors could be avoided to offer a more consistent assessment of individual patients.

Average statistical shape model provides a consistent measurement to quantify disease among different people and over the whole clinical course

IPF is a progressive lung disease that has significant variable expression between different patients. The SSM based quantitative method used here normalized a set of lungs of different shapes into a standard shape model, thus providing a convenient way to make a reliable comparison between different patients or within one patient at different time points. This method makes it possible to capture the disease variation across a population and describe the difference using objective indexes. Furthermore, the progression of disease over time can be analyzed. The goal is that this contributes to helping clinical course of disease.

It is widely acknowledged that there should be some typical symptoms occurring on average 1-2 years before a definite clinical diagnosis with IPF, and some radiographic evidence of IPF may even be found before symptoms occur (Raghu et al., 2011; Devaraj, 2014). Understanding this 'subclinical' period of disease is very important for

developing an early diagnosis of IPF disease. The SSM based method makes it possible to compare the IPF lung with a normal cohort. Through combining the disease progression of successive time points with the difference compared to old normal lungs, we can get a whole prediction of disease prognosis in IPF lungs from normal state to severe injured state. It is helpful for clinician to recognize abnormalities in a 'normal' lung at subclinical stage, and is also a further goal of our research in the next stage.

The shape of basal part of IPF lung is significantly different from old normal lung and correlates with fibrosis extent

The first shape mode of the SSM is significantly different between IPF and normal, and strongly correlates with the percentage of fibrosis. The first shape mode corresponds mainly to the anteroposterior diameter of the lung which results in a variation of diaphragm location. This shape change of the diaphragm can be explained by the spatial distribution of tissue abnormalities. The basal and peripheral location of disease is very likely to increase the stiffness of the lower part of the lung, thus having an impact on the movement of the diaphragm when breathing. Furthermore, fibrosis extent in IPF is found to be related to the ratio of anteroposterior diameter to the height of lung. A larger proportion of fibrosis is usually correlated with a larger ratio of anteroposterior diameter to the height of lung. This "compression effect" on the lung shape may be associated with the reduction in tissue compliance caused by fibrosis. Specifically, since the IPF subject and control imaging used in this chapter were all acquired at the end of inspiration, the lower tissue compliance caused by fibrosis will influence the expansion of the lung during inhalation if inhalation is driven by a normal muscle pressure, and therefore this may have an effect on the lung shape. In addition, it is demonstrated in the lobe volume analysis that the IPF lung has a lower average volume proportion for

the left lower lobe and left upper lobe, which may be also caused by the "compression effect" of the lower lobe in IPF lungs.

The quantification of combined IPF and emphysema is the difficulty and emphasis in the future work

Combined IPF and emphysema (CPFE) has been recognised and defined over the past ten years (Cottin et al., 2005; Meltzer and Noble, 2008). Some researchers suggest that CPFE should be regarded as a distinct clinical entity other than emphysema or IPF alone, since it has a characteristic pulmonary function feature different from pure emphysema or IPF. It is commonly believed that CPFE is strongly associated with heavy smokers, severe dyspnea on exertion, and impaired gas exchange. Emphysema usually appears in the upper lobe whereas IPF disease tends to appear in the lower lobes (Lin and Jiang, 2015) which is consistent with the result of our analysis. However, whether the presence of the two diseases developing in parallel is still unknown (Cottin et al., 2005; King Jr et al., 2011; Lin and Jiang, 2015). In the future work, the image based analysis result will be used as quantitative indexes in a lung functional modeling, which could help understand the relationship between the two diseases and the impact of emphysema on IPF.

4.5 Summary

In this chapter, we analyzed and characterized IPF classified tissue over time using quantitative methods. The result shows that fibrosis had higher tissue density compared with normal tissue, and presented predominantly basally and peripherally. In contrast, emphysema had lower tissue density and mostly located in upper lobes. The first principal

SSM mode ($> 20\%$ of the shape variation in normal lungs) was significantly different between IPF and normal and strongly correlated with fibrosis extent in IPF lungs. This quantitative analysis provides consistent potential tissue-level markers which will be used to guide the computational modeling of IPF lungs in the next chapter.

Chapter 5

Functional modeling of idiopathic pulmonary fibrosis

In Chapter 4, HRCT based quantitative analysis and shape analysis methoda were developed to provide a consistent way of describing the features and progressions of IPF disease. However, it is not clear how - or whether - the spatial distribution of tissue abnormalities in IPF (including classifications of tissue type) correlate with lung function and their change over time, and currently, how to translate these imaging and shape biomarkers into functional biomarkers to directly help with the clinical diagnosis and treatment is still a challenging work. For the patient with IPF, V/Q mismatching and hypoxemia are frequent occurrences. Computational modeling provides a reliable way to simulate how these quantitative indexes contribute to the decline of lung function, therefore build a relationship between image-based biomarkers and functional presentations. This chapter outlines the functional modeling of IPF. The quantitative tissue-level and shape-level features combined with pulmonary functional test (PFT) were used to guide a patient-specific computational modeling of lung function of IPF. The lung function of

old normal people was modeled as well for comparison. This work aims to integrate data from volumetric imaging, PFTs, and computational models for lung function, to understand differences between IPF and normal older lungs. The lung function of IPF has been described in Chapter 2, and the respiratory function in older people will be introduced in Section 5.1.

5.1 Respiratory function in older people

The respiratory system of human keeps developing during the whole life, with the high-point of pulmonary function achieved before 30 years old (Janssens et al., 1999; Sprung et al., 2006). For most people, respiratory performance begins to gradually decline after reaching the maximal status. The ability of the lung to deliver oxygen to tissues decreases by four times from age 20 to age 70 in healthy people (Smith, 1986; Zaugg and Lucchinetti, 2000). Even in older athletes who experience vigorous endurance exercise and have better aerobic ability, the functional capability of lung will progressively deteriorate over time (Mittman et al., 1965; Pollock et al., 1997; McClaran et al., 1995).

The aging-related changes in respiratory physiology are usually associated with structural alterations in both lungs, dilatation of alveoli, enlargement of airspaces, decrease in exchange surface area, and increased residual volume (RV) and functional residual capacity (FRC) (Sprung et al., 2006; Lalley, 2013). There is a reduction in chest wall compliance and the static elastic recoil of the lung, which will lead to static air-trapping, decrease in vital capacity (VC), decrease in expiratory flows and increasing work of breathing compared with younger individuals (Sprung et al., 2006). The strength of respiratory muscles decreases with age, and this is strongly correlated with nutritional status (lean body mass, body weight) and cardiac index (Janssens et al.,

1999). The V/Q ratio heterogeneity tends to diminish results from a closing of dependent airways, and carbon monoxide transfer capability also decreases which is associated with the reduced alveolar surface. Interestingly, despite of these changes, gas exchange almost maintains normal both at rest and during exertion, with only a slight reduction in arterial oxygen tension, but no significant change in arterial carbon dioxide tension (Janssens et al., 1999). These age-associated changes are summarized and described in detail in Table 5.1.

5.1.1 Aging-associated alterations in chest wall and respiratory muscle function

Several morphological changes occur in chest wall and diaphragm in older people that reduce the capability and efficiency of respiratory system. One of the most important changes is the progressive decline in chest wall compliance, which relates to the decrease of cross sectional areas of intercostal muscles, calcification of costal cartilage and rib-vertebral articulations, and narrowing of intervertebral disk spaces (Murray, 1986; Crapo, 1993). The structural changes in chest wall has been found to be associated with the reduction in the curvature of diaphragm and maximal transdiaphragmatic pressure, however the thickness of the diaphragm seems not change significantly with older adults (Zaugg and Lucchinetti, 2000; Sprung et al., 2006). It is noted that the age-associated osteoporosis results in a shape change of the thorax geometry, that is an increase in dorsal kyphosis and anteroposterior chest diameter (Janssens et al., 1999; Sprung et al., 2006).

The reduction in respiratory muscle strength caused by the age-related decrease of maximal static inspiratory and expiratory pressures will lead to lower efficiency of res-

Table 5.1: Age-associated changes in respiratory function and their relationships to clinical presentations (Reproduced from (Sprung et al., 2006; Lalley, 2013))

Measurements	Changes, ≥ 60 yrs.	Clinical presentations
Static lung volumes		
- TLC	Unchanged	
- FRC	Increase	
- IRV	Modest increase	
- ERV	Increase	
- TV	Modest increase	
- VC	Decrease	
- IC	Increase	
- RV	Increase	Impaired gas exchange
Dynamic lung volumes		
- FVC	Decrease	
- FEV_1	Decrease	
- FEV_1/FVC	Decrease	
- Peak expiratory flow	Decrease	
Resistance and compliance		
- Respiratory system resistance	Increase	
- Small airways closure	Increase	Impaired gas exchange
- Chest wall compliance	Decrease	Increase in work of breathing
- Lung compliance	Increase	Decrease in ventilatory response to exercise
Respiratory (muscle) pressures		
- Mean pleural pressure	Unchanged	
- Respiratory muscle strength	Increase	
Gas transfer		
- Ventilation-perfusion mismatch	Increase	Impaired gas exchange
Altered control of breathing		
- Responsiveness to imposed respiratory loads	Decrease	Hypoventilation
- Responsiveness to hypoxemia and hypercarbia	Decrease	Hypoxemia and hypercarbia
- Sensitivity to anesthetic agents and opioids	Increase	Respiratory failure in early postoperative period

TLC: total lung capacity; FRC: functional residual capacity; IRV: inspiratory reserve volume; ERV: expiratory reserve volume; TV: tidal volume; VC: vital capacity; IC: inspiratory capacity; RV: Residual volume; FVC: forced vital capacity; FEV_1 : forced expiratory volume in 1 s; FEV_1/FVC : the ratio of the forced expiratory volume in the first one second to the forced vital capacity of the lungs.

piratory muscle activity (Wijesinghe and Dow, 2005; Sprung et al., 2006; Lalley, 2013). It has been proved that the reduced respiratory muscle strength is associated with the deficient nutritional status in older people, and a strong relationship was found between maximal inspiratory/expiratory pressure and lean body mass (Arora and Rochester, 1982; Janssens et al., 1999). Meanwhile, some study has shown that the electromyographic signal produced by twitch stimulation decreases by around 50% in the 70-year-old people (average 73) compared with young subjects, and this reduction is attributed to the loss of type II fast-twitch muscle fibres (Larsson, 1983).

5.1.2 Aging-associated alterations in pulmonary mechanics and lung volumes

Although the chest wall becomes stiffer in older people, their lung parenchyma actually become more compliant (Mittman et al., 1965; Turner et al., 1968; Zaugg and Lucchinetti, 2000). The elastic recoil pressure of lung tissue gradually reduces by aging, with a decrease rate around 0.1 to 0.2 cmH_2O on average every year (Turner et al., 1968), and this reduction is attributed to the alterations in the spatial distribution of the elastic fibre network (Sprung et al., 2006). In older people, it can be observed that the static pressure-volume curve of the lung was shifted to the left, in contrast, the pressure-volume curve of the thorax was shifted to the right (Zaugg and Lucchinetti, 2000; Sprung et al., 2006).

The tidal volume experiences a slight decrease by aging, whereas the respiratory rate gradually increases (Sprung et al., 2006). As mentioned in Section 5.1.1, the chest wall becomes stiffer by aging, while the lung tissues become more compliant. These changes will lead to an increase in RV and a decrease in VC (Lalley, 2013). Some

research indicates that RV volume will increase by approximate 50% from 20-year-old to 70-year-old averagely, and VC will drop to around 75% of the peak value during this period, with a decrease of 20 to 30 ml per year (Janssens et al., 1999; Sprung et al., 2006). The TLC, which is the air volume in the lungs with a maximum respiratory effort, remains unchanged with age, as the effect of the decreased inward elastic recoil of the lung is offset by the reduction in the outward elastic recoil of the chest wall (Sprung et al., 2006). However, the FRC increases by 1 to 3% per decade, since the rate of decrease in lung recoil exceeds the rate of decrease in chest wall (Janssens et al., 1999; Lalley, 2013). Forced vital capacity (FVC) and forced expiratory volume in one second (FEV₁) have been demonstrated to decrease progressively with aging in both men and women (Knudson et al., 1976), but the volume reduces more rapidly in males than in females (Crapo, 1993). FEV₁ decrease by 20 ml approximately per year in subjects aged 25 to 29 years, but for people more than 65 years old, the average annual rate of reduction is dramatically up to 38 ml (Brandstetter and Kazemi, 1983).

5.1.3 Aging-associated alterations in gas exchange

The inhomogeneity of, or mismatch behavior of ventilation and perfusion increases with age, especially in gravitational dependent regions of the lung where intrapleural pressure becomes higher and the lung tissues become less elastic to keep small airways open (Holland et al., 1968; Paoletti et al., 1985; Lalley, 2013). The increased ventilation-perfusion heterogeneity results in a reduction in P_aO_2 , with a progressive drop from approximate 95 mmHg at 20 years to about 75 mmHg at 70 years. However, $PaCO_2$ remains almost unchanged with increasing age, although PaO_2 declines (Wahba, 1983; Sprung et al., 2006). This can be probably explained by the decreased

rate of basal metabolism and the higher diffusive capability of CO_2 across the alveolar-capillary membrane (Levitzky, 1984). Pulmonary perfusion can also reduce with age in some regions where are well ventilated but not fully perfused, and this alteration is associated with the reduced cardiac output (Levitzky, 1984; Lalley, 2013). The alveolar-arterial pressure difference for oxygen ($P_{A-a}O_2$) increases by aging due to the increased heterogeneity of V/Q, and is probably also related to the increase in closing volume during breathing (Janssens et al., 1999). It can be observed that the arterial oxygen tension reduces at a rate of approximately 5 mm Hg per decade from the age of 20 years, and the increasing alveolar-arterial oxygen gradient and the decreased arterial oxygen tension are expected to be the main reason of the impaired arterial oxygenation in elder people (Smith, 1986; Zaugg and Lucchinetti, 2000). Additionally, the diffusing capacity of the lungs for carbon monoxide (DLCO) decreases with aging (Guenard and Marthan, 1996), with about $0.3 \text{ mL}\cdot\text{min}^{-1}\text{mmHg}^{-1}$ and $0.2 \text{ mL}\cdot\text{min}^{-1}\text{mmHg}^{-1}$ for men and women, respectively (Murray, 1986). The reduction is more significant after 40 yrs of age, and the increased mismatch in V/Q, a decline in the alveolar surface area (Verbeken et al., 1992; Thurlbeck and Angus, 1975), the decreased density of lung capillaries (Butler and Kleinerman, 1970) and the reduction in pulmonary capillary blood volume (Guenard and Marthan, 1996) are all potential factors to cause the impaired diffusion capacity.

5.2 Methods: Patient-specific modeling of IPF lung function

In this section, a patient-specific computational model of lung function is proposed to explore the V/Q matching and the whole lung gas exchange for patient with IPF. In order to make a comparison of lung function between IPF patient and older normal people, for each patient, a subject-specific lung mesh that represents the statistical lung shape of old normal individual with the same age, BMI and pulmonary functional data was predicted using SSM. Anatomically based airway and blood vessel trees were generated derived from HRCT images, respectively matched to IPF lung mesh and the corresponding old normal lung mesh. The ventilation, perfusion and gas exchange models were then constricted to simulate \dot{V} , \dot{Q} distribution and gas transport in normal and disease constricted condition, respectively. During this process, individual's lung parenchymal tissue classification and quantification data was mapped to model of IPF patient, with fibrosis reducing tissue compliance and narrowing vessels. Data from PFTs were used to parameterize the models and set the boundary conditions. The framework of modeling is illustrated in Figure 5.1.

5.2.1 Clinical data

Two patients diagnosed with IPF were selected from the clinical data used in Chapter 4 as representative subjects for functional modeling. Patient 1 is female which has three time points with 12 and 23 month interval, respectively, and patient 2 is a male which has two time points with 46 month interval. The clinical data for each patient includes both HRCT images and PFT results, with less than 3 months between the scan date and

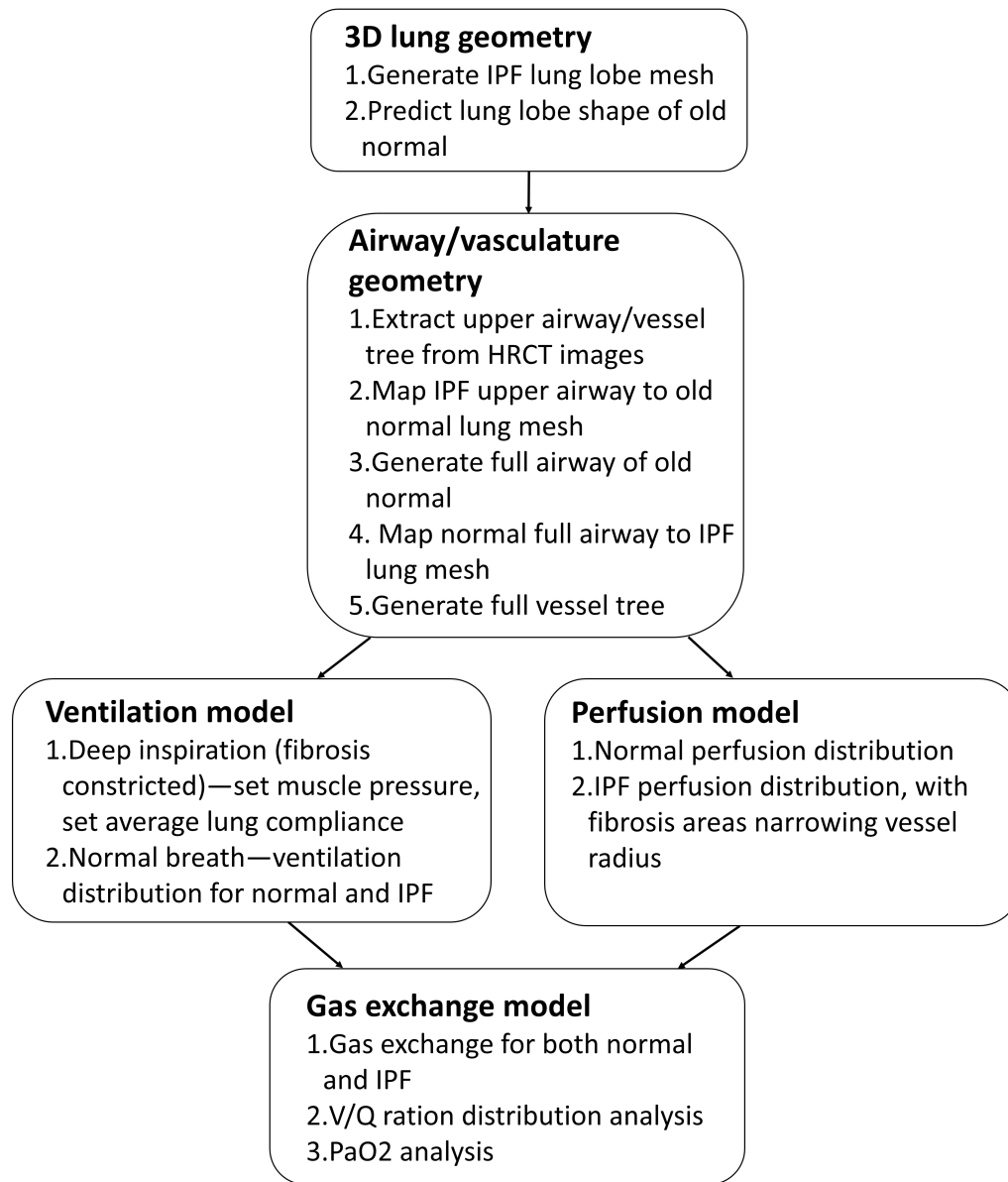


Figure 5.1: Computational modeling framework for IPF and older normal lung function.

the PFT date.

5.2.2 Construction of lung lobe geometry

In Chapter 4, Section 4.3.3 and 4.2.4, we compared the lung lobe shapes and volumes of IPF patients with old normal people. It can be observed that there is a significant difference of lung lobe geometry between IPF and old normal groups, and this alteration in lung shape mainly focuses on the basal part (lower lobe), strongly associated with the distribution of fibrosis in IPF. In order to involve the impact of shape change into the modeling of lung function, SSM of old normal people and patient's individual information were combined to predict an average lung lobe shape of old normal as a control group for each IPF patient. Meanwhile, the lung lobe mesh of each IPF patient was generated using the method introduced in Chapter 3, Section 3.3.2.

Relationship between lung function and lung shape

It is supported by evidence that the age-related changes in lung structures are strongly associated with a series of alterations in respiratory functions (introduced in Section ??). For example, the reduction in chest wall compliance of old people leads to a decrease in VC, while an increased RV in elders usually results in impaired capability of gas exchange which relates to a lower measured DLCO. In a previous study from our research group, the lung structure-function relationships were analyzed through quantifying the correlations of the first three PCA-based mode weights calculated from old normal SSM (introduced in Chapter 3, Section 3.3.3, and Chapter 4, Section 4.2.4) with age, BMI, lung volume and some pulmonary function measurements. For each training subject of SSM, the individual weight scores for each of the first three shape modes which cap-

tures most shape variation were examined. An ordinary least squares regression was applied to test the associations, and P value was used to quantify the strength of each association, with an alpha level of 0.05 considered statistically significant. Analysis result illustrates that Mode 1 has positive relationship with FEV_1 , FEV_1/FVC , Maximal mid-expiratory Flow (FEF25%-75%), BMI and DLCO, while has negative correlation with age, RV and RV/TLC. For Mode 2, only BMI is found a correlation with the shape variation, whereas quite a number of lung volume measurements, including FRC, TLC ,VC and RV show strong relationship with scores of Mode 3.

Shape prediction of old normal lungs

The lung shape prediction of old normal people was developed based on the previous analysis of lung structure-function relationship. Age, BMI, FVC, FEV_1 , FRC, TLC, VC, RV, RV/TLC and DLCO were selected as the individual functional measurements to train the lung shape predictive model, as these parameters show relatively strong correlations with the first three shape modes. The training process of lung shape predictive model is to find optimized equations that can best describe the relationship between the functional measures and the mode weights. For each shape mode, a multivariate regression model was constructed as follows:

$$w_i = \alpha_{0i} + \alpha_{1i}m_1 + \alpha_{2i}m_2 + \dots + \alpha_{ni}m_i + \varepsilon, \quad (5.1)$$

where w_i is the weight score of the i th shape mode, n is the number of functional measures, $\alpha_{0i}, \alpha_{1i}\dots\alpha_{ni}$ are the regression coefficients, in which α_{0i} is the intercept, m_i is the tested value of the i th functional measure, ε is a random error. Here, it is assumed that all the functional measures are independent variables.

Using Equation 5.1, a set of possible regression models can be developed for each shape mode (with different regression coefficients $\alpha_{0i}, \alpha_{1i} \dots \alpha_{ni}$). In order to find the best predictive model from all the possible models, two most common criterions for model selection, Akaike information criterion (AIC) and Bayesian information criterion (BIC), were used to deal with the trade-off between the goodness of fit of the model and the simplicity of the model. Both AIC and BIC are founded on information theory, with calculated by:

$$AIC = 2k - 2\ln L(\theta), \quad (5.2)$$

$$BIC = \ln(n)k - 2\ln L(\theta), \quad (5.3)$$

where k is the number of the estimated parameters (that is functional measures in this study) in the model, $L(\theta)$ is the maximized value of the likelihood function of the model and θ are the parameter values that maximize the likelihood function.

The multivariate regression models with the lowest value of AIC and BIC were selected as the best predictive models, then the models of the first three PCA modes were constructed in the form of Equation 5.1, shown as follows:

$$\begin{aligned} w_1 &= 1.38 + (-0.04 \times Age) + (0.38 \times FVC) + (-0.04 \times DLCO), \\ w_2 &= 3.49 + (-0.16 \times BMI) + 0.02 \times RV/TLC, \\ w_3 &= 4.90 + (-0.02 \times Age) + (-0.45 \times TLC) + (-0.05 \times DLCO), \end{aligned} \quad (5.4)$$

where w_1 , w_2 and w_3 are the weight scores of the first three shape modes. Through

inputting the individual functional measures into the regression models, the weights of first three modes can be calculated. Then the subject-specific predicted shape of old normal lung can be reconstructed with adding linear combination of the first three modes into the average SSM:

$$S_{pred} = S_{mean} + \sum_{i=1}^3 \mathbf{u}_i w_i, \quad (5.5)$$

where S_{mean} is the mean shape of SSM for older normal people, S_{pred} is the subject-specific predicted lung shape.

5.2.3 Construction of airway/vasculature geometry

Subject-specific conducting airway trees and pulmonary vasculature trees were constructed in both IPF and predicted old normal lung mesh. The geometry of pulmonary airway and vasculature are representative of the important structural features of the pulmonary circulation, therefore are the basis on which the following anatomically based functional models can develop. In this section, airway/vasculature trees were firstly generated with filling 1-D finite element branches in the predicted old normal lung mesh, then were deformed to the shape of IPF lung mesh which presents a compression effect in the lower lobes in our previous analysis. The airway/vasculature diameters were assigned to each branch as a postprocessing step specific to IPF and old normal geometry respectively. Using this way, the branches of IPF and old normal airway/vasculature will be kept in the same geometric connectivity and same lobar distribution, but with different radius and length.

Airway tree

In order to generate airway tree in the lung shape, the bi-cubic Hermite finite element mesh of lung surface was converted to a tri-cubic Hermite volumetric mesh which has been introduced in Chapter 4, Section 4.2.1. An anatomical based structure of the bronchial airways (from trachea to terminal bronchioles) was generated using the methods developed by Tawhai et al, as described in details in Tawhai et al. (2000, 2004). In brief, the centerlines of the largest airways (trachea, left and right pulmonary airway branches of the first 6 generations) were manually segmented from the subject's HRCT images, which provides an incomplete description of the airway tree. Then, the larger airways was used as initial condition to generate the branches down to the level of the terminal bronchioles (smaller airways) within the subject's lung mesh using a volume-filling branching algorithm. The steps to generate patient-specific airways in IPF and old normal lungs were summarized as follows:

1. 1-D finite element mesh of the centerlines of IPF larger airways were created manually from HRCT raw images of IPF patient (shown in Figure 5.2a).
2. The 1-D tree of central airways obtained above was mapped to the volumetric mesh of old normal lung. The nodal positions inside the mesh were mapped through calculating the local coordination ξ_i with respect to its element (details in Chapter 4, Section 4.2.1). The branches outside the mesh were then scaled to match the target lung volume, followed by a manual adjustment. The element connectivity remains the same during mapping.
3. The mapped larger airway in step 2 was used as a starting geometry for generating a full airway tree by volume-filling branching algorithm (Tawhai et al., 2000, 2004), to fill the lung-shaped of old normal volumetric mesh. Briefly, uniformed spaced grid seed

points were created within the 3D volumetric lung mesh. The number of seed points is around 32000 (45% for left lung and %55 for right lung) which equals to the number of pulmonary density of acinar units in the lung (Haefeli-Bleuer and Weibel, 1988). The branching algorithm was designed to generate a branching structure recursively towards the center of mass of seed point units, until each seed point was assigned a terminal bronchiole (shown in Figure 5.2b).

4. The generated linear mesh of full airway tree in step 3 was mapped back to the volumetric lung mesh of IPF patient using the same method in step 2.

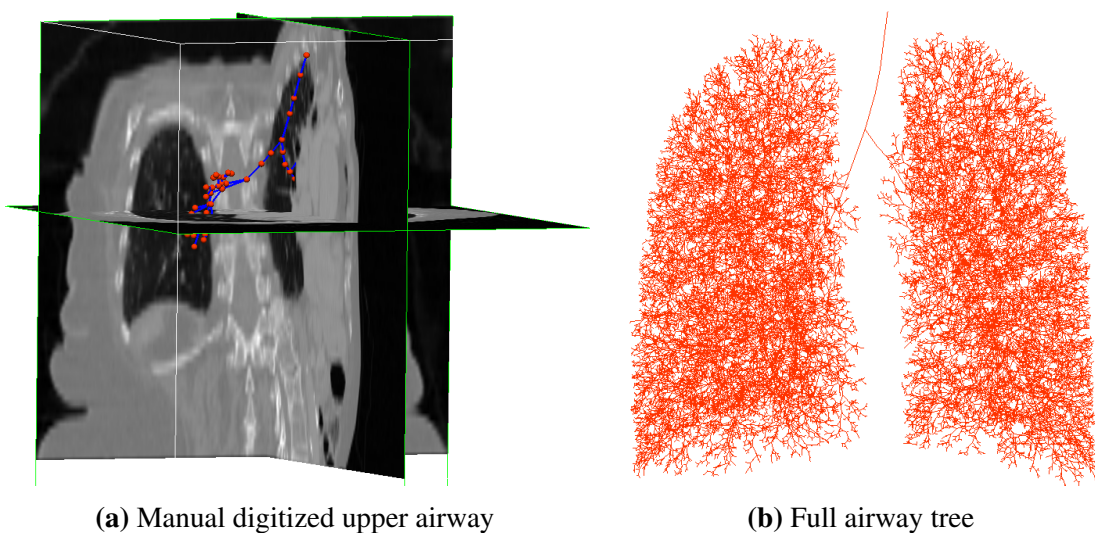


Figure 5.2: Generation of airway tree. (a) Manual digitized upper airway tree from HRCT images in 3D. Blue lines are the centerlines of upper airway tree, and red points represent airway nodes. (b) Geometry of full conducting airway tree generated using volume-filling algorithm. The model is shown from the anterior view, with the left lung on right, and right lung on left.

In the next stage, the diameters of airway branches were calculated for both IPF and old normal geometry, the method proceeds as follows:

1. The trachea radius of IPF was measured from segmented HRCT images through averaging the values at the position of 1/4, 1/2 and 3/4 along the centerline of the trachea,

with treating trachea as a circular cross-section.

2. Radius of the terminal branch of IPF was assumed to be constricted based on a found that 70% of the IPF patients occur narrowed airways (Crystal et al., 1976). The radius of narrowed terminal branch was calculated by:

$$RdT_{IPF} = RdT_{normal} \times \sqrt[3]{\frac{FRC_{IPF}}{FRC_{Normal}}}, \quad (5.6)$$

where FRC_{IPF} is the measured FRC volume of IPF patient and FRC_{Normal} is the reference FRC volume of old normal people obtained from PFT report. RdT_{normal} is the terminal bronchiole radius of normal lung, estimated to be around 0.2mm (Horsfield et al., 1976). RdT_{IPF} is the constricted IPF terminal radius.

3. Radius of the other airway branches of IPF were calculated after initializing the trachea radius and Horsfield diameter ratios (R_dH). The R_dH was adjusted during each calculation until the terminal radius RdT_{IPF} can touch the value obtained from step 3. The conducting airway volume of IPF was then acquired by summing up the branch volume from distal to the trachea.

4. It has been proved by evidence that an increase in airway volume occurs in IPF lung, therefore, here the conducting airway volume of old normal lung was predicted using a statistically measured ratio R_{volume} , which represents the ratio of IPF conducting airway volume to the old normal conducting airway volume (Plantier et al., 2016). By setting up the normal terminal radius with 0.2mm and the predicted conducting airway volume, the R_dH and the radius of other branches for old normal airway tree can be specially calculated. During this process, the normal range of trachea radius of the human lung (5mm to 11mm for women, 6.5mm to 12mm for man) was also taken into consideration (Breatnach et al., 1984) by adjusting the volume ratio R_{volume} until

the predicted trachea radius can reach the normal range. R_{volume} was initialized as 34.2/45.3 (normal/IPF) which is the average volume ratio measured among a number of IPF patients and normal people.

Using the above steps, patient-specific pulmonary airway geometry for IPF and old normal lung were constructed.

Vasculature tree

The centrelines of large vessel tree (the first two generations) were manually recognized from HRCT images, represented as 1-D finite element mesh. In this thesis, the pulmonary arterial and venous trees of other generations were assumed to be approximate replicas of the airway tree. Using the airway tree to construct vessel geometry is a reasonable assumption at this level, as the pulmonary arteries generate closely surrounding the airways trees, the airways and blood vessels have similar lengths and orientations, airway and vasculature bifurcate in union from larger branch to bronchiole level, and the veins divide at the midpoint between adjacent airway bifurcations (Weibel, 1984; Hsia et al., 2016). The manual branch of the main vessel plus the finite element of airway tree provided a full pulmonary blood vessel geometry of IPF patient. The vasculature structure of old normal was obtained using the same mapping procedure used for airway which has been described previously. Based on the vasculature model developed by Clark et al (Clark et al., 2010, 2011), intra-acinar arterioles and venules (microcirculatory system) were assumed to be connected at each generation through a "ladder-like" pattern that a capillary bed covers the alveoli at the acinar circulatory "unit".

The unstrained (zero transmural pressure (P_{tm})) radius of main pulmonary artery and vein were assigned based on the patient-specific trachea radius and the data from morphometric studies (Horsfield, 1978; Horsfield and Gordon, 1981; Huang et al., 1996).

The radius of all the other arteries and veins down to the distal level were calculated based on a defined rate of increase in diameter with vessel order, Strahler diameter ratio (R_dS). The value of R_dS for arterial tree and venous tree were specified according to the radius of main artery and vein, and the consistency compared with the values from raw human data (Horsfield, 1978; Horsfield and Gordon, 1981; Huang et al., 1996). The vessel radius for IPF and old normal lung were then calculated, respectively.

5.2.4 Construction of computational models

In this thesis, the computational modeling of lung function integrates previously published models of ventilation (Swan et al., 2012), perfusion (Clark et al., 2010, 2011) and gas exchange (Swan and Tawhai, 2010) to simulate \dot{V} , \dot{Q} distribution and oxygen and carbon dioxide exchange during tidal breathing in the upright posture. The patient-specific geometry of airways and vessels were used as input for these models. A brief introduction of the model components is summarized below, details can be found in the reference papers.

Ventilation model

The ventilation model developed by Swan et al. (2012) was used to predict the time-averaged topological distribution of inhaled air in the upright human lung, governed by local tissue deformation, elastic recoil pressure, airway resistance and acinar compliance. Approximate 32000 acinar units were generated subtending each terminal bronchiole, and worked as an individual compliant compartment. The acinar volume and compliance were initialized at FRC state using the tissue mechanics model developed by Tawhai et al. (2009). The anatomical geometry of airways were embedded in the

model, and its relationship to air flow resistance was included in the model construction. The movement of air into each acinar unit was determined by expansion of the alveolar tissue and airway resistance through a temporally changing pleural pressure.

In this model, the flow through conducting airways was assumed to be Poiseuille flow, which was fully developed and laminar with a correction factor to account for additional energy losses occurred according to the work of Pedley et al. (1970). Additional energy losses caused by flow disturbances were created at the airway bifurcations and involved in the calculation of pressure drop across the junction. A correction term, Z_{Pe} , was used to define the ratio of actual energy dissipation to Poiseuille flow dissipation, then the ratio of actural airway resistance (R_{aw}) to its Poiseuille flow equivalent (R_P) can be calculated by (ignoring kinetic energy changes):

$$Z_{Pe} = \frac{R_{aw}}{R_P} = \frac{K_{Pe}}{4\sqrt{2}} \left(R_e \times \frac{2r}{l} \right)^{0.5}, \quad (5.7)$$

where R_e is the Reynolds number, r and l are the radius and length of the airway, respectively. $R_e = \frac{2Q\rho}{\pi r \mu}$, where ρ and μ are the density ($1.51 \times 10^{-6} g.mm^{-3}$) and viscosity ($1.92 \times 10^{-5} Pa.s$) of air, respectively. K_{Pe} is a constant, set to 1.85. Then, the resistance of each airway branch was calculated as the Poiseuile resistance (R_{aw}) multiplied by the term Z_{Pe} , and the Poiseuille flow through conducting airway can be acquired by the following equation:

$$P_{aw_2} - P_{aw_1} = R_{aw} R_P = Z_{Pe} R_P Q = Z_{Pe} \frac{8l\mu}{\pi r^4} Q, \quad (5.8)$$

where P_{aw_1} , P_{aw_2} are the air pressures at the start and end of airway branch, Q is the air flow through the airway. The air flow into the acinar unit (modeled as a compliant unit subtending terminal bronchiole) was derived by an equation of motion that relates

airway resistance, air flow, tissue compliance and the rate of change of internal and external pressures:

$$P_{aw} = \frac{V_A}{C_A} + R_{aw}Q + I\frac{dQ}{dt} - P_l, \quad (5.9)$$

where P_{aw} , R_{aw} and Q are the pressure, Poiseuille resistance and flow in the terminal bronchiole, V_A and C_A are the volume and compliance of the acinar unit, I is inertance of the unit, and P_l is the local pleural pressure (varied sinusoidally) working to expand the unit and drive air flow through conducting airway to terminal acinus.

Here, we assumed that the rate of change of airflow Q is small enough, therefore the item $I\frac{dQ}{dt}$ in Equation 5.9 can be neglected. A suitable small time interval, $\Delta t = t_n - t_{n-1}$, was defined, and the flow at the end of the time period $Q_n = Q(t_n)$ (Q respect to t) can be calculated as:

$$Q_n = C_A(\nu - \beta) + Q_{n-1} - C_A(\nu - \beta)\exp\left(\frac{-\Delta t}{R_{aw}C_A}\right), \quad (5.10)$$

where $Q_{n-1} = Q(t_{n-1})$ is the flow at the end of the previous time period. $\nu = dP_{aw}/DT$, $\beta = dP_l/dt$ are the change of bronchohole pressure and pleural pressure with respect t . This equation is derived from Equation 5.9, the detailed description can be found in Swan et al. (2012).

Perfusion model

The multi-scale pulmonary perfusion model developed by Clark et al. (2011) was used to simulate a time-averaged distribution of blood flow, capillary blood volume and average red blood cell (RBC) transit time for each acinar unit. The full vasculature structure (including arteries, veins, intra-acinar arterioles and venules, capillaries) generated in

Section 5.2.3 was embedded in this model. Distension of blood vessels and hydrostatic effects were also involved in the model, with arterial and venous diameter and the thickness of the capillary sheet assumed proportional to the transmural pressure (P_{tm}). The intra-acinar (extra-capillary) blood flow was modeled in a symmetric ladder structure which relates the vessel diameter, length and the thickness of capillary sheet.

Similarly to air flow, the flow through pulmonary arteries and veins was predicted using a Poiseuille equation with a term of gravitational effects acting on the vessels, and can be described by:

$$\Delta P = P_{b2} - P_{b1} = \frac{128\mu_b L \dot{Q}}{\pi D^4} + \rho_b L g \cos\theta, \quad (5.11)$$

where P_{b1} and P_{b2} are the blood pressures at the beginning and end of the vessel element, μ_b and ρ_b are the viscosity and density of the blood in the vessel, L and D are the vessel length and radius, \dot{Q} is the volumetric flow rate in the vessel, g is the gravitational acceleration ($9.81 m/s^2$), and θ is the angle between the vessel and the direction of gravity.

The term $\rho_b L g \cos\theta$ in Equation 5.11 represents the gravity effects acting on the vessels. In this model, an arteriole and a venule were joined at each generation by a capillary bed, forming a "ladder-like" structure, to construct the intra-acinar circulation. Therefore, the item $\rho_b L g \cos\theta$ can be negligible if the length of acinar arterioles and venules was assumed to be small enough:

$$\Delta P = \frac{128\mu_b L \dot{Q}}{\pi D^4}, \quad (5.12)$$

The deformation of vessels in the axial and radial directions due to the surrounding lung parenchyma and the tethering force of lung tissues was included in the model

through calculating the axial stretch from tissue deformation. The strained diameter D in Equation 5.12 was assumed a linear relationship with the transmural pressure P_{tm} as:

$$\frac{D}{D_0} = \alpha P_{tm} + 1, \quad (5.13)$$

where D_0 is the unstrained vessel diameter, α is the vessel compliance constant. The tethering pressure acting on the blood vessel in the radial direction was assumed to be equal and opposite to the local tissue elastic recoil pressure (P_e), therefore $P_{tm} \approx P_b - P_e$, where P_b is the average blood pressure across the vessel. Then, the blood flow through a capillary sheet (\dot{Q}) was modelled using the classic sheet flow theory developed by Fung and Sobin (1969):

$$\dot{Q} = \frac{SA}{\mu_c f l_C^2} \int H^3 dP_{tm}, \quad (5.14)$$

where A is the alveolar surface area, S is the proportion of alveolar surface area (A) composed of capillaries, μ_c is the apparent viscosity of blood in the capillaries, f is the numerical friction factor, l_C is the average path length through the capillary network between arteriole and venule. H is the thickness of the capillary sheet which was assumed to be approximately linearly dependent on P_{tm} similar to Equation 5.13:

$$\frac{H}{H_0} = \alpha_C P_{tm} + 1, \quad (5.15)$$

where H_0 is the unstrained sheet thickness. In both Equation 5.13 and Equation 5.15, maximum P_{tm} was assumed up to $32cmH_2O(3.1KPa)$. α_C is the compliance of the capillary sheet, which was assumed to reduce linearly with the increasing of transpulmonary pressure (P_{tp}):

$$\alpha_C(P_{tp}) = a + bP_{tp}, \quad (5.16)$$

where a and b are constants, P_{tp} is assumed to be equal and opposite to P_e . The values of a and b were firstly measured for dogs by Glazier et al. (1969), then scaled for human as $a = 0.165\mu m/cmH_2O$, $b = -2.58\mu m/(cmH_2O)^2$.

Gas exchange model

The ventilation and perfusion distribution predicted by the ventilation and perfusion model described in the previous section were used as inputs in the whole lung model of gas transport and exchange. The ventilation model provided the volume change in each acinar unit during inspiration and expiration. The perfusion model determined the acinar capillary blood volume and average RBC transit time. The modeling was based on the assumption that the acinus was well-mixed whinian a gas exchange unit, and the ventilation and perfusion distribution were time-invariant. Then the rate of O_2 removal from the alveolar air and the rate of CO_2 transferred to the well-mixed alveolar compartment of acinus were determined. The steady-state gas transfer model developed by Kapitan and Hempleman (1986); Swan (2010) was used to predict the partial pressure of oxygen in alveolar (P_AO_2) and in arterial blood (P_aO_2).

An 1-D advection-diffusion equation was applied to model the gas transport through the conducting airway. The secondary flows in radial and circumferential directions were neglected here, thus the gas transport was solved in the axial direction along the airway branch at each time step:

$$\frac{\partial c}{\partial t} + u_x \frac{\partial c}{\partial x} = D \frac{\partial^2 c}{\partial x^2}, \quad (5.17)$$

where c is the gas concentration (O_2 or CO_2), x is the axial coordinate along the airway, $0 \leq x \leq L$ (L is the length of airway), u_x is the axial velocity predicted by the ventilation model through conducting airway, D is the binary gas diffusion coefficient of gas. The advection-diffusion equation 5.17 was solved for each 1-D finite element of airway tree.

The flow at the trachea ($Q(0,t)$) was set as a constant square waveform during a respiratory cycle:

$$Q(0, t) = \begin{cases} 0.16Ls^{-1} & \text{during inspiration} \\ -0.16Ls^{-1} & \text{during expiration} \end{cases} \quad (5.18)$$

During inspiration, a zero flux was applied to the end of each terminal bronchiole as boundary condition. During expiration, the terminal bronchiole concentration ($c(L,t)$) was set to be equal to the mixed acinar concentration (c_A):

$$\frac{dc(L, t)}{dx} = 0 \quad \text{during inspiration}, \quad (5.19)$$

$$c(L, t) = c_A \quad \text{during expiration},$$

where $x = 0$ and $x = L$ represent the location of trachea and terminal bronchioles. The volume change of acinar unit during each time step (dV_A) during respiratory cycle was acquired by:

$$dV_A = Q(0, t)\dot{V}_A\Delta t, \quad (5.20)$$

where \dot{V}_A is the proportional ventilation received for that acinar unit to the total lung ventilation, Δt is the time step. Therefore, the updated acinar volume at the n^{th} time

step can be represented as: $V_{A(n)} = V_{A(n-1)} + dV_A$.

Acinar concentration ($c_{A(n)}$) was updated with the inspired air into the acinar unit during inspiration, and with the gas exchange flux during expiration:

$$C_{A(n)} = \begin{cases} \frac{(c_{A(n-1)}V_{A(n-1)} + n_{insp}) + n_{exch}}{V_{A(n)}} & \text{during inspiration} \\ \frac{(c_{A(n-1)}V_{A(n-1)} + n_{exch})}{V_{A(n)}} & \text{during expiration} \end{cases} \quad (5.21)$$

where $n_{insp} = dV_A c(L, t)$ is the mass of inspired O_2 or CO_2 . $n_{exch} = q_A \Delta t$ is the mass of O_2 or CO_2 exchanged with the capillary blood, where q_A is the gas exchange flux for O_2 or CO_2 .

The exchange of O_2 in an acinar unit was predicted at each time step using the model developed by Ben-Tal (2006); Swan and Tawhai (2010); Swan (2010):

$$\frac{dP_aO_2}{dt} = \frac{T_{tO_2}}{\sigma_{O_2} V_b} \left(1 + \frac{4[Hb]_b}{\sigma_{O_2}} \frac{dS_{O_2}}{dP_aO_2}\right)^{-1} \times (P_AO_2 - P_aO_2), \quad (5.22)$$

where P_aO_2 and P_AO_2 are oxygen partial pressure in alveolar and in arterial blood, respectively. σ_{O_2} is the O_2 diffusion coefficient, V_b is the capillary blood volume, $[Hb]_b$ is the concentration of haemoglobin in blood, S_{O_2} is the slope of the oxyhaemoglobin dissociation curve. T_{tO_2} is the oxygen transfer factor which represents the ability of transferring O_2 from lungs into capillary blood by:

$$T_{tO_2} = \left(\left(\frac{\eta \phi S_A}{\tau_h} \right)^{-1} + (V_b \theta_{O_2})^{-1} \right)^{-1}, \quad (5.23)$$

where S_A is the alveolar air surface area in an acinus available for exchange and is assumed to be equal for all acinus. τ_h is the total membrane thickness, η and ϕ are

constants. θ_{O_2} is the rate of O_2 uptake by the whole blood which is determined by:

$$\theta_{O_2} = \dot{k}_c \sigma_{O_2} (1 - S_{O_2}) k [Hb]_b, \quad (5.24)$$

where \dot{k}_c is the forward reaction velocity for O_2 binding to haemoglobin, k is the capacity of O_2 carrying haemoglobin, S_{O_2} is the oxyhaemoglobin saturation. The details of the calculation of S_{O_2} can be found in Swan and Tawhai (2010); Swan (2010).

The exchange of CO_2 was predicted using a simplified model by describing the bicarbonate (HCO_3^-) hydration-dehydration reaction to produce CO_2 and H_2O . The change rate of arterial partial pressure of CO_2 (P_aCO_2) was determined by the amount of CO_2 for exchanging between capillary blood and alveolar air. The CO_2 formed from hydration-dehydration reaction:

$$\frac{dP_aCO_2}{dt} = \frac{T_{tCO_2}}{\sigma_{CO_2} V_b} (P_A CO_2 - P_a CO_2) - \delta k_u P_b CO_2 + \delta \frac{k_v}{\sigma_{CO_2} K} [H]^+ [HCO_3^-], \quad (5.25)$$

where $P_A CO_2$ is the alveolar partial pressure of CO_2 . k_u is CO_2 hydration constant, k_v is constant of HCO_3^- dehydration velocity constant, and δ is a fitted constant of CO_2 hydration reaction acceleration rate. The CO_2 solubility coefficient σ_{CO_2} describes the capacity of carrying CO_2 , $[HCO_3^-]$ and $[H]^+$ are the bicarbonate and hydrogen ion concentrations respectively. T_{tCO_2} is CO_2 transfer factor which measures the capability to transfer CO_2 from capillary blood to the lungs:

$$T_{tCO_2} = ((20 \times T_{MO_2})^{-1} + (\frac{\ln(2)\sigma_{CO_2}}{t_{\frac{1}{2}RBC}(1/V_p + 1/V_r)})^{-1})^{-1}, \quad (5.26)$$

where $T_{MO_2} = (\frac{\mu\phi S_A}{\tau_h})^{-1}$ is the membrane transfer factor for O_2 which equals to the first

term of Equation 5.23. V_p and V_r are the volumes occupied by RBC and plasma respectively, which determines the RBC transfer factor component. $t_{\frac{1}{2}RBC}$ is the half time of equilibration of CO_2 across the erythrocyte membrane measured from experiment.

Some parameter values used in the ventilation, perfusion and gas exchange models are listed in Table 5.2. More details of the models are introduced in Swan and Tawhai (2010); Swan (2010); Clark et al. (2011); Swan et al. (2012).

Table 5.2: Parameter values and their source used in computational models

Parameter	Description	Value	Source
K_{Pe}	Pedley correction factor	1.85	Pedley et al. (1970)
p	Air density	$1.15 \times 10^{-6} g.mm^3$	Ideal gas law (37C)
μ	Air viscosity	1.92×10^{-6}	Sutherland's formula (37C)
α	Vessel compliance	$1.49 \times 10^{-4} Pa^{-1}$	Krenz and Dawson (2003)
μ_b	Blood viscosity	$3.36 \times 10^{-3} Pa/s$	Pries et al. (1996)
ρ_b	Blood density	$1.05 \times 10^{-6} kg/mm^3$	Pries et al. (1996)
μ_c	Apparent viscosity of blood in capillary bed	$1.92 \times 10^{-3} Pa/s$	Fung (2013)
f	Numerical friction factor	21.6	Fung (2013)
α_c	Compliance of capillary sheet	$1.30 \times 10^{-9} Pa/s$	Fung and Sabin (1969)
l_c	Pathlength from arteriole to venule	$11.86 \times 10^{-6} m$	Clark et al. (2010)
$[Hb]_b$	Haemoglobin concentration in blood	$2.33 mM$	Hall (2015)
S_A	Alveolar surface area of the lung	$130 \times 10^4 cm^2$	Weibel et al. (2005)
η	Krogh's permeation coefficient for O_2	$5.5 \times 10^{-10} cm^2 s^{-1} mmHg^{-1}$	Weibel et al. (1993)
ϕ	Correction factor for surface folds	0.8	Weibel et al. (1993)
τ_h	Harmonic mean thickness of the air-blood barrier	$1.11 \times 10^{-4} cm$	Weibel et al. (1993)
\dot{k}_c	Forward reaction velocity $O_2 - Hb$ binding	$4.4 \times 10^2 mM^{-1} s^{-1}$	Weibel (1997)
σ_{O_2}	O_2 solubility coefficient	$1.4 \times 10^{-3} mM mmHg^{-1}$	Keener and Sneyd (1998)
σ_{CO_2}	CO_2 solubility coefficient	$3.5 \times 10^{-2} mM mmHg^{-1}$	Keener and Sneyd (1998)
$t_{\frac{1}{2}RBC}$	Half-time of equilibration for CO_2 diffusion	0.0001s	Hill et al. (1973)
k_u	CO_2 hydration velocity constant	$0.12 s^{-1}$	Hill et al. (1973)
k_v	HCO_3^- dehydration velocity constant	$89 s^{-1}$	Hill et al. (1973)
δ	CO_2 hydration reaction acceleration rate	$10^{1.9}$	Ben-Tal (2006)

5.2.5 Model solutions

Ventilation, perfusion and gas exchange models were solved in normal condition (using lung and airway geometry of older normal people) and diseased condition (using lung and airway geometry of IPF patient), respectively. Individual classified fibrosis from CALIPER data was projected to its IPF airway/vessel trees as labeled disease regions to drive the patient-specific functional modeling of IPF, with fibrosis reducing tissue compliance and narrowing vessel radius. The subject-specific tidal volume, cardiac output, oxygen consumption (VO_2) and carbon dioxide consumption (VCO_2) were estimated based on patient's individual information. Data from PFT result were used as boundary conditions to control the simulation.

Disease region labeling

The different tissue patterns classified by CALIPER were mapped to the individual airway/vessel trees of each subject. For each airway/vessel node, the corresponding tissue pattern it belonged to (surrounded by) was extracted (through finding its closest tissue pattern), so that each terminal node can be labeled as different tissue patterns with an index number. In the meantime, the percentage distribution of each tissue pattern against gravitational height (cranio-caudal axis) quantified in Chapter 4 was also used in the labeling, which means if the initial labeled number of disease nodes can't reach the cranio-caudal percentage, additional disease regions will be added in until the cranio-caudal distribution of disease can match the CALIPER classified data. Figure 5.3 shows the disease labeled airway nodes of one patient diagnosed with IPF.

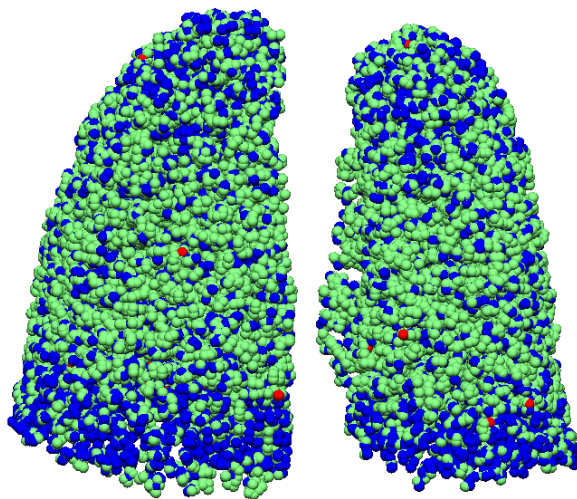


Figure 5.3: Disease labeled airway nodes. Green is the normal region, blue is the fibrosis region, and red is the emphysema region.

Deep inspiration model

Deep inspiration model was constructed based on the ventilation model (introduced in Section 5.2.4) to simulate the deep inspiration from FRC to TLC. For the modeling of old normal people, the reference FRC volume (that is the patient-specific normal volume as reference) from PFT result was used as an initial volume to start inspiration, and the subject-specific muscle pressure was adjusted to drive the lung expand to the target reference TLC volume (acquired from PFT result). For the simulation of IPF patient, the deep inspiration started from the measured FRC volume (acquired from PFT) and the muscle pressure set up in the normal condition was used to guide the lung expansion. Here, we assumed that the inspiratory muscle pressure is normal in IPF patient, as some research indicates that the inspiratory muscle force remains almost the same in IPF lungs compared with normal (De Troyer and Yernault, 1980). The modeling for IPF patient

was divided into two separate stages:

1. The compliance of labeled fibrosis (sum of honeycomb, reticular and ground-glass) acinar unit (connected to its labeled terminal airway node) was reduced to a very low value (less than $0.001 \text{ L/cmH}_2\text{O}$) to make sure the fibrosis tissues were stiff enough. Then, inspiration volume was modeled under this fibrosis constricted condition.

2. The deep inspiration volume acquired in Step 1 was used as the target volume, and the tissue compliance of every acinar unit was scaled down together until the simulated inspiration volume can hit the target, then the corresponding scale factor of total tissue compliance was acquired.

Passive ventilation model

Time-averaged passive ventilation distribution to each acinus within four breath cycles was predicted using the previously described ventilation model. Acinar volumes were initialized at FRC, using reference normal value and measured disease value, respectively. The scale factor of acinar tissue compliance set in the above Step 2 was applied in the simulation of IPF patient. Patient-specific tidal volume was estimated based on patient's weight, gender and height (Gilbert et al., 1972; Pelosi et al., 1998).

Perfusion model

The perfusion model introduced in Section 5.2.4 was used to estimate the distribution of blood. The individual age, weight, height and gender were integrated to predict the cardiac output for each patient (Brandfonbrener et al., 1955; Miyamura and HONDA, 1973; Stelfox et al., 2006), and the inlet and outlet pressure were adjusted in order to match the estimated cardiac output. The blood vessel radius in fibrosis labeled region was narrowed down for the modeling of IPF, so that the blood flow will be constricted

in the lesion area.

Gas exchange model

The gas transport and exchange were simulated using the gas exchange model introduced in Section 5.2.4. The ventilation and perfusion distribution predicted by the ventilation and perfusion model were used as inputs in the normal and disease condition, respectively. Patient-specific oxygen consumption (VO_2) and carbon dioxide consumption (VCO_2) were estimated using the following equations (Kwan et al., 2004; Coelho-Ravagnani et al., 2013):

$$VO_2 = P_{VO_2} \times W, \quad (5.27)$$

$$VCO_2 = VO_2 \times 0.8, \quad (5.28)$$

where P_{VO_2} is the unit oxygen consumption at rest ($P_{VO_2} = 2.84 \pm 0.34 \text{ ml/kg}^{-1}/\text{min}^{-1}$ for male and $P_{VO_2} = 2.82 \pm 0.37 \text{ ml/kg}^{-1}/\text{min}^{-1}$ for female), and W is the weight of the patient.

With setting up the patient-specific tidal volume and dead space, the partial pressure of oxygen in alveolar (P_{AO_2}) and in arterial blood (P_{aO_2}) can be predicted.

5.3 Results

5.3.1 Construction of lung lobe geometry

Table 5.3 lists the age, BMI and functional measures used for normal lung shape prediction of one patient with IPF. The values were from the patient's individual information, among which FVC, TLC, RV/TLC and DLCO were the patient-specific normal reference values acquired from PFT result. Figure 5.4 presents the lung mesh of the IPF patient and its corresponding predicted lung mesh of older normal people.

Table 5.3: Individual information used for normal lung prediction from one patient with IPF

Parameters	Age	BMI	FVC(L)	TLC(L)	RV/TLC	DLCO(mL/mmHg/min)
Values	82	32.77	3.87	7.22	46	25.1

FVC, TLC, RV/TLC and DLCO are the patient-specific normal reference values acquired from PFT results.

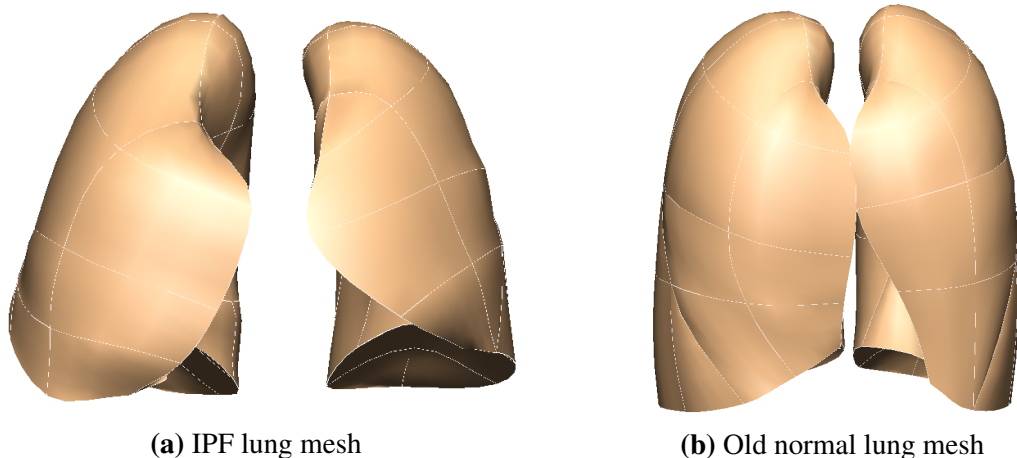


Figure 5.4: Lung mesh of IPF and the corresponding predicted lung mesh of old normal. (a) IPF lung mesh generated from CT imaging of a patient with IPF. (b) Old normal lung mesh predicted with the individual information of the same patient.

The average lobe volume proportion of all IPF lung mesh and all predicted old nor-

mal lung mesh were calculated, shown in Table 5.4.

Table 5.4: Average lobe volume proportion of IPF lung mesh and predicted old normal lung mesh.

Lobe	IPF	Predicted old normal
Left lower lobe	0.231	0.242
Left upper lobe	0.290	0.228
Right lower lobe	0.205	0.272
Right middle lobe	0.130	0.078
Right upper lobe	0.144	0.179

As discussed in Chapter 4, Section 4.2.4, the shape change in IPF lung usually relates to a relatively larger anteroposterior diameter and smaller height of the lung. Meanwhile, IPF lung has a lower average volume proportion for left lower lobe and right lower lobe compared with old normal people. The results illustrated in Figure 5.4 and Table 5.4 are consistent with our previous findings, with predicted lung mesh of old normal showing a "thinner" and "higher" shape and lower average volume of left and right lower lobes compared with the IPF mesh generated from CT imaging.

5.3.2 Construction of airway/vasculature geometry

Airway tree

Figure 5.5 illustrates the generated airway trees of one IPF patient and its corresponding predicted airway tree of old normal.

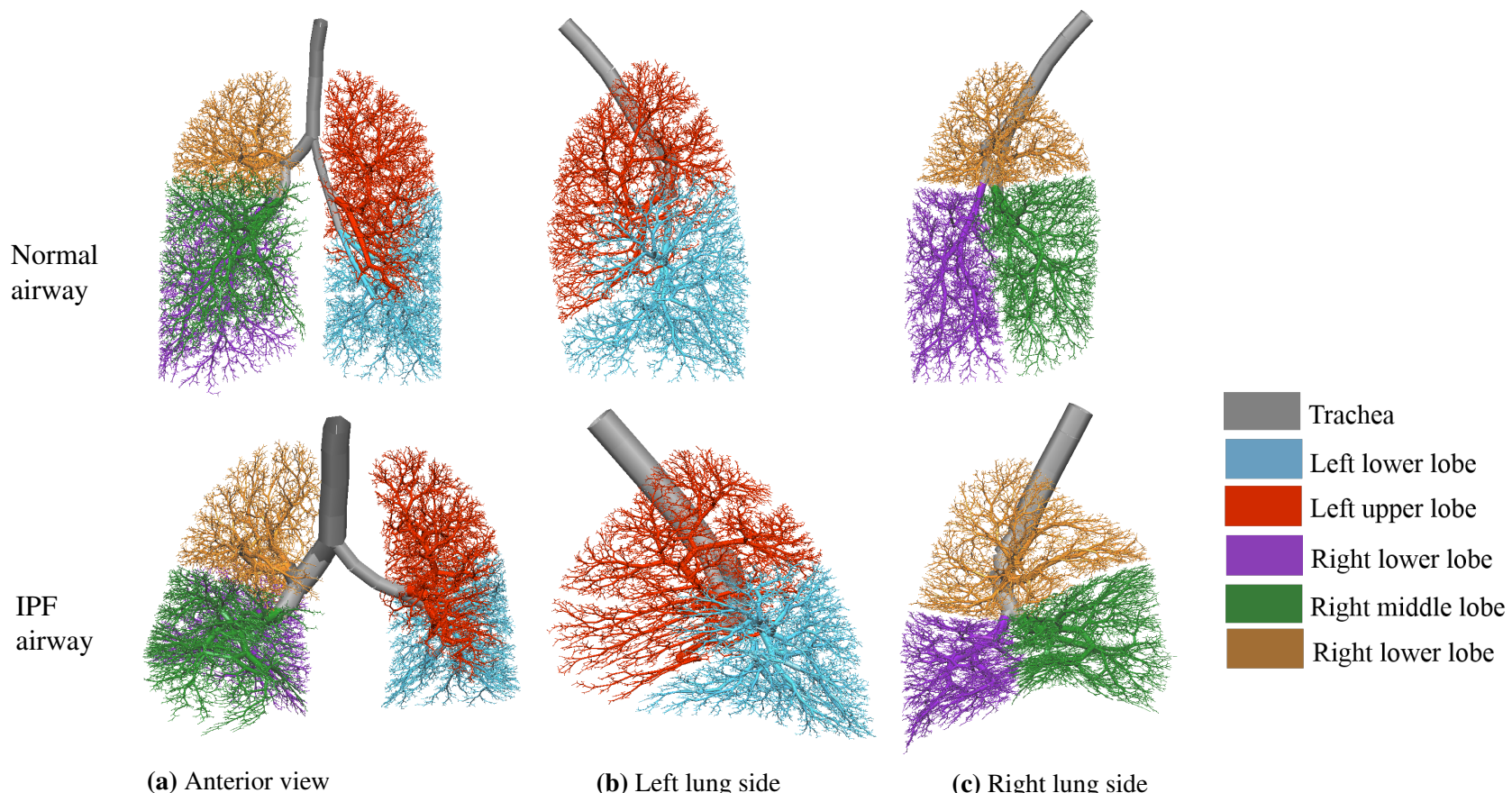


Figure 5.5: Generated normal airway tree (top row) and IPF airway tree (bottom row) for one patient diagnosed with IPF. (a) Anterior view. (b) Left lung side. (c) Right lung side.

From Figure 5.5, it can be seen that compared with old normal airway tree, IPF airway tree has a larger trachea radius (which is associated with the dilation of conducting airway in IPF lung), a relatively smaller lower lobe and a larger anteroposterior diameter. These features are consistent with the SSM based analysis result of IPF lung shape in Chapter 4, which means our method of generating old normal and IPF airway tree is reasonable and acceptable.

Vasculature tree

The generated IPF and old normal vessel trees are shown in Figure 5.6. Table 5.5 lists the parameters used for generating airway tree. Table 5.6 lists the parameters for generating vessel trees.

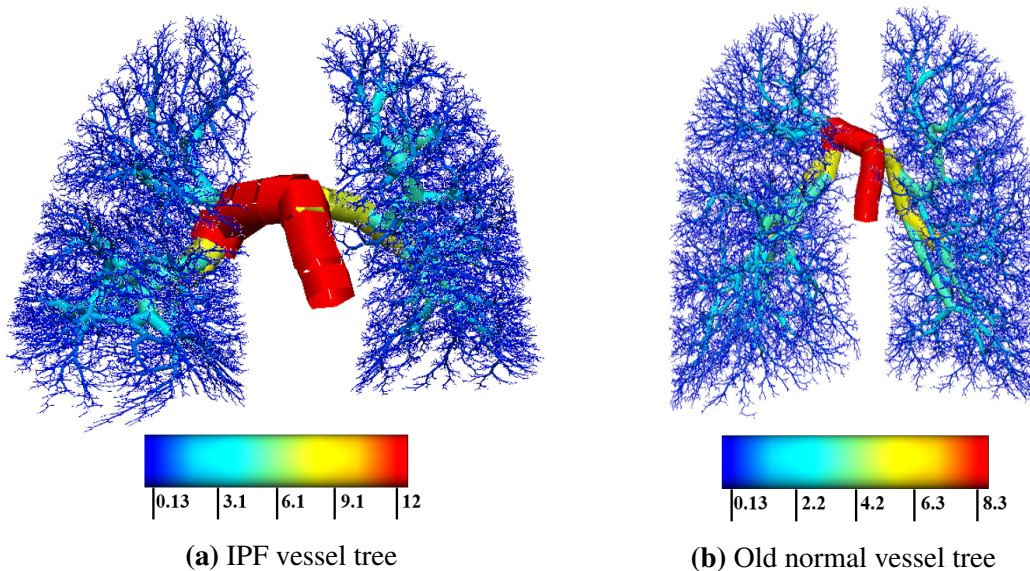


Figure 5.6: Generated geometry of vessel tree. (a) IPF vessel tree. (b) Old normal vessel tree. The radius of branches were visualized with different colors. The colorbar shows the range of radius.

Table 5.5: Parameters of old normal and IPF airway tree

Patient No.	Time point	Trachea radius (mm)		Horsfield diameter ratio(R_dH)		Terminal radius (mm)		Airway volume (ml)	
		Normal	IPF	Normal	IPF	Normal	IPF	Normal	IPF
Patient 1	Time point 1	6.000	8.806	1.139	1.161	0.200	0.182	76.141	99.800
	Time point 2	6.000	9.821	1.139	1.166	0.200	0.184	75.530	123.871
	Time point 3	6.000	10.034	1.139	1.162	0.200	0.185	74.167	134.844
Patient 2	Time point 1	6.500	9.6778	1.137	1.159	0.200	0.180	87.701	110.993
	Time point 2	6.500	8.708	1.137	1.154	0.200	0.182	88.851	111.150

Table 5.6: Parameters of old normal and IPF vessel tree

Patient No.	Time point	Main artery radius (mm)		Artery R_dS		Main vein radius (mm)		Vein R_dS	
		Normal	IPF	Normal	IPF	Normal	IPF	Normal	IPF
Patient 1	Time point 1	7.69	11.28	1.45	1.51	9.17	14.66	1.48	1.54
	Time point 2	7.69	12.58	1.45	1.52	9.17	16.75	1.48	1.56
	Time point 3	7.69	12.86	1.45	1.52	9.17	17.20	1.48	1.56
Patient 2	Time point 1	8.33	12.40	1.52	1.58	11.18	18.38	1.57	1.65
	Time point 2	8.33	11.16	1.52	1.57	11.18	16.11	1.57	1.63

5.3.3 Deep inspiration modeling

Table 5.7 lists the deep inspiration volumes (from FRC to TLC) of reference normal, simulated and measured values (from PFT report). It is shown in the table that the simulated inspiration volume (with CT-based abnormality labeling) of all the time points for these two patients are higher than the measured ones, which means the abnormalities (fibrosis) on the volumetric CT are not sufficient enough to explain the constriction of deep inspiration volume and the increase in lung stiffness of in IPF lung.

Table 5.7: Reference normal, simulated and PFT measured inspiration volume.

Patient No.	Time point	Ref. normal volume	Simulated volume	Measured volume
Patient 1	Time point 1	1.93	1.26	1.16
	Time point 2	1.93	1.27	1.12
	Time point 3	1.84	1.15	1.14
Patient 2	Time point 1	3.4	2.58	2.37
	Time point 2	3.36	2.37	1.93

Based on the inspiration volumes shown in Table 5.7, additional fibrosis was added to the CALIPER classified 'normal' tissues until the modeled inspiration volume can match the PFT measured one. Figure 5.7 shows the inhale pressure curve, CT-based simulated inspiration curve with CAPLIPER fibrosis labeled, and PFT-based simulated inspiration curve with additional fibrosis labeled. With more fibrosis added to the normal region, the inhaled volume is reduced and can match the PFT result. The percentages of CT-based fibrosis (CALIPER classified) and PFT-based fibrosis (CALIPER classified + additional labeled) are listed in Table 5.8.

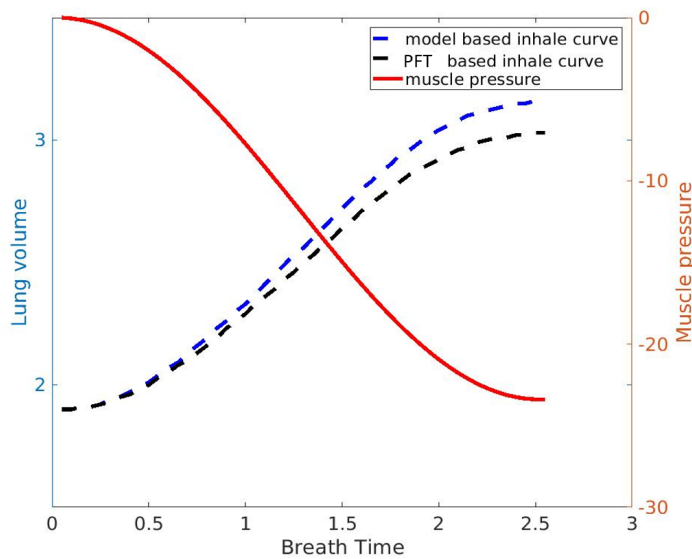


Figure 5.7: Deep inspiration and muscle pressure curve. The red line is the muscle pressure curve. The blue lines is the CT-based simulated inspiration curve with CAPLIPER fibrosis labeled, and red line is the PFT-based simulated inspiration curve with additional fibrosis labeled.

Table 5.8: Percentage of CT-based fibrosis and PFT-based fibrosis.

Patient No.	Time point	CT-based fibrosis (%)	PFT-based fibrosis (%)
Patient 1	Time point 1	17.58	23.67
	Time point 2	18.91	28.87
	Time point 3	22.13	22.86
Patient 2	Time point 1	4.26	11.86
	Time point 2	12.46	29.12

5.3.4 Gas exchange model

Figure B.9 illustrates the distribution of normal, CT-based and PFT-based simulated V/Q ratio and arterial oxygen of one time point from one patient diagnosed with IPF. The figures are shown with V/Q plotted on a logarithmic scale, which is consistent with the presentation of V/Q measurements using the multiple inert gas elimination technique

(MIGET). From the results, the simulation for old normal model (the first row) predicts normal V/Q ratio distribution, with PaO_2 of 89.33 mmHg, a typical value of normal older adult. The model labeled with CT-based fibrosis predicts characteristic bimodal V/Q distributions (the second row), and PaO_2 moderately decreased (71.63 mmHg). A slight shift to the left side is observed for the higher peak of V/Q ratio curve compared with the normal model. The small peak of V/Q ratio appears around 5 (larger than 1), as there is a decrease in perfusion in fibrotic area due to the narrowed vessel radius. The model labeled with PFT-based fibrosis predicts appropriate patient-specific FRC and TLC, and decreases in PaO_2 to 67.85 mmHg. The ventilation flow of the higher peak decreases in comparison to the CT-based model, but increases a little bit for the small peak. That is because with more fibrosis labeled on the normal tissue, the lung becomes stiffer. The lower tissue compliance leads to a reduction in total ventilation flow, therefore it can be seen a reduced ventilation of the higher peak.

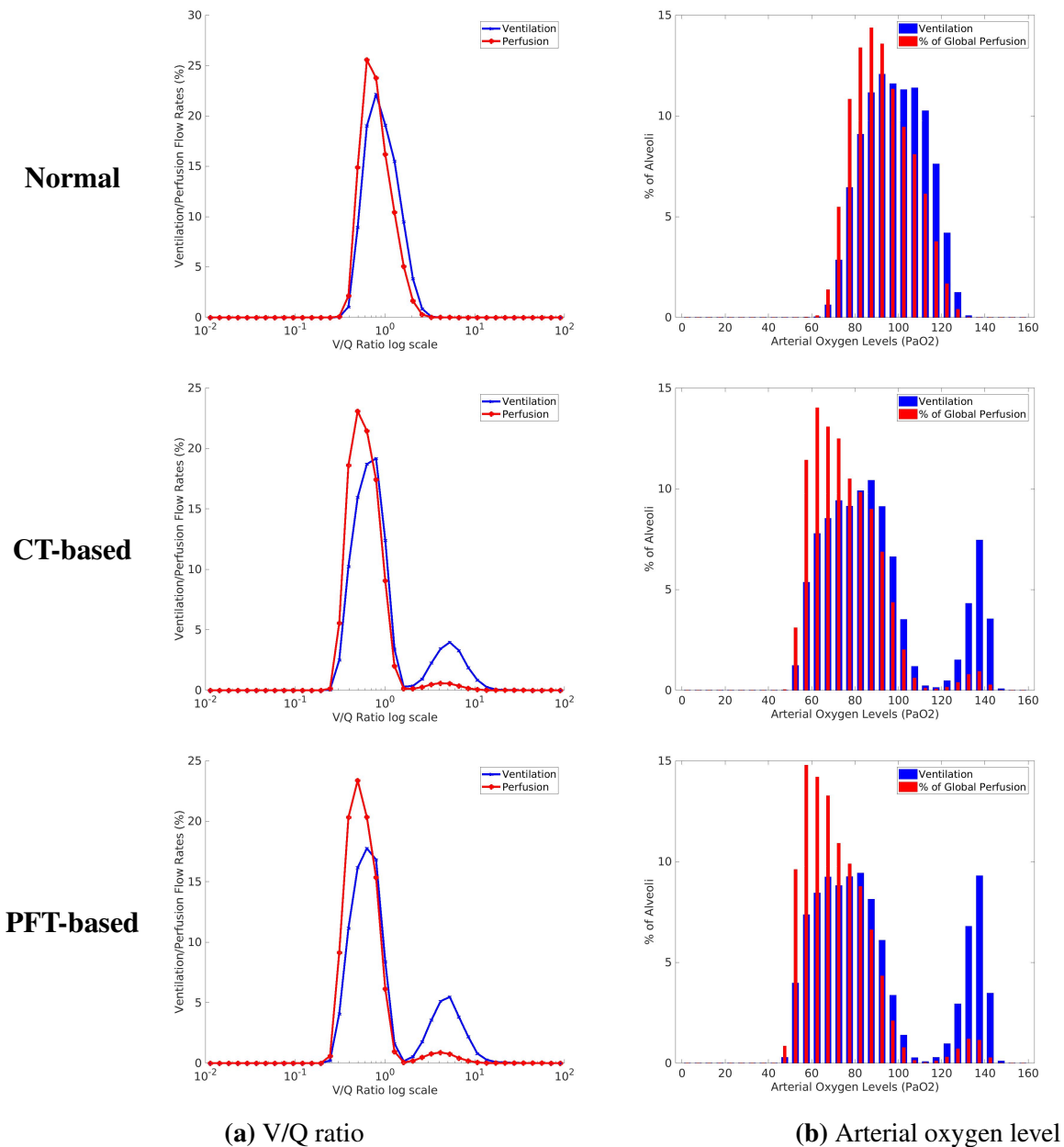


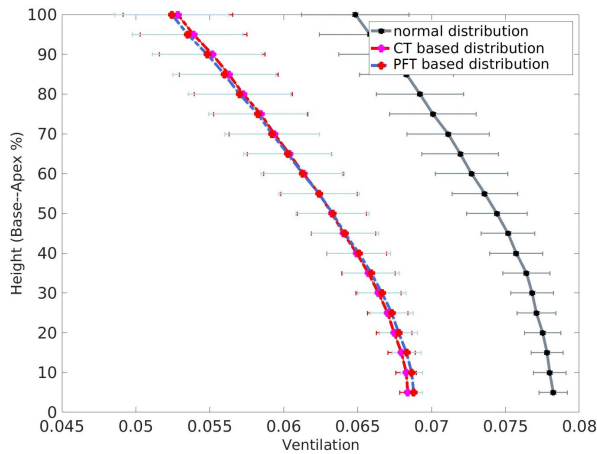
Figure 5.8: V/Q ratio distribution and arterial oxygen distribution of normal, CT-based and PFT-based simulation result of one time point from one patient diagnosed with IPF using MIGET. (a) V and Q flow with respect to V/Q ratio. (b) V and Q percentage with respect to arterial oxygen level.

Figure B.10 shows the V, Q and V/Q ratio distribution against lung height (cranio-caudal axis) simulated by older normal, CT-based and PFT-based model. From the result, the ventilation distributes more in lower region than in upper region which is determined entirely by gravity, and there is a left shift for the two IPF simulated ventilation curves compared with the normal one. The mismatch of perfusion between normal model and the two IPF models mainly happens in the basal part of the lung, where more fibrosis appears in these areas. For the old normal simulation, it can be seen an upward trend in V/Q ratio (around 1) with the increasing of lung height, but higher V/Q ratio (V/Q mismatch) is illustrated in CT-based and PFT-based curves, especially in the regions of base and apex.

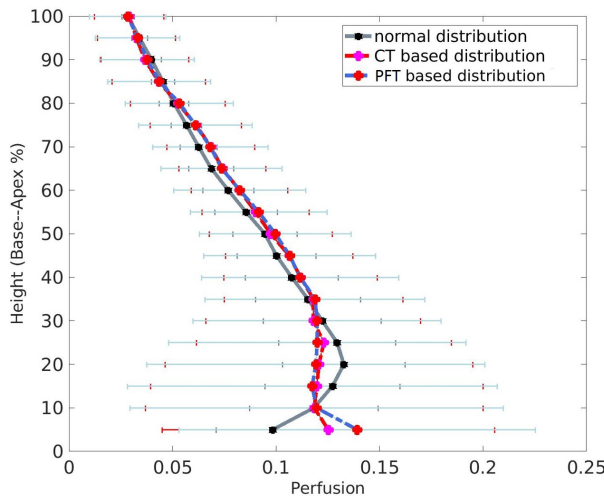
The values of PaO_2 and PaCO_2 of older normal, CT-based and PFT-based model for each time point of these two patients are listed in Table 5.9. For CT-based and PFT-based simulation, PaO_2 experiences a decrease over time for both of these two patients, corresponding to the gradual increase of fibrosis. MIGET plots of V/Q ratio and arterial oxygen distribution, plots of cranio-caudal distribution of V, Q and V/Q ratio of other subjects and time points can be found in Appendix B.

Table 5.9: Values of PaO_2 and PaCO_2 of older normal, CT-based and PFT-based modeling results.

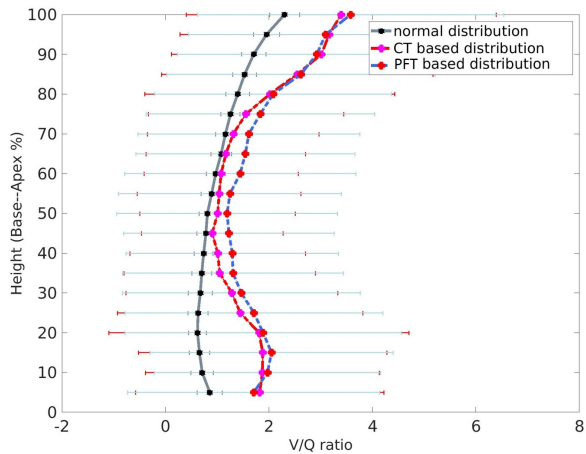
Patient No.	Time point	PaO_2 (mmHg)			PaCO_2 (mmHg)		
		Normal	CT-based	PFT-based	Normal	CT-based	PFT-based
Patient 1	Time point 1	89.33	71.63	67.85	41.87	52.73	53.97
	Time point 2	95.37	64.56	58.72	37.81	57.48	59.58
	Time point 3	87.92	60.43	60.00	42.76	59.83	59.97
Patient 2	Time point 1	92.31	88.52	85.13	39.80	41.74	42.86
	Time point 2	91.72	83.70	75.35	39.09	43.77	46.76



(a) Ventilation distribution



(b) Perfusion distribution



(c) V/Q ratio distribution

Figure 5.9: Ventilation, perfusion and V/Q ratio distribution against lung height (cranio-caudal axis). (a) Ventilation distribution against lung height. (b) Perfusion distribution against lung height. (c) V/Q ratio distribution against lung height.

5.4 Discussion

In this chapter, a SSM was used to make a prediction of older normal lung shape for each patient. The SSM based lung shape prediction provides a reliable way to make a comparison of the lung function between a patient-specific lung and its corresponding lung of older normal people. The patient-specific shape prediction was achieved based on the patient's individual information which shows significant correlations with older normal lung shape, therefore the estimated lung shape is able to represent the statistical lung shape of older normal people as a control group. Through modeling the airway/vessel tree and lung function with predicted normal lung mesh, it is possible for us to quantitatively describe the change of respiratory geometry in IPF lung, the decline of lung function, the severity of disease and the prognosis of development. That could be a promising direction for clinical applications in the future.

The computational modeling in this chapter shows that the abnormalities classified by CALIPER from volumetric CT imaging may be not sufficient enough to explain the increase in lung stiffness and the decline of lung function in IPF patient. V/Q mismatch (impaired gas exchange) present in CT-based abnormal tissue as well as regions that are classified as 'normal'. This will truly happen in some patients, due to the low quality of CT scan and the errors caused by mis-classification of tissue patterns. Moreover, for the patients diagnosed at the early of the disease, some 'sub-clinical' symptoms that can not be visualized on radiological imaging can definitely damage to the lung function. So, in a sense, our computational modeling method provides a potential way to work as supplement for the radiological and biopsy diagnosis of IPF, and help the clinicians to make a better decision of treatment planning at a earlier stage.

However, there are some limitations of the modeling procedure. First, in IPF lung,

there is a dilation in trachea, but a constriction in small airway. In this chapter, the trachea radius of normal lung was scaled from the trachea radius of IPF lung using a statistically measured ratio which represents the trachea difference between normal and IPF. The main limitation of this method is the measured ratio may be not accurate enough for all the subjects even though the standard deviation has been taken into consideration in our research. A potential direction in the future work could be to use the change of dead space in IPF lung in the construction of airway geometry.

Second, the emphysema and the low attenuation area (LAA) are not taken into consideration in this model. Although emphysema classified by CAPLIPER only covers a small proportion of the lung (usually less than 1%), it is believed to have an impact on the deterioration of lung function together with fibrosis in IPF (Cottin et al., 2005; King Jr et al., 2011; Lin and Jiang, 2015). On the other hand, the LAA (mild, moderate and severe) which accounts for a sizable part of the lung may have some correlation with the appearance of emphysema, and both emphysema and LAA are associated with air trapping at the end of inspiration Slebos et al. (2015); Hoessein and De Jong (2017), which will influence the lung volume at FRC and the change of tissue compliance during breathing. Therefore the emphysema and LAA can to be involved in the future work for setting the initial acinar unit volume at FRC.

Third, for some end-stage subject with a large proportion fibrotic lesion and a small constricted FRC volume, a larger muscle pressure may be needed to drive the expansion of the stiffer lung, thus the deep inspiration volume probably won't be estimated accurately with a normal muscle pressure. In the future study, the chest wall resting volume can be used to help with setting up the tissue compliance in IPF lung, which is calculated by:

$$V_{CWRV} = V_{FRC} + C_{cw} \times (-P_{pl}(FRC)), \quad (5.29)$$

where V_{CWRV} is the chest wall resting volume, V_{FRC} is the FRC volume, C_{cw} is the chest wall compliance (fixed to 0.2 L/cmH₂O) and $P_{pl}(FRC)$ is the pleural pressure at FRC. With a fixed chest wall resting volume for both normal and IPF model, the elastic recoil pressure (P_e) which is determined by pleural pressure will be influenced by the constriction of FRC volume, therefore a correlation can be built between chest wall resting volume and tissue compliance.

5.5 Summary

In this chapter, a patient-specific computational modeling method was developed to investigate the lung geometry and lung function in IPF patient. In order to make a comparison between IPF patient and older normal people, SSM was used to make a prediction of the lung shape of old normal for each patient, and V/Q distribution and gas exchange were then simulated in normal and IPF condition, respectively, with CALIPER tissue classification data and PFT result as input. The result shows that our computational model can reasonably predict the patient-specific ventilation, perfusion and gas exchange in IPF lung, and quantify the difference of lung function between IPF patient and older normal people. Moreover, it is suggested from the result that the CT imaging may be not able to provide enough information to explain the decline of lung function in IPF patient, and the impaired gas exchange will happen in not only abnormal region but also in CT-visualized 'normal' tissues.

Chapter 6

Conclusion

This thesis aims to develop a consistent method which integrates volumetric CT data, quantitative analysis, pulmonary functional test and computational modeling to investigate the lung function and disease progression of IPF. This chapter provides a summary of the important outcomes of the research, how the thesis addressed the objectives set out in Chapter 1, Section 1.2, and makes some plans for the future work.

6.1 Thesis Summary

Objective 1: *Develop an automatic lung lobe segmentation method based on HRCT images that can consistently estimate lobar boundaries even if the boundary is not clear along its entire length. The method needs to be tested on both healthy subjects and IPF subjects. Ideally the algorithm will be automatic , or semi-automatic.*

A PCA-based statistical shape model guided method was developed to segment pulmonary lobes from HRCT images in Chapter 3. The method was tested on 20 inspi-

ratory and expiratory CT scans: 10 healthy young subjects and 10 older subjects diagnosed with IPF. Results show that the method can perform well to detect the location of the fissures over most of the fissure surfaces on CT images from normal subjects, and provides a relatively accurate result (compared with some existing tools) for IPF (abnormal) subjects although manual interaction is still needed for a few subjects. The method provided more accurate result on the left oblique fissure than the other two fissures, because the left lung has a simpler anatomic structure with only one fissure. The ability of the method to provide an initial estimate of the fissure locations was compared with two other segmentation softwares which use watershed-based (anatomical knowledge-based) methods. The two segmentation softwares PASS and PTK were unable to segment 9/20 and 7/20 subjects respectively. In contrast, our model-based method can estimate the fissure location for all subjects at all volumes, although PASS can perform better on some young healthy subjects. This new procedure does not depend on prior segmentation of anatomical structures (airway lobar classification) and has promising potential as a clinically useful semi-automatic lobe segmentation procedure.

Objective 2: *Classify and quantify tissue abnormalities from HRCT scans of IPF lungs. Analyze the density, volume, spatial distribution, and their change over time.*

The tissue abnormalities of IPF lungs were classified and analyzed over time using quantitative methods based on HRCT imaging in Chapter 4. Tissue regions of HRCT images were classified using CALIPER software. The classified data was mapped to a statistical shape model, and quantitative approaches was used to analyze tissue density, tissue volume, the spatial distribution of abnormalities, and regional changes in tissue over time. The result shows that tissue density of different tissue CT patterns fluctuate within different ranges over time. The ground-glass region has the highest average

tissue density, whereas emphysema has the lowest average tissue density. Therefore, tissue density can be used as a quantitative biomarker to distinguish the disease regions from other lung parenchyma. However, tissue volume can not be used as a reliable biomarker to interpret the progression of disease, as no regular tendency of the volume change for abnormal tissues (honeycomb, reticular and ground-glass) was observed. It is also illustrated that ground-glass mostly locates in the basal part of lung (lower lobe), while emphysema usually presents in the apex part (upper lobe). The distribution of reticular region mainly focuses on the basal area and apex area. All the abnormalities (emphysema and fibrosis) in IPF lung are peripheral performance and mostly distributes surrounding the surface of the lung. Additionally, the locations of abnormalities in IPF lung keep changing all the time. One kind of disease pattern may change to other patterns over time. The quantitative analysis would potentially provide consistent and reliable tissue-level markers to help with further modeling of ventilation/perfusion mismatch and impaired gas exchange.

Objective 3: *Investigate the difference of lung shape between IPF and older normal lungs, and explore the correlation of lung shape change in IPF with the extent fibrosis.*

In Chapter 4, the geometric mesh of IPF lung and lobes were compared with a statistical shape model of old normal to quantify the lung lobe shape difference between IPF patient and old normal people, and the impact of fibrosis extent on lung shape variation was also investigated. It is found that the first shape mode of SSM (based on PCA) is significantly different between IPF subjects and old normal subjects and strongly correlates with the percentage of fibrosis. The first shape mode corresponds mainly to the anteroposterior diameter of lung which results in a variation of diaphragm. The basal and peripheral performance of disease may increase the stiffness of the lower part of

lung, thus having a impact on the movement of diaphragm when breathing. Fibrosis lesion increases the ratio of anteroposterior diameter to the height of lung, which makes lung become "fatter" and "shorter". Moreover, lobe volume analysis shows that IPF lung has a lower average volume proportion for left lower lobe and left upper lobe compared with old normal lungs. This "compression effect" on the basal part of IPF lung may be associated the reduction in tissue compliance of IPF lungs caused by fibrosis.

Objective 4: *Integrate the image-based tissue quantification, pulmonary functional test and computational modeling to simulate the lung function in IPF, compared with the older normal people, and to use these tools to estimate the impact of CT features of IPF on lung function.*

In Chapter 5, a multiple time point patient-specific computational modeling method was developed with CT feature data and PFT result as input to investigate the lung geometry and lung function in IPF patient. The lung function of V/Q distribution and gas exchange were compared between IPF patient and older normal people. Compared with the older normal people, IPF patient has a lower PaO₂ and a higher V/Q ratio, and it can be seen a decline of lung function in IPF lung over time, with decreasing PaO₂ and more severe V/Q mismatch, due to the increasing stiffness of the lung. From the modeling result, the abnormalities on volumetric CT imaging are probably not sufficient to explain the decline of lung function in IPF patient, and the impaired gas exchange (V/Q mismatch) will appear in not only abnormal region but also in CT-classified 'normal' tissues. The result shows the developed patient-specific modeling method can be used to simulate the ventilation, perfusion and gas exchange in IPF lung, and is able to potentially provide auxiliary information for clinicians to assist with the radiological and biopsy diagnosis at the early stage of IPF.

6.2 Future directions

6.2.1 Improvement of statistical shape model

The SSM used in this thesis was generated using 35 old healthy subjects (AGING) and 15 young healthy subjects (HLA). The main limitation of this model is the small number of HLA subjects used in the training set, and there is a age gap between AGING group and HLA group. In order to capture more kinds of components of shape variation, a larger number of subjects with a wider range of age should be added into the SSM in the future work. With adding more subjects, it is possible to generate a more sophisticated model describing the continuous shape variation from young to old, which may increase the accuracy for estimating the initial fissure locations. Furthermore, the construction of SSM of IPF patients could also be taken into consideration for the future work. In Chapter 4, it has been proved that there is a significant shape difference between IPF and older normal lungs. Therefore, a SSM specific to IPF patients may provide a way to identify shape features of IPF patients, and would be able to provide a better fissure guessing for IPF subjects and further help with statistical analysis of IPF lung function.

6.2.2 Involvement of diffusing capacity for carbon monoxide in the lung functional model

It has been found that DLCO is reduced in 98% of IPF patients at the initial diagnosis (Cortes-Telles et al., 2014), and some study indicated that the impairment of diffusion capacity is one of the reasons to cause chronic arterial hypoxaemia in IPF lung (Plantier et al., 2018). DLCO is an important measurement in PFT report that can help clinicians to make a diagnosis of IPF, thus could be used as a bio-marker in our computational

modeling of IPF lung function in the future work. The value of DLCO is determined by the structural and functional properties of the lung (Graham et al., 2017). The structural properties includes lung gas volume, thickness and area of the alveolar capillary membrane, and the volume of hemoglobin in capillaries. The functional properties are mainly related to absolute levels of ventilation and perfusion, the uniformity of the distribution of ventilation relative to the distribution of perfusion, and the concentration and binding properties of hemoglobin in the alveolar capillaries (Graham et al., 2017). In IPF lung, there will be a reduction in the surface area for diffusion because of emphysema, and a increase in the thickness of the alveolar capillary membrane due to fibrosis. Therefore, through developing a DLCO calculation component in the model, we are able to parameterize the patient-specific properties of alveolar capillary membrane for fibrosis and emphysema areas using the measured DLCO from PFT result, furthermore to investigate if the abnormalities on volumetric are sufficient enough to explain increased lung stiffness and decreases in DLCO over time.

6.2.3 Relationship between lung vasculature and tissue abnormality or lung function in patients with IPF

In Chapter 2, Section 2.6.1, it has been mentioned that vascular alterations are observed in the pulmonary vasculature in patients with IPF, however the vascular factor has not been involved in the modeling of this thesis. The study of Jacob et al. (2016a,b) has pointed out that there is a increase in the pulmonary vessel volume (PVV) in IPF lung, and PVV has strong links with ILD extent (includes ground glass, reticular and honeycomb patterns) ($R^2 = 0.73$, $P < 0.0001$) by using linear regression analysis. Moreover, PVV was demonstrated to be an independent predictor of mortality and a stronger

predictor of mortality than the other traditional CT features and pulmonary functional variables, such as FVC, DLCO, carbon monoxide transfer coefficient and composite physiologic index. Therefore, in the next stage, it would be worthwhile to explore the relationship between the alterations in lung vasculature and tissue abnormality or lung function of IPF. The distribution of PVV in each lung and each lobe could be calculated, and then whether PVV by lung or lobe is associated with regional tissue abnormality or lung function would be tested. Meanwhile, a vascular tree model could be developed to simulate perfusion and vascular distension with subject-specific PVV and tissue abnormalities. Another future direction is to use multiple time point data to further study the association of the change in PVV over time with the progression of IPF.

Appendices

Appendix A

Spatial distribution of abnormalities for each patient

A.1 Basal-to-apical distribution over time for each pa- tient

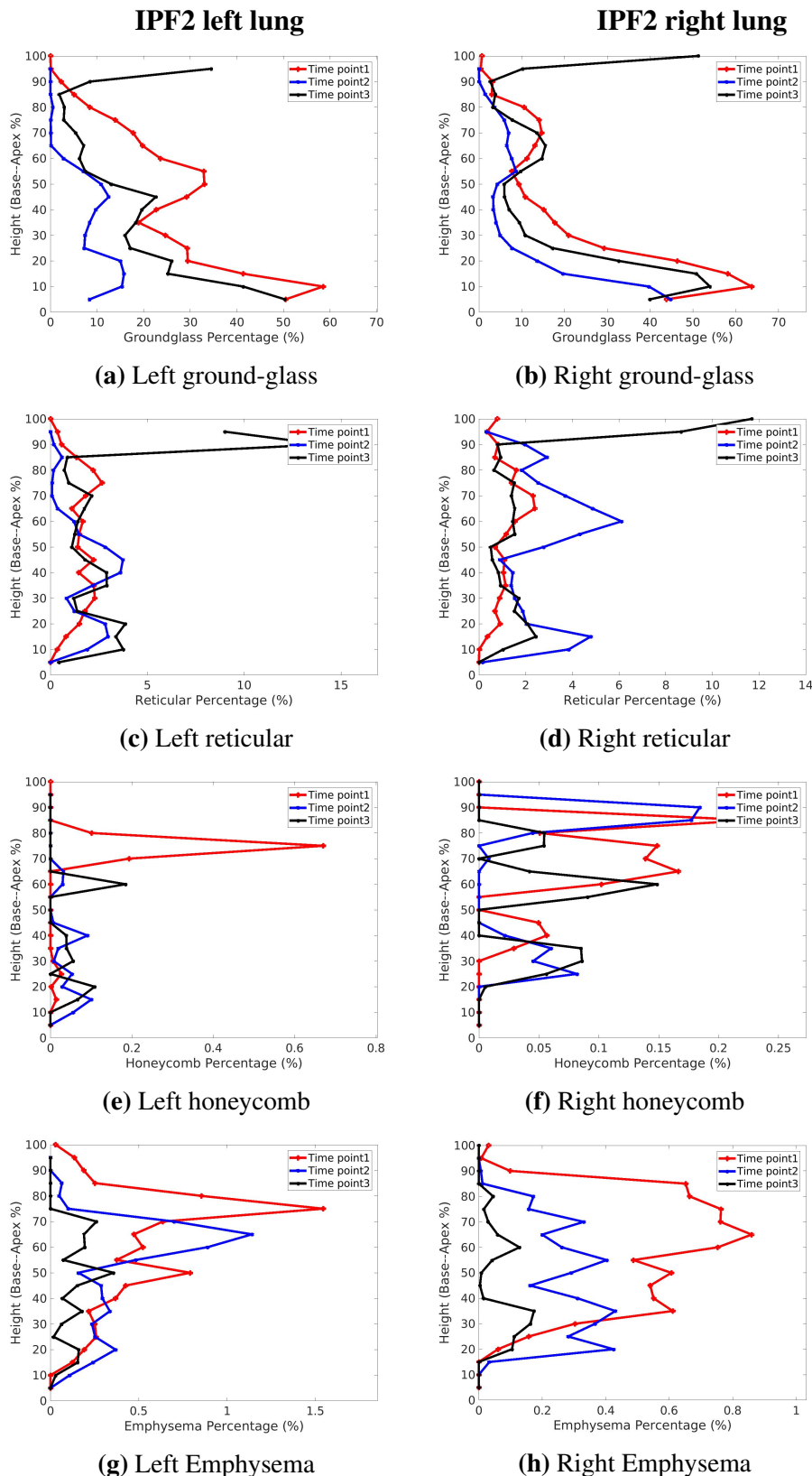


Figure A.1: Volume percentage of each tissue classification plotted against lung height (cranio-caudal axis) of case IPF2 in left and right lungs over time. The average percentage was calculated within 5% sections of the lung height from the base to apex. (a) (b) is ground-glass distribution. (c) (d) is reticular distribution. (e) (f) is honeycomb distribution. (g) (h) is emphysema distribution.

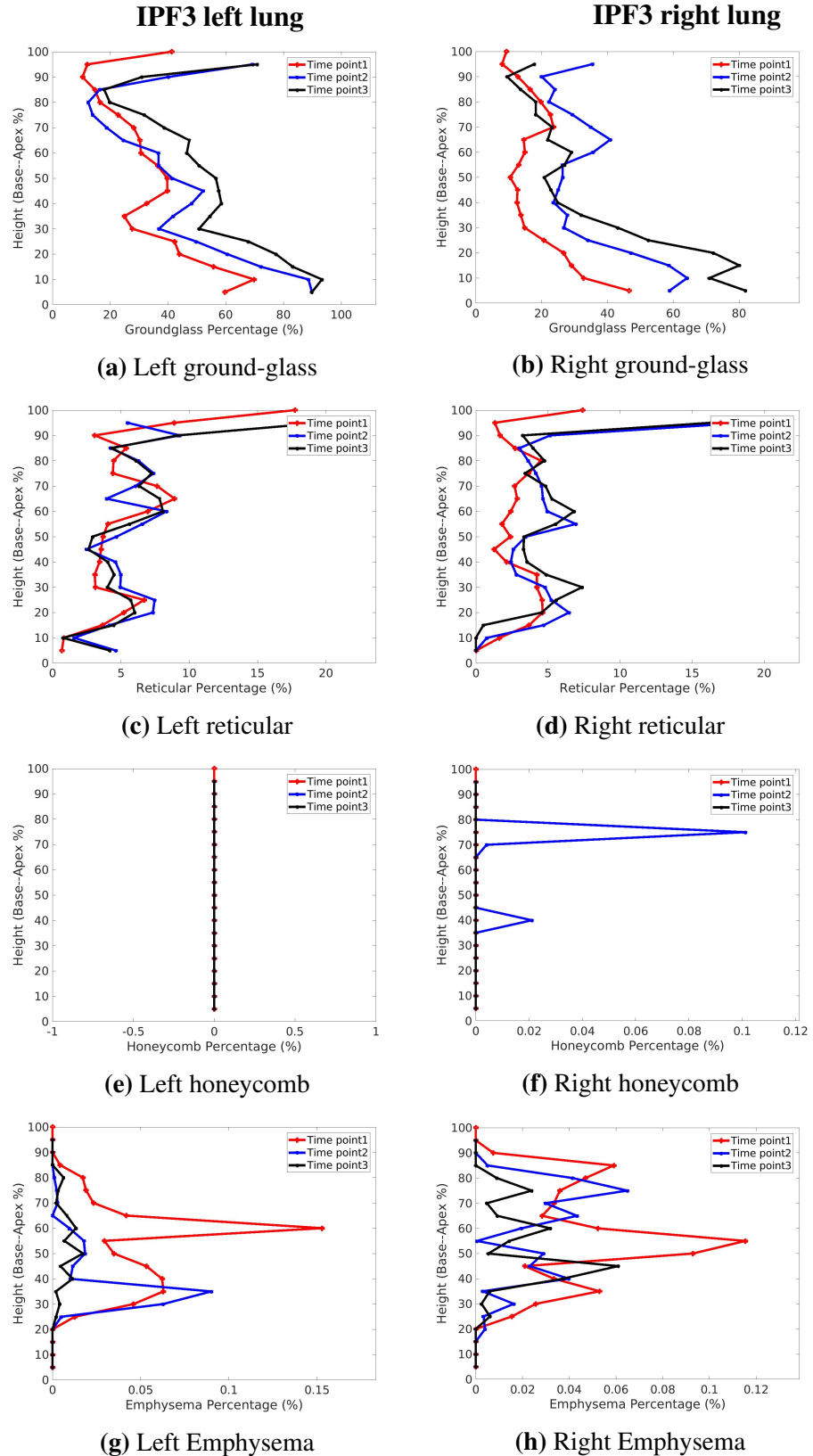


Figure A.2: Volume percentage of each tissue classification plotted against lung height (crano-caudal axis) of case IPF3 in left and right lungs over time. The average percentage was calculated within 5% sections of the lung height from the base to apex. (a) (b) is ground-glass distribution. (c) (d) is reticular distribution. (e) (f) is honeycomb distribution. (g) (h) is emphysema distribution.

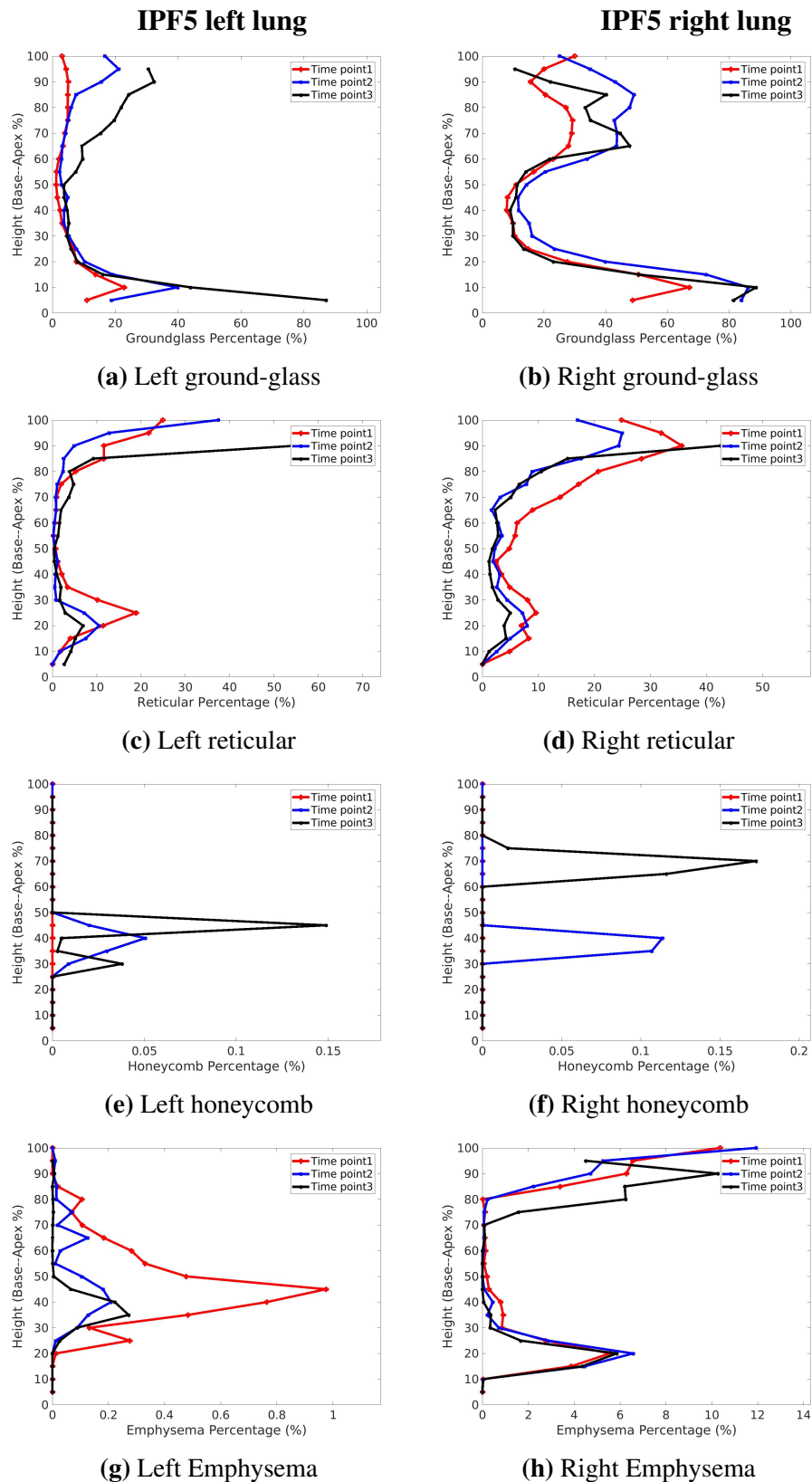


Figure A.3: Volume percentage of each tissue classification plotted against lung height (cranio-caudal axis) of case IPF5 in left and right lungs over time. The average percentage was calculated within 5% sections of the lung height from the base to apex. (a) (b) is ground-glass distribution. (c) (d) is reticular distribution. (e) (f) is honeycomb distribution. (g) (h) is emphysema distribution.

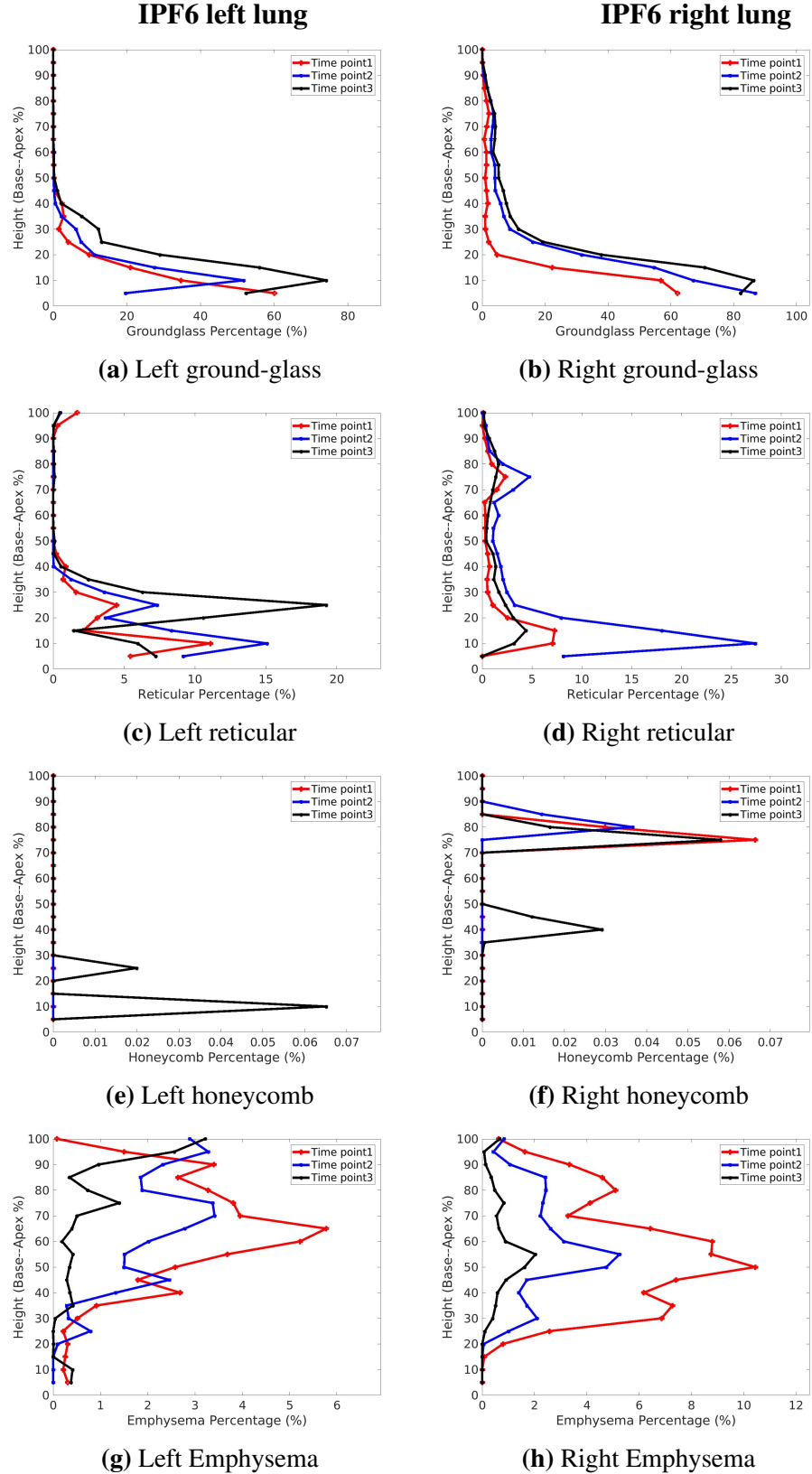


Figure A.4: Volume percentage of each tissue classification plotted against lung height (cranio-caudal axis) of case IPF6 in left and right lungs over time. The average percentage was calculated within 5% sections of the lung height from the base to apex. (a) (b) is ground-glass distribution. (c) (d) is reticular distribution. (e) (f) is honeycomb distribution. (g) (h) is emphysema distribution.

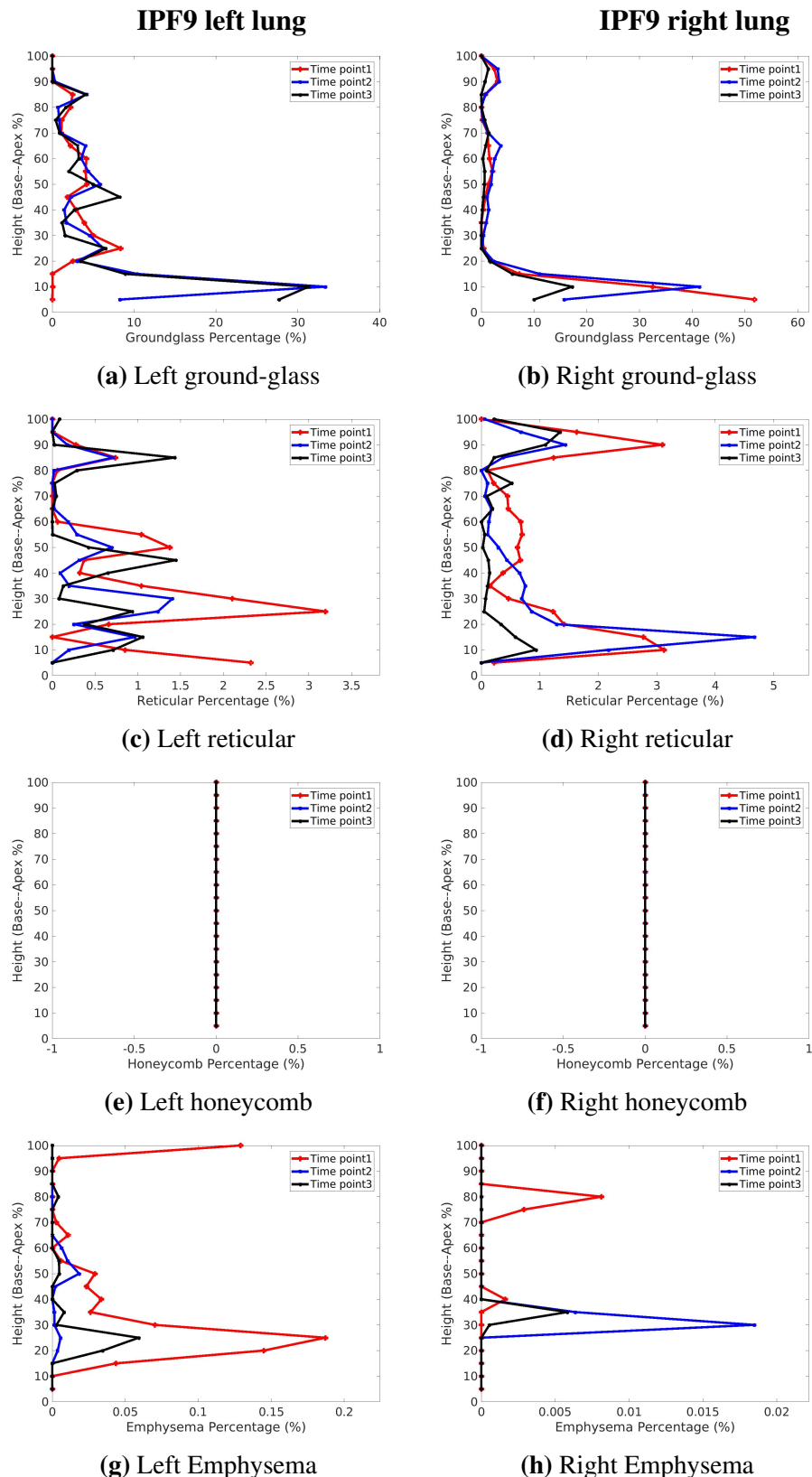


Figure A.5: Volume percentage of each tissue classification plotted against lung height (cranio-caudal axis) of case IPF9 in left and right lungs over time. The average percentage was calculated within 5% sections of the lung height from the base to apex. (a) (b) is ground-glass distribution. (c) (d) is reticular distribution. (e) (f) is honeycomb distribution. (g) (h) is emphysema distribution.

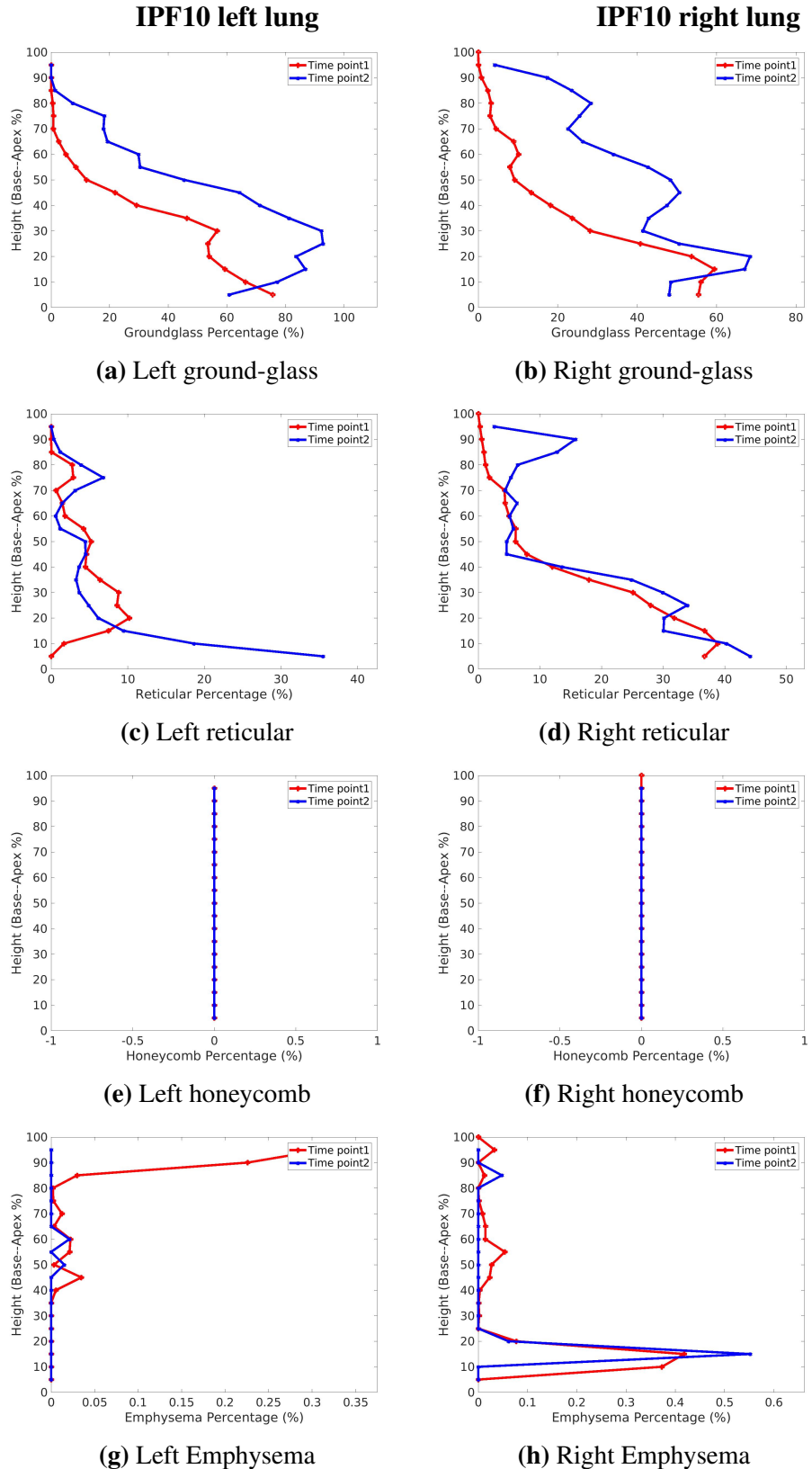


Figure A.6: Volume percentage of each tissue classification plotted against lung height (crano-caudal axis) of case IPF10 in left and right lungs over time. The average percentage was calculated within 5% sections of the lung height from the base to apex. (a) (b) is ground-glass distribution. (c) (d) is reticular distribution. (e) (f) is honeycomb distribution. (g) (h) is emphysema distribution.

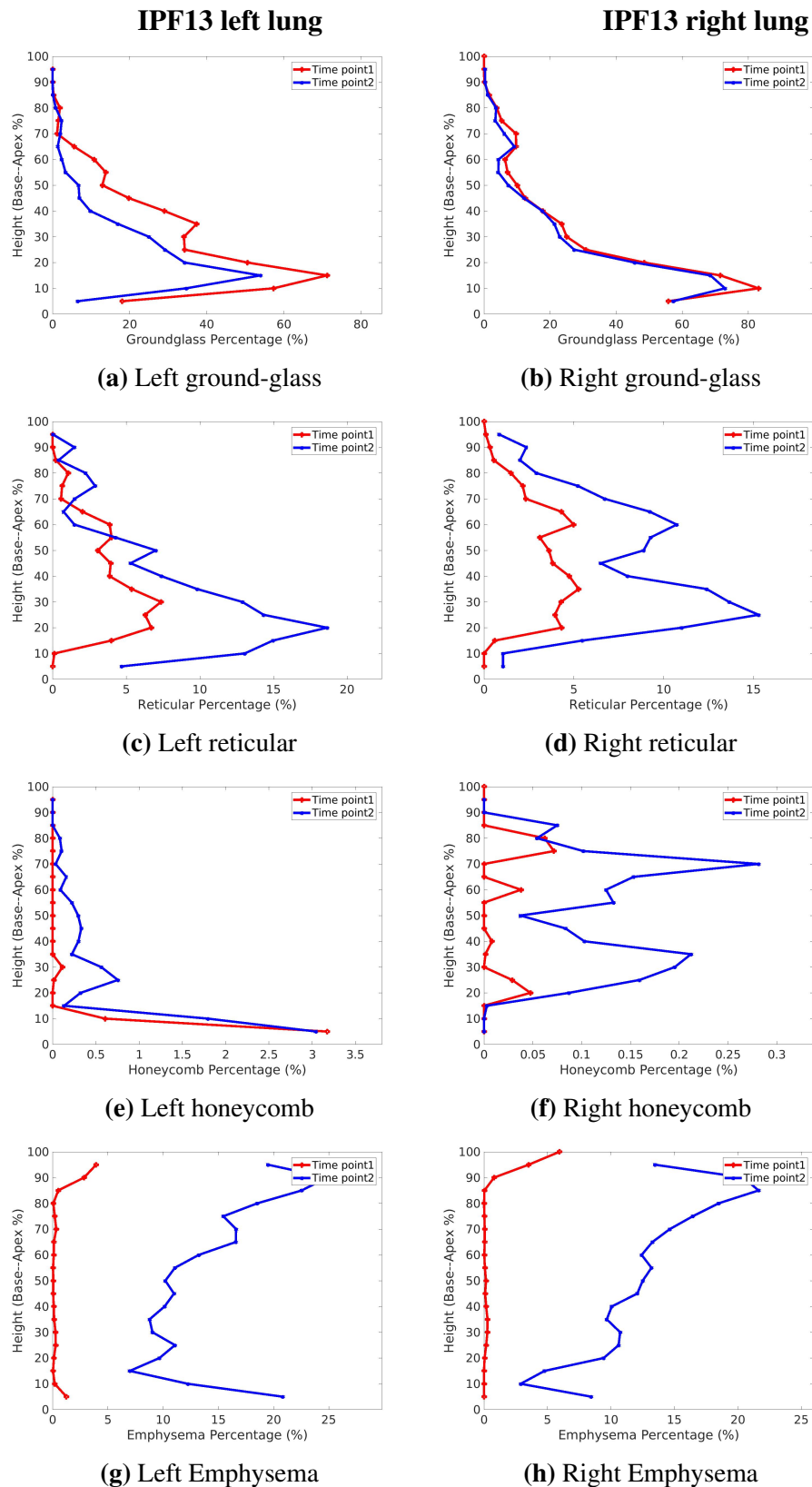


Figure A.7: Volume percentage of each tissue classification plotted against lung height (cranio-caudal axis) of case IPF13 in left and right lungs over time. The average percentage was calculated within 5% sections of the lung height from the base to apex. (a) (b) is ground-glass distribution. (c) (d) is reticular distribution. (e) (f) is honeycomb distribution. (g) (h) is emphysema distribution.

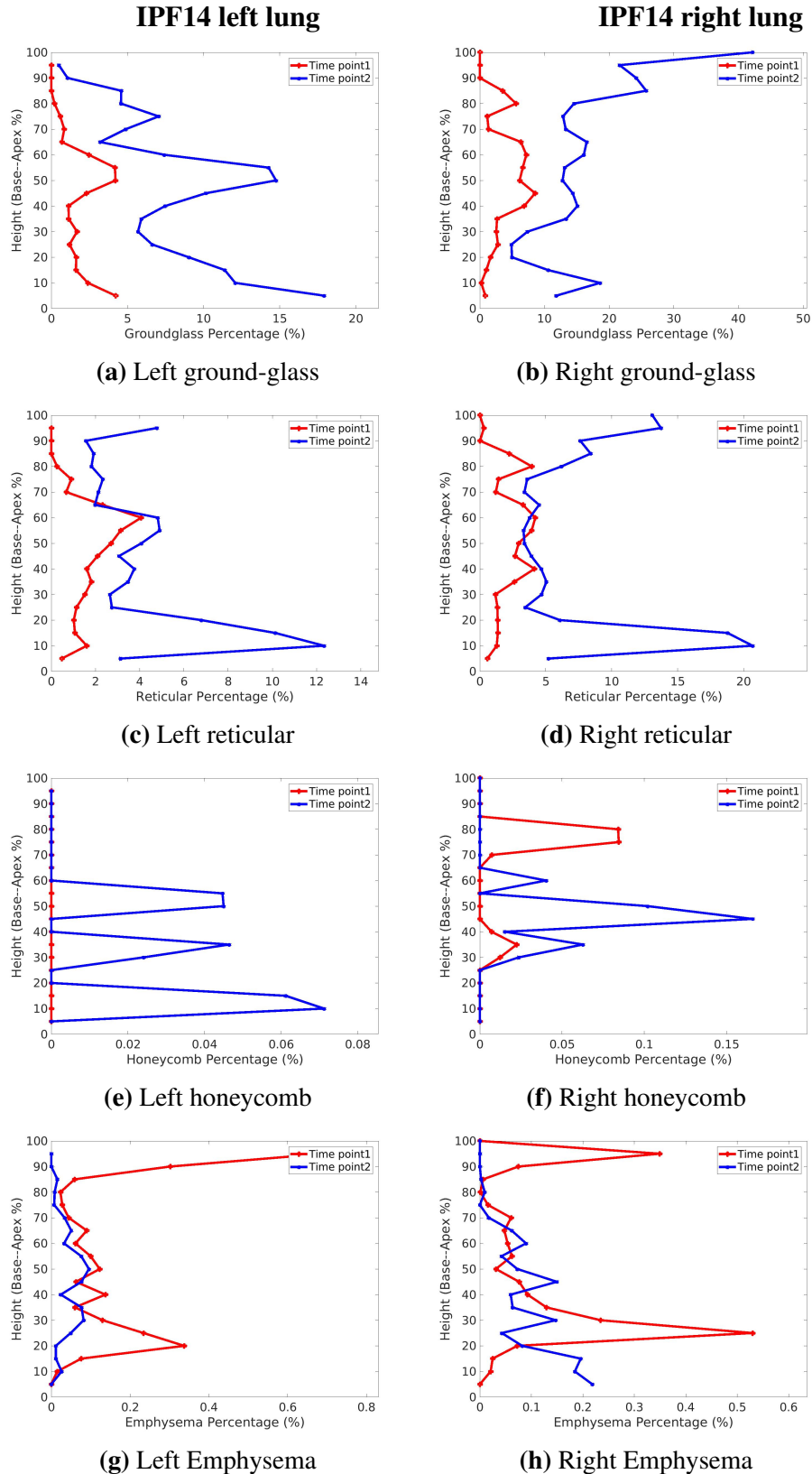


Figure A.8: Volume percentage of each tissue classification plotted against lung height (crano-caudal axis) of case IPF14 in left and right lungs over time. The average percentage was calculated within 5% sections of the lung height from the base to apex. (a) (b) is ground-glass distribution. (c) (d) is reticular distribution. (e) (f) is honeycomb distribution. (g) (h) is emphysema distribution.

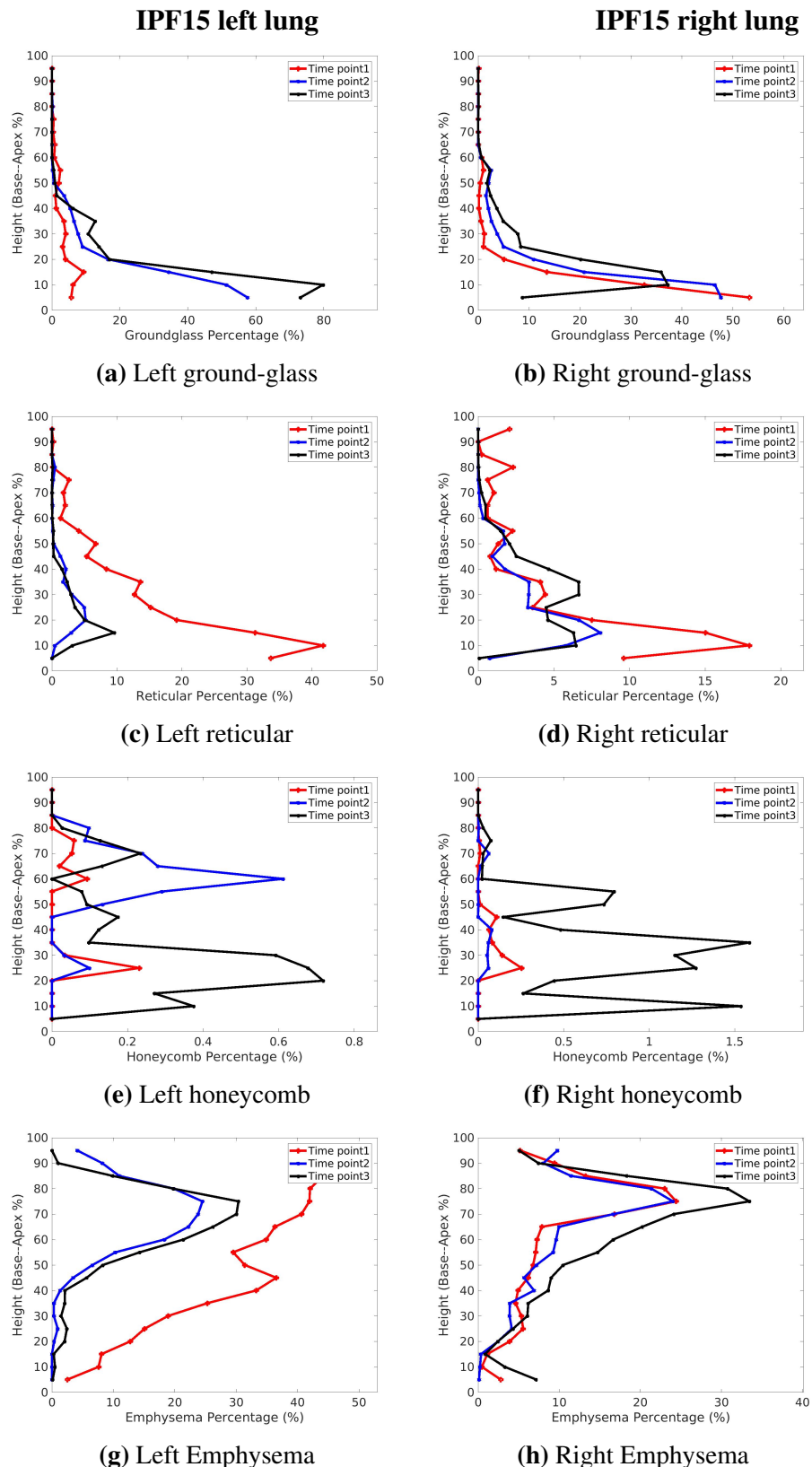


Figure A.9: Volume percentage of each tissue classification plotted against lung height (cranio-caudal axis) of case IPF15 in left and right lungs over time. The average percentage was calculated within 5% sections of the lung height from the base to apex. (a) (b) is ground-glass distribution. (c) (d) is reticular distribution. (e) (f) is honeycomb distribution. (g) (h) is emphysema distribution.

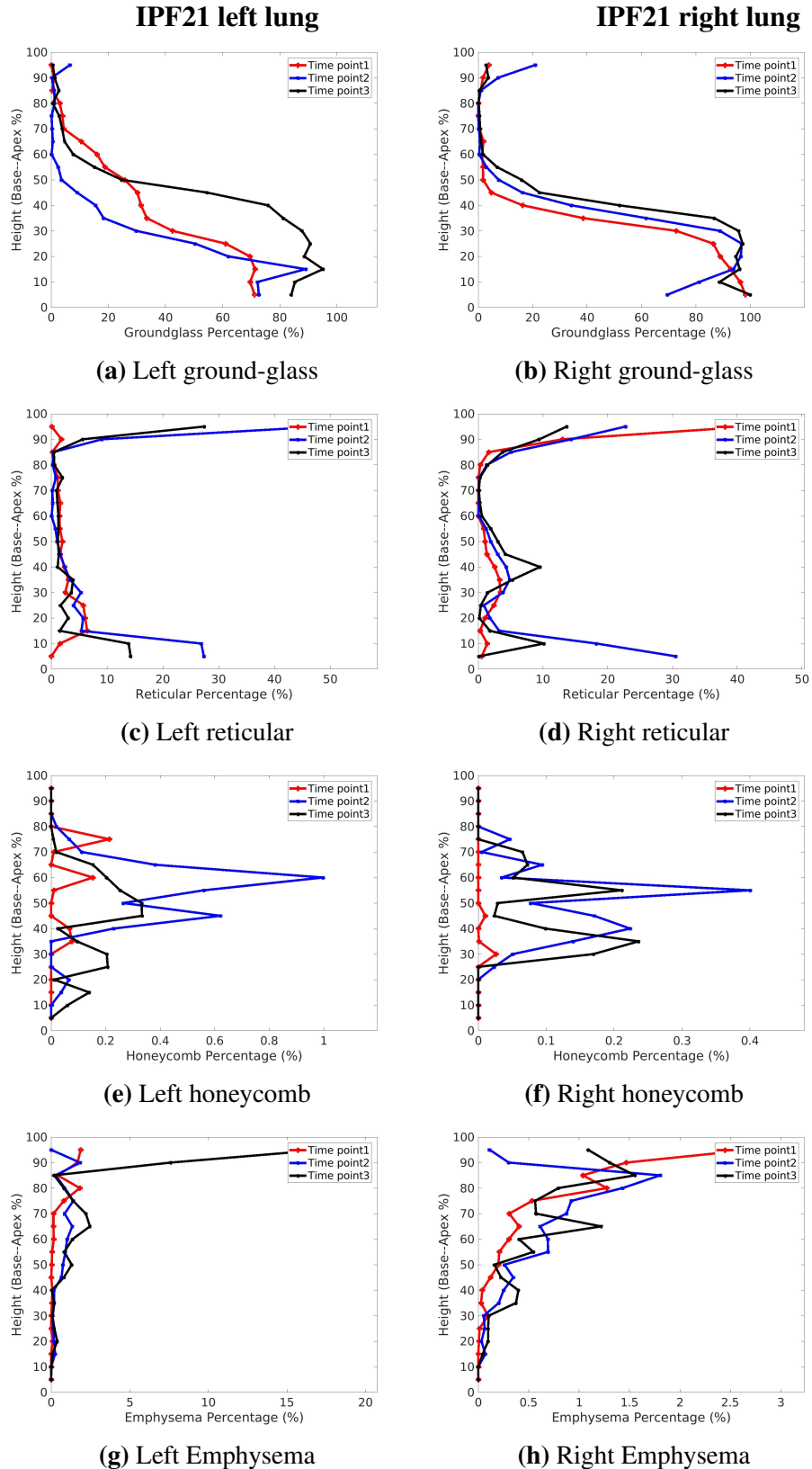


Figure A.10: Volume percentage of each tissue classification plotted against lung height (cranio-caudal axis) of case IPF21 in left and right lungs over time. The average percentage was calculated within 5% sections of the lung height from the base to apex. (a) (b) is ground-glass distribution. (c) (d) is reticular distribution. (e) (f) is honeycomb distribution. (g) (h) is emphysema distribution.

A.2 Dorso-to-ventral distribution over time for each patient

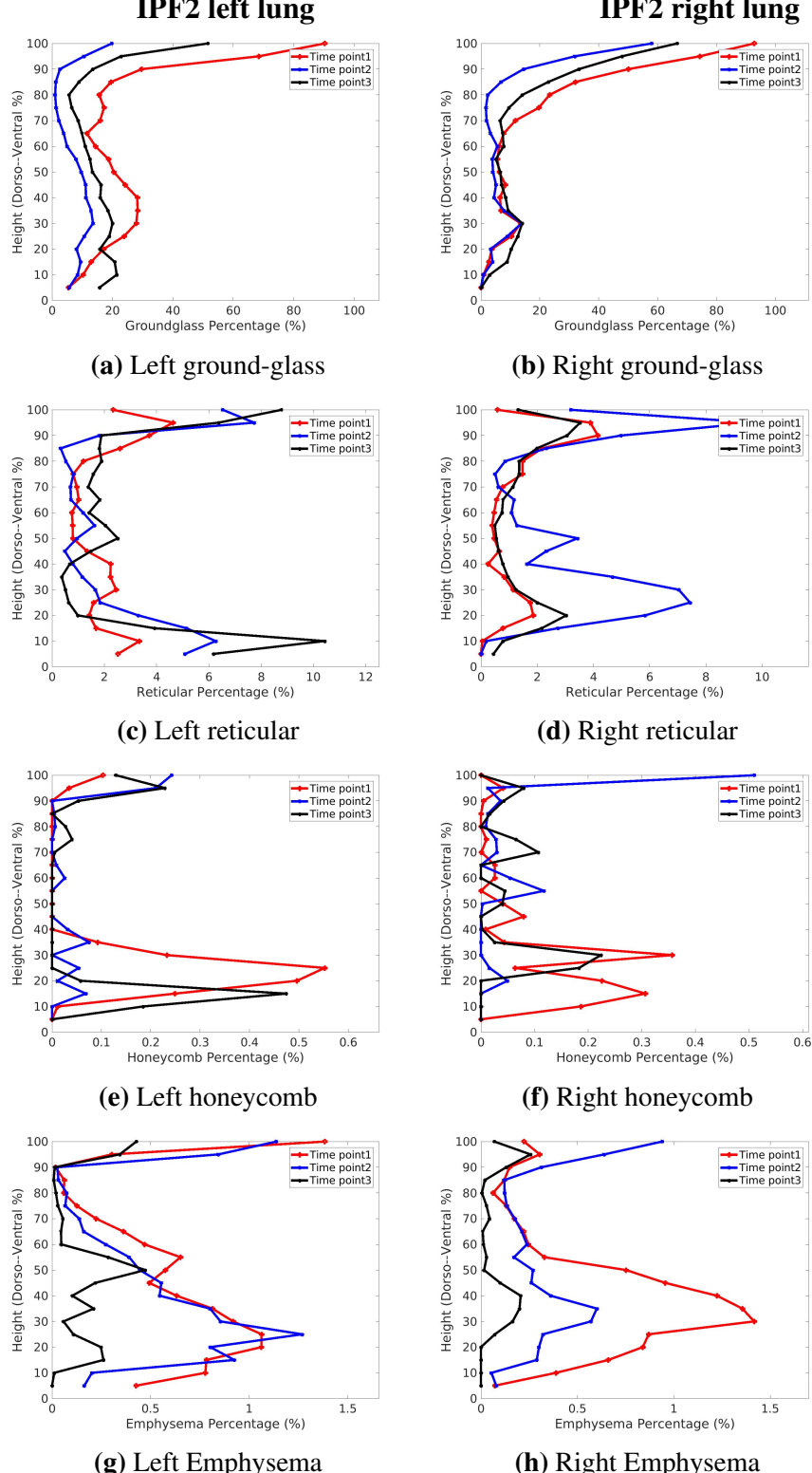


Figure A.11: Volume percentage of each tissue classification plotted in the direction of dorso-ventral axis of case IPF2 in left and right lungs over time. The average percentage was calculated within 5% sections along dorso-ventral axis from the back to front. (a) (b) is ground-glass distribution. (c) (d) is reticular distribution. (e) (f) is honeycomb distribution. (g) (h) is emphysema distribution.

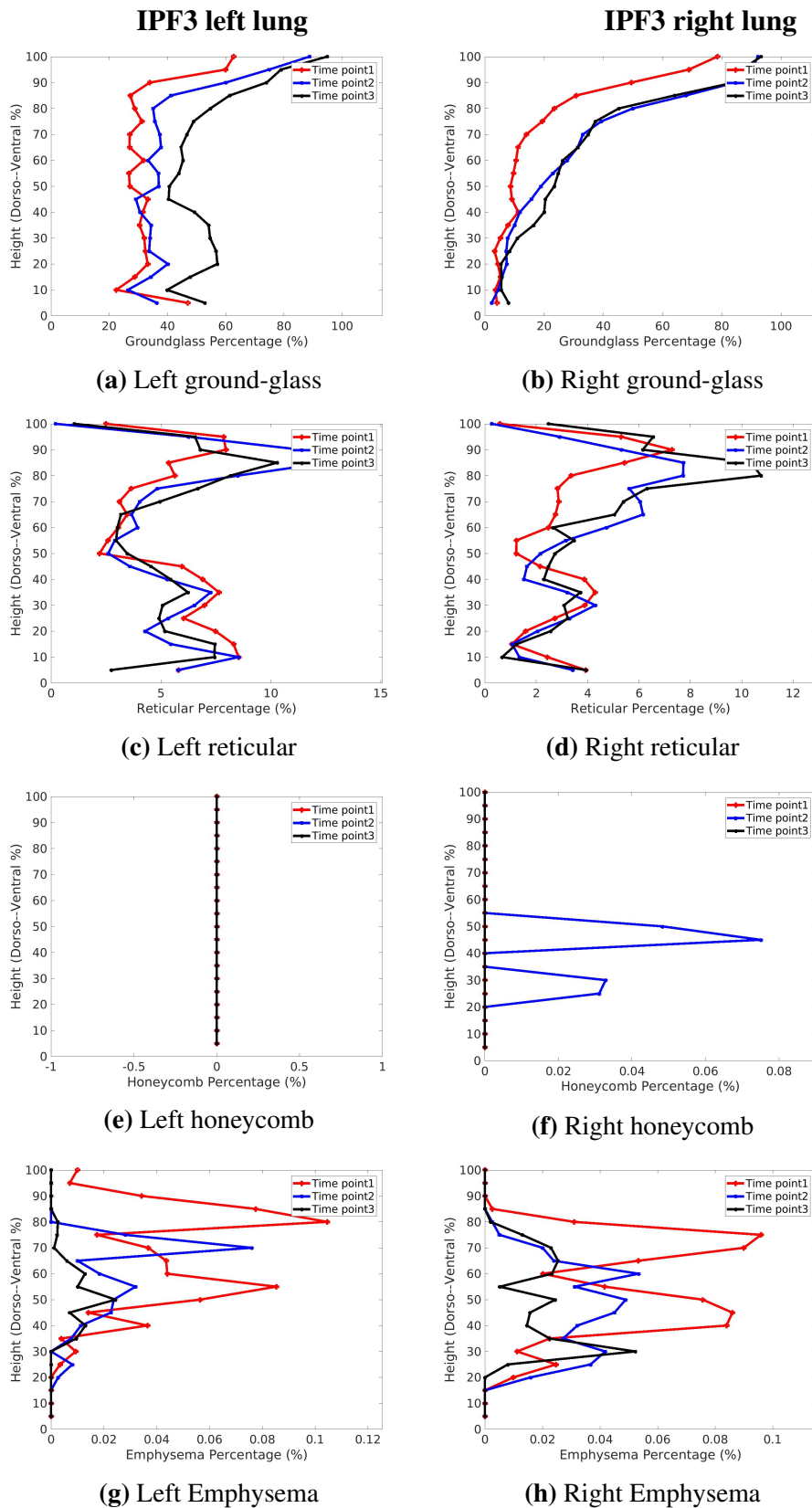


Figure A.12: Volume percentage of each tissue classification plotted in the direction of dorso-ventral axis of case IPF3 in left and right lungs over time. The average percentage was calculated within 5% sections along dorso-ventral axis from the back to front. (a) (b) is ground-glass distribution. (c) (d) is reticular distribution. (e) (f) is honeycomb distribution. (g) (h) is emphysema distribution.

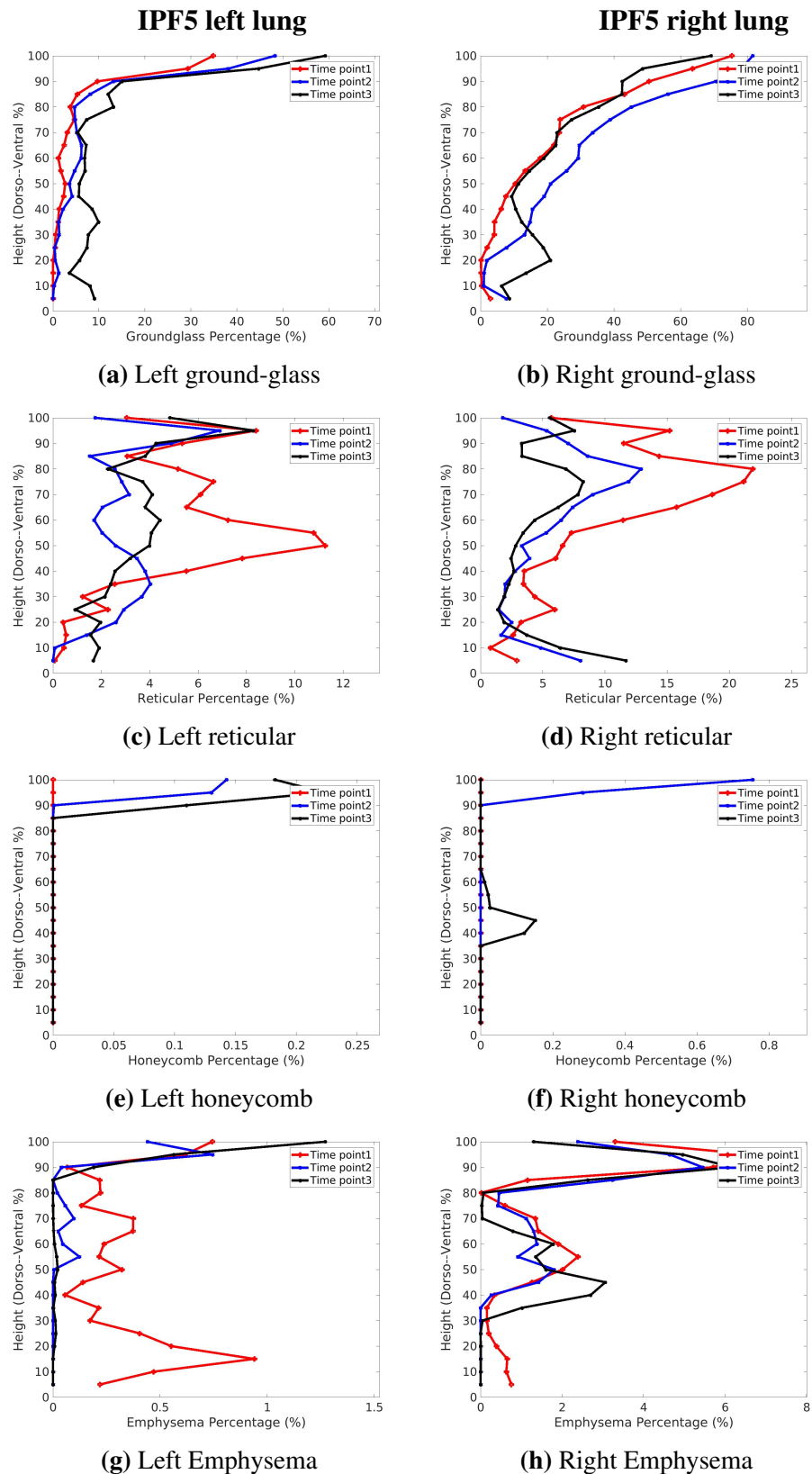


Figure A.13: Volume percentage of each tissue classification plotted in the direction of dorso-ventral axis of case IPF5 in left and right lungs over time. The average percentage was calculated within 5% sections along dorso-ventral axis from the back to front. (a) (b) is ground-glass distribution. (c) (d) is reticular distribution. (e) (f) is honeycomb distribution. (g) (h) is emphysema distribution.

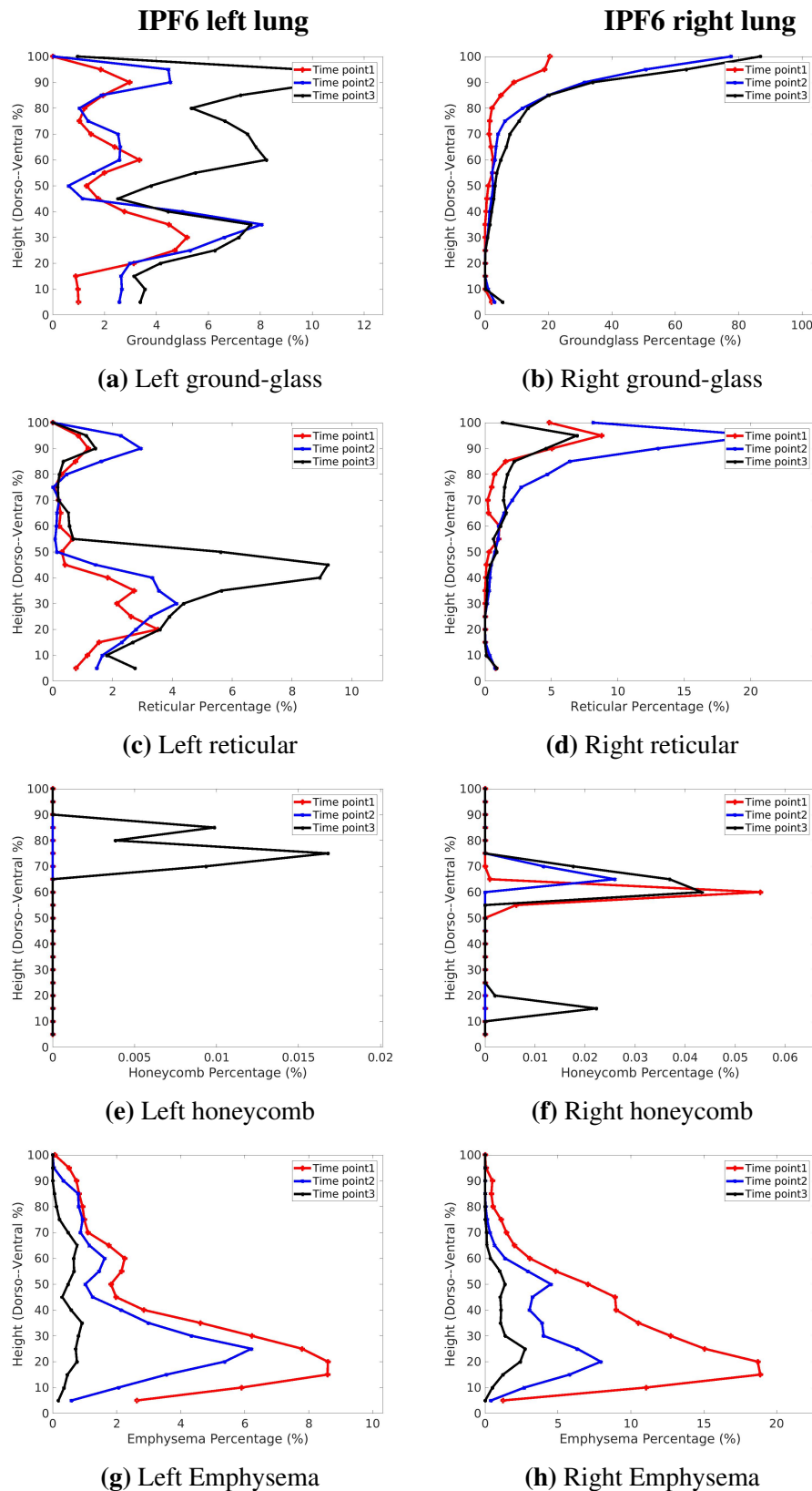


Figure A.14: Volume percentage of each tissue classification plotted in the direction of dorso-ventral axis of case IPF6 in left and right lungs over time. The average percentage was calculated within 5% sections along dorso-ventral axis from the back to front. (a) (b) is ground-glass distribution. (c) (d) is reticular distribution. (e) (f) is honeycomb distribution. (g) (h) is emphysema distribution.

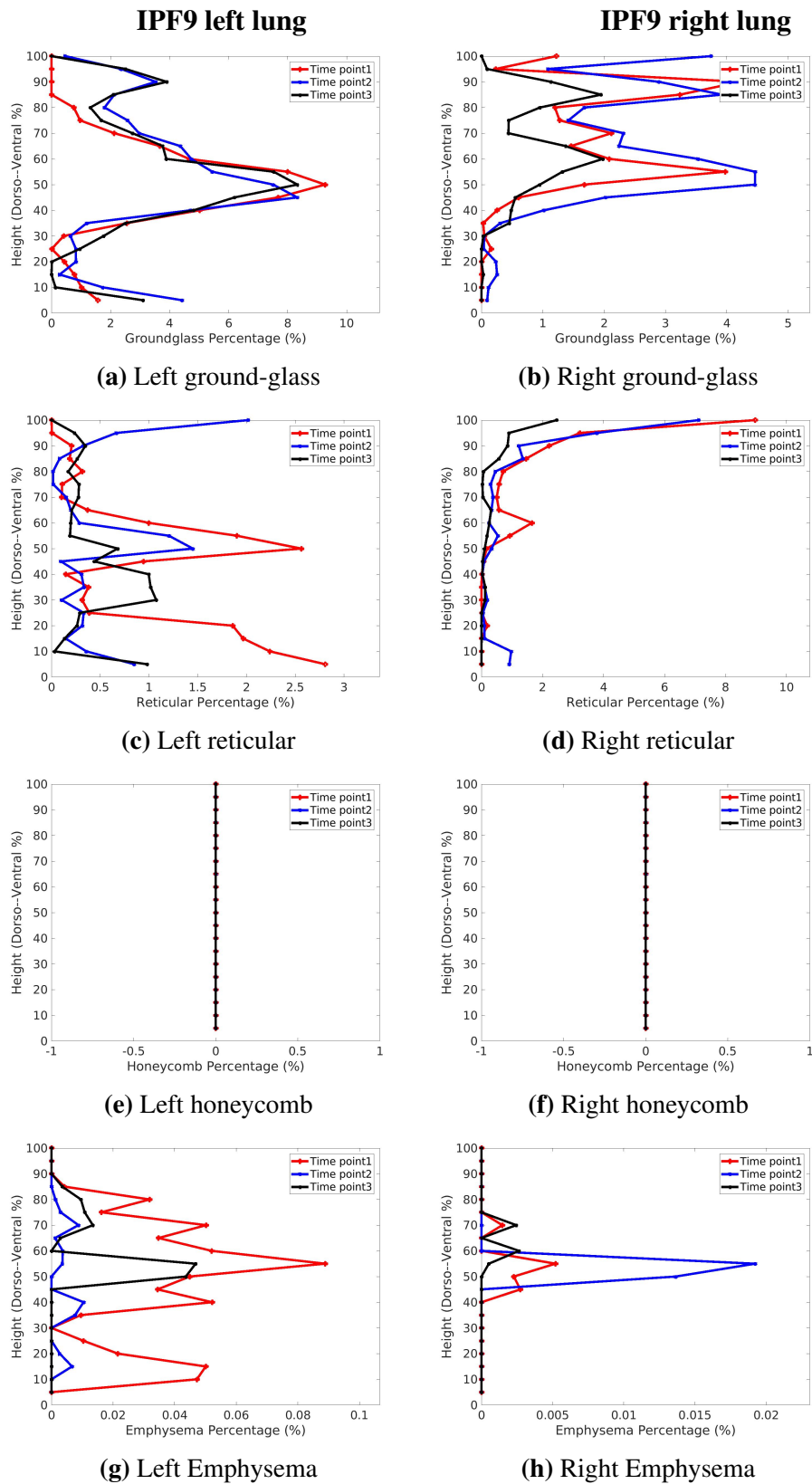


Figure A.15: Volume percentage of each tissue classification plotted in the direction of dorso-ventral axis of case IPF9 in left and right lungs over time. The average percentage was calculated within 5% sections along dorso-ventral axis from the back to front. (a) (b) is ground-glass distribution. (c) (d) is reticular distribution. (e) (f) is honeycomb distribution. (g) (h) is emphysema distribution.

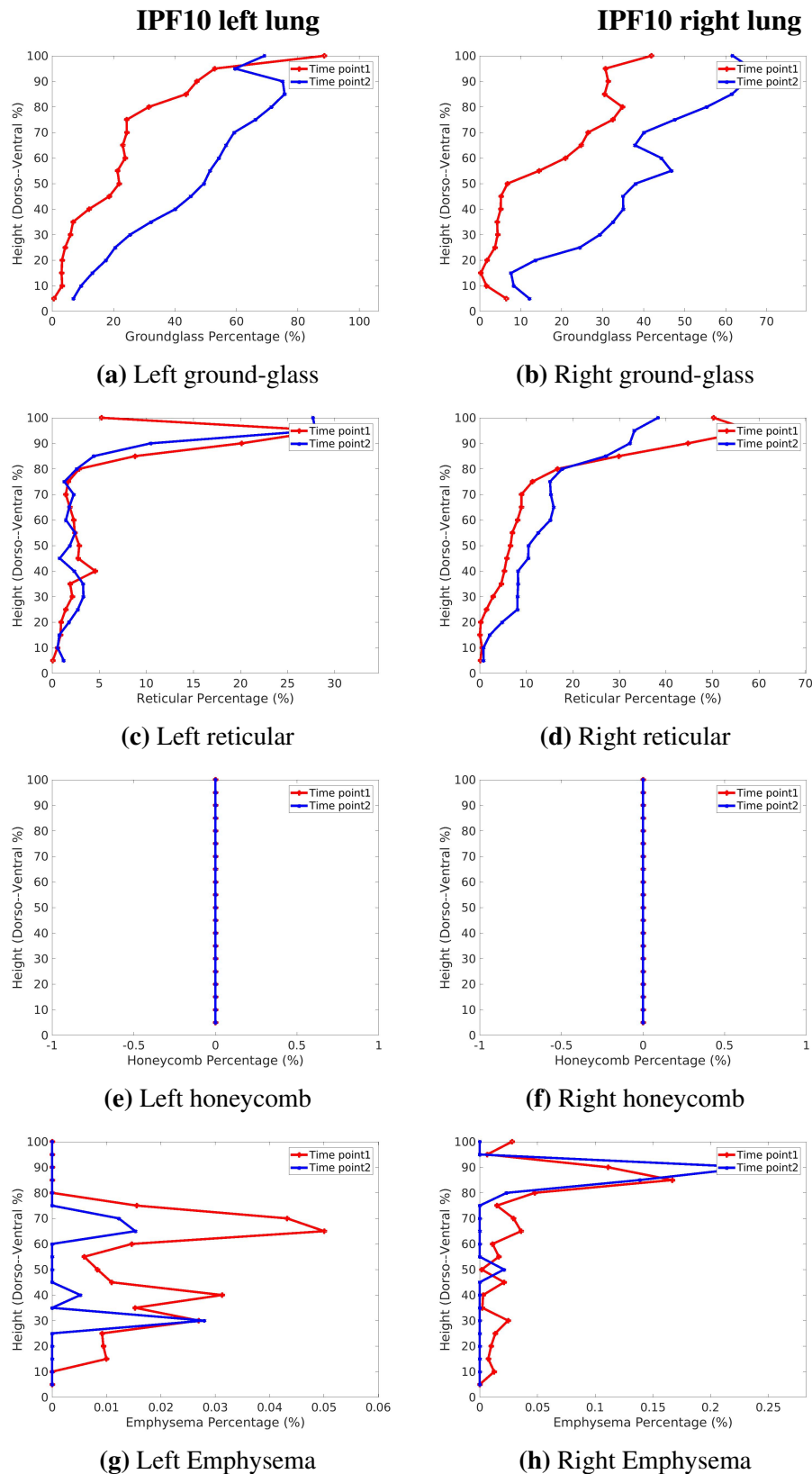


Figure A.16: Volume percentage of each tissue classification plotted in the direction of dorso-ventral axis of case IPF10 in left and right lungs over time. The average percentage was calculated within 5% sections along dorso-ventral axis from the back to front. (a) (b) is ground-glass distribution. (c) (d) is reticular distribution. (e) (f) is honeycomb distribution. (g) (h) is emphysema distribution.

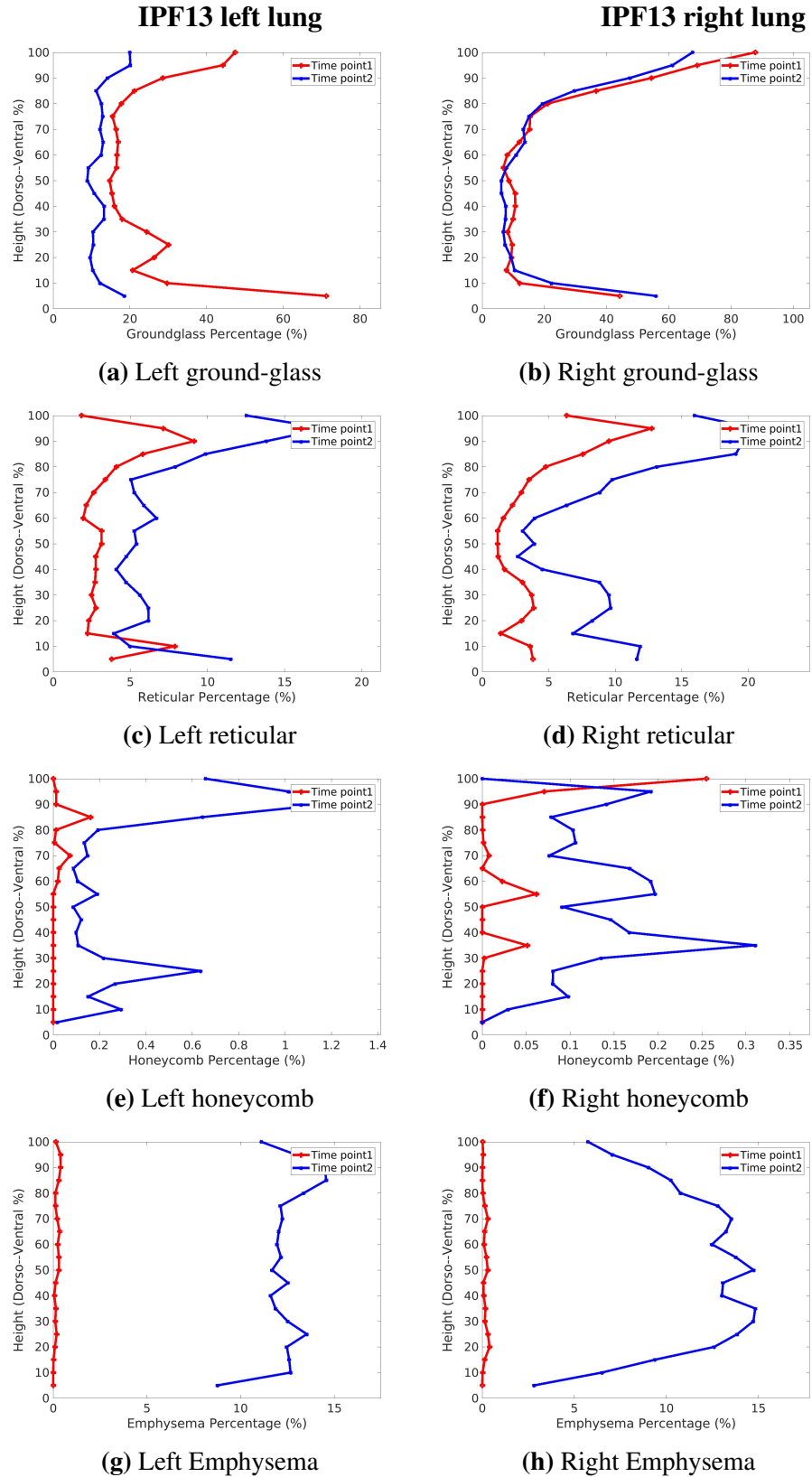


Figure A.17: Volume percentage of each tissue classification plotted in the direction of dorso-ventral axis of case IPF13 in left and right lungs over time. The average percentage was calculated within 5% sections along dorso-ventral axis from the back to front. (a) (b) is ground-glass distribution. (c) (d) is reticular distribution. (e) (f) is honeycomb distribution. (g) (h) is emphysema distribution.

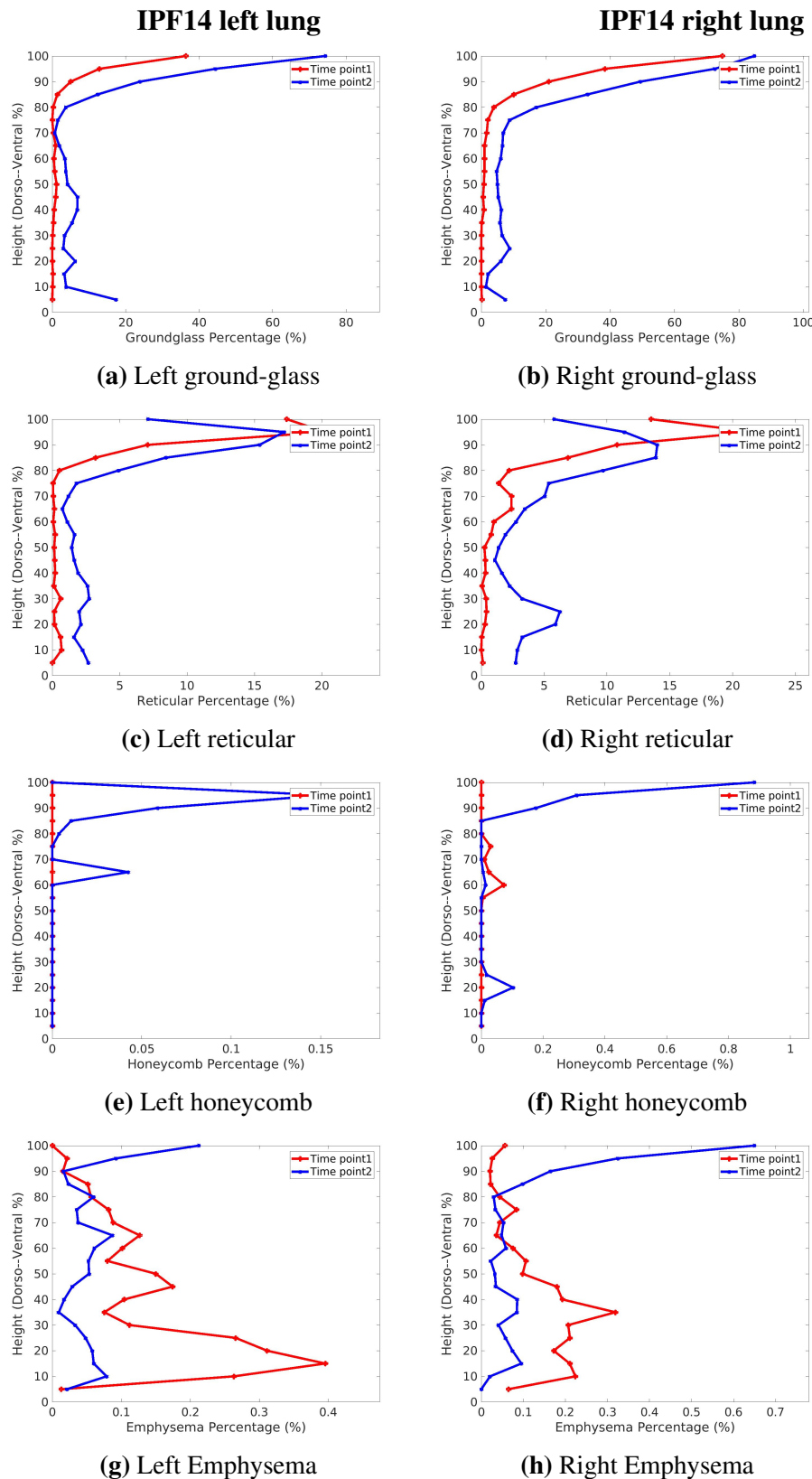


Figure A.18: Volume percentage of each tissue classification plotted in the direction of dorso-ventral axis of case IPF14 in left and right lungs over time. The average percentage was calculated within 5% sections along dorso-ventral axis from the back to front. (a) (b) is ground-glass distribution. (c) (d) is reticular distribution. (e) (f) is honeycomb distribution. (g) (h) is emphysema distribution.

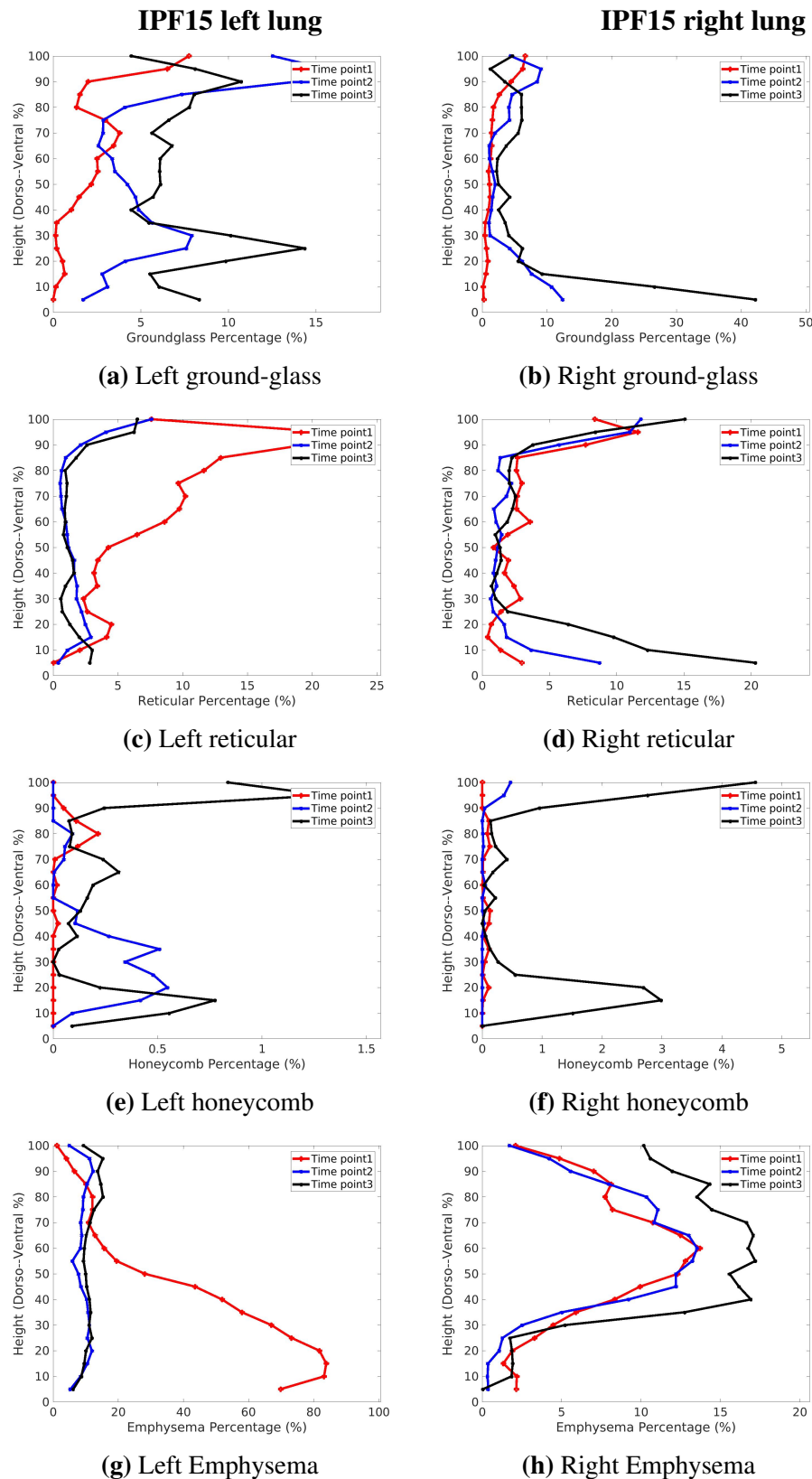


Figure A.19: Volume percentage of each tissue classification plotted in the direction of dorso-ventral axis of case IPF15 in left and right lungs over time. The average percentage was calculated within 5% sections along dorso-ventral axis from the back to front. (a) (b) is ground-glass distribution. (c) (d) is reticular distribution. (e) (f) is honeycomb distribution. (g) (h) is emphysema distribution.

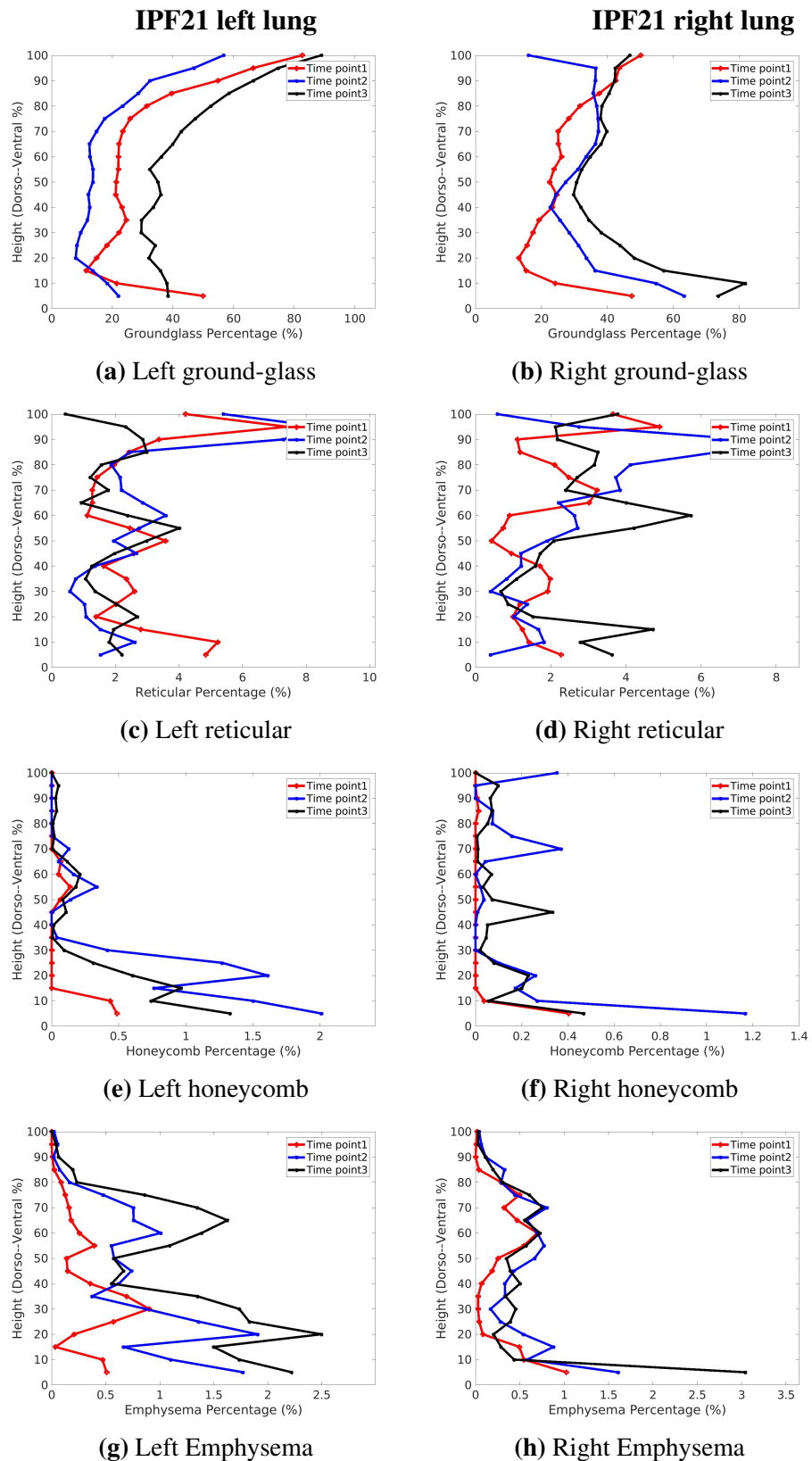


Figure A.20: Volume percentage of each tissue classification plotted in the direction of dorso-ventral axis of case IPF21 in left and right lungs over time. The average percentage was calculated within 5% sections along dorso-ventral axis from the back to front. (a) (b) is ground-glass distribution. (c) (d) is reticular distribution. (e) (f) is honeycomb distribution. (g) (h) is emphysema distribution.

A.3 Lobar distribution over time for each patient

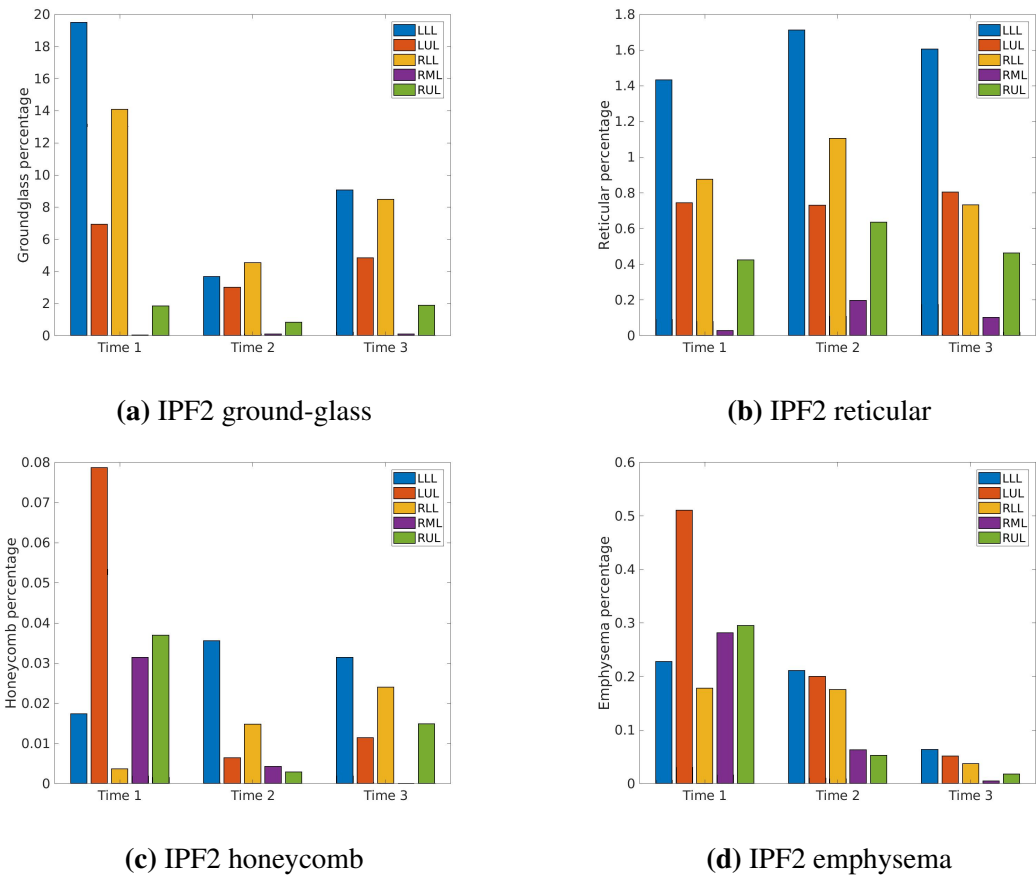


Figure A.21: Lobar distribution of disease CT patterns of case IPF2 diagnosed with IPF over time. The tissue percentage in different lobe is shown in different color, and each bar represents the volume percentage of the CT pattern for one lobe. (a) Ground-glass lobar distribution. (b) Reticular lobar distribution. (c) Honeycomb lobar distribution. (d) Emphysema lobar distribution.

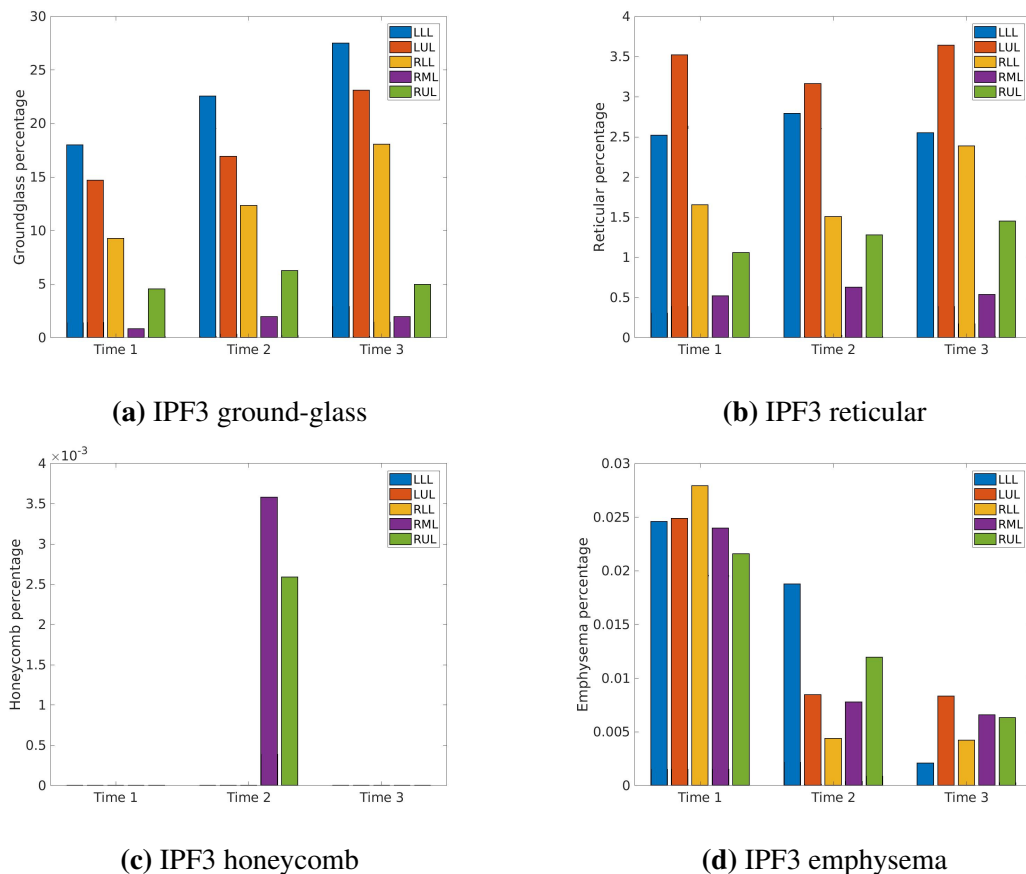


Figure A.22: Lobar distribution of disease CT patterns of case IPF3 diagnosed with IPF over time. The tissue percentage in different lobe is shown in different color, and each bar represents the volume percentage of the CT pattern for one lobe. (a) Ground-glass lobar distribution. (b) Reticular lobar distribution. (c) Honeycomb lobar distribution. (d) Emphysema lobar distribution.

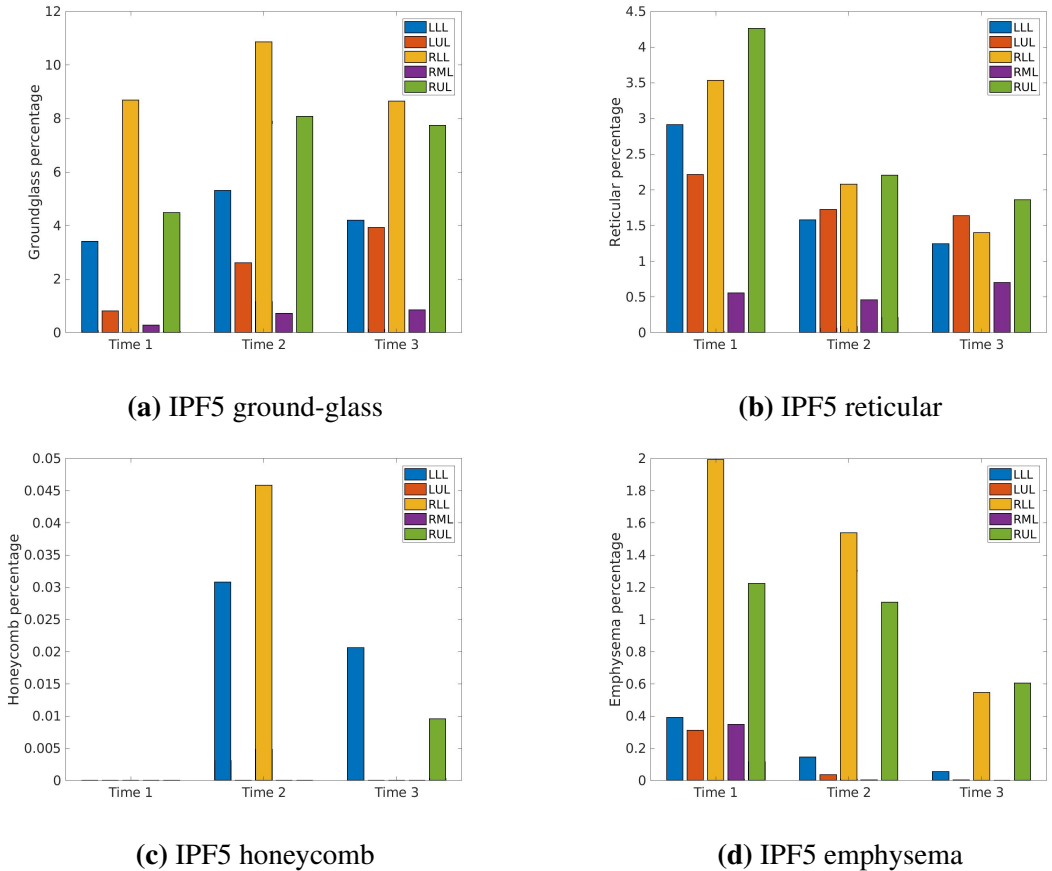


Figure A.23: Lobar distribution of disease CT patterns of case IPF5 diagnosed with IPF over time. The tissue percentage in different lobe is shown in different color, and each bar represents the volume percentage of the CT pattern for one lobe. (a) Ground-glass lobar distribution. (b) Reticular lobar distribution. (c) Honeycomb lobar distribution. (d) Emphysema lobar distribution.

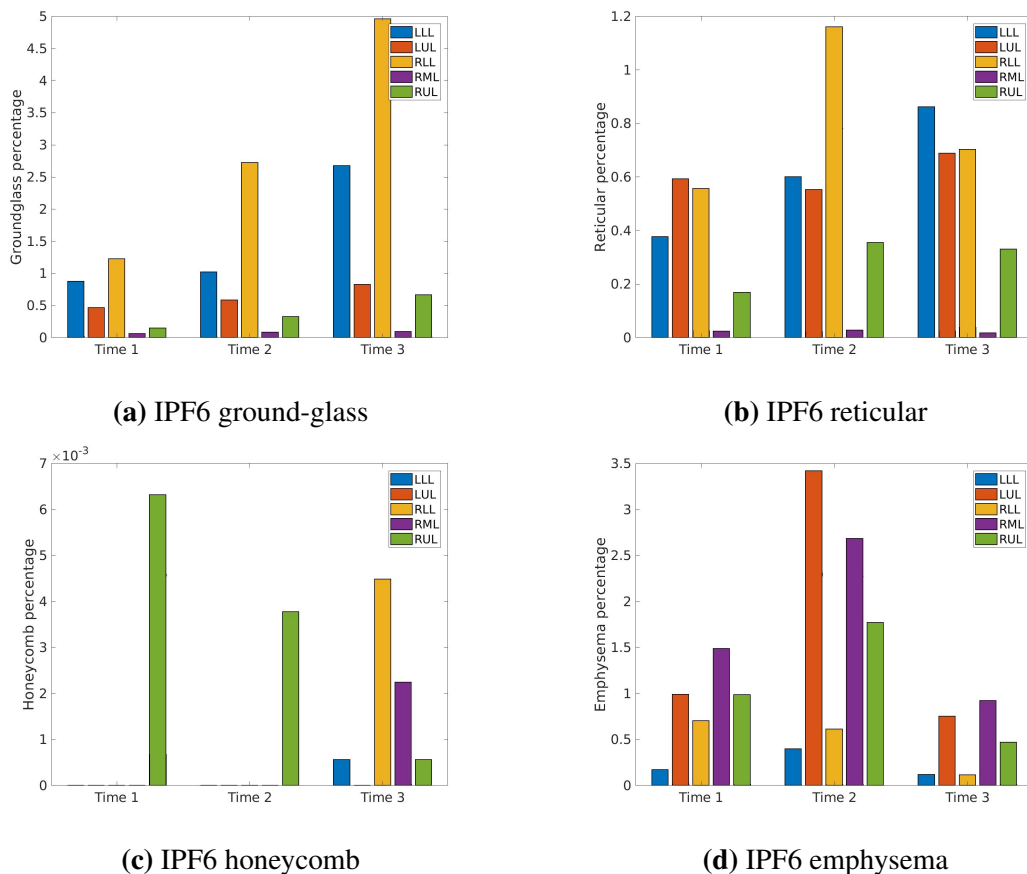


Figure A.24: Lobar distribution of disease CT patterns of case IPF6 diagnosed with IPF over time. The tissue percentage in different lobe is shown in different color, and each bar represents the volume percentage of the CT pattern for one lobe. (a) Ground-glass lobar distribution. (b) Reticular lobar distribution. (c) Honeycomb lobar distribution. (d) Emphysema lobar distribution.

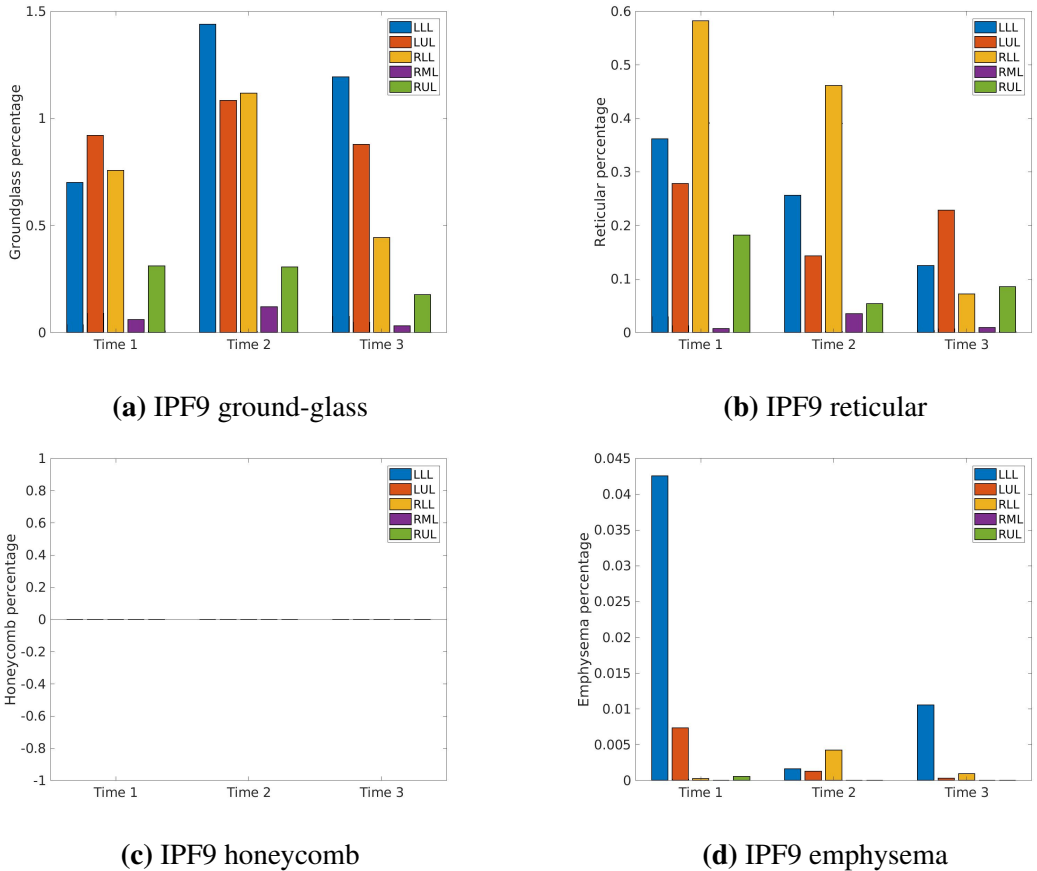


Figure A.25: Lobar distribution of disease CT patterns of case IPF9 diagnosed with IPF over time. The tissue percentage in different lobe is shown in different color, and each bar represents the volume percentage of the CT pattern for one lobe. (a) Ground-glass lobar distribution. (b) Reticular lobar distribution. (c) Honeycomb lobar distribution. (d) Emphysema lobar distribution.

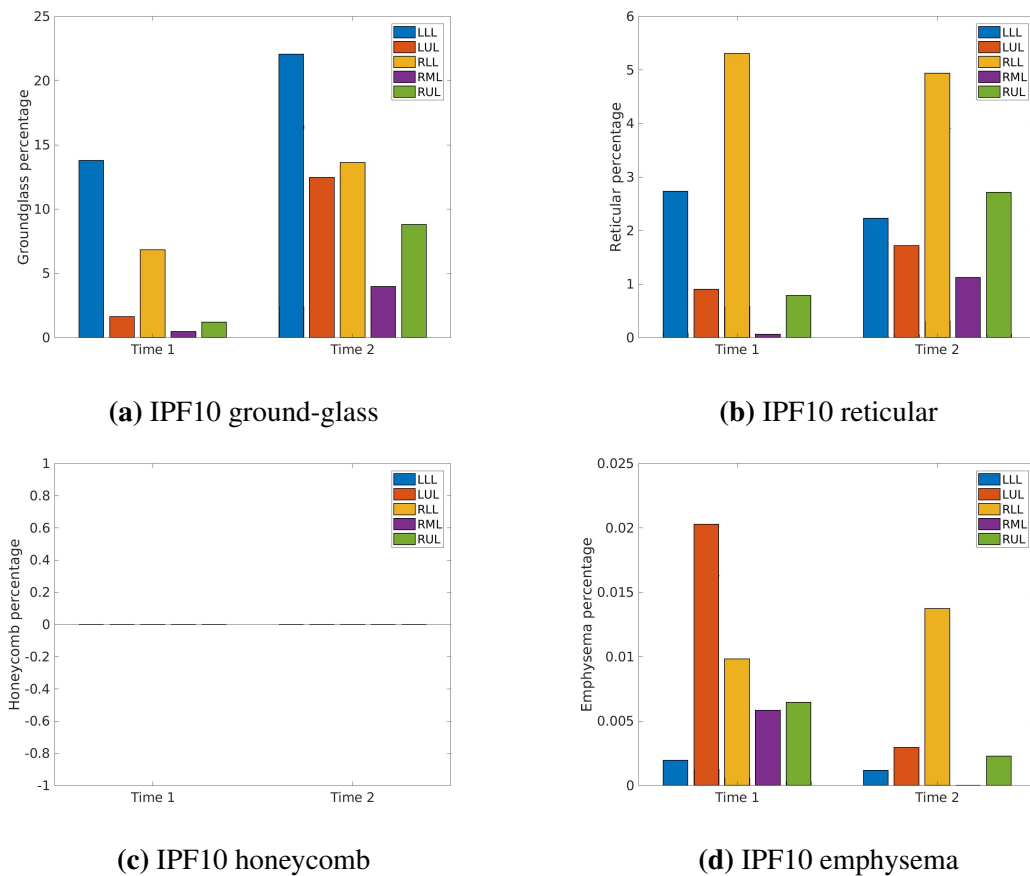


Figure A.26: Lobar distribution of disease CT patterns of case IPF10 diagnosed with IPF over time. The tissue percentage in different lobe is shown in different color, and each bar represents the volume percentage of the CT pattern for one lobe. (a) Ground-glass lobar distribution. (b) Reticular lobar distribution. (c) Honeycomb lobar distribution. (d) Emphysema lobar distribution.

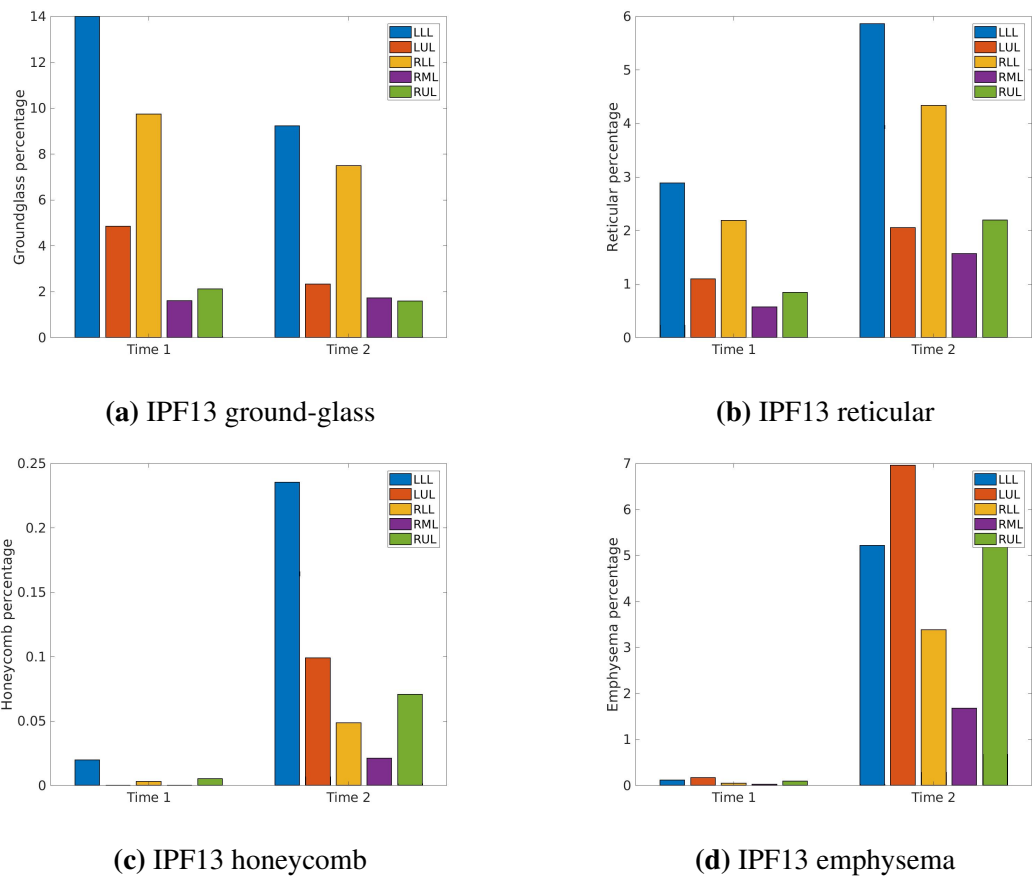


Figure A.27: Lobar distribution of disease CT patterns of case IPF13 diagnosed with IPF over time. The tissue percentage in different lobe is shown in different color, and each bar represents the volume percentage of the CT pattern for one lobe. (a) Ground-glass lobar distribution. (b) Reticular lobar distribution. (c) Honeycomb lobar distribution. (d) Emphysema lobar distribution.

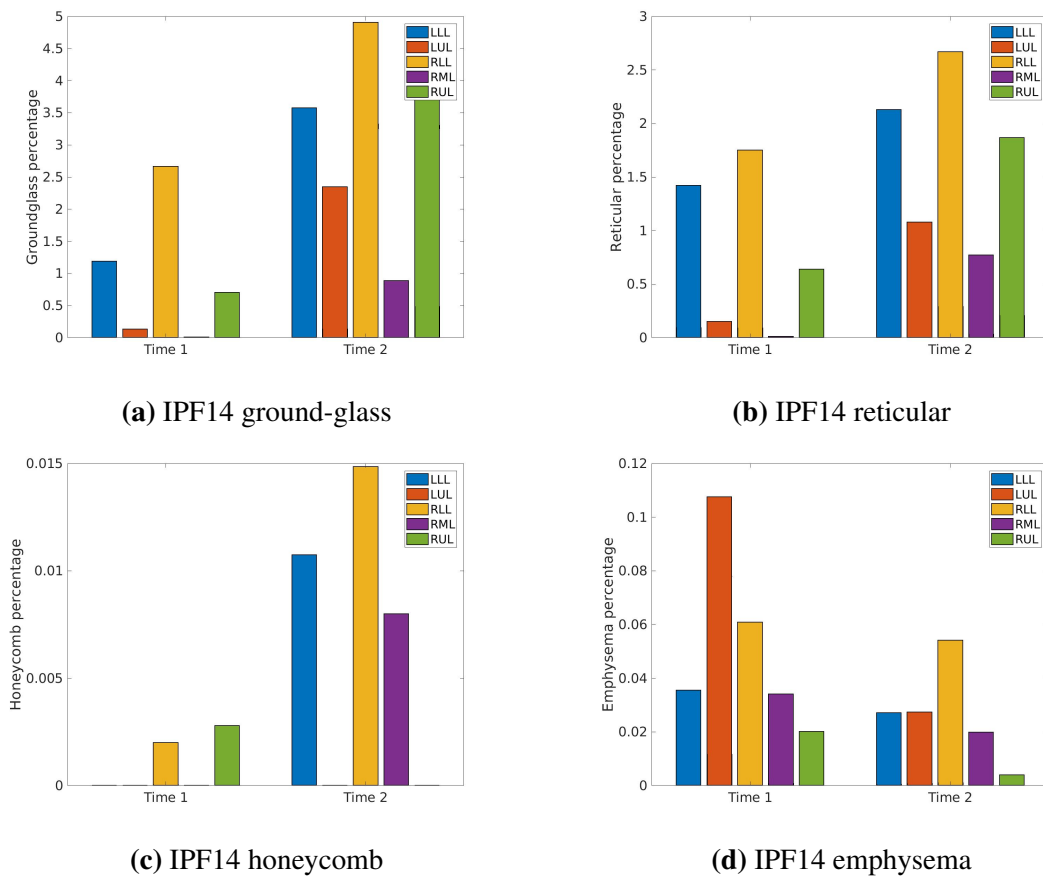


Figure A.28: Lobar distribution of disease CT patterns of case IPF14 diagnosed with IPF over time. The tissue percentage in different lobe is shown in different color, and each bar represents the volume percentage of the CT pattern for one lobe. (a) Ground-glass lobar distribution. (b) Reticular lobar distribution. (c) Honeycomb lobar distribution. (d) Emphysema lobar distribution.

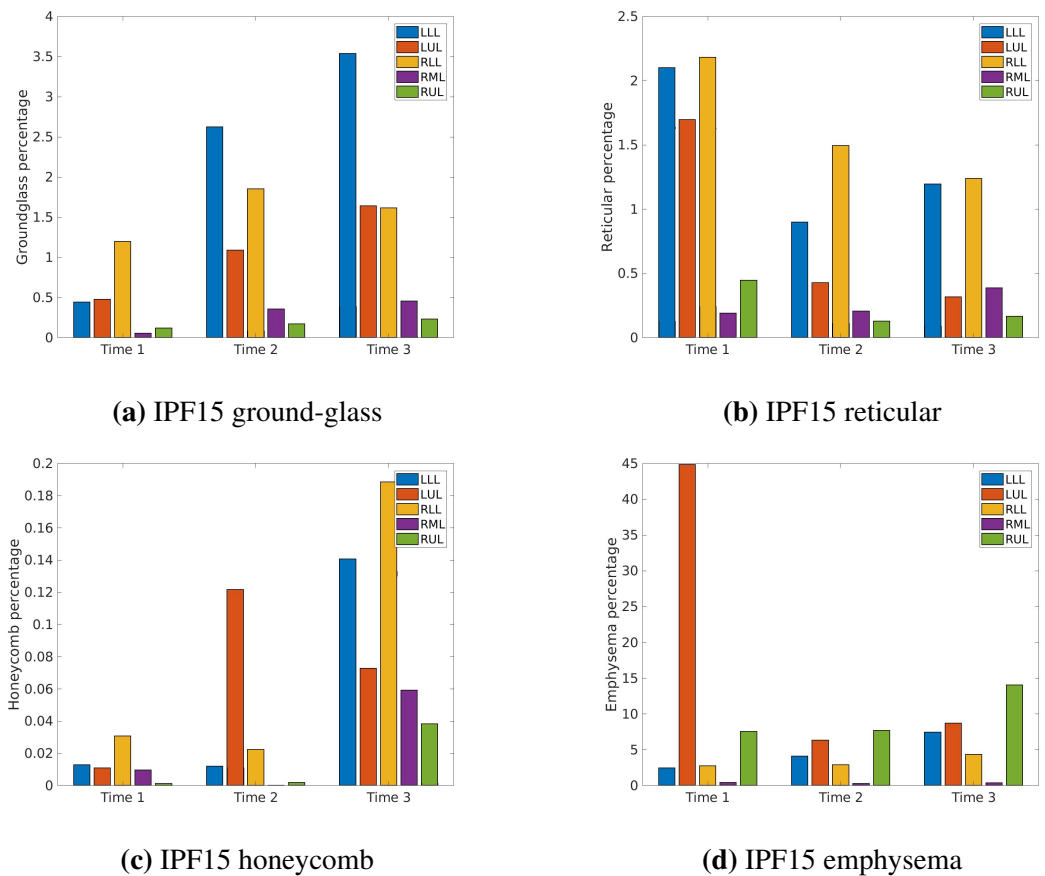


Figure A.29: Lobular distribution of disease CT patterns of case IPF15 diagnosed with IPF over time. The tissue percentage in different lobe is shown in different color, and each bar represents the volume percentage of the CT pattern for one lobe. (a) Ground-glass lobular distribution. (b) Reticular lobular distribution. (c) Honeycomb lobular distribution. (d) Emphysema lobular distribution.

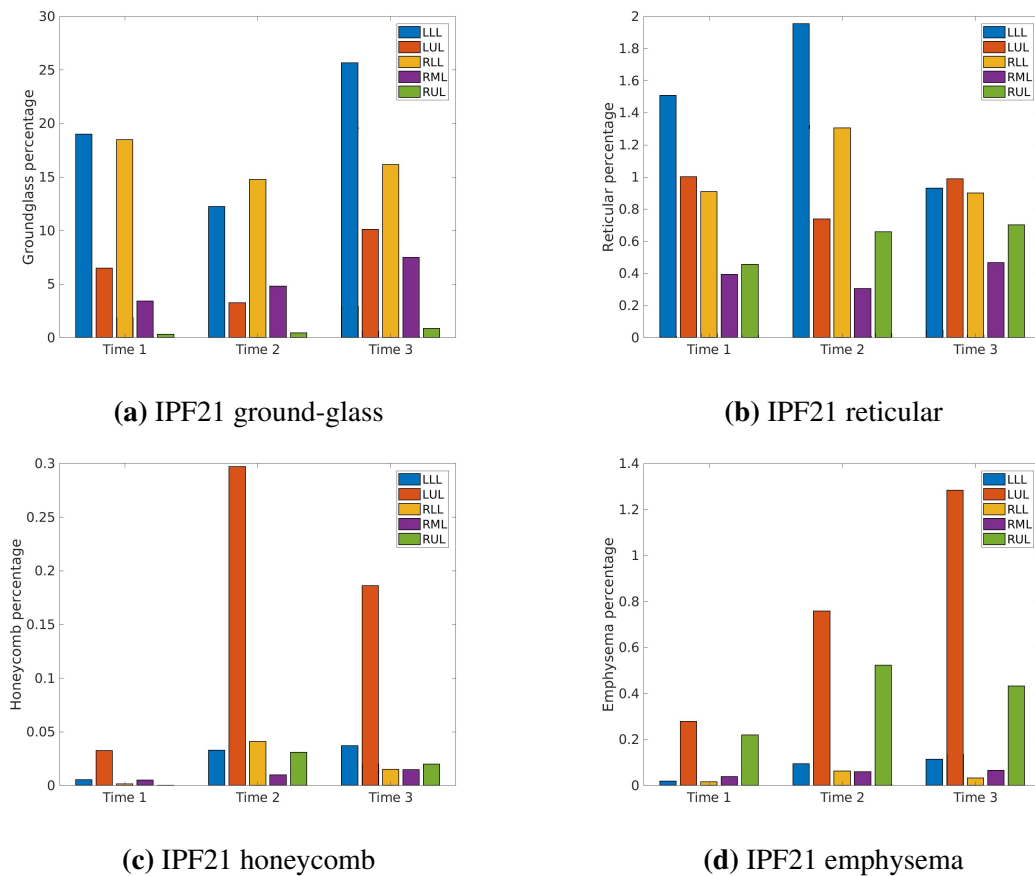


Figure A.30: Lobar distribution of disease CT patterns of case IPF21 diagnosed with IPF over time. The tissue percentage in different lobe is shown in different color, and each bar represents the volume percentage of the CT pattern for one lobe. (a) Ground-glass lobar distribution. (b) Reticular lobar distribution. (c) Honeycomb lobar distribution. (d) Emphysema lobar distribution.

Appendix B

Figures of V/Q ratio and arterial oxygen distribution

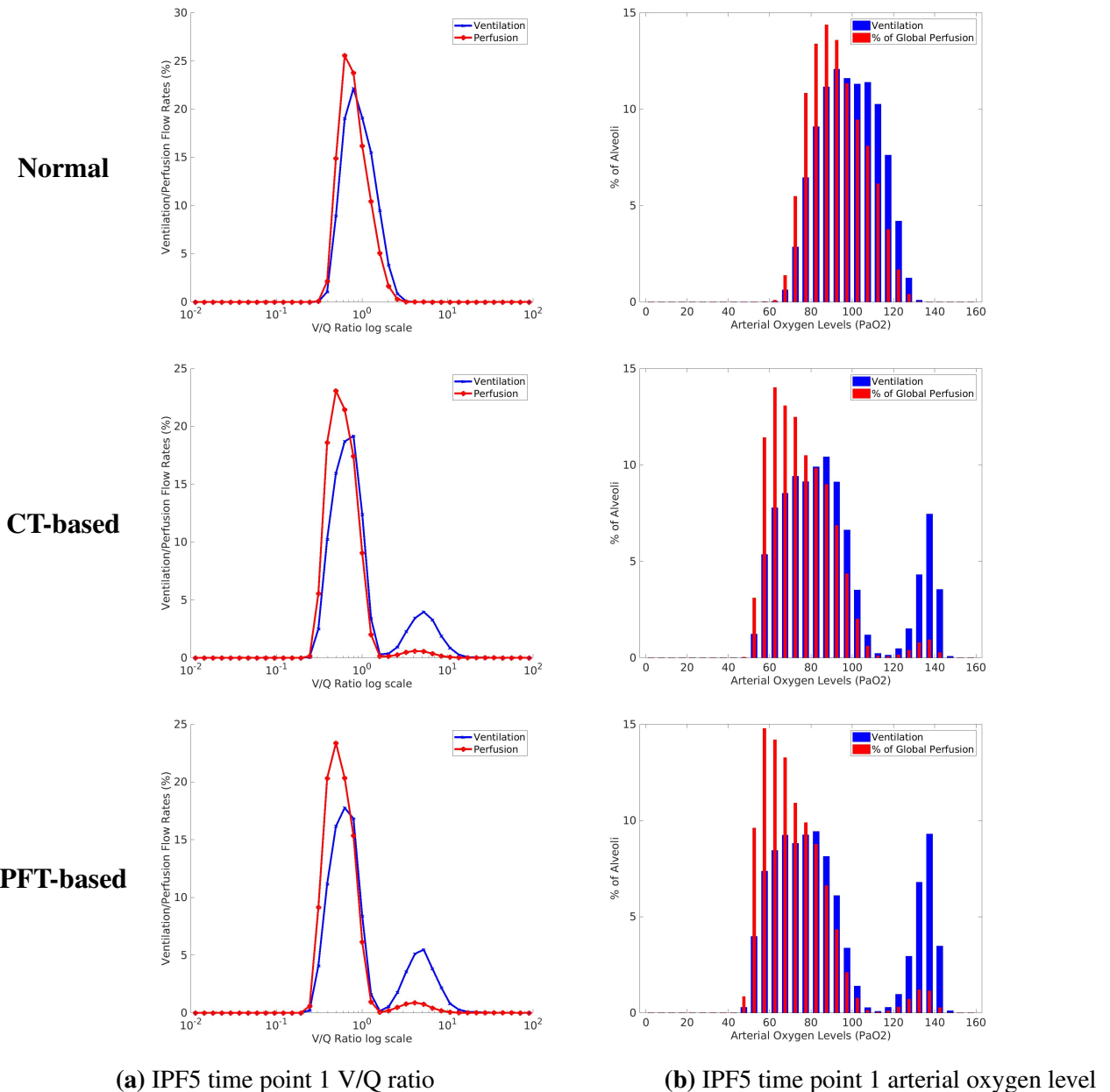
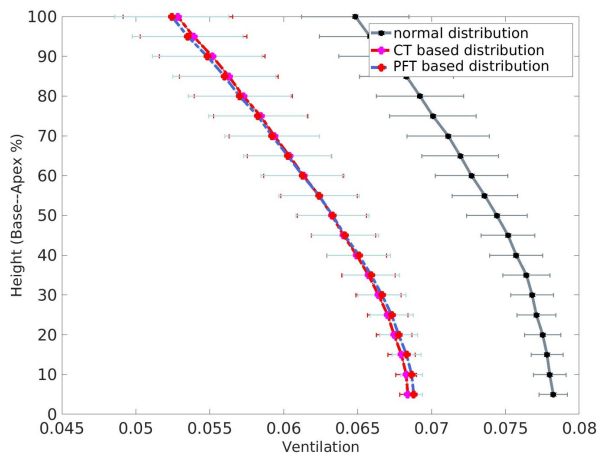
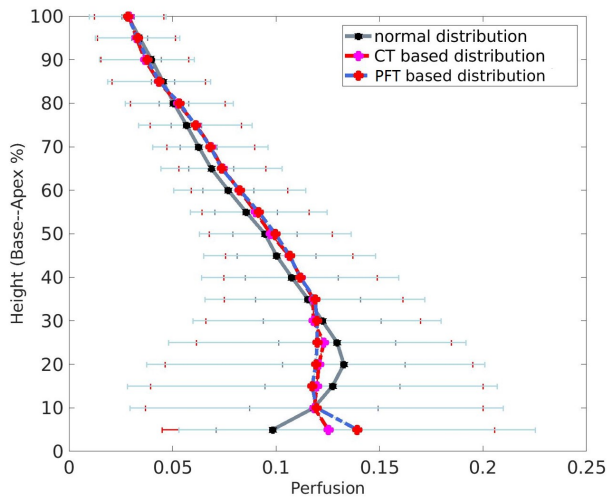


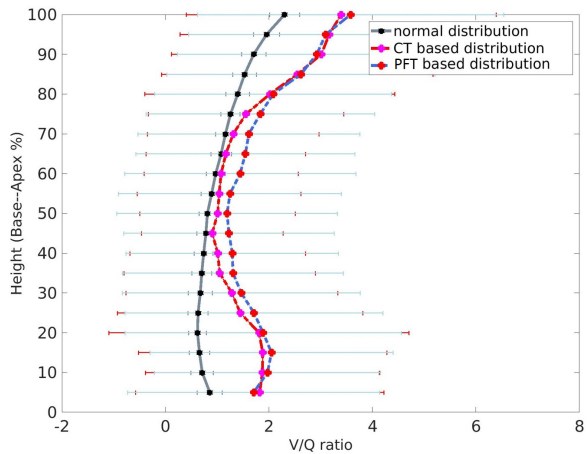
Figure B.1: V/Q ratio distribution and arterial oxygen distribution of normal, CT-based and PFT-based simulation result of the first time point of case IPF5 using MIGET. (a) V and Q flow with respect to V/Q ratio. (b) V and Q percentage with respect to arterial oxygen level.



(a) IPF5 time point 1 ventilation distribution



(b) IPF5 time point 1 perfusion distribution



(c) IPF5 time point 1 V/Q ratio distribution

Figure B.2: Ventilation, perfusion and V/Q ratio distribution against lung height (cranio-caudal axis) of the first time point of case IPF5. (a) Ventilation distribution against lung height. (b) Perfusion distribution against lung height. (c) V/Q ratio distribution against lung height.

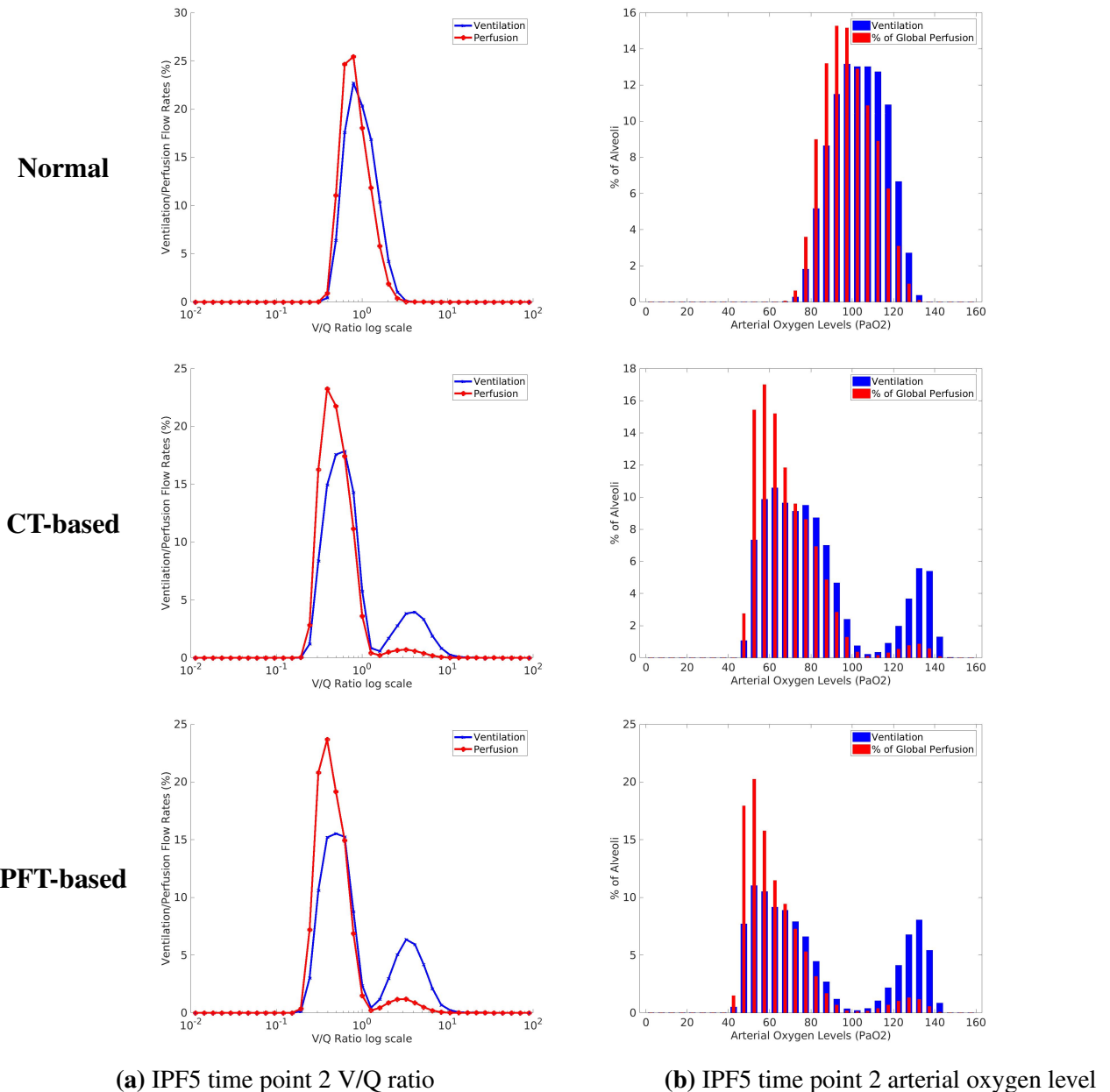
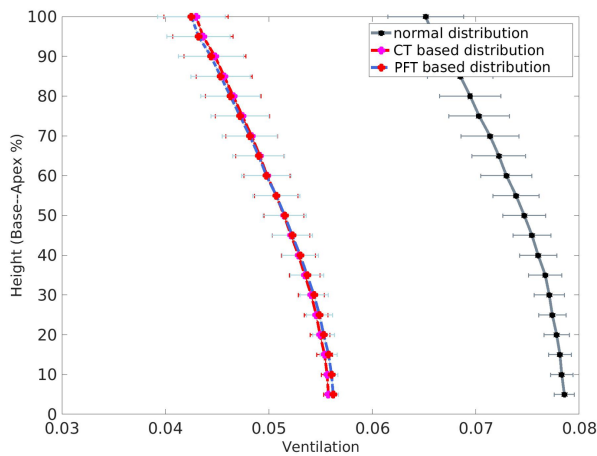
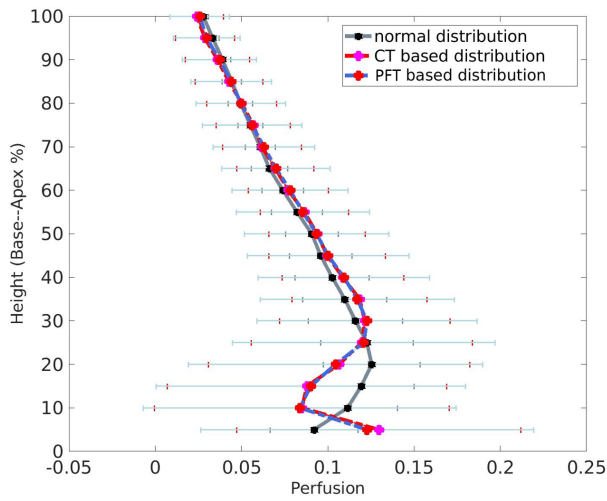


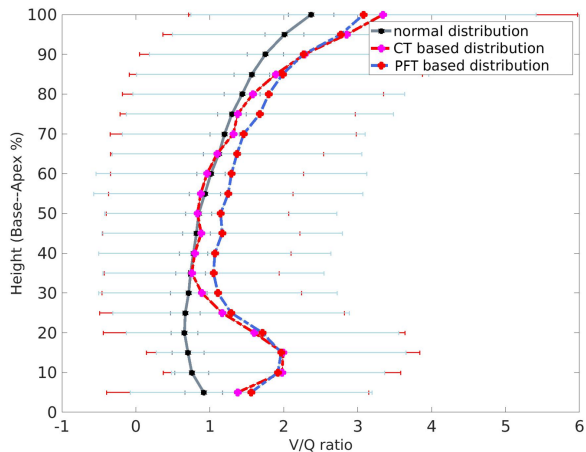
Figure B.3: V/Q ratio distribution and arterial oxygen distribution of normal, CT-based and PFT-based simulation result of the second time point of case IPF5 using MIGET. (a) V and Q flow with respect to V/Q ratio. (b) V and Q percentage with respect to arterial oxygen level.



(a) IPF5 time point 2 ventilation distribution



(b) IPF5 time point 2 perfusion distribution



(c) IPF5 time point 2 V/Q ratio distribution

Figure B.4: Ventilation, perfusion and V/Q ratio distribution against lung height (cranio-caudal axis) of the second time point of case IPF5. (a) Ventilation distribution against lung height. (b) Perfusion distribution against lung height. (c) V/Q ratio distribution against lung height.

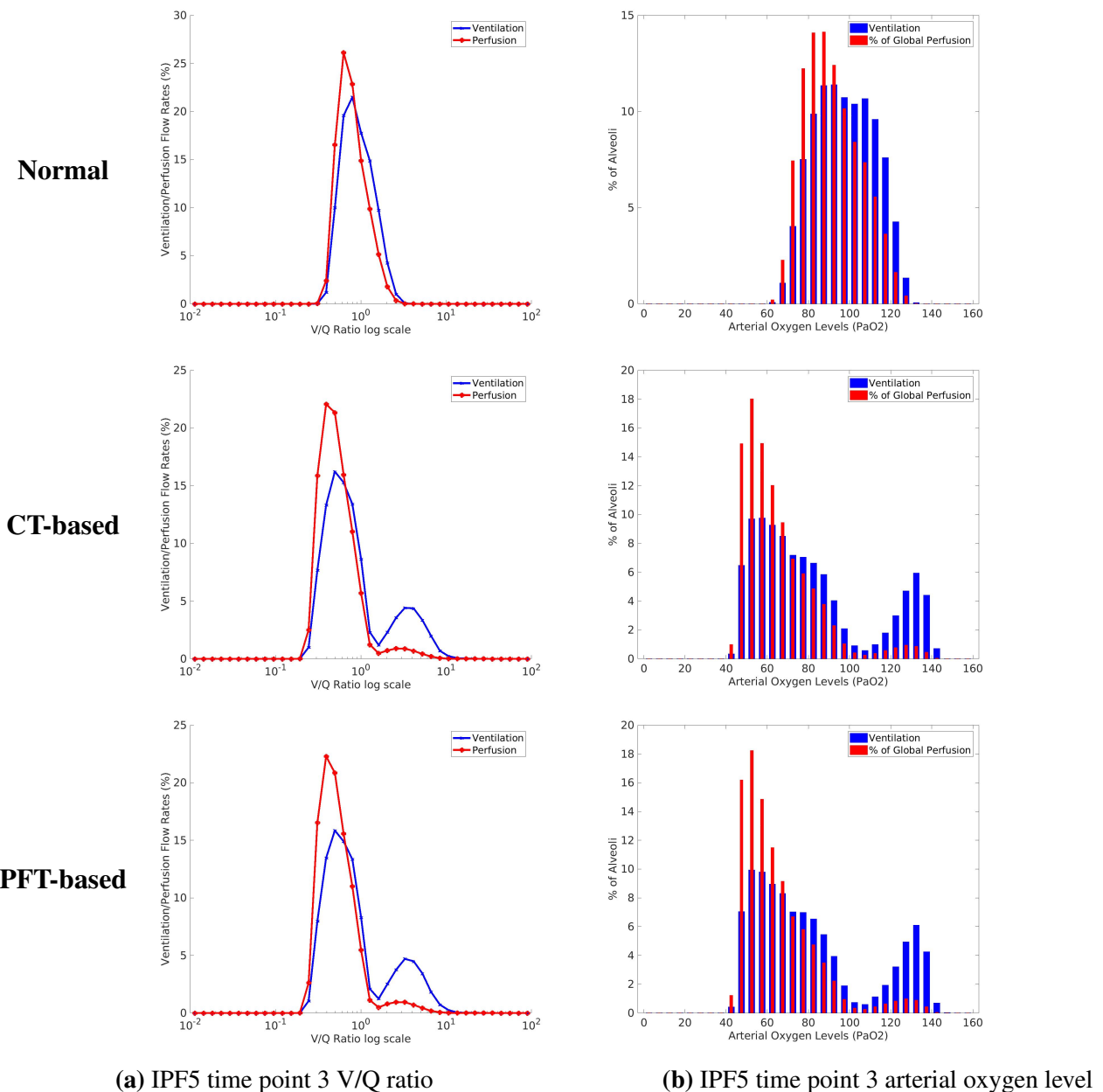
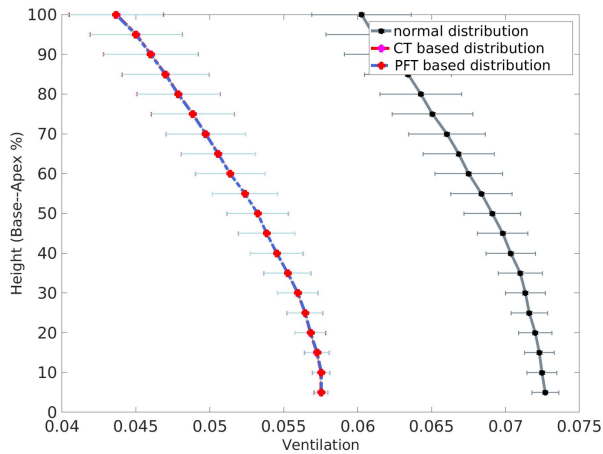
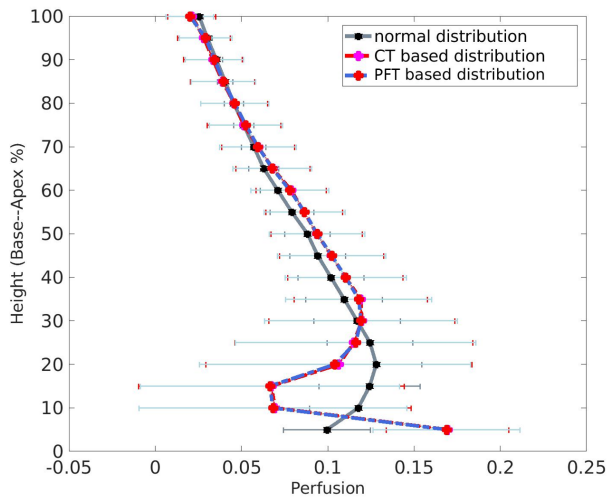


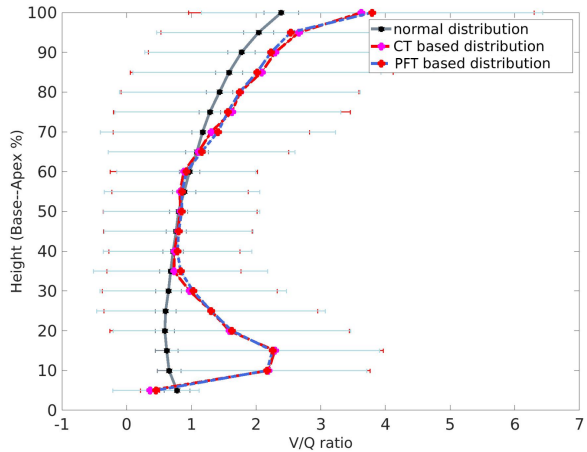
Figure B.5: V/Q ratio distribution and arterial oxygen distribution of normal, CT-based and PFT-based simulation result of the third time point of case IPF5 using MIGET. (a) V and Q flow with respect to V/Q ratio. (b) V and Q percentage with respect to arterial oxygen level.



(a) IPF5 time point 3 ventilation distribution



(b) IPF5 time point 3 perfusion distribution



(c) IPF5 time point 3 V/Q ratio distribution

Figure B.6: Ventilation, perfusion and V/Q ratio distribution against lung height (cranio-caudal axis) of the third time point of case IPF5. (a) Ventilation distribution against lung height. (b) Perfusion distribution against lung height. (c) V/Q ratio distribution against lung height.

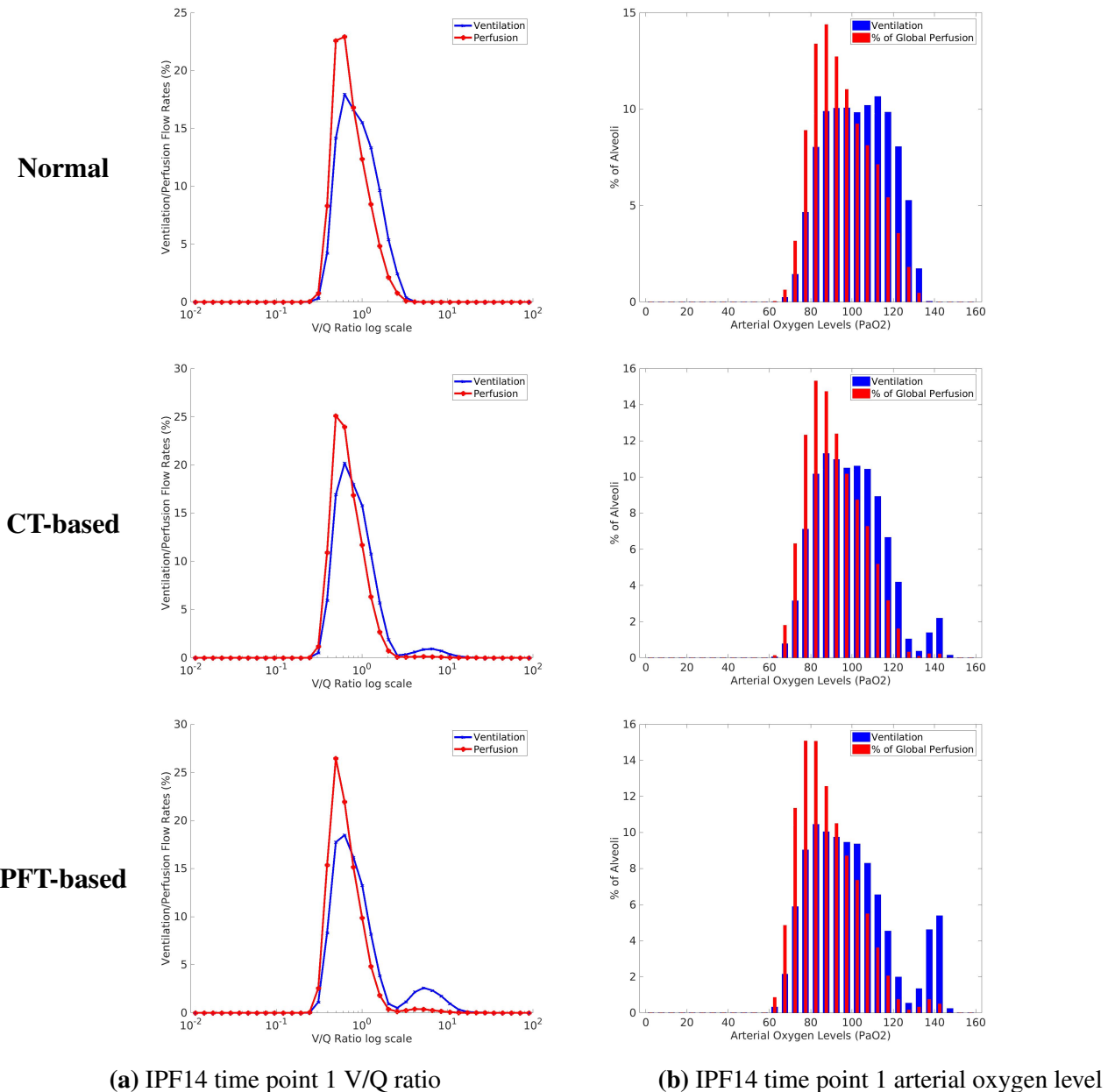
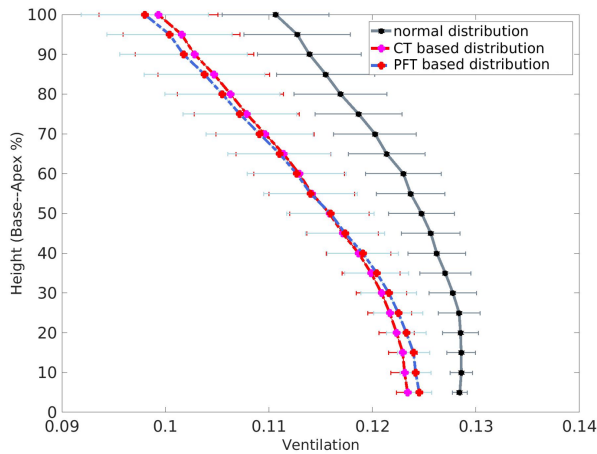
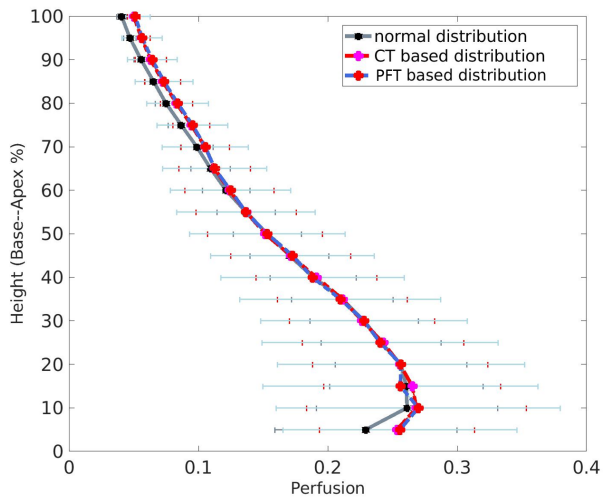


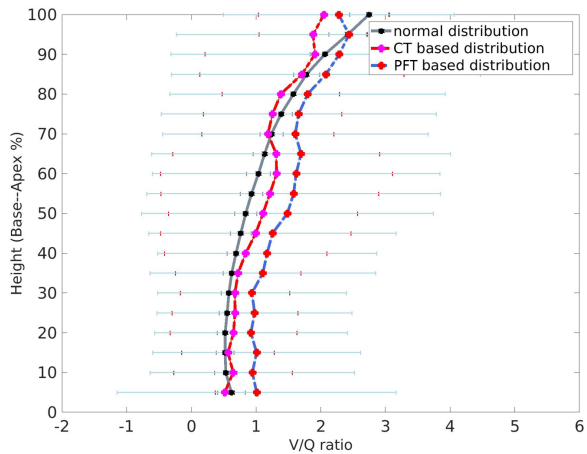
Figure B.7: V/Q ratio distribution and arterial oxygen distribution of normal, CT-based and PFT-based simulation result of the first time point of case IPF14 using MIGET). (a) V and Q flow with respect to V/Q ratio. (b) V and Q percentage with respect to arterial oxygen level.



(a) IPF14 time point 1 ventilation distribution



(b) IPF14 time point 1 perfusion distribution



(c) IPF14 time point 1 V/Q ratio distribution

Figure B.8: Ventilation, perfusion and V/Q ratio distribution against lung height (cranio-caudal axis) of the first time point of case IPF14. (a) Ventilation distribution against lung height. (b) Perfusion distribution against lung height. (c) V/Q ratio distribution against lung height.

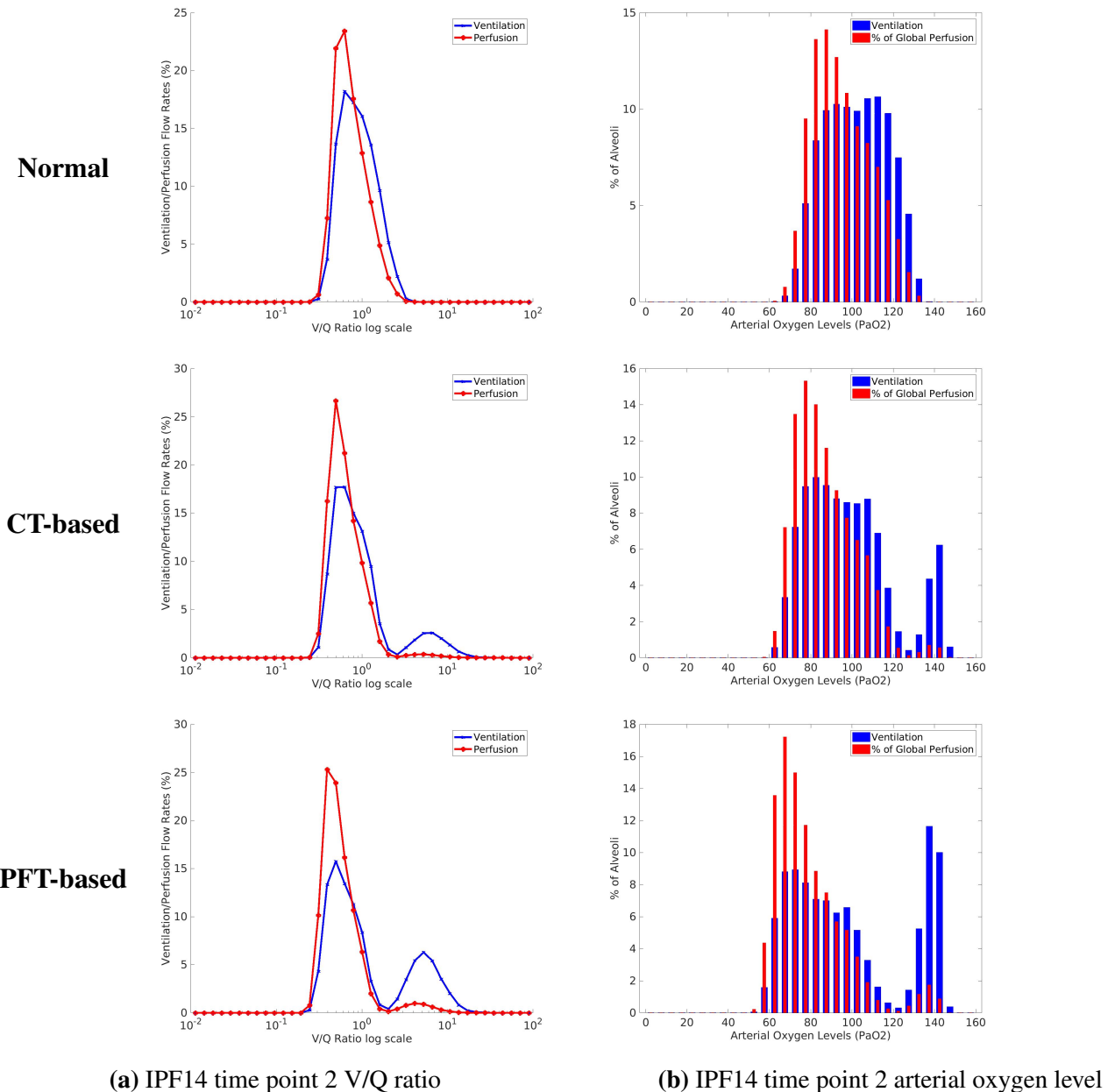
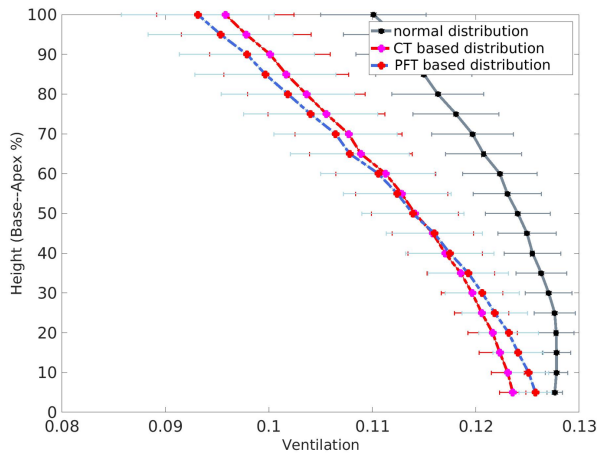
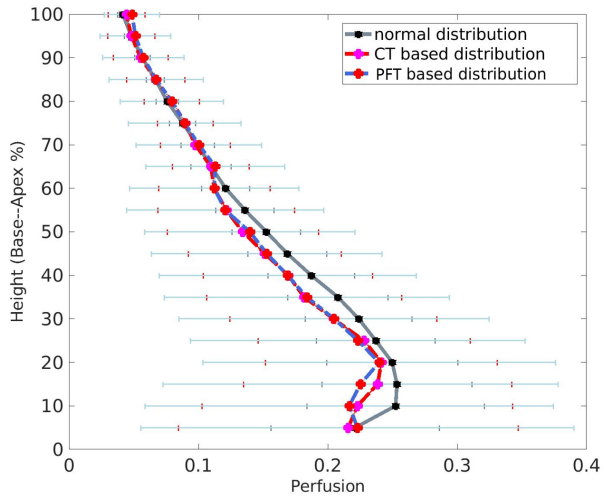


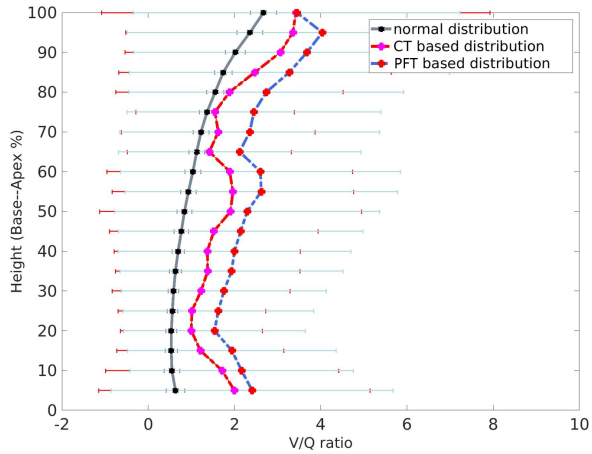
Figure B.9: V/Q ratio distribution and arterial oxygen distribution of normal, CT-based and PFT-based simulation result of the second time point of case IPF14 using MIGET. (a) V and Q flow with respect to V/Q ratio. (b) V and Q percentage with respect to arterial oxygen level.



(a) IPF14 time point 2 ventilation distribution



(b) IPF14 time point 2 perfusion distribution



(c) IPF14 time point 2 V/Q ratio distribution

Figure B.10: Ventilation, perfusion and V/Q ratio distribution against lung height (cranio-caudal axis) of the second time point of case IPF14. (a) Ventilation distribution against lung height. (b) Perfusion distribution against lung height. (c) V/Q ratio distribution against lung height.

List of References

- Agustí, A. G., Roca, J., Gea, J., Wagner, P. D., Xaubet, A., and Rodriguez-Roisin, R. (1991). Mechanisms of gas-exchange impairment in idiopathic pulmonary fibrosis. *American Review of Respiratory Disease*, 143(2):219–225. [Cited on pages 30 and 32.]
- Agusti, C., Xaubet, A., Agusti, A., Roca, J., Ramirez, J., and Rodriguez-Roisin, R. (1994). Clinical and functional assessment of patients with idiopathic pulmonary fibrosis: results of a 3 year follow-up. *European Respiratory Journal*, 7(4):643–650. [Cited on page 30.]
- Ahluwalia, N., Shea, B. S., and Tager, A. M. (2014). New therapeutic targets in idiopathic pulmonary fibrosis. aiming to rein in runaway wound-healing responses. *American journal of respiratory and critical care medicine*, 190(8):867–878. [Cited on page 8.]
- Alder, J. K., Chen, J. J.-L., Lancaster, L., Danoff, S., Su, S.-c., Cogan, J. D., Vulto, I., Xie, M., Qi, X., Tuder, R. M., et al. (2008). Short telomeres are a risk factor for idiopathic pulmonary fibrosis. *Proceedings of the National Academy of Sciences*, 105(35):13051–13056. [Cited on page 12.]
- Allam, J. S. and Limper, A. H. (2006). Idiopathic pulmonary fibrosis: is it a familial disease? *Current opinion in pulmonary medicine*, 12(5):312–317. [Cited on page 12.]
- Ambrosini, V., Cancellieri, A., Chilosi, M., Zompatori, M., Trisolini, R., Saragoni, L.,

- and Poletti, V. (2003). Acute exacerbation of idiopathic pulmonary fibrosis: report of a series. *European Respiratory Journal*, 22(5):821–826. [Cited on page 20.]
- Armato, S. G. and Sensakovic, W. F. (2004). Automated lung segmentation for thoracic ct: Impact on computer-aided diagnosis1. *Academic Radiology*, 11(9):1011–1021. [Not cited.]
- Arora, N. S. and Rochester, D. F. (1982). Respiratory muscle strength and maximal voluntary ventilation in undernourished patients. *American Review of Respiratory Disease*, 126(1):5–8. [Not cited.]
- Arzhaeva, Y., Prokop, M., Tax, D. M., De Jong, P. A., Schaefer-Prokop, C. M., and van Ginneken, B. (2007). Computer-aided detection of interstitial abnormalities in chest radiographs using a reference standard based on computed tomography. *Medical Physics*, 34(12):4798–4809. [Not cited.]
- Azuma, A., Nukiwa, T., Tsuboi, E., Suga, M., Abe, S., Nakata, K., Taguchi, Y., Nagai, S., Itoh, H., Ohi, M., et al. (2005). Double-blind, placebo-controlled trial of pirfenidone in patients with idiopathic pulmonary fibrosis. *American journal of respiratory and critical care medicine*, 171(9):1040–1047. [Cited on page 20.]
- Bartholmai, B. J., Raghunath, S., Karwoski, R. A., Moua, T., Rajagopalan, S., Maldonado, F., Decker, P. A., and Robb, R. A. (2013). Quantitative ct imaging of interstitial lung diseases. *Journal of thoracic imaging*, 28(5). [Not cited.]
- Baumgartner, K. B., Samet, J. M., Stidley, C. A., Colby, T. V., and Waldron, J. A. (1997). Cigarette smoking: a risk factor for idiopathic pulmonary fibrosis. *American journal of respiratory and critical care medicine*, 155(1):242–248. [Cited on page 11.]
- Behr, J., Mehnert, F., Beinert, T., et al. (1992). Evaluation of interstitial lung disease by quantitative high-resolution computed tomography. *Am Rev Respir Dis*, 145(Suppl.):A191. [Not cited.]

- Ben-Tal, A. (2006). Simplified models for gas exchange in the human lungs. *Journal of Theoretical Biology*, 238(2):474–495. [Not cited.]
- Best, A. C., Lynch, A. M., Bozic, C. M., Miller, D., Grunwald, G. K., and Lynch, D. A. (2003). Quantitative ct indexes in idiopathic pulmonary fibrosis: relationship with physiologic impairment. *Radiology*, 228(2):407–414. [Not cited.]
- Best, A. C., Meng, J., Lynch, A. M., Bozic, C. M., Miller, D., Grunwald, G. K., and Lynch, D. A. (2008). Idiopathic pulmonary fibrosis: physiologic tests, quantitative ct indexes, and ct visual scores as predictors of mortality. *Radiology*, 246(3):935–940. [Not cited.]
- Bjoraker, J. A., Ryu, J. H., Edwin, M. K., Myers, J. L., Tazelaar, H. D., Schroeder, D. R., and Offord, K. P. (1998). Prognostic significance of histopathologic subsets in idiopathic pulmonary fibrosis. *American journal of respiratory and critical care medicine*, 157(1):199–203. [Cited on pages 19 and 95.]
- Bradley, C., Pullan, A., and Hunter, P. (1997). Geometric modeling of the human torso using cubic hermite elements. *Annals of biomedical engineering*, 25(1):96–111. [Not cited.]
- Brandfonbrener, M., Landowne, M., and Shock, N. W. (1955). Changes in cardiac output with age. *Circulation*, 12(4):557–566. [Not cited.]
- Brandstetter, R. D. and Kazemi, H. (1983). Aging and the respiratory system. *Medical Clinics of North America*, 67(2):419–431. [Not cited.]
- Breatnach, E., Abbott, G. C., and Fraser, R. G. (1984). Dimensions of the normal human trachea. *American Journal of Roentgenology*, 142(5):903–906. [Not cited.]
- Butler, C. and Kleinerman, J. (1970). Capillary density: alveolar diameter, a morphometric approach to ventilation and perfusion. *American Review of Respiratory Disease*, 102(6):886–894. [Not cited.]

- Carrington, C. B., Gaensler, E. A., Coutu, R. E., FitzGerald, M. X., and Gupta, R. G. (1978). Natural history and treated course of usual and desquamative interstitial pneumonia. *New England Journal of Medicine*, 298(15):801–809. [Cited on page 19.]
- Castaldi, P. J., San José Estépar, R., Mendoza, C. S., Hersh, C. P., Laird, N., Crapo, J. D., Lynch, D. A., Silverman, E. K., and Washko, G. R. (2013). Distinct quantitative computed tomography emphysema patterns are associated with physiology and function in smokers. *American journal of respiratory and critical care medicine*, 188(9):1083–1090. [Not cited.]
- Chabat, F., Yang, G.-Z., and Hansell, D. M. (2003). Obstructive lung diseases: texture classification for differentiation at ct. *Radiology*, 228(3):871–877. [Not cited.]
- Cherniack, R. M., Colby, T. V., Flint, A., Thurlbeck, W. M., Waldron Jr, J. A., Ackerson, L., Schwarz, M. I., and King Jr, T. E. (1995). Correlation of structure and function in idiopathic pulmonary fibrosis. *American journal of respiratory and critical care medicine*, 151(4):1180–1188. [Cited on page 26.]
- Chilosi, M., Poletti, V., Murer, B., Lestani, M., Cancellieri, A., Montagna, L., Piccoli, P., Cangi, G., Semenzato, G., and Doglioni, C. (2002). Abnormal re-epithelialization and lung remodeling in idiopathic pulmonary fibrosis: the role of δ n-p63. *Laboratory investigation*, 82(10):1335. [Cited on page 27.]
- Clark, A. R., Burrowes, K. S., and Tawhai, M. H. (2010). Contribution of serial and parallel microperfusion to spatial variability in pulmonary inter-and intra-acinar blood flow. *Journal of applied physiology*, 108(5):1116–1126. [Not cited.]
- Clark, A. R., Tawhai, M. H., Hoffman, E. A., and Burrowes, K. S. (2011). The interdependent contributions of gravitational and structural features to perfusion distribution in a multiscale model of the pulmonary circulation. *Journal of applied physiology*, 110(4):943–955. [Not cited.]

- Coelho-Ravagnani, C. d. F., Melo, F. C. L., Ravagnani, F. C., Burini, F. H. P., and Burini, R. C. (2013). Estimation of metabolic equivalent (met) of an exercise protocol based on indirect calorimetry. *Revista Brasileira de Medicina do Esporte*, 19(2):134–138. [Not cited.]
- Cootes, T. F., Taylor, C. J., Cooper, D. H., and Graham, J. (1995). Active shape models—their training and application. *Computer vision and image understanding*, 61(1):38–59. [Not cited.]
- Corte, T. J., Collard, H., and Wells, A. U. (2015). Idiopathic interstitial pneumonias in 2015: A new era. *Respirology*, 20(5):697–698. [Cited on page 9.]
- Cortes-Telles, A., Forkert, L., O'Donnell, D. E., and Morán-Mendoza, O. (2014). Idiopathic pulmonary fibrosis: New insights to functional characteristics at diagnosis. *Canadian respiratory journal*, 21(3):e55–e60. [Cited on pages 24, 30, and 195.]
- Cosgrove, G. P., Brown, K. K., Schiemann, W. P., Serls, A. E., Parr, J. E., Geraci, M. W., Schwarz, M. I., Cool, C. D., and Worthen, G. S. (2004). Pigment epithelium-derived factor in idiopathic pulmonary fibrosis: a role in aberrant angiogenesis. *American journal of respiratory and critical care medicine*, 170(3):242–251. [Cited on page 28.]
- Costabel, U., Du Bois, R. M., and Egan, J. J. (2007). Diffuse parenchymal lung disease, volume 36. Karger Medical and Scientific Publishers. [Not cited.]
- Cottin, V., Le Pavec, J., Prévot, G., Mal, H., Humbert, M., Simonneau, G., Cordier, J.-F., et al. (2010). Pulmonary hypertension in patients with combined pulmonary fibrosis and emphysema syndrome. *European Respiratory Journal*, 35(1):105–111. [Cited on page 22.]
- Cottin, V., Nunes, H., Brillet, P., Delaval, P., Devouassoux, G., Tillie-Leblond, I., Israel-Biet, D., Valeyre, D., Cordier, J., et al. (2005). Combined pulmonary fibro-

- sis and emphysema: a distinct underrecognised entity. *European Respiratory Journal*, 26(4):586–593. [Cited on pages 22, 143, and 188.]
- Coxson, H. (2007). Computed tomography and monitoring of emphysema. [Not cited.]
- Crapo, R. (1993). The aging lung. *Lung biology in health and disease*, 63:1–25. [Not cited.]
- Crystal, R. G., Fulmer, J. D., Roberts, W. C., Moss, M. L., Line, B. R., and Reynolds, H. Y. (1976). Idiopathic pulmonary fibrosis: clinical, histologic, radiographic, physiologic, scintigraphic, cytologic, and biochemical aspects. *Annals of internal medicine*, 85(6):769–788. [Cited on pages 24, 28, 29, 30, 31, 32, and 159.]
- da Silva Felix, J. H., Cortez, P. C., Rebouças Filho, P. P., de Alexandria, A. R., Costa, R. C. S., and Holanda, M. A. (2008). Identification and quantification of pulmonary emphysema through pseudocolors. In Mexican International Conference on Artificial Intelligence, pages 957–964. Springer. [Not cited.]
- De Troyer, A. and Yernault, J.-C. (1980). Inspiratory muscle force in normal subjects and patients with interstitial lung disease. *Thorax*, 35(2):92–100. [Not cited.]
- Delorme, S., Keller-Reichenbecher, M.-A., Zuna, I., Schlegel, W., and Van Kaick, G. (1997). Usual interstitial pneumonia: quantitative assessment of high-resolution computed tomography findings by computer-assisted texture-based image analysis. *Investigative radiology*, 32(9):566–574. [Not cited.]
- Depeursinge, A., Iavindrasana, J., Hidki, A., Cohen, G., Geissbuhler, A., Platon, A., Poletti, P.-A., and Müller, H. (2010). Comparative performance analysis of state-of-the-art classification algorithms applied to lung tissue categorization. *Journal of digital imaging*, 23(1):18–30. [Not cited.]
- Devaraj, A. (2014). Imaging: how to recognise idiopathic pulmonary fibrosis. *European Respiratory Review*, 23(132):215–219. [Not cited.]

- Diaz, A. A., Valim, C., Yamashiro, T., EstÃŠpar, R. S. J., Ross, J. C., Matsuoka, S., Bartholmai, B., Hatabu, H., Silverman, E. K., and Washko, G. R. (2010). Airway count and emphysema assessed by chest ct imaging predicts clinical outcome in smokers. *CHEST Journal*, 138(4):880–887. [Not cited.]
- Diette, G. B., Scatarige, J. C., Haponik, E. F., Merriman, B., and Fishman, E. K. (2005). Do high-resolution ct findings of usual interstitial pneumonitis obviate lung biopsy? *Respiration*, 72(2):134–141. [Not cited.]
- Doel, T., Gavaghan, D. J., and Grau, V. (2015). Review of automatic pulmonary lobe segmentation methods from ct. *Computerized Medical Imaging and Graphics*, 40:13–29. [Not cited.]
- Doel, T., Matin, T. N., Gleeson, F. V., Gavaghan, D. J., and Grau, V. (2012). Pulmonary lobe segmentation from ct images using fissureness, airways, vessels and multilevel b-splines. In *Biomedical Imaging (ISBI), 2012 9th IEEE International Symposium on*, pages 1491–1494. IEEE. [Not cited.]
- Doherty, M., Pearson, M., O’grady, E., Pellegrini, V., and Calverley, P. (1997). Cryptogenic fibrosing alveolitis with preserved lung volumes. *Thorax*, 52(11):998–1002. [Cited on page 27.]
- Douglas, W. W., Ryu, J. H., and Schroeder, D. R. (2000). Idiopathic pulmonary fibrosis: impact of oxygen and colchicine, prednisone, or no therapy on survival. *American journal of respiratory and critical care medicine*, 161(4):1172–1178. [Cited on pages 13 and 14.]
- Dryden, I. L. and Mardia, K. V. (1998). *Statistical shape analysis*, volume 4. Wiley Chichester. [Not cited.]
- Du Bois, R. M., Weycker, D., Albera, C., Bradford, W. Z., Costabel, U., Kartashov, A., Lancaster, L., Noble, P. W., Raghu, G., Sahn, S. A., et al. (2011). Ascertainment of

- individual risk of mortality for patients with idiopathic pulmonary fibrosis. *American journal of respiratory and critical care medicine*, 184(4):459–466. [Cited on page 27.]
- Ebina, M., Shimizukawa, M., Shibata, N., Kimura, Y., Suzuki, T., Endo, M., Sasano, H., Kondo, T., and Nukiwa, T. (2004). Heterogeneous increase in cd34-positive alveolar capillaries in idiopathic pulmonary fibrosis. *American journal of respiratory and critical care medicine*, 169(11):1203–1208. [Cited on page 28.]
- Ecabert, O., Peters, J., Schramm, H., Lorenz, C., von Berg, J., Walker, M. J., Vembar, M., Olszewski, M. E., Subramanyan, K., Lavi, G., et al. (2008). Automatic model-based segmentation of the heart in ct images. *IEEE transactions on medical imaging*, 27(9):1189–1201. [Not cited.]
- El-Baz, A., Beach, G. M., Gimel’farb, G., Suzuki, K., Okada, K., Elnakib, A., Soliman, A., and Abdollahi, B. (2013). Computer-aided diagnosis systems for lung cancer: challenges and methodologies. *International journal of biomedical imaging*, 2013. [Not cited.]
- Fernandez, J. W. (2004). An anatomically based finite element model of patella articulation: towards a diagnostic tool. PhD thesis, University of Auckland. [Not cited.]
- Finley, T., Swenson, E., and Comroe, J. (1962). The cause of arterial hypoxemia at rest in patients with alveolar-capillary block syndrome. *The Journal of clinical investigation*, 41(3):618–622. [Cited on page 32.]
- Flaherty, K., Thwaite, E., Kazerooni, E., Gross, B., Toews, G., Colby, T. V., Travis, W., Mumford, J., Murray, S., Flint, A., et al. (2003). Radiological versus histological diagnosis in uip and nsip: survival implications. *Thorax*, 58(2):143–148. [Cited on page 17.]
- Flaherty, K., Toews, G., Travis, W., Colby, T., Kazerooni, E., Gross, B., Jain, A., Strawderman, R., Paine, R., Flint, A., et al. (2002). Clinical significance of histologi-

- cal classification of idiopathic interstitial pneumonia. *European Respiratory Journal*, 19(2):275–283. [Cited on page 19.]
- Flaherty, K. R., Andrei, A.-C., King Jr, T. E., Raghu, G., Colby, T. V., Wells, A., Bassily, N., Brown, K., Du Bois, R., Flint, A., et al. (2007). Idiopathic interstitial pneumonia: do community and academic physicians agree on diagnosis? *American journal of respiratory and critical care medicine*, 175(10):1054–1060. [Not cited.]
- Flaherty, K. R., King Jr, T. E., Raghu, G., Lynch III, J. P., Colby, T. V., Travis, W. D., Gross, B. H., Kazerooni, E. A., Toews, G. B., Long, Q., et al. (2004). Idiopathic interstitial pneumonia: what is the effect of a multidisciplinary approach to diagnosis? *American journal of respiratory and critical care medicine*, 170(8):904–910. [Cited on pages 12 and 95.]
- Flaherty, K. R., Travis, W. D., Colby, T. V., Toews, G. B., Kazerooni, E. A., Gross, B. H., Jain, A., STRAWDERMAN III, R. L., Flint, A., LYNCH III, J. P., et al. (2001). Histopathologic variability in usual and nonspecific interstitial pneumonias. *American journal of respiratory and critical care medicine*, 164(9):1722–1727. [Not cited.]
- Florack, L. M., ter Haar Romeny, B. M., Koenderink, J. J., and Viergever, M. A. (1992). Scale and the differential structure of images. *Image and vision computing*, 10(6):376–388. [Not cited.]
- Frangi, A. F., Niessen, W. J., Vincken, K. L., and Viergever, M. A. (1998). Multiscale vessel enhancement filtering. In *International Conference on Medical Image Computing and Computer-Assisted Intervention*, pages 130–137. Springer. [Not cited.]
- Fulmer, J., Roberts, W., von Gal, E. R., and Crystal, R. (1979). Morphologic-physiologic correlates of the severity of fibrosis and degree of cellularity in idiopathic pulmonary fibrosis. *The Journal of clinical investigation*, 63(4):665–676. [Cited on page 26.]

- Fulmer, J. D., Crystal, R. G., and Roberts, W. C. (1976). Diffuse fibrotic lung disease: a correlative study. *Chest*, 69(2):263–265. [Cited on page 30.]
- Fung, Y. and Sabin, S. (1969). Theory of sheet flow in lung alveoli. *Journal of Applied Physiology*, 26(4):472–488. [Not cited.]
- Fung, Y.-c. (2013). Biomechanics: circulation. Springer Science & Business Media. [Not cited.]
- Galbán, C. J., Han, M. K., Boes, J. L., Chughtai, K. A., Meyer, C. R., Johnson, T. D., Galbán, S., Rehemtulla, A., Kazerooni, E. A., Martinez, F. J., et al. (2012). Computed tomography-based biomarker provides unique signature for diagnosis of copd phenotypes and disease progression. *Nature medicine*, 18(11):1711. [Not cited.]
- Gietema, H. A., Müller, N. L., Fauerbach, P. V. N., Sharma, S., Edwards, L. D., Camp, P. G., Coxson, H. O., of COPD Longitudinally to Identify Predictive Surrogate Endpoints (ECLIPSE) investigators, E., et al. (2011). Quantifying the extent of emphysema:: Factors associated with radiologists estimations and quantitative indices of emphysema severity using the eclipse cohort. *Academic radiology*, 18(6):661–671. [Not cited.]
- Gilbert, R., Auchincloss Jr, J., Brodsky, J., and Boden, W. a. (1972). Changes in tidal volume, frequency, and ventilation induced by their measurement. *Journal of Applied Physiology*, 33(2):252–254. [Not cited.]
- Gilman, M. J., Laurens, J. R., Somogyi, J. W., and Honig, E. G. (1983). Ct attenuation values of lung density in sarcoidosis. *Journal of computer assisted tomography*, 7(3):407–410. [Not cited.]
- Glazier, J., Hughes, J., Maloney, J., and West, J. (1969). Measurements of capillary dimensions and blood volume in rapidly frozen lungs. *Journal of Applied Physiology*, 26(1):65–76. [Not cited.]

- Gotway, M. B., Freemer, M. M., and King, T. E. (2007). Challenges in pulmonary fibrosis- 1: Use of high resolution ct scanning of the lung for the evaluation of patients with idiopathic interstitial pneumonias. *Thorax*, 62(6):546–553. [Not cited.]
- Gould, G., MacNee, W., McLean, A., Warren, P., Redpath, A., Best, J., Lamb, D., and Flenley, D. (1988). Ct measurements of lung density in life can quantitate distal airspace enlargementan essential defining feature of human emphysema. *American Review of Respiratory Disease*, 137(2):380–392. [Not cited.]
- Graham, B. L., Brusasco, V., Burgos, F., Cooper, B. G., Jensen, R., Kendrick, A., MacIntyre, N. R., Thompson, B. R., and Wanger, J. (2017). 2017 ers/ats standards for single-breath carbon monoxide uptake in the lung. *European Respiratory Journal*, 49(1):1600016. [Cited on pages 29 and 196.]
- Graham, M. W., Gibbs, J. D., Cornish, D. C., and Higgins, W. E. (2010). Robust 3-d airway tree segmentation for image-guided peripheral bronchoscopy. *IEEE transactions on medical imaging*, 29(4):982–997. [Not cited.]
- Gross, P. (1962). The concept of the hamman-rich syndrome: a critique. *American Review of Respiratory Disease*, 85(6):828–832. [Cited on page 20.]
- Gross, T. J. and Hunninghake, G. W. (2001). Idiopathic pulmonary fibrosis. *New England Journal of Medicine*, 345(7):517–525. [Cited on page 19.]
- Guenard, H. and Marthan, R. (1996). Pulmonary gas exchange in elderly subjects. *European Respiratory Journal*, 9(12):2573–2577. [Not cited.]
- Gülsün, M., Ariyürek, O. M., Cömert, R. B., and Karabulut, N. (2006). Variability of the pulmonary oblique fissures presented by high-resolution computed tomography. *Surgical and Radiologic Anatomy*, 28(3):293–299. [Not cited.]
- Gunther, A., Schmidt, R., Nix, F., Yabut-Perez, M., Guth, C., Rousseau, S., Siebert, C., Grimminger, F., Morr, H., Velcovsky, H., et al. (1999). Surfactant abnormalities in id-

- iopathic pulmonary fibrosis, hypersensitivity pneumonitis and sarcoidosis. *European Respiratory Journal*, 14(3):565–573. [Cited on page 24.]
- Guo, J., Fuld, M., Alford, S., Reinhardt, J., and Hoffman, E. (2008). Pulmonary analysis software suite 9.0: Integrating quantitative measures of function with structural analyses. In First International Workshop on Pulmonary Image Analysis, pages 283–292. [Not cited.]
- Haefeli-Bleuer, B. and Weibel, E. R. (1988). Morphometry of the human pulmonary acinus. *The Anatomical Record*, 220(4):401–414. [Not cited.]
- Hall, J. E. (2015). Guyton and Hall textbook of medical physiology e-Book. Elsevier Health Sciences. [Not cited.]
- Hamada, K., Nagai, S., Tanaka, S., Handa, T., Shigematsu, M., Nagao, T., Mishima, M., Kitaichi, M., and Izumi, T. (2007). Significance of pulmonary arterial pressure and diffusion capacity of the lung as prognosticator in patients with idiopathic pulmonary fibrosis. *Chest*, 131(3):650–656. [Cited on page 30.]
- Hansell, D. M., Bankier, A. A., MacMahon, H., McLoud, T. C., Muller, N. L., and Remy, J. (2008). Fleischner society: glossary of terms for thoracic imaging. *Radiology*, 246(3):697–722. [Cited on page 14.]
- Harari, S., Madotto, F., Caminati, A., Conti, S., and Cesana, G. (2016). Epidemiology of idiopathic pulmonary fibrosis in northern italy. *PLoS One*, 11(2):e0147072. [Cited on page 21.]
- Hayes Jr, D., Black, S. M., Tobias, J. D., Kirkby, S., Mansour, H. M., and Whitson, B. A. (2016). Influence of pulmonary hypertension on patients with idiopathic pulmonary fibrosis awaiting lung transplantation. *The Annals of thoracic surgery*, 101(1):246–252. [Cited on page 23.]

- Hedlund, L., Anderson, R. F., Goulding, P., Beck, J., Effmann, E., and Putman, C. (1982). Two methods for isolating the lung area of a ct scan for density information. *Radiology*, 144(2):353–357. [Not cited.]
- Heimann, T. and Meinzer, H.-P. (2009). Statistical shape models for 3d medical image segmentation: a review. *Medical image analysis*, 13(4):543–563. [Not cited.]
- Hempleman, S. C. and Hughes, J. (1991). Estimating exercise dlo2 and diffusion limitation in patients with interstitial fibrosis. *Respiration physiology*, 83(2):167–178. [Cited on page 32.]
- Hill, E. P., Power, G. G., and Longo, L. (1973). A mathematical model of carbon dioxide transfer in the placenta and its interaction with oxygen. *American Journal of Physiology-Legacy Content*, 224(2):283–299. [Not cited.]
- Hoesein, F. A. M. and De Jong, P. A. (2017). Air trapping on computed tomography: regional versus diffuse. [Not cited.]
- Hoffman, E. A. (1985). Effect of body orientation on regional lung expansion: a computed tomographic approach. *Journal of Applied Physiology*, 59(2):468–480. [Not cited.]
- Hoffman, E. A. and McLennan, G. (1997). Assessment of the pulmonary structure-function relationship and clinical outcomes measures: quantitative volumetric ct of the lung. *Academic radiology*, 4(11):758–776. [Not cited.]
- Hoffman, E. A. and Ritman, E. L. (1985). Effect of body orientation on regional lung expansion in dog and sloth. *Journal of Applied Physiology*, 59(2):481–491. [Not cited.]
- Hoffman, E. A., Simon, B. A., and McLennan, G. (2006). State of the art. a structural and functional assessment of the lung via multidetector-row computed tomography:

- phenotyping chronic obstructive pulmonary disease. *Proceedings of the American Thoracic Society*, 3(6):519–532. [Not cited.]
- Hoffman, E. A., Sinak, L., Robb, R. A., and Ritman, E. L. (1983). Noninvasive quantitative imaging of shape and volume of lungs. *Journal of Applied Physiology*, 54(5):1414–1421. [Not cited.]
- Holland, J., Milic-Emili, J., Macklem, P., and Bates, D. (1968). Regional distribution of pulmonary ventilation and perfusion in elderly subjects. *The Journal of clinical investigation*, 47(1):81–92. [Not cited.]
- Horsfield, K. (1978). Morphometry of the small pulmonary arteries in man. *Circulation research*, 42(5):593–597. [Not cited.]
- Horsfield, K. and Gordon, W. (1981). Morphometry of pulmonary veins in man. *Lung*, 159(1):211–218. [Not cited.]
- Horsfield, K., Relea, F. G., and Gumming, G. (1976). Diameter, length and branching ratios in the bronchial tree. *Respiration physiology*, 26(3):351–356. [Not cited.]
- Hsia, C. C., Hyde, D. M., and Weibel, E. R. (2016). Lung structure and the intrinsic challenges of gas exchange. *Comprehensive Physiology*, 6(2):827. [Not cited.]
- Hu, S., Hoffman, E. A., and Reinhardt, J. M. (2001). Automatic lung segmentation for accurate quantitation of volumetric x-ray ct images. *IEEE transactions on medical imaging*, 20(6):490–498. [Not cited.]
- Huang, W., Yen, R., McLaurine, M., and Bledsoe, G. (1996). Morphometry of the human pulmonary vasculature. *Journal of applied physiology*, 81(5):2123–2133. [Not cited.]
- Hughes, J., Lockwood, D., Jones, H., and Clark, R. (1991). DLCO/q and diffusion limitation at rest and on exercise in patients with interstitial fibrosis. *Respiration physiology*, 83(2):155–166. [Cited on page 32.]

- Hunninghake, G. W., Zimmerman, M. B., Schwartz, D. A., KING JR, T. E., Lynch, J., Hegele, R., Waldron, J., Colby, T., Muller, N., Lynch, D., et al. (2001). Utility of a lung biopsy for the diagnosis of idiopathic pulmonary fibrosis. *American journal of respiratory and critical care medicine*, 164(2):193–196. [Cited on page 17.]
- Hwang, J.-H., Misumi, S., Sahin, H., Brown, K. K., Newell, J. D., and Lynch, D. A. (2009). Computed tomographic features of idiopathic fibrosing interstitial pneumonia: comparison with pulmonary fibrosis related to collagen vascular disease. *Journal of computer assisted tomography*, 33(3):410–415. [Cited on page 14.]
- Hyldgaard, C., Hilberg, O., Muller, A., and Bendstrup, E. (2014). A cohort study of interstitial lung diseases in central denmark. *Respiratory medicine*, 108(5):793–799. [Cited on page 10.]
- Jacob, J., Bartholmai, B. J., Rajagopalan, S., Brun, A. L., Egashira, R., Karwoski, R., Kokosi, M., Wells, A. U., and Hansell, D. M. (2016a). Evaluation of computer-based computer tomography stratification against outcome models in connective tissue disease-related interstitial lung disease: a patient outcome study. *Bmc Medicine*, 14(1):190. [Cited on pages 28 and 196.]
- Jacob, J., Bartholmai, B. J., Rajagopalan, S., Kokosi, M., Nair, A., Karwoski, R., Walsh, S. L., Wells, A. U., and Hansell, D. M. (2016b). Mortality prediction in ipf: evaluation of automated computer tomographic analysis with conventional severity measures. *European Respiratory Journal*, 49(1):ERJ–01011–2016. [Cited on pages 29 and 196.]
- Janssens, J.-P., Pache, J.-C., and Nicod, L. (1999). Physiological changes in respiratory function associated with ageing. *European Respiratory Journal*, 13(1):197–205. [Not cited.]
- Jeffery, P. K. (1998). Structural and inflammatory changes in copd: a comparison with asthma. *Thorax*, 53(2):129. [Not cited.]

- Johkoh, T., Muller, N. L., Cartier, Y., Kavanagh, P. V., Hartman, T. E., Akira, M., Ichikado, K., Ando, M., and Nakamura, H. (1999). Idiopathic interstitial pneumonias: diagnostic accuracy of thin-section ct in 129 patients. *Radiology*, 211(2):555–560. [Cited on page 14.]
- Jones, N., McHardy, G., Naimark, A., and Campbell, E. (1966). Physiological dead space and alveolar-arterial gas pressure differences during exercise. *Clinical science*, 31(1):19–29. [Cited on page 30.]
- Kalender, W. A., Fichte, H., Bautz, W., and Skalej, M. (1991). Semiautomatic evaluation procedures for quantitative ct of the lung. *Journal of computer assisted tomography*, 15(2):248–255. [Not cited.]
- Kapitan, K. S. and Hempleman, S. C. (1986). Computer simulation of mammalian gas-exchange. *Computers in biology and medicine*, 16(2):91–101. [Not cited.]
- Katzenstein, A.-L. A. and Myers, J. L. (1998). Idiopathic pulmonary fibrosis: clinical relevance of pathologic classification. *American journal of respiratory and critical care medicine*, 157(4):1301–1315. [Cited on page 9.]
- Kazerooni, E. A. (2001). High-resolution ct of the lungs. *American Journal of Roentgenology*, 177(3):501–519. [Not cited.]
- Kazerooni, E. A., Martinez, F. J., Flint, A., Jamadar, D. A., Gross, B. H., Spizarny, D. L., Cascade, P. N., Whyte, R. I., Lynch 3rd, J., and Toews, G. (1997). Thin-section ct obtained at 10-mm increments versus limited three-level thin-section ct for idiopathic pulmonary fibrosis: correlation with pathologic scoring. *AJR. American journal of roentgenology*, 169(4):977–983. [Not cited.]
- Keener, J. P. and Sneyd, J. (1998). *Mathematical physiology*, volume 1. Springer. [Not cited.]

- Kelemen, A., Székely, G., and Gerig, G. (1999). Elastic model-based segmentation of 3-d neuroradiological data sets. *IEEE Transactions on medical imaging*, 18(10):828–839. [Not cited.]
- Keller, J. M., Edwards, F. M., and Rundle, R. (1981). Automatic outlining of regions on ct scans. *Journal of Computer Assisted Tomography*, 5(2):240–245. [Not cited.]
- Kemerink, G. J., Lamers, R. J., Pellis, B. J., Kruize, H. H., and Van Engelshoven, J. (1998). On segmentation of lung parenchyma in quantitative computed tomography of the lung. *Medical Physics*, 25(12):2432–2439. [Not cited.]
- Kim, D., Park, J., Park, B., Lee, J., Nicholson, A., and Colby, T. (2006a). Acute exacerbation of idiopathic pulmonary fibrosis: frequency and clinical features. *European Respiratory Journal*, 27(1):143–150. [Cited on page 20.]
- Kim, D. S., Collard, H. R., and King Jr, T. E. (2006b). Classification and natural history of the idiopathic interstitial pneumonias. *Proceedings of the American Thoracic Society*, 3(4):285–292. [Cited on pages 19 and 20.]
- Kim, E. Y., Lee, K., Chung, M., Kwon, O. J., Kim, T., and Hwang, J. (1999). Non-specific interstitial pneumonia with fibrosis: serial high-resolution ct findings with functional correlation. *AJR. American journal of roentgenology*, 173(4):949–953. [Not cited.]
- Kim, H., Tashkin, D., Clements, P., Li, G., Brown, M., Elashoff, R., Gjertson, D., Abtin, F., Lynch, D., Strollo, D., et al. (2010). A computer-aided diagnosis system for quantitative scoring of extent of lung fibrosis in scleroderma patients. *Clinical and experimental rheumatology*, 28(5 Suppl 62):S26. [Not cited.]
- Kim, H. J., Brown, M. S., Chong, D., Gjertson, D. W., Lu, P., Kim, H. J., Coy, H., and Goldin, J. G. (2015a). Comparison of the quantitative ct imaging biomarkers

- of idiopathic pulmonary fibrosis at baseline and early change with an interval of 7 months. *Academic radiology*, 22(1):70–80. [Not cited.]
- Kim, H. J., Brown, M. S., Elashoff, R., Li, G., Gjertson, D. W., Lynch, D. A., Strollo, D. C., Kleerup, E., Chong, D., Shah, S. K., et al. (2011). Quantitative texture-based assessment of one-year changes in fibrotic reticular patterns on hrct in scleroderma lung disease treated with oral cyclophosphamide. *European radiology*, 21(12):2455–2465. [Not cited.]
- Kim, H. J., Perlman, D., and Tomic, R. (2015b). Natural history of idiopathic pulmonary fibrosis. *Respiratory medicine*, 109(6):661–670. [Cited on pages 8 and 21.]
- Kim, K. G., Goo, J. M., Kim, J. H., Lee, H. J., Min, B. G., Bae, K. T., and Im, J.-G. (2005). Computer-aided diagnosis of localized ground-glass opacity in the lung at ct: initial experience. *Radiology*, 237(2):657–661. [Not cited.]
- King, C. S. and Nathan, S. D. (2017). Idiopathic pulmonary fibrosis: effects and optimal management of comorbidities. *The Lancet Respiratory Medicine*, 5(1):72–84. [Cited on pages 21 and 23.]
- King Jr, T. E., Pardo, A., and Selman, M. (2011). Idiopathic pulmonary fibrosis. *The Lancet*, 378(9807):1949–1961. [Cited on pages xvii, 1, 7, 8, 12, 13, 14, 16, 19, 20, 21, 22, 23, 24, 94, 143, and 188.]
- KING JR, T. E., Schwarz, M. I., Brown, K., Tooze, J. A., Colby, T. V., WALDRON JR, J. A., Flint, A., Thurlbeck, W., and Cherniack, R. M. (2001). Idiopathic pulmonary fibrosis: relationship between histopathologic features and mortality. *American journal of respiratory and critical care medicine*, 164(6):1025–1032. [Cited on page 19.]
- King Jr, T. E., Tooze, J. A., Schwarz, M. I., BROWN, K. R., and CHERNIACK, R. M. (2001). Predicting survival in idiopathic pulmonary fibrosis: scoring system and sur-

- vival model. *American journal of respiratory and critical care medicine*, 164(7):1171–1181. [Cited on page 13.]
- Kinsella, M., Müller, N. L., Abboud, R. T., Morrison, N. J., and DyBuncio, A. (1990). Quantitation of emphysema by computed tomography using a density mask program and correlation with pulmonary function tests. *Chest*, 97(2):315–321. [Not cited.]
- Kitasaka, T., Mori, K., Hasegawa, J.-i., and Toriwaki, J.-i. (2003). Lung area extraction from 3d chest x-ray ct images using a shape model generated by a variable bézier surface. *Systems and Computers in Japan*, 34(4):60–71. [Not cited.]
- Kitasaka, T., Nakada, Y., Mori, K., Suenaga, Y., Mori, M., Takabatake, H., and Natori, H. (2006). Recognition of lung lobes and its application to the bronchial structure analysis. In *Pattern Recognition, 2006. ICPR 2006. 18th International Conference on*, volume 3, pages 288–291. IEEE. [Not cited.]
- Knudson, R. J., Slatin, R. C., Lebowitz, M. D., and Burrows, B. (1976). The maximal expiratory flow-volume curve: normal standards, variability, and effects of age. *American Review of Respiratory Disease*, 113(5):587–600. [Not cited.]
- Knudson, R. J., Standen, J. R., Kaltenborn, W. T., Knudson, D. E., Rehm, K., Habib, M. P., and Newell, J. D. (1991). Expiratory computed tomography for assessment of suspected pulmonary emphysema. *Chest*, 99(6):1357–1366. [Not cited.]
- Koenderink, J. J. (1984). The structure of images. *Biological cybernetics*, 50(5):363–370. [Not cited.]
- Kondoh, Y., Taniguchi, H., Kataoka, K., Keisuke, K., Suzuki, R., Ogura, T., Johkoh, T., Yokoi, T., Wells, A. U., and Kitaichi, M. (2010). Prognostic factors in rapidly progressive interstitial pneumonia. *Respirology*, 15(2):257–264. [Cited on page 20.]
- Kondoh, Y., Taniguchi, H., Kawabata, Y., Yokoi, T., Suzuki, K., and Takagi, K. (1993).

- Acute exacerbation in idiopathic pulmonary fibrosis: analysis of clinical and pathologic findings in three cases. *Chest*, 103(6):1808–1812. [Cited on page 20.]
- Korfiatis, P., Kalogeropoulou, C., Karahaliou, A., Kazantzi, A., Skiadopoulos, S., and Costaridou, L. (2008). Texture classification-based segmentation of lung affected by interstitial pneumonia in high-resolution ct. *Medical physics*, 35(12):5290–5302. [Not cited.]
- Kornbluth, R. and Turino, G. (1980). Respiratory control in diffuse interstitial lung disease and diseases of the pulmonary vasculature. *Clinics in chest medicine*, 1(1):91–102. [Cited on page 28.]
- Krenz, G. S. and Dawson, C. A. (2003). Flow and pressure distributions in vascular networks consisting of distensible vessels. *American Journal of Physiology-Heart and Circulatory Physiology*, 284(6):H2192–H2203. [Not cited.]
- Kreuter, M., Ehlers-Tenenbaum, S., Palmowski, K., Bruhwyl, J., Oltmanns, U., Muley, T., Heussel, C. P., Warth, A., Kolb, M., and Herth, F. J. (2016). Impact of comorbidities on mortality in patients with idiopathic pulmonary fibrosis. *PLoS One*, 11(3):e0151425. [Cited on page 21.]
- Krumpe, P. E., Knudson, R. J., Parsons, G., and Reiser, K. (1985). The aging respiratory system. *Clinics in geriatric medicine*, 1(1):143–175. [Not cited.]
- Kuhnigk, J., Dicken, V., Zidowitz, S., Bornemann, L., Kuemmerlen, B., Krass, S., Peitgen, H., Yuval, S., Jend, H., Rau, W., et al. (2005). Informatics in radiology (inforad): New tools for computer assistance in thoracic ct. part 1. functional analysis of lungs. Lung Lobes, and Bronchopulmonary Segments. *RadioGraphics* 2005; 25: 525, 536. [Not cited.]
- Kuhnigk, J.-M., Hahn, H., Hindennach, M., Dicken, V., Krass, S., and Peitgen, H.-O.

- (2003). Lung lobe segmentation by anatomy-guided 3 d watershed transform. In Proceedings of SPIE, volume 5032, pages 1482–1490. [Not cited.]
- Kundel, H. L. (2006). History of research in medical image perception. *Journal of the American College of Radiology*, 3(6):402–408. [Not cited.]
- Kwan, M., Woo, J., and Kwok, T. (2004). The standard oxygen consumption value equivalent to one metabolic equivalent (3.5 ml/min/kg) is not appropriate for elderly people. *International journal of food sciences and nutrition*, 55(3):179–182. [Not cited.]
- Lalley, P. M. (2013). The aging respiratory systempulmonary structure, function and neural control. *Respiratory physiology & neurobiology*, 187(3):199–210. [Not cited.]
- Larsson, L. (1983). Histochemical characteristics of human skeletal muscle during aging. *Acta physiologica Scandinavica*, 117(3):469–471. [Not cited.]
- Lassen, B., Kuhnigk, J.-M., Friman, O., Krass, S., and Peitgen, H.-O. (2010). Automatic segmentation of lung lobes in ct images based on fissures, vessels, and bronchi. In Biomedical Imaging: From Nano to Macro, 2010 IEEE International Symposium on, pages 560–563. IEEE. [Not cited.]
- Lassen, B., Kuhnigk, J.-M., Van Rikxoort, E. M., and Peitgen, H.-O. (2011). Interactive lung lobe segmentation and correction in tomographic images. In Medical Imaging 2011: Computer-Aided Diagnosis, volume 7963, page 79631S. International Society for Optics and Photonics. [Not cited.]
- Lassen, B., van Rikxoort, E. M., Schmidt, M., Kerkstra, S., van Ginneken, B., and Kuhnigk, J.-M. (2013). Automatic segmentation of the pulmonary lobes from chest ct scans based on fissures, vessels, and bronchi. *IEEE transactions on medical imaging*, 32(2):210–222. [Not cited.]

- Leader, J. K., Zheng, B., Rogers, R. M., Sciurba, F. C., Perez, A., Chapman, B. E., Patel, S., Fuhrman, C. R., and Gur, D. (2003). Automated lung segmentation in x-ray computed tomography: development and evaluation of a heuristic threshold-based scheme1. *Academic radiology*, 10(11):1224–1236. [Not cited.]
- Lee, H.-L., Ryu, J. H., Wittmer, M. H., Hartman, T. E., Lymp, J. F., Tazelaar, H. D., and Limper, A. H. (2005). Familial idiopathic pulmonary fibrosis: clinical features and outcome. *Chest*, 127(6):2034–2041. [Cited on page 12.]
- Lee, S., Wolberg, G., and Shin, S. Y. (1997). Scattered data interpolation with multilevel b-splines. *IEEE transactions on visualization and computer graphics*, 3(3):228–244. [Not cited.]
- Lettieri, C. J., Nathan, S. D., Barnett, S. D., Ahmad, S., and Shorr, A. F. (2006). Prevalence and outcomes of pulmonary arterial hypertension in advanced idiopathic pulmonary fibrosis. *Chest*, 129(3):746–752. [Cited on pages 19, 20, and 23.]
- Leung, A. N. (1999). Pulmonary tuberculosis: the essentials. *Radiology*, 210(2):307–322. [Not cited.]
- Levitzky, M. G. (1984). Effects of aging on the respiratory system. *Physiologist*, 27(2):102–107. [Not cited.]
- Ley, B., Collard, H. R., and King Jr, T. E. (2011). Clinical course and prediction of survival in idiopathic pulmonary fibrosis. *American journal of respiratory and critical care medicine*, 183(4):431–440. [Cited on pages xvi, 19, 20, and 21.]
- Ley-Zaporozhan, J., Ley, S., Weinheimer, O., Iliyushenko, S., Erdugan, S., Eberhardt, R., Fuxa, A., Mews, J., and Kauczor, H.-U. (2008). Quantitative analysis of emphysema in 3d using mdct: influence of different reconstruction algorithms. *European journal of radiology*, 65(2):228–234. [Not cited.]

- Li, Q., Sone, S., et al. (2003). Selective enhancement filters for nodules, vessels, and airway walls in two-and three-dimensional ct scans. *Medical physics*, 30(8):2040–2051. [Not cited.]
- Lin, H. and Jiang, S. (2015). Combined pulmonary fibrosis and emphysema (cpfe): an entity different from emphysema or pulmonary fibrosis alone. *Journal of thoracic disease*, 7(4):767. [Cited on pages 22, 38, 143, and 188.]
- Lorenz, C., Carlsen, I.-C., Buzug, T. M., Fassnacht, C., and Weese, J. (1997). Multi-scale line segmentation with automatic estimation of width, contrast and tangential direction in 2d and 3d medical images. In *CVRMed-MRCAS'97*, pages 233–242. Springer. [Not cited.]
- Lynch, D. A. (2007). Quantitative ct of fibrotic interstitial lung disease. *Chest*, 131(3):643–644. [Not cited.]
- Lynch, D. A., Godwin, J. D., Safrin, S., Starko, K. M., Hormel, P., Brown, K. K., Raghu, G., King Jr, T. E., Bradford, W. Z., Schwartz, D. A., et al. (2005). High-resolution computed tomography in idiopathic pulmonary fibrosis: diagnosis and prognosis. *American journal of respiratory and critical care medicine*, 172(4):488–493. [Not cited.]
- Lynch, J. P., Saggar, R., Weigt, S. S., Zisman, D. A., and White, E. S. (2006). Usual interstitial pneumonia. In *Seminars in respiratory and critical care medicine*, volume 27, pages 634–651. Copyright© 2006 by Thieme Medical Publishers, Inc., 333 Seventh Avenue, New York, NY 10001, USA. [Cited on page 18.]
- Maldonado, F., Moua, T., Rajagopalan, S., Karwoski, R. A., Raghunath, S., Decker, P. A., Hartman, T. E., Bartholmai, B. J., Robb, R. A., and Ryu, J. H. (2013). Automated quantification of radiologic patterns predicts survival in idiopathic pulmonary fibrosis. *European Respiratory Journal*, pages erj00718–2012. [Not cited.]

- Martinez, F. J., Collard, H. R., Pardo, A., Raghu, G., Richeldi, L., Selman, M., Swigris, J. J., Taniguchi, H., and Wells, A. U. (2017). Idiopathic pulmonary fibrosis. *Nature Reviews Disease Primers*, 3:17074. [Cited on pages xv, 8, 15, 21, and 22.]
- Martinez, F. J. and Flaherty, K. (2006). Pulmonary function testing in idiopathic interstitial pneumonias. *Proceedings of the American Thoracic Society*, 3(4):315–321. [Cited on pages 26 and 27.]
- McClaran, S., Babcock, M., Pegelow, D., Reddan, W., and Dempsey, J. (1995). Longitudinal effects of aging on lung function at rest and exercise in healthy active fit elderly adults. *Journal of Applied Physiology*, 78(5):1957–1968. [Not cited.]
- Mejía, M., Carrillo, G., Rojas-Serrano, J., Estrada, A., Suárez, T., Alonso, D., Barrientos, E., Gaxiola, M., Navarro, C., and Selman, M. (2009). Idiopathic pulmonary fibrosis and emphysema: decreased survival associated with severe pulmonary arterial hypertension. *Chest*, 136(1):10–15. [Cited on pages 19, 22, and 23.]
- Meltzer, E. B. and Noble, P. W. (2008). Idiopathic pulmonary fibrosis. *Orphanet journal of rare diseases*, 3(1):8. [Cited on pages 1, 7, 8, 9, 10, 11, 19, 20, 22, and 143.]
- Miki, K., Maekura, R., Hiraga, T., Hashimoto, H., Kitada, S., Miki, M., Yoshimura, K., Tateishi, Y., Fushitani, K., and Motone, M. (2009). Acidosis and raised norepinephrine levels are associated with exercise dyspnoea in idiopathic pulmonary fibrosis. *Respirology*, 14(7):1020–1026. [Cited on page 30.]
- Misumi, S. and Lynch, D. A. (2006). Idiopathic pulmonary fibrosis/usual interstitial pneumonia: imaging diagnosis, spectrum of abnormalities, and temporal progression. *Proceedings of the American Thoracic Society*, 3(4):307–314. [Not cited.]
- Mittman, C., Edelman, N. H., Norris, A. H., and Shock, N. W. (1965). Relationship between chest wall and pulmonary compliance and age. *Journal of Applied Physiology*, 20(6):1211–1216. [Not cited.]

- Miyamura, M. and HONDA, Y. (1973). Maximum cardiac output related to sex and age. *The Japanese journal of physiology*, 23(6):645–656. [Not cited.]
- Monaghan, H., Wells, A. U., Colby, T. V., Du Bois, R. M., Hansell, D. M., and Nicholson, A. G. (2004). Prognostic implications of histologic patterns in multiple surgical lung biopsies from patients with idiopathic interstitial pneumonias. *Chest*, 125(2):522–526. [Not cited.]
- Mueller-Mang, C., Grosse, C., Schmid, K., Stiebellehner, L., and Bankier, A. A. (2007). What every radiologist should know about idiopathic interstitial pneumonias. *Radiographics*, 27(3):595–615. [Not cited.]
- Müller, N. L., Staples, C. A., Miller, R. R., and Abboud, R. T. (1988). density mask: an objective method to quantitate emphysema using computed tomography. *Chest*, 94(4):782–787. [Not cited.]
- Mura, M., Zompatori, M., Pacilli, A. M. G., Fasano, L., Schiavina, M., and Fabbri, M. (2006). The presence of emphysema further impairs physiologic function in patients with idiopathic pulmonary fibrosis. *Respiratory care*, 51(3):257–265. [Cited on page 27.]
- Murray, J. F. (1986). The normal lung: the basis for diagnosis and treatment of pulmonary disease. WB Saunders Company. [Not cited.]
- Musk, A., Zilko, P., Manners, P., Kay, P., and Kamboh, M. (1986). Genetic studies in familial fibrosing alveolitis: possible linkage with immunoglobulin allotypes (gm). *Chest*, 89(2):206–210. [Cited on page 12.]
- Nadrous, H. F., Pellikka, P. A., Krowka, M. J., Swanson, K. L., et al. (2005). The impact of pulmonary hypertension on survival in patients with idiopathic pulmonary fibrosis. *Chest*, 128(6):616S. [Cited on page 23.]

- Naidich, D. P. (2005). Imaging of the airways: functional and radiologic correlations. Lippincott Williams & Wilkins. [Not cited.]
- Nava, S. and Rubini, F. (1999). Lung and chest wall mechanics in ventilated patients with end stage idiopathic pulmonary fibrosis. *Thorax*, 54(5):390–395. [Cited on page 26.]
- Nicholson, A. G., Colby, T. V., Dubois, R. M., Hansell, D. M., and Wells, A. U. (2000). The prognostic significance of the histologic pattern of interstitial pneumonia in patients presenting with the clinical entity of cryptogenic fibrosing alveolitis. *American journal of respiratory and critical care medicine*, 162(6):2213–2217. [Cited on page 19.]
- Nishimura, K., Kitaichi, M., Izumi, T., Nagai, S., Kanaoka, M., and Itoh, H. (1992). Usual interstitial pneumonia: histologic correlation with high-resolution ct. *Radiology*, 182(2):337–342. [Cited on page 14.]
- Ochs, R. A., Goldin, J. G., Abtin, F., Kim, H. J., Brown, K., Batra, P., Roback, D., McNitt-Gray, M. F., and Brown, M. S. (2007). Automated classification of lung bronchovascular anatomy in ct using adaboost. *Medical image analysis*, 11(3):315–324. [Not cited.]
- Okada, T., Shimada, R., Hori, M., Nakamoto, M., Chen, Y.-W., Nakamura, H., and Sato, Y. (2008). Automated segmentation of the liver from 3d ct images using probabilistic atlas and multilevel statistical shape model. *Academic radiology*, 15(11):1390–1403. [Not cited.]
- Olson, A. L., Swigris, J. J., Lezotte, D. C., Norris, J. M., Wilson, C. G., and Brown, K. K. (2007). Mortality from pulmonary fibrosis increased in the united states from 1992 to 2003. *American journal of respiratory and critical care medicine*, 176(3):277–284. [Not cited.]

- Orens, J. B., Kazerooni, E. A., Martinez, F. J., Curtis, J. L., Gross, B. H., Flint, A., and Lynch III, J. P. (1995). The sensitivity of high-resolution ct in detecting idiopathic pulmonary fibrosis proved by open lung biopsy: a prospective study. *Chest*, 108(1):109–115. [Cited on page 26.]
- Organ, L., Bacci, B., Koumoundouros, E., Barcham, G., Milne, M., Kimpton, W., Samuel, C., and Snibson, K. (2015). Structural and functional correlations in a large animal model of bleomycin-induced pulmonary fibrosis. *BMC pulmonary medicine*, 15(1):81. [Cited on page 26.]
- Paoletti, P., Viegi, G., Pistelli, G., Di Pede, F., Fazzi, P., Polato, R., Saetta, M., Zambon, R., Carli, G., Giuntini, C., et al. (1985). Reference equations for the single-breath diffusing capacity: a cross-sectional analysis and effect of body size and age. *American Review of Respiratory Disease*, 132(4):806–813. [Not cited.]
- Parambil, J. G., Myers, J. L., and Ryu, J. H. (2005). Histopathologic features and outcome of patients with acute exacerbation of idiopathic pulmonary fibrosis undergoing surgical lung biopsy. *Chest*, 128(5):3310–3315. [Cited on page 20.]
- Pastre, J., Plantier, L., Planes, C., Borie, R., Nunes, H., Delclaux, C., and Israël-Biet, D. (2015). Different k_{CO} and V_A combinations exist for the same DL_{CO} value in patients with diffuse parenchymal lung diseases. *BMC pulmonary medicine*, 15(1):100. [Cited on pages 27 and 30.]
- Pedley, T., Schroter, R., and Sudlow, M. (1970). Energy losses and pressure drop in models of human airways. *Respiration physiology*, 9(3):371–386. [Not cited.]
- Pelosi, P., Croci, M., Ravagnan, I., Tredici, S., Pedoto, A., Lissoni, A., and Gattinoni, L. (1998). The effects of body mass on lung volumes, respiratory mechanics, and gas exchange during general anesthesia. *Anesthesia & Analgesia*, 87(3):654–660. [Not cited.]

- Plantier, L., Cazes, A., Dinh-Xuan, A.-T., Bancal, C., Marchand-Adam, S., and Crestani, B. (2018). Physiology of the lung in idiopathic pulmonary fibrosis. *European Respiratory Review*, 27(147):170062. [Cited on pages xxxvii, 24, 25, 26, 27, 28, 29, 30, 32, and 195.]
- Plantier, L., Debray, M.-P., Estellat, C., Flamant, M., Roy, C., Bancal, C., Borie, R., Israël-Biet, D., Mal, H., Crestani, B., et al. (2016). Increased volume of conducting airways in idiopathic pulmonary fibrosis is independent of disease severity: a volumetric capnography study. *Journal of breath research*, 10(1):016005. [Cited on pages 27, 28, 30, and 159.]
- Pollock, M. L., Mengelkoch, L. J., Graves, J. E., Lowenthal, D. T., Limacher, M. C., Foster, C., and Wilmore, J. H. (1997). Twenty-year follow-up of aerobic power and body composition of older track athletes. *Journal of Applied Physiology*, 82(5):1508–1516. [Not cited.]
- Prasad, M. N., Brown, M. S., Ahmad, S., Abtin, F., Allen, J., da Costa, I., Kim, H. J., McNitt-Gray, M. F., and Goldin, J. G. (2008). Automatic segmentation of lung parenchyma in the presence of diseases based on curvature of ribs. *Academic radiology*, 15(9):1173–1180. [Not cited.]
- Pries, A., Secomb, T., and Gaehtgens, P. (1996). Biophysical aspects of blood flow in the microvasculature. *Cardiovascular research*, 32(4):654–667. [Not cited.]
- Pu, J., Leader, J. K., Zheng, B., Knollmann, F., Fuhrman, C., Sciurba, F. C., and Gur, D. (2009a). A computational geometry approach to automated pulmonary fissure segmentation in ct examinations. *IEEE transactions on medical imaging*, 28(5):710–719. [Not cited.]
- Pu, J., Paik, D. S., Meng, X., Roos, J., and Rubin, G. D. (2011). Shape break-and-

- repair strategy and its application to automated medical image segmentation. *IEEE transactions on visualization and computer graphics*, 17(1):115–124. [Not cited.]
- Pu, J., Roos, J., Chin, A. Y., Napel, S., Rubin, G. D., and Paik, D. S. (2008). Adaptive border marching algorithm: automatic lung segmentation on chest ct images. *Computerized Medical Imaging and Graphics*, 32(6):452–462. [Not cited.]
- Pu, J., Zheng, B., Leader, J. K., Fuhrman, C., Knollmann, F., Klym, A., and Gur, D. (2009b). Pulmonary lobe segmentation in ct examinations using implicit surface fitting. *IEEE transactions on medical imaging*, 28(12):1986–1996. [Not cited.]
- Quadrelli, S., Molinari, L., Ciallella, L., Spina, J. C., Sobrino, E., and Chertcoff, J. (2010). Radiological versus histopathological diagnosis of usual interstitial pneumonia in the clinical practice: does it have any survival difference? *Respiration*, 79(1):32–37. [Cited on page 17.]
- Raghu, G. (1987). Idiopathic pulmonary fibrosis: a rational clinical approach. *Chest*, 92(1):148–154. [Cited on page 19.]
- Raghu, G., Amatto, V. C., Behr, J., and Stowasser, S. (2015). Comorbidities in idiopathic pulmonary fibrosis patients: a systematic literature review. *European Respiratory Journal*, 46(4):1113–1130. [Cited on page 22.]
- Raghu, G., Collard, H. R., Egan, J. J., Martinez, F. J., Behr, J., Brown, K. K., Colby, T. V., Cordier, J.-F., Flaherty, K. R., Lasky, J. A., et al. (2011). An official ats/ers/jrs/alat statement: idiopathic pulmonary fibrosis: evidence-based guidelines for diagnosis and management. *American journal of respiratory and critical care medicine*, 183(6):788–824. [Cited on pages xvi, 1, 2, 7, 8, 10, 11, 12, 13, 14, 15, 16, 17, 18, 19, 20, 21, 23, 24, 94, and 141.]
- Raghu, G., Mageto, Y. N., Lockhart, D., Schmidt, R. A., Wood, D. E., and Godwin, J. D. (1999). The accuracy of the clinical diagnosis of new-onset idiopathic pulmonary

- fibrosis and other interstitial lung disease: a prospective study. *Chest*, 116(5):1168–1174. [Cited on page 17.]
- Raghu, G., Weycker, D., Edelsberg, J., Bradford, W. Z., and Oster, G. (2006). Incidence and prevalence of idiopathic pulmonary fibrosis. *American journal of respiratory and critical care medicine*, 174(7):810–816. [Cited on pages 10 and 14.]
- Raghunath, S., Rajagopalan, S., Karwoski, R. A., Maldonado, F., Peikert, T., Moua, T., Ryu, J. H., Bartholmai, B. J., and Robb, R. A. (2014). Quantitative stratification of diffuse parenchymal lung diseases. *PLoS One*, 9(3):e93229. [Not cited.]
- Rees, D. and Murray, J. (2007). Silica, silicosis and tuberculosis [state of the art series. occupational lung disease in high-and low-income countries, edited by m. chan-yeung. number 4 in the series]. *The International Journal of Tuberculosis and Lung Disease*, 11(5):474–484. [Not cited.]
- Renzi, G., Milic-Emili, J., and Grassino, A. (1982). The pattern of breathing in diffuse lung fibrosis. *Bulletin europeen de physiopathologie respiratoire*, 18(3):461–472. [Cited on page 28.]
- Richeldi, L., Collard, H. R., and Jones, M. G. (2017). Idiopathic pulmonary fibrosis. *The Lancet*, 389(10082):1941–1952. [Cited on pages 1, 2, 8, 10, 11, 12, 13, 14, 15, 16, and 94.]
- Rohlf, F. J. (1999). Shape statistics: Procrustes superimpositions and tangent spaces. *Journal of Classification*, 16(2):197–223. [Not cited.]
- Rosenberg, E. (1996). The 1995 update of recommendations for a standard technique for measuring the single-breath carbon monoxide diffusing capacity (transfer factor). *American journal of respiratory and critical care medicine*, 154(3):827–828. [Cited on page 29.]

- Ross, J. C., Estépar, R. S. J., Kindlmann, G., Díaz, A., Westin, C.-F., Silverman, E. K., and Washko, G. R. (2010). Automatic lung lobe segmentation using particles, thin plate splines, and maximum a posteriori estimation. In International Conference on Medical Image Computing and Computer-Assisted Intervention, pages 163–171. Springer. [Not cited.]
- Ross, J. C., Kindlmann, G. L., Okajima, Y., Hatabu, H., Díaz, A. A., Silverman, E. K., Washko, G. R., Dy, J., and Estépar, R. S. J. (2013). Pulmonary lobe segmentation based on ridge surface sampling and shape model fitting. *Medical physics*, 40(12). [Not cited.]
- Rudd, R. M., Prescott, R. J., Chalmers, J., and Johnston, I. D. (2007). British thoracic society study on cryptogenic fibrosing alveolitis: response to treatment and survival. *Thorax*, 62(1):62–66. [Cited on page 19.]
- Ryu, J. H., Moua, T., Daniels, C. E., Hartman, T. E., Eunhee, S. Y., Utz, J. P., and Limper, A. H. (2014). Idiopathic pulmonary fibrosis: evolving concepts. In Mayo Clinic proceedings, volume 89, pages 1130–1142. Elsevier. [Cited on pages 19 and 20.]
- Saita, S., Kubo, M., Kawata, Y., Niki, N., Ohmatsu, H., and Moriyama, N. (2006). An algorithm for the extraction of pulmonary fissures from low-dose multislice ct image. *Systems and Computers in Japan*, 37(9):63–76. [Not cited.]
- Sakamoto, K., Taniguchi, H., Kondoh, Y., Ono, K., Hasegawa, Y., and Kitaichi, M. (2009). Acute exacerbation of idiopathic pulmonary fibrosis as the initial presentation of the disease. *European Respiratory Review*, 18(112):129–132. [Cited on page 20.]
- Saketkoo, L. A., Matteson, E. L., Brown, K. K., Seibold, J. R., and Strand, V. (2011). Developing disease activity and response criteria in connective tissue disease-related interstitial lung disease. *The Journal of rheumatology*, 38(7):1514–1518. [Not cited.]

- Sato, Y., Westin, C.-F., Bhalerao, A., Nakajima, S., Shiraga, N., Tamura, S., and Kikinis, R. (2000). Tissue classification based on 3d local intensity structures for volume rendering. *IEEE transactions on visualization and computer graphics*, 6(2):160–180. [Not cited.]
- Schmidt, R., Meier, U., Markart, P., Grimminger, F., Velcovsky, H., Morr, H., Seeger, W., and Gunther, A. (2002). Altered fatty acid composition of lung surfactant phospholipids in interstitial lung disease. *American Journal of Physiology-Lung Cellular and Molecular Physiology*, 283(5):L1079–L1085. [Cited on page 24.]
- Seibold, M. A., Wise, A. L., Speer, M. C., Steele, M. P., Brown, K. K., Loyd, J. E., Finerlin, T. E., Zhang, W., Gudmundsson, G., Groshong, S. D., et al. (2011). A common muc5b promoter polymorphism and pulmonary fibrosis. *New England Journal of Medicine*, 364(16):1503–1512. [Cited on page 12.]
- Selman, M., Carrillo, G., Estrada, A., Mejia, M., Becerril, C., Cisneros, J., Gaxiola, M., Pérez-Padilla, R., Navarro, C., Richards, T., et al. (2007). Accelerated variant of idiopathic pulmonary fibrosis: clinical behavior and gene expression pattern. *PloS one*, 2(5):e482. [Cited on page 19.]
- Shikata, H., McLennan, G., Hoffman, E. A., and Sonka, M. (2009). Segmentation of pulmonary vascular trees from thoracic 3d ct images. *Journal of Biomedical Imaging*, 2009:24. [Not cited.]
- Silva, C. I. S., Muller, N. L., Lynch, D. A., Curran-Everett, D., Brown, K. K., Lee, K. S., Chung, M. P., and Churg, A. (2008a). Chronic hypersensitivity pneumonitis: differentiation from idiopathic pulmonary fibrosis and nonspecific interstitial pneumonia by using thin-section ct. *Radiology*, 246(1):288–297. [Cited on page 18.]
- Silva, D. R., Gazzana, M. B., Barreto, S. S. M., and Knorst, M. M. (2008b). Idiopathic

- pulmonary fibrosis and emphysema in smokers. *Jornal Brasileiro de Pneumologia*, 34(10):779–786. [Cited on page 22.]
- Slebos, D.-J., van Rikxoort, E. M., and van der Bij, W. (2015). Air trapping in emphysema. *American journal of respiratory and critical care medicine*, 192(5):e45–e45. [Not cited.]
- Sluimer, I., Prokop, M., and Van Ginneken, B. (2005). Toward automated segmentation of the pathological lung in ct. *IEEE transactions on medical imaging*, 24(8):1025–1038. [Not cited.]
- Smith, T. (1986). Respiratory effects of aging. In *Seminars in Anesthesia*, volume 5, pages 14–22. WB SAUNDERS CO INDEPENDENCE SQUARE WEST CURTIS CENTER, STE 300, PHILADELPHIA, PA 19106-3399. [Not cited.]
- Society, A. T. et al. (2000). Idiopathic pulmonary fibrosis: diagnosis and treatment: international consensus statement. *Am J Respir Crit Care Med*, 161:646–664. [Cited on pages 15, 24, 26, 28, 29, 31, and 32.]
- Souza, C. A., Muller, N. L., Lee, K. S., Johkoh, T., Mitsuhiro, H., and Chong, S. (2006). Idiopathic interstitial pneumonias: prevalence of mediastinal lymph node enlargement in 206 patients. *American Journal of Roentgenology*, 186(4):995–999. [Cited on page 14.]
- Sprung, J., Gajic, O., and Warner, D. O. (2006). age related alterations in respiratory functionanesthetic considerations. *Canadian journal of anesthesia*, 53(12):1244. [Not cited.]
- Steele, M. P., Speer, M. C., Loyd, J. E., Brown, K. K., Herron, A., Slifer, S. H., Burch, L. H., Wahidi, M. M., Phillips III, J. A., Sporn, T. A., et al. (2005). Clinical and pathologic features of familial interstitial pneumonia. *American journal of respiratory and critical care medicine*, 172(9):1146–1152. [Cited on page 12.]

- Stegmann, M. B. and Gomez, D. D. (2002). A brief introduction to statistical shape analysis. *Informatics and mathematical modelling*, Technical University of Denmark, DTU, 15(11). [Not cited.]
- Stelfox, H. T., Ahmed, S. B., Ribeiro, R. A., Gettings, E. M., Pomerantsev, E., and Schmidt, U. (2006). Hemodynamic monitoring in obese patients: the impact of body mass index on cardiac output and stroke volume. *Critical care medicine*, 34(4):1243–1246. [Not cited.]
- Strickland, N., Hughes, J., Hart, D., Myers, M., and Lavender, J. (1993). Cause of regional ventilation-perfusion mismatching in patients with idiopathic pulmonary fibrosis: a combined ct and scintigraphic study. *AJR. American journal of roentgenology*, 161(4):719–725. [Cited on pages 30 and 31.]
- Styner, M., Gerig, G., Lieberman, J., Jones, D., and Weinberger, D. (2003). Statistical shape analysis of neuroanatomical structures based on medial models. *Medical image analysis*, 7(3):207–220. [Not cited.]
- Sumikawa, H., Johkoh, T., Colby, T. V., Ichikado, K., Suga, M., Taniguchi, H., Kondoh, Y., Ogura, T., Arakawa, H., Fujimoto, K., et al. (2008). Computed tomography findings in pathological usual interstitial pneumonia: relationship to survival. *American journal of respiratory and critical care medicine*, 177(4):433–439. [Cited on pages 28 and 96.]
- Sun, S., Bauer, C., and Beichel, R. (2012). Automated 3-d segmentation of lungs with lung cancer in ct data using a novel robust active shape model approach. *IEEE transactions on medical imaging*, 31(2):449–460. [Not cited.]
- Sun, X., Zhang, H., and Duan, H. (2006). 3d computerized segmentation of lung volume with computed tomography. *Academic radiology*, 13(6):670–677. [Not cited.]

- Sverzellati, N., Devaraj, A., Desai, S. R., Quigley, M., Wells, A. U., and Hansell, D. M. (2011). Method for minimizing observer variation for the quantitation of high-resolution computed tomographic signs of lung disease. *Journal of computer assisted tomography*, 35(5):596–601. [Not cited.]
- Swan, A. (2010). A multi-scale computational model of pulmonary gas exchange. PhD thesis, University of Auckland. [Not cited.]
- Swan, A. J., Clark, A. R., and Tawhai, M. H. (2012). A computational model of the topographic distribution of ventilation in healthy human lungs. *Journal of Theoretical Biology*, 300:222–231. [Not cited.]
- Swan, A. J. and Tawhai, M. H. (2010). Evidence for minimal oxygen heterogeneity in the healthy human pulmonary acinus. *Journal of applied physiology*, 110(2):528–537. [Not cited.]
- Swigris, J. J., Han, M., Vij, R., Noth, I., Eisenstein, E. L., Anstrom, K. J., Brown, K. K., and Fairclough, D. (2012). The ucsd shortness of breath questionnaire has longitudinal construct validity in idiopathic pulmonary fibrosis. *Respiratory medicine*, 106(10):1447–1455. [Cited on page 30.]
- Taskar, V. S. and Coultas, D. B. (2006). Is idiopathic pulmonary fibrosis an environmental disease? *Proceedings of the American Thoracic Society*, 3(4):293–298. [Cited on page 11.]
- Tawhai, M. H. and Burrowes, K. S. (2003). Developing integrative computational models of pulmonary structure. *The Anatomical Record*, 275(1):207–218. [Not cited.]
- Tawhai, M. H., Hunter, P., Tschirren, J., Reinhardt, J., McLennan, G., and Hoffman, E. A. (2004). Ct-based geometry analysis and finite element models of the human and ovine bronchial tree. *Journal of applied physiology*, 97(6):2310–2321. [Not cited.]

- Tawhai, M. H., Nash, M. P., Lin, C.-L., and Hoffman, E. A. (2009). Supine and prone differences in regional lung density and pleural pressure gradients in the human lung with constant shape. *Journal of Applied Physiology*, 107(3):912–920. [Not cited.]
- Tawhai, M. H., Pullan, A., and Hunter, P. (2000). Generation of an anatomically based three-dimensional model of the conducting airways. *Annals of biomedical engineering*, 28(7):793–802. [Not cited.]
- Taylor, C., Cootes, T., Hill, A., and Haslam, J. (1995). Medical image segmentation using active shape models. *STUDIES IN HEALTH TECHNOLOGY AND INFORMATICS*, 19:121–144. [Not cited.]
- Thurlbeck, W. M. and Angus, G. E. (1975). Growth and aging of the normal human lung. *Chest*, 67(2 Suppl):3S–6S. [Not cited.]
- Trahan, S., Hanak, V., Ryu, J. H., and Myers, J. L. (2008). Role of surgical lung biopsy in separating chronic hypersensitivity pneumonia from usual interstitial pneumonia/idiopathic pulmonary fibrosis*: Analysis of 31 biopsies from 15 patients. *Chest*, 134(1):126–132. [Cited on page 18.]
- Travis, W. D., Costabel, U., Hansell, D. M., King Jr, T. E., Lynch, D. A., Nicholson, A. G., Ryerson, C. J., Ryu, J. H., Selman, M., Wells, A. U., et al. (2013). An official american thoracic society/european respiratory society statement: update of the international multidisciplinary classification of the idiopathic interstitial pneumonias. *American journal of respiratory and critical care medicine*, 188(6):733–748. [Cited on pages 10 and 94.]
- Travis, W. D., King, T. E., Bateman, E. D., Lynch, D. A., Capron, F., Center, D., Colby, T. V., Cordier, J. F., DuBois, R. M., Galvin, J., et al. (2002). American thoracic society/european respiratory society international multidisciplinary consensus classi-

- fication of the idiopathic interstitial pneumonias. *American journal of respiratory and critical care medicine*, 165(2):277–304. [Cited on page 16.]
- Troy, L. and Corte, T. J. (2012). Management of the idiopathic interstitial pneumonias. *Australian Prescriber*, 35(6):202–6. [Cited on pages xv and 9.]
- Tsai, A., Yezzi, A., Wells, W., Tempany, C., Tucker, D., Fan, A., Grimson, W. E., and Willsky, A. (2003). A shape-based approach to the segmentation of medical imagery using level sets. *IEEE transactions on medical imaging*, 22(2):137–154. [Not cited.]
- Tukiainen, P., Taskinen, E., Holsti, P., Korhola, O., and Valle, M. (1983). Prognosis of cryptogenic fibrosing alveolitis. *Thorax*, 38(5):349–355. [Cited on page 19.]
- Turner, J. M., Mead, J., and Wohl, M. E. (1968). Elasticity of human lungs in relation to age. *Journal of applied physiology*, 25(6):664–671. [Not cited.]
- Uchiyama, Y., Katsuragawa, S., Abe, H., Shiraishi, J., Li, F., Li, Q., Zhang, C.-T., Suzuki, K., et al. (2003). Quantitative computerized analysis of diffuse lung disease in high-resolution computed tomography. *Medical Physics*, 30(9):2440–2454. [Not cited.]
- Ukil, S. and Reinhardt, J. M. (2005). Smoothing lung segmentation surfaces in three-dimensional x-ray ct images using anatomic guidance1. *Academic radiology*, 12(12):1502–1511. [Not cited.]
- Ukil, S. and Reinhardt, J. M. (2009). Anatomy-guided lung lobe segmentation in x-ray ct images. *IEEE transactions on medical imaging*, 28(2):202–214. [Not cited.]
- Uppaluri, R., Hoffman, E. A., Sonka, M., Hartley, P. G., Hunninghake, G. W., and McLennan, G. (1999a). Computer recognition of regional lung disease patterns. *American journal of respiratory and critical care medicine*, 160(2):648–654. [Not cited.]

- Uppaluri, R., Hoffman, E. A., Sonka, M., Hunninghake, G. W., and McLennan, G. (1999b). Interstitial lung disease: a quantitative study using the adaptive multiple feature method. *American journal of respiratory and critical care medicine*, 159(2):519–525. [Not cited.]
- Van Ginneken, B., Katsuragawa, S., ter Haar Romeny, B. M., Doi, K., and Viergever, M. A. (2002). Automatic detection of abnormalities in chest radiographs using local texture analysis. *IEEE transactions on medical imaging*, 21(2):139–149. [Not cited.]
- van Rikxoort, E. M., de Hoop, B., Viergever, M. A., Prokop, M., and van Ginneken, B. (2009). Automatic lung segmentation from thoracic computed tomography scans using a hybrid approach with error detection. *Medical physics*, 36(7):2934–2947. [Not cited.]
- Van Rikxoort, E. M. and Van Ginneken, B. (2013). Automated segmentation of pulmonary structures in thoracic computed tomography scans: a review. *Physics in medicine and biology*, 58(17):R187. [Not cited.]
- van Rikxoort, E. M., van Ginneken, B., Klik, M., and Prokop, M. (2008). Supervised enhancement filters: Application to fissure detection in chest ct scans. *IEEE Transactions on Medical Imaging*, 27(1):1–10. [Not cited.]
- Verbeken, E. K., Cauberghe, M., Mertens, I., Clement, J., Lauweryns, J. M., and Van de Woestijne, K. P. (1992). The senile lung: comparison with normal and emphysematosus lungs 1. structural aspects. *Chest*, 101(3):793–799. [Not cited.]
- Vuorinen, K., Ohlmeier, S., Leppäranta, O., Salmenkivi, K., Myllärniemi, M., and Kinula, V. L. (2008). Peroxiredoxin ii expression and its association with oxidative stress and cell proliferation in human idiopathic pulmonary fibrosis. *Journal of Histotechnology & Cytochemistry*, 56(10):951–959. [Cited on page 27.]

- Wagner, P., Dantzker, D., Dueck, R., De Polo, J., Wasserman, K., and West, J. (1976). Distribution of ventilation-perfusion ratios in patients with interstitial lung disease. *Chest*, 69(2):256–257. [Cited on pages 31 and 32.]
- Wahba, W. (1983). Influence of aging on lung function-clinical significance of changes from age twenty. *Anesthesia & Analgesia*, 62(8):764–776. [Not cited.]
- Wallaert, B., Wemeau-Stervinou, L., Salleron, J., Tillie-Leblond, I., and Perez, T. (2012). Do we need exercise tests to detect gas exchange impairment in fibrotic idiopathic interstitial pneumonias? *Pulmonary medicine*, 2012. [Cited on page 30.]
- Walsh, S. L., Wells, A. U., Sverzellati, N., Devaraj, A., von der Thüsen, J., Yousem, S. A., Colby, T. V., Nicholson, A. G., and Hansell, D. M. (2015). Relationship between fibroblastic foci profusion and high resolution ct morphology in fibrotic lung disease. *BMC medicine*, 13(1):241. [Cited on page 28.]
- Wang, J., Betke, M., and Ko, J. P. (2004). Shape-based curve growing model and adaptive regularization for pulmonary fissure segmentation in ct. In International Conference on Medical Image Computing and Computer-Assisted Intervention, pages 541–548. Springer. [Not cited.]
- Wang, J., Betke, M., and Ko, J. P. (2006). Pulmonary fissure segmentation on ct. *Medical Image Analysis*, 10(4):530–547. [Not cited.]
- Wang, J., Li, F., and Li, Q. (2009). Automated segmentation of lungs with severe interstitial lung disease in ct. *Medical physics*, 36(10):4592–4599. [Not cited.]
- Wang, J.-S., Cherng, J.-M., Perng, D.-S., Lee, H.-S., and Wang, S. (2013). High-resolution computed tomography in assessment of patients with emphysema. *Respiratory care*, 58(4):614–622. [Not cited.]
- Wasserman, K. and Whipp, B. J. (1975). Exercise physiology in health and disease. *American Review of Respiratory Disease*, 112(2):219–249. [Cited on page 30.]

- Watadani, T., Sakai, F., Johkoh, T., Noma, S., Akira, M., Fujimoto, K., Bankier, A. A., Lee, K. S., Müller, N. L., Song, J.-W., et al. (2013). Interobserver variability in the ct assessment of honeycombing in the lungs. *Radiology*, 266(3):936–944. [Not cited.]
- Wei, Q., Hu, Y., Gelfand, G., and Macgregor, J. H. (2009). Segmentation of lung lobes in high-resolution isotropic ct images. *IEEE Transactions on biomedical engineering*, 56(5):1383–1393. [Not cited.]
- Weibel, E. (1997). Design and morphometry of the pulmonary gas exchanger. *The lung: scientific foundations*, 1:1147–57. [Not cited.]
- Weibel, E. R. (1984). *The pathway for oxygen: structure and function in the mammalian respiratory system*. Harvard University Press. [Not cited.]
- Weibel, E. R., Federspiel, W. J., Fryder-Doffey, F., Hsia, C. C., König, M., Stalder-Navarro, V., and Vock, R. (1993). Morphometric model for pulmonary diffusing capacity i. membrane diffusing capacity. *Respiration physiology*, 93(2):125–149. [Not cited.]
- Weibel, E. R., Sapoval, B., and Filoche, M. (2005). Design of peripheral airways for efficient gas exchange. *Respiratory physiology & neurobiology*, 148(1-2):3–21. [Not cited.]
- Wells, A. U., Desai, S. R., Rubens, M. B., Goh, N. S., Cramer, D., Nicholson, A. G., Colby, T. V., Du Bois, R. M., and Hansell, D. M. (2003). Idiopathic pulmonary fibrosis: a composite physiologic index derived from disease extent observed by computed tomography. *American journal of respiratory and critical care medicine*, 167(7):962–969. [Cited on pages 19, 22, 95, and 96.]
- Wells, A. U., King, A. D., Rubens, M. B., Cramer, D., Du Bois, R., and Hansell, D. M. (1997). Lone cryptogenic fibrosing alveolitis: a functional-morphologic correlation

- based on extent of disease on thin-section computed tomography. *American journal of respiratory and critical care medicine*, 155(4):1367–1375. [Cited on pages 22 and 30.]
- Wiemker, R., Bülow, T., and Blaffert, T. (2005). Unsupervised extraction of the pulmonary interlobar fissures from high resolution thoracic ct data. In *International Congress Series*, volume 1281, pages 1121–1126. Elsevier. [Not cited.]
- Wijesinghe, M. and Dow, L. (2005). The effect of aging on the respiratory skeletal muscles. *Principles and Practice of Geriatric Medicine*, 2:671–683. [Not cited.]
- Wootton, S. C., Kim, D. S., Kondoh, Y., Chen, E., Lee, J. S., Song, J. W., Huh, J. W., Taniguchi, H., Chiu, C., Boushey, H., et al. (2011). Viral infection in acute exacerbation of idiopathic pulmonary fibrosis. *American journal of respiratory and critical care medicine*, 183(12):1698–1702. [Cited on page 20.]
- Xaubet, A., Ancochea, J., and Molina-Molina, M. (2017). Idiopathic pulmonary fibrosis. *Medicina Clínica (English Edition)*, 148(4):170–175. [Cited on pages 2, 8, 10, 11, 12, 19, 21, 22, and 23.]
- Xu, Y., Sonka, M., McLennan, G., Guo, J., and Hoffman, E. A. (2006a). Mdct-based 3-d texture classification of emphysema and early smoking related lung pathologies. *IEEE transactions on medical imaging*, 25(4):464–475. [Not cited.]
- Xu, Y., van Beek, E. J., Hwanjo, Y., Guo, J., McLennan, G., and Hoffman, E. A. (2006b). Computer-aided classification of interstitial lung diseases via mdct: 3d adaptive multiple feature method (3d amfm). *Academic radiology*, 13(8):969–978. [Not cited.]
- Yamamoto, T., Kabus, S., Klinder, T., Lorenz, C., Von Berg, J., Blaffert, T., Loo Jr, B. W., and Keall, P. J. (2011). Investigation of four-dimensional computed tomography-based pulmonary ventilation imaging in patients with emphysematous lung regions. *Physics in medicine and biology*, 56(7):2279. [Not cited.]

- Zaugg, M. and Lucchinetti, E. (2000). Respiratory function in the elderly. *Anesthesiology Clinics of North America*, 18(1):47–58. [Not cited.]
- Zavaletta, V. A., Bartholmai, B. J., and Robb, R. A. (2007). High resolution multidetector ct-aided tissue analysis and quantification of lung fibrosis. *Academic radiology*, 14(7):772–787. [Not cited.]
- Zavaletta, V. A., Karwoski, R. A., Bartholmai, B., and Robb, R. A. (2006). High resolution multidetector ct aided tissue analysis and quantification of lung fibrosis. In *Medical Imaging 2006: Physiology, Function, and Structure from Medical Images*, volume 6143, page 61432Z. International Society for Optics and Photonics. [Not cited.]
- Zhang, J. (2013). Development of an automated system for building a large population-based statistical model of femur morphology. PhD thesis, ResearchSpace@ Auckland. [Not cited.]
- Zhang, L., Hoffman, E. A., and Reinhardt, J. M. (2006). Atlas-driven lung lobe segmentation in volumetric x-ray ct images. *IEEE transactions on medical imaging*, 25(1):1–16. [Not cited.]
- Zhang, X., Smith, N., and Webb, A. (2011). Medical imaging. In Feng, D. D., editor, *Biomedical Information Technology*. Elsevier Science, Oxford. [Not cited.]
- Zhou, X., Hayashi, T., Hara, T., Fujita, H., Yokoyama, R., Kiryu, T., and Hoshi, H. (2004). Automatic recognition of lung lobes and fissures from multislice ct images. In *Proceedings of SPIE*, volume 5370, pages 1629–1633. [Not cited.]
- Zhu, C., Qi, S., van Triest, H., Wang, S., Kang, Y., and Yue, Y. (2010). Automatic 3d segmentation of human airway tree in ct image. In *Biomedical Engineering and Informatics (BMEI), 2010 3rd International Conference on*, volume 1, pages 132–136. IEEE. [Not cited.]

Zielonka, T., Demkow, U., Radzikowska, E., Bialas, B., Filewska, M., Zycinska, K., Obrowski, M., Kowalski, J., Wardyn, K., and Skopinska-Rozewska, E. (2010). Angiogenic activity of sera from interstitial lung disease patients in relation to pulmonary function. *European journal of medical research*, 15(2):229. [Cited on page 26.]